Synthesis and Characterization of Magnetic Nanoparticles with Enhanced Thermal Stability

By

SUDHANSHU SHEKHAR PATI

Enrolment No: CHEM02200804010

Indira Gandhi Centre for Atomic Research, Kalpakkam,
Tamil Nadu, India 603 102

A Thesis submitted to the Board of Studies in Chemical Sciences
In partial fulfillment of requirements
For the degree of

DOCTOR OF PHILOSOPHY

of

HOMI BHABHA NATIONAL INSTITUTE

December, 2013

Homi Bhabha National Institute

Recommendations of the Viva Voce Board

As members of the Viva Voce Board, we certify that we have read the dissertation prepared by **SUDHANSHU SHEKHAR PATI** entitled **"Synthesis and Characterization of Magnetic Nanoparticles with Enhanced Thermal Stability"** and recommend that it may be accepted as fulfilling the dissertation requirement for the Degree of Doctor of Philosophy.

______________________________ **Date:** 30-5-14

Chairman- **Dr. M. Sai Baba**

______________________________ **Date:** 30.05.2014

Convener- **Dr. John Philip**

______________________________ **Date:** 30.5.2014

Examiner- **Prof. K.G. Suresh**

______________________________ **Date:** 30/5/2014

Member 1- **Dr. K.V.G. Kutty**

V. Jayaraman

______________________________ **Date:** 30.05.2014.

Member 2- **Dr. V. Jayaraman**

Final approval and acceptance of this dissertation is contingent upon the candidate's submission of the final copies of the dissertation to HBNI.

CERTIFICATE

I hereby certify that I have read this dissertation prepared under my direction and recommend that it may be accepted as fulfilling the dissertation requirement.

Date: 30.05.2014
Place: Kalpakkam

Dr. John Philip 30/5/14
(Convener/Guide)

STATEMENT BY AUTHOR

This dissertation has been submitted in partial fulfillment of requirements for an advanced degree at Homi Bhabha National Institute (HBNI) and is deposited in the Library to be made available to borrowers under rules of the HBNI.

Brief quotations from this dissertation are allowable without special permission, provided that accurate acknowledgement of source is made. Requests for permission for extended quotation from or reproduction of this manuscript in whole or in part may be granted by the Competent Authority of HBNI when in his or her judgment the proposed use of the material is in the interests of scholarship. In all other instances, however, permission must be obtained from the author.

Sudhanshu Shekhar Pati.

(S. S. Pati)

Kalpakkam
December, 2013

DECLARATION

I, hereby declare that the investigation presented in the thesis entitled "*Synthesis and Characterization of Magnetic Nanoparticles with Enhanced Thermal Stability*" submitted to **Homi Bhabha National Institute (HBNI)**, Mumbai, India, for the award of **Doctor of Philosophy** in **Chemical Sciences** is the record of work carried out by me during the period from August 2008 to August 2013 under the guidance of **Dr. John Philip**, Head, SMARTS, Metallurgy and Materials Group, Indira Gandhi Centre for Atomic Research, Kalpakkam. The work is original and has not been submitted earlier as a whole or in part for a degree/diploma at this or any other Institution/University.

Sudhanshu Shekhar Pati.

(S. S. Pati)

Kalpakkam
December, 2013

LIST OF PUBLICATIONS

Published

1. "High temperature phase transformation studies in magnetite nanoparticles doped with Co^{2+} ion", S. S. Pati, S. Gopinath, G. Panneerselvam, M. P. Antony and J. Philip, *J. Appl. Phys.*, **2012**, 112, 054320.

2. "A facile approach to enhance the high temperature stability of magnetite nanoparticles with improved magnetic property", S. S. Pati and J. Philip, *J. Appl. Phys.*, **2013**, 113, 044314.

3. "A simple approach to produce stable ferrofluids without surfactants and with high temperature stability", S. S. Pati, V. Mahendran and J. Philip, *J. Nanofluids*, **2013**, 2, 94-103.

4. "Effect of Cation Trapping on Thermal Stability of Fe_3O_4 Nanoparticles", S. S. Pati and J. Philip, *J. Nanosci. Nanotechnol.*, **2014**, 13,4114-23.

Accepted

5. "Microwave Assisted Synthesis of Magnetite Nanoparticles", S. S. Pati, S. Kalyani, V. Mahendran and John Philip, *J. Nanosci. Nanotechnol.* **2014** (In press).

Communicated

6. "Synthesis of $Mn_xZn_{1-x}Fe_2O_4$ Nanoparticles with Tunable Curie Temperature using Microwave Assisted Method", S. S. Pati, S. Kalyani, V. Mahendran and J. Philip (Under review).

CONFERENCES & WORKSHOPS

1. Two days workshop on electron microscopy held at Indira Gandhi Centre for Atomic Research (IGCAR), Kalpakkam, Oct 12-13 (2009).

2. Conference on chemistry in societal and environmental needs held at Central Leather Research Institute, Chennai, Aug 29-31(2011).
3. S. S. Pati and John Philip, “Enhancement in maghemite to hematite phase transition temperature with very low fraction of Co (II) doping”, International Conference on Nanoscience Engineering and Technology (ICONSET), Sathyabhama University, Chennai Nov 28-30 (2011), pp 323-325.

DEDICATION

Solely dedicated to my family,

Teachers & friends

ACKNOWLEDGEMENT

First and foremost, I would like to acknowledge and owe my deep sense of indebtedness to my supervisor, **Dr. John Philip** for all the care, help, support and other countless reasons which I cannot enumerate in its full verbosity. He has been a source of inspiration and role model and in my endeavor to follow his footprints, although I could not inherit his erudite, the trail of his nobleness and virtuosity that I carry forward is certainly a priceless treasure trove for the rest of my life. His selfless guidance gave shape to my scientific intuition and research aptitude in the formative years of my career.

I would like to thank **Dr. Baldev Raj**, former Director, IGCAR, for his support, encouragement and affection to the research scholars which provided me a homely feeling in this institute for pursuing Ph.D.

I would also like to thank **Shri S. C. Chetal,** former Director, IGCAR and **Dr. P. R. Vasudeva Rao**, Director, IGCAR for allowing me to pursue my research at this premier institute. I am also thankful to **Dr. T. Jayakumar** Director, Metallurgy and Materials Group (MMG) for giving continuous support in my research work. I would like to acknowledge **Dr. V. Ganesan**, Dean, Chemical Sciences for his support and encouragement.

I express my sincere thanks to my doctoral committee members **Dr. M. Sai Baba**, **Dr. K.V.G. Kutty** and **Dr. V. Jayaraman** for their guidance, precious suggestions and constant support.

I am thankful to **Dr. M. Sai Baba** for making my stay at JRF enclave pleasant. I thank all the staff members of SMARTS (*T. Muthukumaran, J. Sangeetha, Gopinath,* and

Kalyani), RTS (*Dr. T Sarvanan, S. Bagavathiappan, K. Arunmuthu* and *Barid Lahiri*) and NDED for their continuous help and support, and I always cherish the wonderful atmosphere here.

My special thanks to *Herojit, Surajit, Leona, Anbumozhi, Mahendran, Zaibudin* for their valuable discussions, support and encouragement during my research period. I am also thankful to my seniors *Dr. Gnanaprakash, Dr. Ayyappan, Dr. Shima, Dr. Junaid Laskar* and *Dr. Joy Shankar* for their valuable advice, discussions and understanding during the early part of my research.

It is my pleasure to thank *Herojit, Pradeep, Bubhati, Sharath, Naveen, Jammu Ravi, Lakshmoji, Mahavishnu, Illairaja, Maneesha, Pravati, Debasmita, Priyada, Jagadish, Marriyappa, Siva Srinivas, Shashwat, Uma, Manas, Subrato, Jun, Shashank, Shweta, Ajit, Jaya, Pranaya, Jayaraman* for making my stay pleasant and entertaining at Kalpakkam.

I thank my beloved wife **Smt. Smiti Suhani Pati** for her patience and support during all up and down moments during my research work. I am thankful to my family members for their constant support and care throughout my career. Last but not the least, I thank all my *friends, cricket teammates* and *everyone in the JRF enclave* for creating joyful environment and making my stay comfortable.

(S. S. Pati)

Kalpakkam
December, 2013

CONTENTS

Chapter I

Introduction

Chapter II

Synthesis and Characterization Techniques

Chapter III

High temperature phase transformation studies in $Co_xFe_{3-x}O_4$ nanoparticles

Chapter IV

High temperature phase transition studies in $Zn_xFe_{3-x}O_4$ nanoparticles

Chapter V

Effect of Na^+ doping on the thermal stability of magnetite nanoparticles and magnetic fluids

Chapter VI

Microwave assisted synthesis of magnetite nanoparticles and their phase stability

Chapter VII

Microwave assisted synthesis of $Mn_xZn_{1-X}Fe_2O_4$ nanoparticles with tunable Curie temperature

Chapter VIII

Summary and Future Scopes

SYNOPSIS

Nanostructured materials are at the helm of advanced materials development that has witnessed an explosion of interest during recent years. At nanoscale, surface effects become more significant due to the increased fraction of surface atoms within the tiny particle. Interesting physical and chemical properties of nanomaterials, originating from the surface and quantum effects, are being used in developing applications in the manufacturing of faster and smaller communications devices, electronics and medical gadgets, ultrasensitive and fast sensors, safety and security devices[1]. Among various nanostructured materials, magnetic nanomaterials are one of the most important classes of nanostructured materials due to their potential applications in biomedical, environmental remediation and electronic industries. In magnetic nanomaterials, the magnetic structure at the surface layer is greatly different from that in the interior of nanoparticle as the symmetry is reduced for the cations at the surface due to the incomplete coordination sphere. The finite-size and surface effects drastically change the magnetic properties of nanoparticles in comparison with their bulk counterpart. Further, below a critical size, the nanoparticle becomes a single magnetic domain where the particle no longer sustains a domain wall and consists of a uniformly magnetized core carrying a net magnetic super-moment frozen along one of its magnetocrystalline easy directions[2].

Magnetic iron-oxide nanoparticles contribute significantly to the current revolution in nanomedicine due to their unique properties such as high surface area to volume ratios and superparamagnetism[3, 4]. Superparamagnetic properties are being exploited in medical applications such as magnetic resonance imaging (MRI) [5], drug and gene delivery[6], tissue engineering[7], magnetic hyperthermia[8] and bioseparation[9]. Iron-oxide nanoparticles of mean particle diameter less than 100 nm are ideal for biomedical applications[3]. The beauty of working with such particles is that they can be manipulated by an external magnetic field. Besides biomedical applications, Iron oxide nanoparticles have been found to have applications in heat transfer,[10] sensors,[11] ferrofluids,[12, 13] and catalysis[14]. They have also been used as a model system to probe weak molecular interaction between colloidal materials[15].

Many efficient synthetic routes have been developed to produce shape-controlled, highly stable, and monodisperse magnetic nanoparticles[1]. Techniques such as co-precipitation,[16] thermal decomposition,[17] reverse micelle synthesis,[18] hydrothermal synthesis,[19] laser pyrolysis[20], and microwave assisted[21] synthesis have been used to produce high-quality magnetic nanoparticles. Among various techniques for magnetite synthesis, the co-precipitation method is a convenient approach to produce nanoparticles from aqueous salt solution. The advantages of co-precipitation process are that it does not produce or use any toxic intermediates or solvents, does not require precursor complexes and high reaction temperatures. It has become a popular technique because of its ability to be scaled up, its reproducibility and its eco-friendly reaction conditions[1, 22]. The formation pathways of magnetite in co-precipitation process depend on the rate of alkali addition. The akaganeite (β-FeO(OH)) undergoes a transformation to magnetite through goethite (α-FeO(OH)) when the alkali is added slowly to the iron salt solution. During rapid alkali addition, an additional phase of ferrous hydroxide is nucleated, which is subsequently converted to magnetite through an intermediate phase of lepidocrocite (γ-FeO(OH)). In co-precipitation reaction, the magnetite formation pathways co-exist and always take place through iron hydroxide intermediate, but the dominant process is the topotactic transformation of goethite to magnetite[23].

In recent years, microwave assisted synthesis method is widely used to produce nanocrystalline materials with higher yield over conventional heating techniques[21]. Specially designed microwave synthesis reactor allows an exquisite control on reaction temperature, stirring rate and pressure inside the reaction vessel which is the unique features of microwave apparatus over conventional heating apparatus. The heating effect in the microwave arises from the interaction of the electric field component of the microwave with charged particles in the material through both conduction and polarization.

Under oxidative atmosphere, magnetic iron oxide nanoparticles (Fe_3O_4 and γ-Fe_2O_3) undergo a phase transition to a thermodynamically stable and compact antiferromagnetic hematite (α-Fe_2O_3) phase at ~450 ºC that limits the applications of iron oxide nanoparticles beyond this temperature [24]. Therefore, it is necessary to augment the γ-Fe_2O_3 to α-Fe_2O_3 phase transition temperature without affecting the magnetic properties of iron oxide nanoparticles. Studies show that the γ-Fe_2O_3 (maghemite) to α-Fe_2O_3 (hematite) phase transition temperature can be enhanced by doping with suitable elements,[25, 26] appropriate coating[27] and by using core-shell structure[28]. Early studies show that the presence of foreign material like alumina can enhance the activation energy for the γ-Fe_2O_3 to α-Fe_2O_3 phase transition[29]. It has also been shown that a strong oxide-oxide bonding between Fe_3O_4 and SiO_2 can lead to an enhanced maghemite to hematite phase transition temperature[27]. Lai et al. observed an enhancement in the stability of maghemite phase till 550 ºC with 8.5% of Mn doping.[25] Gnanaprakash et al. showed that the alkali used in the synthesis has a crucial role in the phase transition temperature of iron oxide nanoparticles [24]. It was found that ammonia based magnetite nanoparticles are transformed to hematite at 500 ºC whereas particles prepared by NaOH retain the magnetic (maghemite) phase upto 600 ºC. The enhancement was found to be due to the presence of Na^+ ions in the magnetite crystal structure. It was shown that a shell of SnO_2 over iron oxide nanoparticles is a good protecting agent up to 600 ºC[28]. Such non-magnetic shell can reduce the saturation magnetization drastically. In general, core-shell structures were found to be more reliable as protecting agents for high temperature applications. However, the non-magnetic shell reduces the magnetic properties, thus limiting their applications. Irrespective of the advances in this field, preparation of magnetic nanomaterials with high thermal stability and high saturation magnetization is still a challenge. Further, for effective utilization of ferrite nanoparticles for practical applications, control on monodisperity, purity, magnetization and high temperature stability of synthesized particle are prerequisites. This was one of the motivations to undertake the studies in this thesis.

Tuning of curie temperature in ferrite nanoparticles is important for applications such as heat transfer and magnetic hyperthermia[30]. Ferrite nanoparticles with curie temperature very close to room temperature can be produced by suitable doping, thereby compromising magnetic properties or purity[31]. Therefore, developing new synthesis routes for producing pure ferrites with Curie temperature near room temperature with high saturation magnetization is important. Also, understanding of magnetic properties of fine ferrite nanoparticles is important for their technological applications.

The major objectives of the present study are:

- To develop methodologies to enhance the high temperature phase stability of magnetite nanoparticles
- To obtain insight into the effects of cation doping on thermal stability and magnetic properties of magnetite nanoparticles.
- To study the effect of reaction temperatures (during synthesis) on high temperature phase stability and magnetic properties.
- To tailor ferrite nanoparticles with tunable magnetic properties like curie temperature and saturation magnetization

This thesis presents the studies on the effect of different doping elements (Co, Zn, Na and Mn) on the phase transition and magnetic properties of ferrite nanoparticles prepared using coprecipitation and microwave method. It consists of eight chapters. The summary of each chapter is given below

Chapter 1 gives a brief introduction to magnetic nanomaterials and their technological applications. The structure and magnetism of ferrite nanoparticles are discussed in detail. An extensive literature review on synthesis and phase transition studies in iron oxide nanoparticles has been presented. Various methods adopted for preparing magnetite nanoparticles with high temperature phase stability by doping, coating, core-shell etc. are also discussed.

The synthesis methods and characterization techniques used for the studies are presented in **Chapter 2**. Magnetic nanoparticles were prepared using both coprecipitation and microwave synthesis methods. The advantages of these methods over other synthesis methods are explained. The details of structural analysis and phase identification by XRD, shape and particle size distribution analysis using transmission electron microscopy (TEM) and small angle X-ray scattering (SAXS) experiments, determination of trace element concentrations by atomic absorption spectroscopy (AAS) technique and structural bonding information by Fourier transform infrared spectroscopy (FTIR) studies are presented. Weight loss and phase transformation studies using thermogravimetric (TGA) and differential scanning calorimetry (DSC) and magnetic property measurements using cryogen-free Vibrating sample magnetometer are also discussed in this chapter. Besides, the details of the horizontal tube furnace used for the air annealing of nanoparticles and the working principle of zeta potential measurements to assess the stability of nanofluids are also discussed.

In **Chapter 3**, the effect of Co^{2+} ion doping in magnetite (Fe_3O_4) on its crystal structure, magnetic properties and phase stability during air and vacuum annealing are discussed. The nanoparticles are prepared by co-precipitation method. The SAXS analysis on the doped samples shows that the most probable size, shape and the polydispersity of particles, synthesized with different fractions of Co^{2+} ion doping (0 to 0.6) remain almost the same. On increasing cobalt content, the ferrimagnetic to the antiferromagnetic hematite (α-Fe_2O_3) phase transformation temperature is found to increase dramatically.

For 0.1 fraction of Co^{2+} metal ion doping, an enhancement of 100 ºC in the magnetic to α-Fe_2O_3 phase transition temperature is observed in the air annealed samples, whereas the magnetite phase is found to be maintained up to 1000 ºC in vacuum annealed samples. The observed enhancement in the phase transition temperature is attributed to the increased activation energy for phase transformation in the presence of Co^{2+} due to the formation of stronger metal-oxide bond (Co-O). Further, the DSC results corroborate the finding of an increase in the maghemite to hematite phase transition temperature with increase in cobalt fraction (x). A decrease in enthalpy from 89.86 to 17.62 Jg^{-1} with an increase in cobalt content indicates that the degree of conversion of maghemite to hematite is decreasing with the cobalt content, which is in good agreement with the Rietveld analysis. The decrease in the saturation magnetization value in air annealed sample is attributed to the re-distribution of Co^{2+} and Fe^{3+}cations in the tetrahedral and octahedral sites. This study suggests that a very small percentage of Co^{2+} metal ion doping can dramatically enhance the thermal stability of magnetite nanoparticles.

Chapter 4 discusses the effect of Zn^{2+} doping on the crystal structure, magnetic properties and the high temperature phase stability of magnetite nanoparticles under air and vacuum annealing. The Zn^{2+} doped nanoparticles ($Zn_xFe_{3-x}O_4$ with x = 0, 0.2, 0.4 & 0.6) are prepared by co-precipitation technique. High temperature XRD studies show that the decomposition of pure magnetite (Fe_3O_4) in vacuum is increased by 300 ºC, with 0.2 fraction of Zn^{2+} doping. The DSC studies under air environment also confirm that the γ-Fe_2O_3 to α-Fe_2O_3 phase transition temperature increases with the zinc fraction. The increase in transition temperature is attributed to the increase in the activation energy of the maghemite to hematite phase transition after the replacement of Fe^{3+} with larger diameter Zn^{2+} in the tetrahedral site and also due to the strong Zn-O metal oxide bond strength. The saturation magnetization increases from 61 to 69 emu/g upon 0.2 fraction of Zn^{2+}, which augments the utility of the Zn doped compound for practical applications. All the Zn^{2+} doped samples showed superparamagnetic nature. This study led to the development of an extremely useful method to produce superparamagnetic nanoparticles with enhanced magnetic properties for high temperature applications.

The synthesis of magnetite nanoparticles doped with Na^+ ions by co-precipitation method is discussed in **Chapter 5**. The γ-Fe_2O_3 to α-Fe_2O_3 phase transition temperature is found to increase with Na^+ concentration and the saturation magnetization is found to decrease from 65 to 48 emu/g with 500 ppm of Na^+. The samples with 500 ppm of Na^+, retained the saturation magnetization of 46 emu/g, even after air annealing at 600 ºC. The phase analysis done using Rietveld shows that the percentage of hematite (α-Fe_2O_3) formed after air annealing at 600 ºC is found to decrease with increase in Na^+ concentration. The DSC studies further confirm the enhanced temperature stability upon Na doping. The zeta potential of undoped and Na^+ doped magnetite particles are found to be -28 and -37 mV, respectively. The enhanced zeta potential of doped particles unambiguously confirms that Na^+ ions are diffused into the crystals, which enhances the electrostatic stabilization of suspended particles.

Chapter 6 deals with the effect of synthesis reaction temperature on the phase stability of magnetite nanoparticles prepared using microwave method. Magnetite nanoparticles of size raging from 7-10 nm are prepared from aqueous solutions of Fe^{2+} and Fe^{3+} salts by microwave irradiation at different reaction temperatures ranging from 50 to 200 ºC. The average particle size of prepared particles, obtained from SAXS, is found to vary from 11 to 15±1 nm as the reaction temperature is increased from 50 to 200 ºC. The weight gain curves under an external magnetic field show slope changes at 300 and 596 ºC, which are attributed to the magnetite to maghemite phase transition and ferrimagnetic to paramagnetic magnetic transition (Curie point), respectively. The γ-Fe_2O_3 to α-Fe_2O_3 phase transition temperature is found to be enhanced by 154 ºC for the nanoparticles prepared at 200 ºC, probably due to enhanced activation energy for the cubic to a more compact hexagonal transition. The observed increase in the phase stability of nanoparticles prepared at elevated temperature is attributed to the diffusion of Na^+ in the spinel structure during synthesis using NaOH. These results are useful to tailor magnetic particles with enhanced thermal stability for practical applications.

The tuning of Curie temperature of Mn doped $ZnFe_2O_4$ nanoparticles are discussed in **Chapter 7**. Microwave assisted synthesis method has been used to prepare $Mn_xZn_{1-x}Fe_2O_4$ nanoparticles, with x varying from 0 to 1. The X-ray diffraction revealed a single phase crystalline spinel phase with crystallite size varying from 5.9 to 16 nm as the Mn fraction increases from 0 to 1. The average particle size obtained from SAXS distribution curve is found to be consistent with the TEM results. The observed increase in lattice constant with increasing Mn concentration (between x=0.35 to 1) is attributed to the replacement of smaller ionic radius Zn^{2+} cations by larger diameter Mn^{2+} cations. The saturation magnetization varies from 6 to 52 emu/g for x= 0 to 1. The Curie point was found to increase linearly from 226 to 390 K as the Mn fraction increases from 0.3 to 0.55. These results confirm that the relative fraction of Mn and Zn in the mixed ferrite structure and their distribution in the A or B sites influences the particle size, lattice parameter, Curie temperature and the magnetic properties. By varying the relative fraction of Mn and Zn in ferrite structure, the particle size, lattice parameter, Curie temperature and the magnetic properties are tuned, which makes them suitable for temperature sensitive applications such as magnetic hyperthermia and electronic cooling.

A summary of the experiments done on high temperature phase transition studies and tuning of Curie temperature are presented in **Chapter 8**.

It has been demonstrated that the thermal stability of Fe_3O_4 nanoparticles can be dramatically enhanced by doing it with a low concentration of Co, Zn and Na. Under air atmosphere, the maghemite to hematite phase transition is enhanced by 100 ºC under air annealing with 0.1 fraction of Co. The enthalpy change corresponding to γ-Fe_2O_3 to α-Fe_2O_3 phase transition decreases from 90 to 17 J/g as the Co fraction increased from 0 to 0.6 which indicates that the degree of conversion from maghemite to hematite decreases with Co content. Under air atmosphere, the magnetic phase (γ-Fe_2O_3) is retained till 656 ºC with 0.6 fraction of Zn doping. The saturation magnetization increases from 61 to 69 emu/g with 0.2 fraction of Zn doping. The Na doping in Fe_3O_4 nanoparticles confirms that γ-Fe_2O_3 to α-Fe_2O_3 phase transition temperature increases with Na^+. The zeta potential results confirm that the Na^+ ions are diffused into the magnetic crystals. *In situ* XRD study, under vacuum annealing, on Zn doped Fe_3O_4 system shows that 0.2 fraction of Zn doping can enhance the phase transformation temperature of spinel ferrite by ~300 ºC. The spinel ferrite phase is found to be stable upto 1000 ºC, with 0.1 fraction of Co. Under vacuum annealing, no phase transition is observed up to 1000 ºC with 500 ppm of Na doping in Fe_3O_4 nanoparticles.

Pure magnetite nanoparticles of size raging from 7-10 nm are prepared for the first time by varying the reaction temperature from 50 to 200 ºC using microwave assisted method. The ferromagnetic γ-Fe_2O_3 to antiferromagnetic α-Fe_2O_3 phase transition temperature is found to increase by 154 ºC for the sample prepared at 200 ºC, which is attributed to the diffusion of Na^+ within the cubic lattice. Microwave assisted synthesis method has also been successfully used to prepare $Mn_xZn_{1-x}Fe_2O_4$ nanoparticles. The Curie point was found to increase linearly from 148 to 390 K as the Mn fraction is increased from 0.1 to 0.55. The results show that by varying the relative fraction of Mn and Zn in ferrite structure, the particle size, lattice parameter, Curie temperature and the magnetic properties can be tuned.

References

[1] S. Laurent, D. Forge, M. Port, A. Roch, C. Robic, L.V. Elst, R.N. Muller, Magnetic Iron Oxide Nanoparticles: Synthesis, Stabilization, Vectorization, Physicochemical Characterizations, and Biological Applications, Chem. Rev. 108 (2008) 2064–2110.

[2] B.D. Cullity, Introduction to magnetic materials, Addision - Wesley, New York, 1972.

[3] C. Boyer, M.R. Whittaker, V. Bulmus, J. Liu, T.P. Davis, The design and utility of polymer-stabilized iron-oxide nanoparticles for nanomedicine applications, NPG Asia Mater. 2 (2010) 23-30.

[4] Y.W. Jun, J.H. Lee, J. Cheon, Chemical Design of Nanoparticle Probes for High-Performance Magnetic Resonance Imaging, Angew. Chem. Int. Ed. 47 (2008) 5122-5135.

[5] S.A. Corr, S.J. Byrne, R. Tekoriute, C.J. Meledandri, D.F. Brougham, M. Lynch, C. Kerskens, L. O’Dwyer, Y.K. Gunko, Linear Assemblies of Magnetic Nanoparticles as MRI Contrast Agents, J. Am. Chem. Soc. 130 (2008) 4214–4215.

[6] J. Dobson, A twist on tumour targeting, Nat. Mater. 9 (2010) 95-96.

[7] M.R. Dzamukova, E.A. Naumenko, N.I. Lannik, R.F. Fakhrullin, Surface-modified magnetic human cells for scaffold-free tissue engineering, Biomaterials Science 1 (2013) 810-813.

[8] C. Martinez-Boubeta, K. Simeonidis, A. Makridis, M. Angelakeris, O. Iglesias, P. Guardia, A. Cabot, L. Yedra, S. Estradé, F. Peiró, Z. Saghi, P.A. Midgley, I. Conde-Leborán, D. Serantes, D. Baldomir, Learning from Nature to Improve the Heat Generation of Iron-Oxide Nanoparticles for Magnetic Hyperthermia Applications, Sci. Rep. 3 (2013) 1652.

[9] S.J. Son, J. Reichel, B. He, M. Schuchman, S.B. Lee, Magnetic nanotubes for magnetic-field-assisted bioseparation, biointeraction, and drug delivery, J. Am. Chem. Soc. 127 (2005) 7316–7317.

[10] P.D. Shima, J. Philip, B. Raj, Magnetically controllable nanofluid with tunable thermal conductivity and viscosity, Appl. Phys. Lett. 95 (2009) 133112.

[11] J. Philip, V.Mahendran, L.J. Felicia, A Simple, in-expensive and ultrasensitive magnetic nanofluid based sensor for detection of toxic cations, ethanol and ammonia-A Review, J. Nanofluids 2 (2013) 112-119.

[12] P. Berger, N.B. Adelman, K.J. Beckman, D.J. Campbell, A.B. Ellis, G.C. Lisensky, Preparation and Properties of an Aqueous Ferrofluid, J. Chem. Educ. 76 (1999) 943.

[13] M.A.G. Soler, E.C.D. Lima, S.W.d. Silva, T.F.O. Melo, A.C.M. Pimenta, J.P. Sinnecker, R.B. Azevedo, V.K. Garg, A.C. Oliveira, M.A. Novak, P.C. Morais, Aging Investigation of Cobalt Ferrite Nanoparticles in Low pH Magnetic Fluid, Langmuir 23 (2007) 9611-9617.

[14] D.T. Mitchell, S.B. Lee, L. Trofin, N. Li, T.K. Nevanen, H. Soderlund, C.R. Martin, Smart Nanotubes for Bioseparations and Biocatalysis, J. Am. Chem. Soc. 124 (2002) 11864-11685.

[15] J. Philip, T. Jaykumar, P. Kalyanasundaram, B. Raj, O. Mondain-Monval, Effect of polymer-surfactant association on colloidal force, Phys. Rev. E 66 (2002) 011406

[16] R. Massart, Preparation of Aqueous Magnetic Liquids in Alkaline and Acidic Media IEEE Trans. Magn. 17 (1981) 1247-1248.

[17] W.W. Yu, J.C. Falkner, C.T. Yavuz, V.L. Colvin, Synthesis of monodisperse iron oxide nanocrystals by thermal decomposition of iron carboxylate salts, Chem. Commun. (2004) 2306-2307.

[18] Y. Lee, J. Lee, C.J. Bae, J.G. Park, H.J. Noh, J.H. Park, T. Hyeon, Large scale synthesis of uniform and crystalline mangetic nanoparticles using reverse micelles as nanoreactors under reflux conditions, Adv. Funct. Mater. 15 (2005) 503-509.

[19] A. Cabanas, M. Poliakoff, The continuous hydrothermal synthesis of nano-particulate ferrites in near critical and supercritical water, J. Mater. Chem. 11 (2001) 1408-1416.

[20] M.P. Morales, S. Veintemillas-Verdaguer, C.J. Serna, Magnetic properties of uniform γ–Fe_2O_3 nanoparticles smaller than 5 nm prepared by laser pyrolysis, J. Mater. Res 14 (1999) 3066-3072.

[21] M. Baghbanzadeh, L. Carbone, P.D. Cozzoli, C.O. Kappe, Microwave-Assisted Synthesis of Colloidal Inorganic Nanocrystals, Angew. Chem. Int. Ed. 50 (2011) 11312–11359.

[22] A.-H. Lu, E.L. Salabas, F. Schuth, Magnetic Nanoparticles: Synthesis, Protection, Functionalization, and Application, Angew. Chem. Int. Ed. 46 (2007) 1222-1244.

[23] T. Ahn, J.H. Kim, H.M. Yang, J.W. Lee, J.D. Kim, Formation Pathways of Magnetite Nanoparticles by Coprecipitation Method, J. Phys. Chem. C 116 (2012) 6069–6076.

[24] G. Gnanaprakash, S. Ayyappan, T. Jayakumar, J. Philip, B. Raj, Magnetic nanoparticles with enhanced γ -Fe_2O_3 to α-Fe_2O_3 phase transition temperature Nanotechnology 17 (2006) 5851-5857.

[25] J. Lai, K.V.P.M. Shafi, K. Loos, A. Ulman, Y. Lee, T. Vogt, C. Estournes, Doping g-Fe_2O_3 Nanoparticles with Mn(III) Suppresses the Transition to the a-Fe_2O_3 Structure, J. Am. Chem. Soc. 125 (2003) 11470-11471.

[26] S. Deka, P.A. Joy, Enhancement of the phase transition temperature of g-Fe_2O_3 by Zn^{2+} doping, J. Mater. Chem. 17 (2007) 453-456.

[27] C.R.F. Lund, J.A. Dumesic, Strong oxide-oxide interactions in silica-supported magnetite catalysts. 1. X-ray diffraction and Moessbauer spectroscopy evidence for interaction, J. Phys. Chem. 85 (1981) 3175-3180.

[28] X. Xu, M. Ge, C. Wang, J.Z. Jiang, High temperature stable monodisperse superparamagnetic core-shell iron-oxide@SnO2 nanoparticles, Appl. Phys. Lett. 95 (2009) 183112.

[29] F.E. DeBoer, P.W. Selwood, The Activation Energy for the Solid State Reaction γ-$Fe_2O_3 \rightarrow \alpha$-$Fe_2O_3$, J. Am. Chem. Soc. 76 (1954) 3365-3367.

[30] Z. Beji, A. Hanini, L.S. Smiri, J. Gavard, K. Kacem, F. Villain, J.M. Grenèche, F. Chau, S. Ammar, Magnetic properties of Zn-substituted $MnFe_2O_4$ nanoparticles synthesized in polyol as potential heating agents for hyperthermia. Evaluation of their toxicity on Endothelial cells, Chem. Mater. 22 (2010) 5420–5429.

[31] C. Rath, S. Anand, R.P. Das, K.K. Sahu, S.D. Kulkarni, S.K. Date, N.C. Mishra, Dependence on cation distribution of particle size, lattice parameter, and magnetic properties in nanosize Mn–Zn ferrite, J. Appl. Phys. 91 (2002) 2211.

LIST OF FIGURES

LIST OF TABLES

LIST OF ABBREVIATIONS

AAS	Atomic absorption spectroscopy
AES	Atomic emission spectroscopy
BCC	Body centered cubic
DSC	Differential scanning calorimetry
DLS	Dynamic light scattering
emu	Electromagnetic unit
FCC	Face centered cubic
FC	Field cooling
FTIR	Fourier transform infrared spectroscopy
GoF	Goodness of fit
HTXRD	High temperature X-ray diffraction
JCPDS	Joint committee on powder diffraction standards
MAUD	Materials analysis using diffraction
MRI	Magnetic resonance imaging
nm	nanometer
PMMA	Poly(methyl methacrylate)
SAXS	Small angle X-ray scattering
SEM	Scanning electron microscopy
STM	Scanning tunneling microscopy
TEM	Transmission electron microscopy
TGA	Thermogravimetric analysis
VSM	Vibrating sample magnetometer
XRD	X-Ray diffraction
ZFC	Zero field cooling

LIST OF SYMBOLS

a	Lattice parameter
A	Arrhenius constant
Å	Angstrom
d	Particle diameter
d_{avg}	Average particle diameter
d_{hkl}	Inter planar distance
D	Diffusion constant
D_0	Maximum diffusion
l	Diffusion length
J_D	Diffusion flux
K	Anisotropic energy
V	Volume
T_B	Blocking temperature
h	Plank’s constant
λ	Wavelength
T	Absolute temperature
λ_C	Correlation length constant
χ	susceptibility
μ_0	Magnetic permeability in free space
μ_H	Magnetic moment per atom
μ_B	Bohr’s magnetron
g	Shell thickness
θ	Diffraction angle
ΔG	Change in free energy
ΔH	Change in enthalpy
ΔS	Change in entropy
p	Momentum
T_C	Curie temperature
$T_C (\infty)$	Bulk Curie temperature

D_{SD}	Single domain particle diameter
M	Magnetization
M_S	Saturation magnetization
M_r	Remanant magnetization
H_C	Coercive magnetic field
η	Viscosity
H	Magnetic field
T_N	Neel temperature
S	Spin magnetic moment
J	Total angular moment
k_B	Boltzmann's constant
R	Universal gas constant
δ	Structure inversion parameter
α	Magnetic dipolar constant
M^{2+}	Divalent metal ion
n	Crystal plane
β	Full width at half maxima
$D(d,d_0,\sigma)$	Particle size distribution
F (q)	Form factor
S(q)	Structure factor
q	Wave vector
I	Intensity
ρ	Density
U_E	Electrophoretic mobility
ζ	Zeta potential
ϵ	Dielectric constant
κ	Debye length
σ_0	Standard deviation
σ_{eff}	Polydispersity
E_a	Activation energy

Chapter I

Introduction

1.1 Nanomaterials: An Overview

The word ‘nano’ is derived from the Greek word ‘nanos’ which means dwarf. The nanoscale is the intermediary between the atom and the bulk solid. Atoms are below a nanometer in size, whereas many molecules, including some proteins, range from a nanometer upwards. The concept of nanotechnology was first discussed in 1959 by the physicist Richard Feynman, in his lecture ‘There’s plenty of room at the bottom’[1]. In his visionary lecture, he talked about the possibility of miniaturization by manipulating material at nanoscale.

Nanotechnology deals with the manipulation of matter at the nanoscale, to create new materials, structures and devices[2]. Nanoscience is broadly understood as the science behind the ability to employ nanotechnology. The nanomaterials are likely to revolutionalize human life, by developing materials for faster and smaller communication devices, electronic equipments, medical gadgets, ultrasensitive and fast sensors, safety and security devices[3]. Nanomaterials exhibit a variety of interesting properties due to high surface area to volume ratio than that of their bulk counterparts. The large surface area of nanoparticles augments their chemical reactivity, surface free energy, physical, electrical and mechanical properties. Nanomaterials also exhibit quantum effect because the length scales of these materials are comparable to de Broglie wavelength (λ=h/p)[4].

Nanomaterials have exciting applications in medicine[3, 5, 6]. Colloidal gold[7] and iron oxide nanoparticles [8, 9] are exclusively studied for drug delivery applications[10]. Nanomaterials are also used as therapeutic and diagnostic agents which can be encapsulated, covalently attached or adsorbed on to nanocarriers[5]. Another area of application is tissue engineering[11]. In the recent years, optical detection schemes using magnetic nanomaterials have been developed for real time and label-free detection and recognition of single viruses and larger proteins[12]. Besides, dispersion of magnetic nanoparticles (ferrofluids) are also used in sealing, damping, hydrodynamic bearings etc[13]. Despite these promising applications, nanotechnology faces many challenges in fabrication of materials and devices.

Advances in characterization tools such as transmission electron microscopes (TEM), scanning-tunneling microscopes (STM) and atomic force microscopes (AFM), X-ray and neutron scattering and spectrometry have provided further impetus to the current developments of nanoscience. Intense research and developments in this field has boosted the production and applications of nanoscale materials during the last decade. Several new nanomaterials have been inducted into products starting from household appliances tomicrochips.

1.2 Magnetic properties of nanoparticles

Magnetite (Fe_3O_4) is the first magnetic material known to man. Bulk ferromagnetic specimens consist of number of small regions, called domains[16],which are separated by boundaries called domain walls. In bulk ferromagnetic materials, the direction of magnetization of the individual domains are distributed in random directions, so that the magnetic flux circuit lies almost entirely within the specimen. These multi domain materials can be saturated only by application of magnetic field larger than the demagnetizing field. When the size of the magnetic particle is reduced below a critical size, the multi domains become a single domain with a colossal spin is formed, where a large fraction of atoms reside at the surface of the particles with broken translation symmetry. In such single domain particles, the magnetic behavior is highly dependent on the magnetic anisotropy energy of the individual particle and the magnetic dipole-dipole interaction between the particles. When the magnetic anisotropy is greater than the dipole-dipole interaction, the system follows Neel-Brown relaxation and exhibits superparmagnetism. On the other hand, if the dipole-dipole interaction is of the order of magnetic anisotropy energy, then the system behaves like a super spin glass[17, 18].

The coercive force is a very sensitive property of ferromagnetic materials, and is one of the most important criteria in the selection of ferromagnetic materials for practical applications. The increasing of the coercive force with reducing particle size has been considered as a substantial evidence for the real existence of single domain particles[19]. The multidomain state (bulk) is energetically favorable if the energy consumption for the formation of domain walls is lower than the difference between the magnetostatic energies of the single-domain and multi domain states. As the dimensions of the specimen are reduced (nanoparticles), the relative contributions of the various energy terms to the total energy of ferromagnetic specimen are changed, and the surface energy of domain walls becomes more important than the magnetostatic volume energy. There is a critical size D_{SD}, at which the single domain is energetically more favorable than multi domains[20]. The configuration of the magnetization inside a single-domain particle depends strongly on the magnetic anisotropy and particle's shape[21]. If a ferromagnetic ellipsoidal (or spherical) particle has a negligibly small crystalline anisotropy, the atomic magnetic moment may be expected to point along closed rings, so that total magnetic moment of the particle is equal to zero. If the crystalline anisotropy is relatively large, most of the atomic magnetic moments are expected to lie along easy directions and can behave as a permanent magnet. Due to the decrease in magnetic domains and restriction in the domain wall movements, the coercivity of the materials increases with decrease in particle size. Schematic representation of coercivity as a function of particle size for ferromagnetic/ferrimagnetic materials is shown in Fig 1.1.

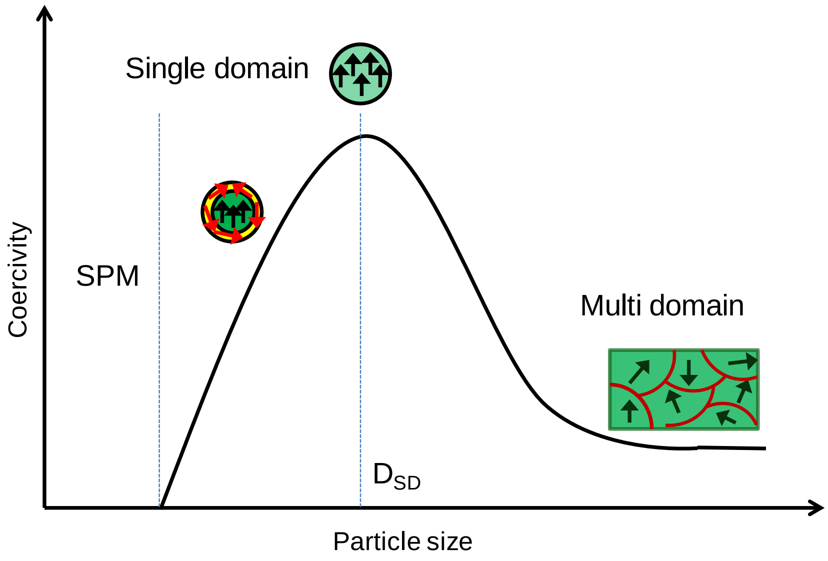

Fig 1.1: Schematic representation of coercivity as a function of particle size for ferromagnetic/ferrimagnetic materials.

Below a critical single domain size, the spin contribution from surface atoms starts dominating which leads to a decrease in coercivity. Below a certain size, the coercivity becomes zero and the particles are termed as superparamagnetic in nature. Superparamagnetism is a phenomenon by which magnetic materials may exhibit a behavior similar to paramagnetism at temperatures below the Curie temperature. Normally, coupling forces in magnetic materials cause the magnetic moments of neighboring atoms to align, resulting in very large internal magnetic fields. At temperatures above the Curie temperature the thermal energy is sufficient to overcome the coupling forces, causing the atomic magnetic moments to fluctuate randomly. Because there is no longer magnetic ordering, the internal magnetic field no longer exists and the material exhibits paramagnetic behavior. Superparamagnetism occurs when the material is composed of very small crystallites (below 14 nm for magnetite). In this case even though the temperature is below the Curie or Neel temperature, the thermal energy is sufficient to overcome the coupling forces between neighboring atoms and hence, the thermal energy is sufficient to change the direction of magnetization of the entire crystallite. The magnetic moment flips between two antiparallel axes at normal temperature and the time required for changing its magnetic spin direction is known as Neel relaxation time. The resulting fluctuations in the direction of magnetization cause the magnetic field to average to zero. The material behaves in a manner similar to paramagnetism, except that instead of each individual atom being independently influenced by an external magnetic field, the magnetic moment of the entire crystallite tends to align with the magnetic field. The energy required to change the direction of magnetization of a crystallite is called the crystalline anisotropy energy that depends both on the material properties and the crystallite size. As the crystallite size decreases, so does the crystalline anisotropy energy, resulting in a decrease in the temperature at which the material becomes superparamagnetic.

Surface effects are due to the lack of translational symmetry at outer boundaries of a particle, reduced coordination number and broken magnetic exchange bonds of surface atoms. Decreasing the particle size can increase the ratio of surface spins to the total number of spins. In a certain sense, surface effects can be considered as a sort of finite-size effects since the surface influence is most significant in smallest nanoparticles and should vanish in very large particles. Physical properties of the surface and the core of a nanoparticle can differ very much. Hence, the competition between surface and core magnetic subsystems determines the magnetic parameters of nanoparticle as a whole. As the specimen characteristic dimension ‘d’ approaches nanosize values and since the magnetic correlation length diverges at T_C, the correlated fluctuating magnetic moments in a volume are influenced by the finite size of the specimen. The T_C is then reduced as

$$\frac{T_c(d) - T_c(\infty)}{T_c(\infty)} = \pm \left(d \middle/ d0 \right)^{-\lambda_C} \qquad 1.1$$

where $T_C(\infty)$ is the bulk Curie temperature, λ_c is related to correlation length exponent, and d_0 is an order of the characteristic microscopic dimension[22]. Hence, as particle size decreases, one would expect that the Curie temperature decreases. However, changing of crystallographic parameters or composition, both in the particle core or its surface layer, can mask or even inverse this effect[23-25].

1.3 Ferrite Nanoparticles

There is a growing interest in magnetic ferrite nanomaterials because of their interesting physical properties and applications. Superparamagnetic ferrite nanoparticles and their dispersions have been a topic of intense research for the last few decades because of their applications in the field of heat transfer[26], biomedical applications[27], defect sensors[28] and ion sensors[29, 30]. Besides, they have been model systems to probe molecular interactions[31]. Ferrites are classified as “soft” or “hard” depending on their magnetic properties. Ferrites with low coercivity are termed as soft ferrites and their magnetization can easily reverse direction without much loss of energy. Because of their comparatively low loss at high frequencies, they are extensively used in the cores of radio frequency transformers and inductors in applications such as switched-mode power supplies. Manganese zinc ferrites and nickel zinc ferrites are the common examples of this category. In contrast, ferrites with high coericivity and remanence are termed as hard ferrites. These ferrites are also highly resistant to demagnetization, an essential characteristic of permanent magnet. They also conduct magnetic flux well and have a high magnetic permeability which enables them to store more data. Some of the examples of hard ferrites include cobalt ferrite and barium ferrite.

1.3.1 Structure

Transition metal oxide ferrites have cubic spinel structure with the general formula $(M^{2+}_{\delta}Fe^{3+}_{1-\delta})_A[M^{2+}_{1-\delta}Fe^{3+}_{1+\delta}]_BO_4$ where, δ is the inversion parameter, A and B represents tetrahedral and octahedral sites, respectively[16]. M^{2+} represents the divalent metal ion (e.g. Fe^{2+}, Zn^{2+}, Co^{2+}, Mn^{2+}, Ni^{2+} etc.). The large oxygen ions (radius ~1.3 Å) are packed quite closer in a face-centered cubic arrangement, and the much smaller metal ions (radii ~ 0.7 to 0.8 Å) occupy the spaces between them. In A-site, the metal atom is located at the center of a tetrahedron whose corners are occupied by oxygen ions whereas in B-site, the metal ion is surrounded by the oxygen ions at the corners of an octahedron. The crystallographic environments of the A and B sites are therefore distinctly different. In a cubic spinel structure, only one-eighth of the A sites and one-half of the B sites are occupied. A ferrite crystal has 64 tetrahedral and 32 octahedral sites. Out of this, only 8 tetrahedral and 16 octahedral sites are occupied. The ferrites can be classified into three categories depending on the inversion parameter.

Normal spinel: For $\delta=1$, the general formula becomes $M^{2+}_A[Fe^{3+}_2]_BO_4$ and termed as normal spinel (Fig 1.2). In this case, the tetrahedral site is occupied by the divalent (M^{2+}) metal ions completely and the octahedral site is occupied by trivalent (Fe^{3+}) metal ions. Examples of normal spinel are $ZnFe_2O_4$ and $CdFe_2O_4$.

Inverse spinel: For $\delta=0$, the formula of the ferrite becomes $Fe^{3+}_A[M^{2+}Fe^{3+}]_BO_4$ and is known as inverse spinel (Fig 1.2). In an inverse spinel structure, the tetrahedral site is fully occupied by trivalent (Fe^{3+}) metal ions and the octahedral site is equally shared by divalent (M^{2+}) and trivalent (Fe^{3+}) metal ions. The common examples of inverse spinel are Fe_3O_4 and $CoFe_2O_4$.

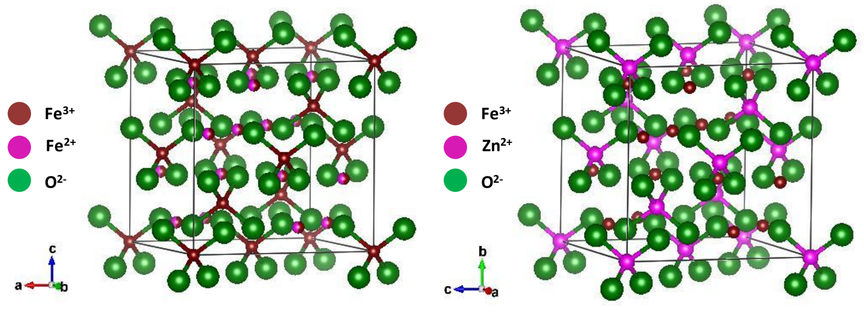

Fe_3O_4 (Inverse spinel) $ZnFe_2O_4$ (Normal spinel)

Fig 1.2: Crystal structure of Fe_3O_4 (inverse spinel) and $ZnFe_2O_4$ (normal spinel).

Mixed spinel: For $0<\delta<1$, the general formula can be represented as $(M^{2+}_{\delta}Fe^{3+}_{1-\delta})_A[M^{2+}_{1-\delta}Fe^{3+}_{1+\delta}]_BO_4$ and termed as mixed spinel structure. In mixed spinel, both the tetrahedral and octahedral sites are shared by divalent (M^{2+}) and trivalent (Fe^{3+}) metal ions. The degree of inversion of the structure depends on the cationic distributions in both the sites. Examples of mixed spinel are $MnFe_2O_4$ and $Ni_xZn_{1-x}Fe_2O_4$.

1.3.2 Magnetic interactions

The magnetic properties of ferrite nanoparticles are much different from that of their bulk counterparts because of a combination of magnetic interactions such as dipolar, exchange, superexchange, and double exchange interactions[32]. Each of them can be explained as follows

Dipolar interaction (dipolar coupling): It is the direct long range interaction between two magnetic dipoles where the potential energy of this type of interaction is given by

$$E = \left(\frac{\alpha_0}{4\pi r^3}\right)\overline{m_1}.\overline{m_2} - \left({}^{3}\!/_{r^2}\right)(\overline{m_1}.\bar{r})(\overline{m_2}.\bar{r}) \tag{1.2}$$

where, m_1 and m_2 are the magnetic moments of individual dipoles separated by a distance r and α_0 is the dipolar interaction constant. The strength of this interaction depends on the distance of separation and degree of mutual alignment.

Exchange interaction: The spin only interaction between electrons is termed as exchange interaction. It takes place when the wave functions of indistinguishable particles are being subject to exchange symmetry. In a crystal, generalization of the Heisenberg Hamiltonian in which the sum is taken over the exchange Hamiltonians for all the (*i*,*j*) pairs of atoms of the many electron system can be presented as

$$H = \sum_{i,j} J_{ij} \vec{S}_i . \vec{S}_j \qquad 1.3$$

where, J_{ij} is the exchange coupling constant, S_i and S_j are the spin only components of the i^{th} and j^{th} electrons.

Superexchange interaction: Super exchange interaction is the strong antiferromagnetic coupling between two next to nearest neighbor cations through a non-magnetic anion[33]. This interaction is a result of the electrons having come from the same donor atom and being coupled with the receiving ions spins (e.g. - Fe^{3+}-O^{2-}-Fe^{3+} in magnetite). If the two next to nearest neighbor positive ions are connected at 90 degrees to the bridging non-magnetic anion, then the interaction can be a ferromagnetic interaction.

Double-exchange mechanism: The double-exchange mechanism is a type of magnetic exchange that may arise between ions in different oxidation state. This interaction is superficially equivalent to superexchange interaction. However, in superexchange interaction, a ferromagnetic or antiferromagnetic alignment occurs between two atoms with the same valence; while in double-exchange, the interaction occurs only when one atom has an extra electron compared to the other.

In general, the magnetic properties of ferrites are explained by the superexchange interaction between metal ions present in tetrahedral (A) and octahedral (B) sites. In Fe_3O_4 nanoparticles, the superexchange interaction occurs among Fe^{3+} ions in A and B sites through non-magnetic O^{2-} [34]. This leads to coupling of spins in such a way that the adjacent atoms align antiparallel to each other and then their magnetism cancels due to equal distribution of Fe^{3+} in both A and B sites. However, the little magnetic units in A and B sites may not be of the same magnitude. Although they are oriented antiparallel so as to offset one another, they can give rise to a net magnetic effect due to unequal distribution of atoms in A and B sites. This resultant magnetic effect gives rise to ferrimagnetism in Fe_3O_4 nanoparticles. Magnetic property in ferrites strongly depends on their cationic distributions. For example, $ZnFe_2O_4$ is paramagnetic in nature due to presence of Zn^{2+} in tetrahedral site (normal spinel) and $CoFe_2O_4$ is ferromagnetic in nature due to the presence of Co^{2+} in octahedral site (inverse spinel).

1.3.3 Synthesis Methods

Many efficient synthesis routes to produce shape-controlled, highly stable, and monodisperse magnetic nanoparticles have been developed in recent years[3]. Techniques such as co-precipitation[35], thermal decomposition[36], sol-gel[37], solvothermal synthesis[38, 39], laser pyrolysis[40], microemulsion[41, 42], microbial[43, 44] and microwave assisted[45] techniques have been used for the synthesis of magnetic nanoparticles. Details of these methods are described below:

Co-precipitation: Among various techniques for magnetite synthesis, the co-precipitation method is a convenient approach to produce nanoparticles from aqueous metal salt solutions. The first controlled synthesis of ferrite nanoparticles using co-precipitation method was performed by Massart[35], who obtained superparamagnetic iron oxide nanoparticles by precipitating $FeCl_2$ and $FeCl_3$ using NH_4OH as alkali. The overall chemical reaction of magnetite formation can be represented as

$$Fe^{2+} + 2Fe^{3+} + 8OH^{-} \rightarrow Fe_3O_4 + 4H_2O \quad 1.4$$

The formation pathways of magnetite in co-precipitation process depend on the rate of alkali addition[46]. The akaganeite (β-FeO(OH)) undergoes a transformation to magnetite through goethite when the alkali is added slowly to the salt solution. During rapid alkali addition, an additional pathway in which ferrous hydroxide nucleated and transformed through lepidocrocite (γ-FeO(OH)) to magnetite. In co-precipitation reaction, the magnetite formation take place through iron hydroxide intermediate, but the dominant process is the topotactic transformation of goethite (α-FeO(OH)) to magnetite. The size and shape of the nanoparticles can be tuned using this method by varying the parameters like pH, ionic strength, temperature and nature of salt solution[47].

The advantage of co-precipitation process is that it does not produce or use any toxic intermediates or solvents and does not require precursor complexes or high temperature reaction environment. It has become a popular technique because of its ability to be scaled up, reproducibility and co-friendly reaction conditions[48]. The type of salts used, Fe^{2+}/Fe^{3+} ratio, reaction temperature, pH value and the ionic strength of the media are the key parameters to control the size, shape and composition of the magnetic nanoparticles by this method. However, the experimental challenge in the synthesis of Fe_3O_4 by co-precipitation lies in the control of particle size and achieving a narrow particle size distribution[48].

Solvothermal: Solvothermal synthesis is usually performed in autoclaves or reactors by maintaining pressure more than 2000 psi at temperature ~ 200 ºC. There are two types of solvothermal processes carried out for synthesis of ferrite nanoparticles; solvolysis of metal salt solution and oxidation or neutralization of mixed metal hydroxide[49]. A typical experimental set up of solvothermal method is shown in Fig 1.3. In this method, metal oxide nanoparticles are prepared by decomposing organometallic compounds such as metal acetyl-acetonates in high boiling organic solvents containing surfactants. Fe_3O_4 nanoparticles are prepared by decomposing salts such as $[Fe(acac)_3]$ in presence of 1,2-hexadecanediol, oleylamine and oleic acid in phenol ether[39, 50]. The factors such as the ratios of the starting reagents including organometallic compounds, surfactant and solvent are the decisive parameters for controlling of the size and morphology of magnetic nanoparticles. Also, the nature of particles formed in this method depends on the reaction conditions such as temperature and time[51]. In this method, the particle size is controlled through nucleation and growth process. At high reaction temperature, the nucleation might be faster than the growth while at long reaction time, growth process is favored. This method is suitable only for small scale but not for industrial applications due to the high temperature requirement. Fe_3O_4 nanoparticles prepared in this method are usually dispersed in organic solvent. Recently, it was demonstrated that water soluble Fe_3O_4 nanoparticles (4-60 nm) can be prepared by decomposing $FeCl_3 \cdot 6H_2O$ at 245 ºC and 2-pyrrolidone or α,ω-dicarboxyl-terminated poly(ethylene glycol) as coordinating agent under reflux[52, 53].

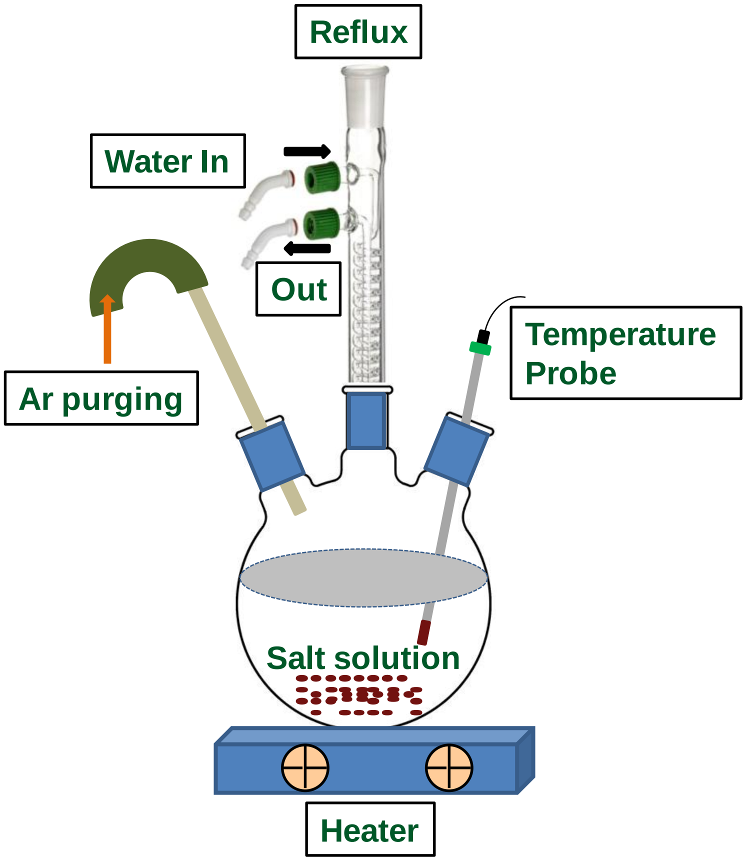

Fig 1.3: Schematic representation of solvothermal synthesis.

Sol-Gel Method: This method is based on the hydroxylation and condensation of metal salt solutions leading to the formation of 'sol', which on further condensation and polymerization form a three dimensional metal oxide 'gel'[54]. The final crystalline state of the nanoparticles is obtained by heating it at high temperatures. The main parameters controlling the growth kinetics, structure and properties of the nanoparticles are solvent, temperature, concentration of salt solution, pH and agitation[54-56]. This method allows synthesis of monodisperse nanoparticles of desired particle size, microstructure, homogeneity, and functionalization [57].

Polyol Approach: This is a special kind of sol-gel method where the solvent used is a polyol (ex-polyethylene glycol). Owing to the high boiling point and high dielectric constant of these solvents, they offer a wide range of reaction temperature[58]. They act as reducing agent and also prevent growth and aggregation of nanoparticles by acting as a stabilizer. This is a versatile method for synthesizing particle of nano as well as micro range with desired size and shape. In this method, the precursor compound is suspended in liquid polyol and heated to the boiling point of polyol at constant stirring. During this process, the precursor gets dissolved in the polyol leading to the formation of an intermediate followed by reduction to form nanoparticles. This method allows preparation of water based nanoparticles by coating hydrophilic polyol over the nanoparticles, producing particles with higher crystallinity that leads to a better saturation magnetization and narrow particle size distribution compared to the traditional methods[59].

Sonolysis: Ferrite nanoparticles can also be prepared by decomposition of organometallic precursors using sonolysis or thermolysis. In this method, a very high temperature is applied by rapid collapse of sonically generated cavities which allows the conversion of ferrous salts into magnetic nanopaticles[60]. This method can be used to prepare superparamagnetic ferrite nanoparticles with high saturation magnetization[61]. The growth of the particles is controlled by polymers, organic capping agents or structural hosts. Ultrasonic irradiation causes cavitations in an aqueous medium where the formation, growth and collapse of micro bubbles can occur. In many cases thermally induced processes provide crystalline nanoparticles. Ultrasonic driven reactions yield amorphous materials due to enormous cooling rates during quenching[62].

Flow Injection Method: This method was developed by Alvarez et al.[63] which consists of a continuous or segmented mixing of precursors under laminar flow regime in a capillary reactor. The experimental set up includes a multi-channel peristaltic pump, Teflon tubing lines, a T-shaped injector and an injection valve. The nature of the particles prepared in this method can be controlled by controlling the injection and the time of cycle. The advantages of this method are high reproducibility because of the plug flow and laminar conditions, high mixing homogeneity and precise external control on the process parameters.

Pyrolysis: Spray and laser pyrolysis techniques are useful for the direct and continuous high rate production of desired magnetic nanoparticles under exhaustive control of experimental conditions[64]. In spray pyrolysis method, ferric salt solution along with a reducing agent in organic solvent are sprayed into a series of reactors, where the aerosol solute condenses and the solvent evaporates[65]. The resulting size of the particles depends on the initial droplet size. This technique has been used to prepare maghemite nanoparticles (5 to 60 nm) with different shapes using different iron precursor salts in alcoholic solution[66].

The laser pyrolysis technique is based on the resonant interaction between laser photons and gaseous species, reactant or sensitizer[67]. The sensitizer is an energy transfer agent which is excited by CO_2 laser radiation and transfers the energy to the reactants by collision[68]. In laser pyrolysis, a gaseous mixture of iron precursor and a flowing mixture of gas are heated using laser to produce small and non aggregating particles with narrow size distribution[25]. The size of the particles can be tuned by adjusting the experimental conditions.

Although, pyrolysis methods yield high quality products but the percentage yield is usually low. The purity of the product obtained in these methods can be controlled by oxygen concentration, gas phase impurities and the heating time. Besides, the equipments used in pyrolysis methods are also expensive.

Microbial Approach: In this method the metal salt solution is incubated with the reducing bacteria at low temperature for several days[43]. It is useful in synthesizing ferrite nanoparticles with a wide size range. Magnetite nanoparticles can be extracted from magnetotactic bacteria which involves numerous discrete steps. The first step involves the formation of magnetite bio-mineralization which undergoes transformation to magnetosome vesicles[69]. The magnetosome vesicle is is reduced from Fe (III) to Fe (II) with its subsequent uptake and transport inside the vesicle. The process of iron uptake in magnetotactic bacteria occur either by siderophores or by iron reduction[70, 71]. The last step in magnetite formation is controlled by bio-mineralization of magnetite.

Magnetite nanoparticles can also be synthesized by iron reducing bacteria. Bacteria synthesizes magnetite extracellularly in the surrounding environment under strictly anaerobic conditions[72, 73]. In this process, magnetite is synthesized by coupling the oxidation of organic matter to the reduction of ferric iron during the metabolism of the bacteria. Generally, poorly crystalline ferrihydrite is used as an electron acceptor by the iron reducing bacteria which in turn is reduced to magnetite.

Reverse Micelle Approach: In this technique, surfactant stabilized water in oil emulsion containing the aqueous solution of the precursor is prepared[42]. By mixing two identical water-in-oil micro-emulsions containing the desired reactants, the microdroplets will continuously collide, coalesce and finally forms precipitates in the micelles. The precipitate can be extracted using solvents such as acetone and ethanol by centrifuging the mixture. In this sense, a microemulsion can be used as a nanoreactor for the formation of nanoparticles. Although this method has been used for synthesis of a wide variety of nanoparticles, the shape and size usually vary over a wide range. The working window is very narrow and only a small amount can be prepared using this technique. It also requires a large amount of solvent. A typical schematic for synthesis of ferrite nanoparticles by reverse microemulsion method is shown in Fig. 1.4.

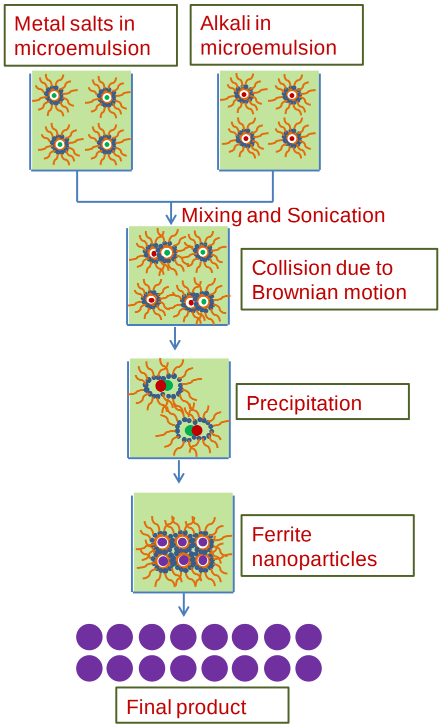

Fig 1.4: A schematic representation of reverse micellar reaction mechanism (Courtesy Rana et al.[42]).

Microwave Assisted Method: In recent years, microwave assisted synthesis method is widely used over conventional heating techniques to produce nanocrystals with higher yield [45]. Specially designed microwave synthesis reactor allows an exquisite control on reaction temperature, stirring rate and pressure inside the reaction vessel which is the unique features of microwave apparatus over conventional heating principles. The heating effect in the microwave arises from the interaction of the electric field component of the microwave with charged particles in the material through both conduction and polarization. The use of microwave heating as a non-classical energy source has been shown to dramatically reduce reaction times, increase product yields and enhance purity or material properties compared to conventionally processed experiments.

In conventional methods, heating chemical reactions have been achieved using mantles, oil baths, hot plates, reflux set-up where the highest reaction temperature achievable is dictated by the boiling point of the solvent used. This traditional form of heating is rather slow and has low efficiency for transferring energy to a reaction mixture as it depends on convective currents and on the thermal conductivity of various compounds or materials that have to be penetrated. This often results in the temperature of the reaction vessel being higher than that of the reaction solution. In contrast, microwave irradiation produces efficient volumetric heating by raising the temperature uniformly throughout the whole liquid volume by direct coupling of microwave energy to the molecules that are present in the reaction mixture.

Fig 1.5: Schematic representation of some of the synthesis methods used for the synthesis of ferrite nanoparticles by (a) polyol[74] (b) microwave (c) co-precipitation [75](d) pyrolysis[76] (e) hydrothermal [77]and (f) emulsion techniques[42].

1.3.4 Applications

Ferrite nanoparticles are used in various biomedical and electronic industries due to their fascinating magnetic properties[5, 78]. Molecular imaging is one of the most promising applications of iron oxide nanoparticles[79]. Various applications using targeted iron oxide nanoparticles have already been evaluated in animal experiments. Different antibodies directed to several types of receptors have been coupled to iron oxide nanoparticles and tested in vitro or in vivo[3]. A demonstration of multimodal imaging in a rat is shown in Fig 1.6. The functionalizaed of iron oxide nanoparticles are used in protein or cell separation [80].

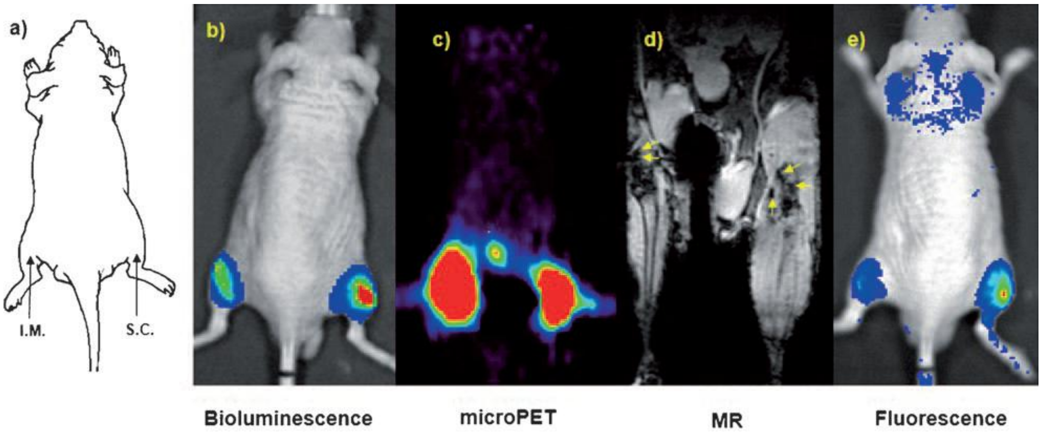

Fig 1.6: Multimodal imaging demonstration. The multimodal probe labeled with C6 cells were (a) transplanted into the left and right thighs of nude mice through intramuscular and subcutaneous injection. Then the animal was scanned by optical bioluminescence (B), positron emission tomography (C), MRI (D) and fluorescence (E) (Courtesy Hwang et al[81]).

Magnetic separation techniques are simple and inexpensive compared to traditional separation procedures because all the steps of purification can take place in one test tube without expensive liquid chromatography systems. Magnetic nanoparticles are also useful candidates for localized drug delivery[10]. A schematic of controlled and targeted drug delivery in presence of magnetic field is shown in Fig 1.7. In conventional drug delivery process, poor specificity to the site of action and reduced drug diffusion through biological barriers, leads to a suboptimal pharmacological activity and high incidence of adverse effects. Encapsulation and delivery of drugs using nanodevices can potentially overcome these limitations.

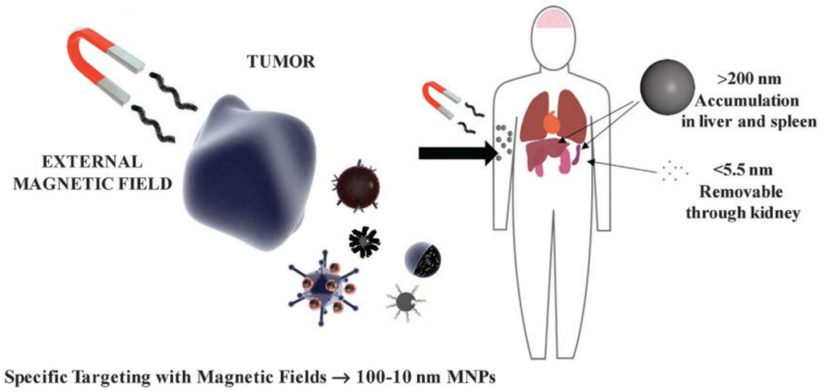

Fig 1.7: Targeted drug delivery using magnetic nanoparticles in presence of external magnetic field (Courtesy Colombo et al[83]).

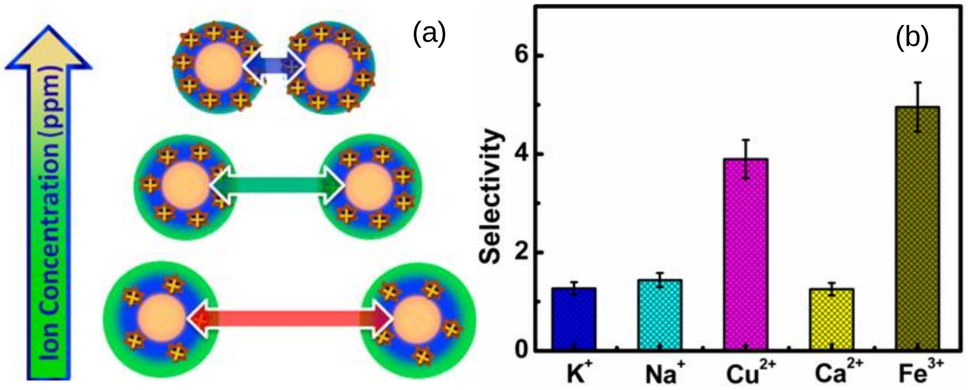

Fig 1.8: (a) Schematic representation of the emulsion droplets in the presence of metal ions and adsorbed surfactant molecules and (b) Slopes (indicating the selectivity) of λ_{max} shift as a function of cation concentration for different ions (Courtesy Mahendran et al.[29]).

In recent decades, carrier-mediated drug delivery has received significant attention because this approach has resulted in improved pharmacokinetics and pharmacodynamics of the drugs. Ferrofluids are also a very powerful material for therapeutic purposes[82]. They have high efficiency to absorb the energy of an oscillating magnetic field and convert it into heat. This property can be used to increase the temperature of tumor tissue and to destroy the pathological cells by hyperthermia. A survey on clinical studies using hyperthermia in combination with radiation therapy have shown that 83.7% of patients had a reduced tumor mass, of which 37.4% had a complete tumor regression while 24.5% exhibited a >50% tumor reduction[83]. In a recent study, Vadahanambi et al. have shown that three-dimensional graphene-carbon nanotube-iron oxide nanostructures can be an efficient agent for removal of arsenic from contaminated water[84]. Magnetic nanoparticles are also used for treatment of contaminated water[85]. They are also being used as a catalyst or catalyst supports in chemical reactions[86]. Magnetic nanoemulsions are also used as ionic sensors for the detection of cations such as Na^+, K^+, Ca^{2+}, Cu^{2+} and Fe^{3+} in presence of an external magnetic field[29]. Magnetic nanoemulsions have also been used as a model system to probe intermolecular forces[87-89]. Fig 1.8 demonstrates the selective detection of metal ions using magnetic nanofluids. Liu et al. have developed a multifunctional Fe_3O_4-polydopamine core shell structure which can serve as catalyst, drug delivery and carbon adsorbent[90]. Exploiting the concept of high affinity specific interactions between molecular pairs to achieve reciprocal recognition and trigger signaling processes, functionalized magnetic nanoparticles can also be used for localized drug delivery in biomedical applications[83]. This allows controlling the localization of selected biological targets by applying an external magnetic field gradient and isolating them. Also, it exploits the unique superparamagnetic character of magnetic nanoparticles to interact with an external magnetic field inducing de-phasing of spin–spin relaxation times with the surrounding water protons of the solvent, in which they are immersed.

1.4 Phase transitions

1.4.1 Introduction

A phase is defined as the part of the thermodynamic system which possesses uniform physical properties throughout[91]. Thermodynamic transformation of one phase to another is commonly known as phase transition. Melting of ice (solid-liquid), evaporation of water (liquid-gas), ordering of magnetic spins (paramagnetic-ferromagnetic), aggregation of block polymers (sol-gel) are some of the common examples of phase transitions. There are various parameters governing phase transitions of matter such as temperature, pressure, entropy, free energy etc. The phase of a system depends on its Gibb's free energy, which can be expressed as; $\Delta G = \Delta H\text{-}T\Delta S$ where, ΔG is the change in free energy, ΔH is the change in enthalpy, T is the absolute temperature and ΔS is the change in entropy. The phase transition becomes spontaneous when ΔG is negative, achieves equilibrium when the net ΔG is zero and becomes non-spontaneous when ΔG is positive. The mechanism of phase transition is explained by interaction energy and thermal energy which decides the net free energy of the system.

1.4.2 Phase transitions in iron oxide

There is a great interest in iron oxides, especially in nanosized form, because of both fundamental and practical reasons. Nanosized γ-Fe_2O_3 and Fe_3O_4 are very useful material in nanotechnological applications because of their interesting magnetic and surface properties. They are also nontoxic, biodegradable, biocompatible, and chemically stable in nature. Iron oxide nanoparticles can exist in different polymorphic forms in nature which are significantly different in their structural and magnetic properties[92]. The most common and technologically important forms of iron oxide are Fe_3O_4 (magnetite), α-Fe_2O_3 (hematite), γ-Fe_2O_3 (maghemite) and FeO (Wustite). Except these, iron oxides are also exist as β-Fe_2O_3 and ε-Fe_2O_3 forms, which are observed only in nano phase. In addition, Iron oxide is also found as oxyhydroxide such as goethite, lepidocrocite, akaganeite.

Fe_3O_4 and γ-Fe_2O_3 nanoparticles with sizes of ~10 nm or less exhibit superparamagnetic nature. γ-Fe_2O_3 is thermodynamically unstable and is converted either directly or indirectly (with ε-Fe_2O_3 as an intermediate product) to α-Fe_2O_3 above certain temperature.

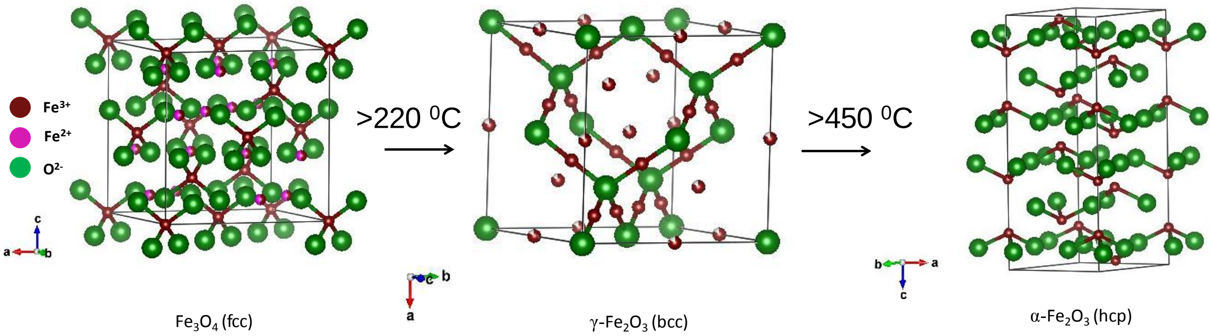

Fe_3O_4 (fcc)

γ-Fe_2O_3 (bcc)

α-Fe_2O_3 (hcp)

Fig 1.9: Schematic representation of different phases of iron oxide nanoparticles at high temperatures under air annealing.

The transition temperature is dependent on several physicochemical parameters[92]. Emmett et al. [93] reported that the cubic (magnetite and maghemite) oxide can be changed into the more stable rhombohedral (hematite) phase between 550 and 1000 ºC. Fig 1.9 shows the schematic representation of different phases of iron oxide nanoparticles at high temperatures under air annealing.

The transition temperature also depends upon the method of preparation and the impurities present in the sample. Due to this phase transition from γ-Fe_2O_3 to α-Fe_2O_3, the applications of iron oxides are limited upto the non-magnetic transition temperatures. Therefore, for applications beyond phase transition temperatures, augmentation of γ-Fe_2O_3 to α-Fe_2O_3 phase transition temperature is a prerequisite. A study on activation energy of γ-Fe_2O_3 to α-Fe_2O_3 phase transition shows that the stability of γ-Fe_2O_3 increases by the presence of alumina, lowered by lanthana, and unaffected by gallia[94]. The aluminium ion (Al^{3+}) with smallest size increases the activation energy for γ-Fe_2O_3 to α-Fe_2O_3 phase transition temperature whereas the lanthanum ion (La^{3+}) decreases the activation energy. Gallia (Ga^{3+}) did not affect the phase transition temperature due to the similar ionic radii of gallium and Fe^{3+} ion. It was assumed that in larger particles (> 300 nm), spontaneous nucleation of α-Fe_2O_3 takes place because of greater lattice strain during oxidation[95]. Colombo et al. [96] suggested that magnetite can never be oxidized to α-Fe_2O_3 below 600 ºC unless α-Fe_2O_3 nuclei are present in the starting material. But in another study by Feitknecht et al.[97] reported that the conversion of γ-Fe_2O_3 to α-Fe_2O_3 occur at 250 ºC. It was also observed by Gallagher et al. [98] that the magnetite nanoparticles of size about 300 nm can be oxidized to α-Fe_2O_3 at temperature about 180 ºC, even without having α-Fe_2O_3 nuclei in the original Fe_3O_4. The difference in the observed phase transition behavior was attributed to the use of starting material from different sources (natural magnetite by Colombo et al. and pure synthesized magnetite by Gallagher et al.). It was also observed that for particle size below 300 nm, Fe_3O_4 nanoparticles oxidizes to γ-Fe_2O_3 below 220 ºC. In larger size particles, an intermediate phase of Fe_2O_3 and Fe_3O_4 exist below this temperature and then undergo disproportionation to Fe_3O_4 and α-Fe_2O_3. Fe_3O_4 formed in this step converts directly to α-Fe_2O_3 at higher temperatures.

Table 1.1: Reported values of γ-α phase transition temperatures, crystallite size, saturation magnetization and method of synthesis of bare Fe_3O_4 nanoparticles in air atmosphere.

System	Preparation Method	Size (nm)	M_s (emu/g)	γ-Fe_2O_3 to α- Fe_2O_3 transition temperature (^oC)	Ref.
Fe_3O_4	Co-precipitation	3 4.8 5	- ~19 ~22	500 600 450	[99] [100] [100]
	Wet chemical	5 12	- -	390 580	[101] [102]
	Sonochemical	15	50	500	[103]
	Combustion	39	-	395	[104]
	Oxidation	55		500	[105]

It was also reported that at very low concentration gradient in the core of magnetite nanoparticles during oxidation causes most of the change in lattice parameter in small particles. But above a certain critical size, the unequal contraction within the surface layer causes the lattice strain to reach a level sufficient to activate the nucleation of the more stable α-Fe_2O_3 phase and increases the lattice strain in the larger size particles. Kinetic studies on phase conversion of magnetite to maghemite (~7 to 22 nm) by chemical analysis shows that the activation temperature is relatively lower for ultrafine particles and the frequency factor increases from $1.6x10^{11}$ to $5.7x10^{13}$ with increase in particle size from 7.7 to 22 nm[106].

Lund et al.[107] studied the effect of silica support on the thermal stability of magnetite nanoparticles at high temperatures. They found that a strong oxide-oxide interaction exists between Fe_3O_4 and SiO_2 in a silica-supported magnetite which was oxidized at a temperatures of 800 K yielding γ-Fe_2O_3 rather than α-Fe_2O_3. It was suggested that the origin of the interaction between iron oxide and silica is the substitution of Si^{4+} with tetrahedral Fe^{3+} in Fe_3O_4 due to the preference of Si for tetrahedral coordination in oxides because of covalence and ionic size consideration. In a study on the effect of trace element substitution on magnetite nanoparticles, it was observed that during the transformation of maghemite to hematite as much as about 60% of the Co, Ni, Zn, and Cu present in the crystal structure of maghemite is ejected from the crystals, whereas the Mn, Cr, and A1 present in maghemite are redistributed in hematite particles[108]. This requires some additional activation energy over that required for the transformation of pure maghemite to eject or redistribute these doping elements. The enhanced activation energy with dopants reduces the transformation rate of maghemite to hematite. Studies on γ-Fe_2O_3 to α-Fe_2O_3 phase transition temperature of pure γ-Fe_2O_3 showed no changes in maghemite phase below 300 ºC for a period of 5 days[105]. However, annealing of maghemite at >320 ºC produced hematite, but the transformation rate was very slow at <450 ºC. On further increasing in the annealing temperature to 500 ºC, the maghemite to hematite phase transformation became rapid and was completed within 3 hrs. The γ-Fe_2O_3 to α-Fe_2O_3 phase transition temperature observed through calorimetric measurements was found to increase from 532 to 640 ºC with 1% Zn doping[105]. The transition temperature was found to increase to ~ 566, 570, 598, and 601 ºC with 0.09% of Cu, 0.37% of Co, 0.48% of Ni, and 0.89% of Mn doping, respectively. Sarda et al.[109] studied the effect of Ba doping on phase transformation temperatures of magnetite nanoparticles and found that the oxidation temperature of Fe_3O_4 to γ-Fe_2O_3 increases from 120 to 247 ºC with a 2.47 wt% Ba doping. It was attributed that the barium located in the surface layers of the particles, oppose the migrations of Fe^{2+} ions towards the solid-gas interface. The diffusion barrier in turn increases the activation energy for the oxidation process of Fe_3O_4 to γ-Fe_2O_3. The phase transformation temperature of γ-Fe_2O_3 to α-Fe_2O_3 was found to increase linearly from 493 to 749 ºC by increasing the Ba doping concentration from 0.29 to 2.09 wt%, but remains constant on further increasing of the Ba doping concentration. It was attributed to the fact that the addition of Ba atoms to the surface layers stabilizes the surface layer of the spinel structure, creating bonds with the atoms that have uncoordinated links. Ye et al.[102] studied the thermal stability of nanocrystaline γ-Fe_2O_3 prepared by wet chemical method. For 12 nm particles of γ-Fe_2O_3, they observed that the γ-Fe_2O_3 to α-Fe_2O_3 phase transition occurs at 500 ºC. The growth of particles was slow before the phase transition and found to increase rapidly after the formation of α-Fe_2O_3 phase. Yen et al. studied the variation of crystallite size during the phase transformation of γ-Fe_2O_3 to α-Fe_2O_3[110]. It was observed that the γ-Fe_2O_3 to α-Fe_2O_3 phase transformation takes place when the crystallite size increases from 5 to 25 nm for γ-Fe_2O_3 prepared using γ-FeO(OH) and from 15 to 25 nm when derived from Fe_3O_4. Lai et al.[103] studied the effect of Mn (III) doping on γ-Fe_2O_3 to α-Fe_2O_3 phase transition in ambient atmosphere. In pure γ-Fe_2O_3 nanoparticles prepared by irradiating with ultrasonic waves, they observed that the conversion to α-Fe_2O_3 phase occurs above an annealing temperature of 500 ºC for 3 hrs whereas the particles remain as γ-Fe_2O_3 phase after doping with 8.5% of Mn (III). Doped samples are found to require higher temperatures to completely convert into the α-phase, indicating the high activation energy requirement. The delayed γ-Fe_2O_3 (maghemite) to α-Fe_2O_3 (hematite) transition was attributed to the requirement of higher activation energy for the transition to a more compact α-phase, which requires lattice contraction. It is reported that the phase transformation temperature of γ-Fe_2O_3 to α-Fe_2O_3 is increased by 100 ºC with 15 mol% Zn^{2+} doping in nanocrystalline γ-Fe_2O_3[104]. It was observed that formation of α-Fe_2O_3 takes place along with γ-Fe_2O_3 at lower concentrations of Zn and the amount of α-Fe_2O_3 decreases with increasing amount of Zn (only 5% of α-Fe_2O_3 phase was formed when more than 0.125 moles of Zn are used). The magnetic to non-magnetic transition is observed at 395 ºC for pure γ-Fe_2O_3 while for 2.5% doped sample, the magnetic transition was observed at 450 ºC.

Table 1.2: γ-Fe_2O_3 to α-Fe_2O_3 phase transition temperature under air annealing of Fe_3O_4 nanoparticles with different doping /coating/shells prepared using various techniques.

Doping /Coating/Shell	Dopant conc. (%)/Shell thickness	Synthesis Method	Experimental Tool Used	γ-Fe_2O_3 to α- Fe_2O_3 transition temperature (^oC)	Ref.
Co (Doping %)	0.1	Combustion	DSC	598	[105]
	0.2	Precipitation	DSC	612	[111]
	0.43			687	
	0.67			731	
	0.9			723	
Mn (Doping %)	8.5	Sonochemical	XRD	600	[103]
	0.46	Combustion	DSC	622	[105]
	5.7	Precipitation	DSC	630	[111]
	11.86			645	
	16.98			647	
	22.4			649	
Zn (Doping %)	0.05	Combustion	DSC	642	[105]
	1			660	
	15	Combustion	VSM	500	[104]
Ni (Doping %)	0.21	Combustion	DSC	623	[105]
	6.28	Precipitation	DSC	592	[111]
	12.56			667	
	17.67			745	
	22.33			722	
Cu (Doping %)	0.09	Combustion	DSC	608	[105]
Cr (Doping %)	0.49	Combustion	DSC	605	[105]
	4.19	Precipitation	DSC	563	[111]
	7.21			653	
	9.77			651	
	11.74			676	
Al (Doping %)	0.5	Combustion	DSC	592	[105]
Ti (Doping %)	2.56	Precipitation	DSC	632	[111]
	10.7			720	
	12.33			727	
	16.74			735	
V (Doping %)	0.48	Combustion	DSC	629	[105]
	4.53	Precipitation	DSC	590	[111]
	8.95			546	
	14.07			527	
Oleic Acid (Coating)	-	Co-precipitation	XRD	600	[112]
SnO_2 (Shell)	1-5 nm	Thermal decomposition	XRD	600	[113]
SiO_2 (Shell)	-	Oxidation	XRD & Mossbauer	527	[107]
PMMA (Shell)	-	Decomposition	XRD	500	[114]
Caprylate (Shell)	-	Decomposition	XRD	400	

For 15% doping, the transition temperature was observed at 500 ºC, an increase of 100 ºC from that of the undoped γ-Fe_2O_3 sample. On further increasing the doping fraction to 20%, the phase transition temperature obtained was comparable to that of 15% doping. Gnanaprakash et al.[100] reported that the alkali used in the iron oxide preparation (NaOH and NH_4OH) has an influence on the maghemite (γ-Fe_2O_3) to hematite (α-Fe_2O_3) phase transition temperature. A compressive study on maghemite to hematite phase transitions by doping with Ti, Cr, Mn, Co, V and Ni in Fe_3O_4 shows that the phase transition temperature depends on the metal-oxygen bond strength[111]. The γ-Fe_2O_3 to α-Fe_2O_3 phase transition temperature increases in the case of Ti, Cr, Mn, Co and Ni doping due to formation of a stronger metal-oxide bond after the substitution. But in case of V doping, the phase transition temperature decreases due to a lower bond strength of V-O. The monodisperse superparamagnetic SnO_2 coated (shell thickness 1-5 nm) iron oxide nanopaticles (16 nm) prepared using thermal decomposition method was found to be stable upto 600 ºC with relatively high saturation magnetization (18 Am^2/kg) in air atmosphere[113]. It was attributed that the SnO_2 shell acts as a protecting layer and prevents the conversion of γ -Fe_2O_3 to α-Fe_2O_3. Also, reports show that the silica and silane coating are useful to protect the iron oxide cores from the undesirable phase transformations during high temperature treatment of conductive or magnetic nanocomposites[115]. Recently, it was observed that γ -Fe_2O_3 nanoparticles dispersed in silica matrix have a high resistance against grain growth and transformation into hematite up to 840 ºC[116]. A comparative study on thermal properties of γ-Fe_2O_3/poly(methyl methacrylate) (PMMA) core/shell and caprylate capped magnetite nanoparticles with an average core size of 4 nm shows that the formation of α-Fe_2O_3 phase takes place above 400 ºC for caprylate capped magnetite nanoparticles[114]. But in the case of γ-Fe_2O_3/PMMA core shell, pure γ -Fe_2O_3 phase was observed after 400 ºC air annealing. On further increasing the annealing temperature to 500 ºC, a mixed phase of γ -Fe_2O_3 and α-Fe_2O_3 was observed. It was attributed to the Fe–Si oxide or silica formation on the surface thereby protecting the γ -Fe_2O_3 particles from undergoing γ – α phase transformation.

Magnetite nanoparticles behave differently under vacuum annealing conditions. It was found that the magnetite phase remains intact till 600 ºC and undergoes phase decomposition to γ-Fe_2O_3 and FeO above 700 ºC[112]. Reports show that the phase decomposition temperature of Fe_3O_4 enhances when doped with cobalt and zinc[117, 118]. However, vacuum annealing of magnetite nanoparticles coated with oleic acid was different from that of uncoated Fe_3O_4. It was observed that oleic acid coated Fe_3O_4 nanoparticles exist in cubic spinel structure till 500 ºC under vacuum annealing and above which undergoes a phase decomposition to γ-Fe_2O_3 and FeO[112], which was attributed to the formation of CO and CO_2 (500 ºC) during vacuum annealing that causes the reduction of iron oxide nanoparticles. A recent *in situ* high temperature XRD study shows that as the particle size of Fe_3O_4 was reduced from 7 to 3 nm, the metallic α-Fe phase reduction temperature was increased from 400 to 600 ºC, whereas α-Fe_2O_3 formation temperature was reduced from 1000 to 800 ºC[119]. Table1.2 summarizes the γ -Fe_2O_3 to α-Fe_2O_3 phase transition temperature observed with different percentage of doping or coating or shell thickness and prepared using various techniques.

1.5 Motivation

Studies show that the γ -Fe_2O_3 to α-Fe_2O_3 phase transition temperature can be enhanced with doping or with protective shell. Although coating enhances the phase transition temperature, they also reduce the magnetic nature of particles. Doping is found to be a more convenient method for practical applications as it does not affect the magnetic nature much. Irrespective of the advances in this field, preparation of magnetic nanomaterials with high thermal stability and high saturation magnetization is still a challenge. Further, for effective utilization of ferrite nanoparticles for practical applications, control on monodispersity, purity, magnetization and high temperature stability are necessary. This was one of the motivations to undertake the studies in this thesis. Besides, tuning of Curie temperature in ferrite nanoparticles was another objective, which is important for applications such as heat transfer and magnetic hyperthermia. This thesis reports (1) enhancement of γ -Fe_2O_3 to α-Fe_2O_3 phase transition temperature with various doping elements (Co, Zn, Na), without compromising its magnetic properties and (2) preparation of pure ferrite nanoparticles with tunable Curie temperatures near room temperature.

1.6 Objectives

The major objectives of the present study are:

- To develop methodologies to enhance the high temperature phase stability of magnetite nanoparticles
- To obtain insight into the effects of cation doping on thermal stability and magnetic properties of magnetite nanoparticles.
- To study the effect of reaction temperatures (during synthesis) on high temperature phase stability and magnetic properties.
- To tailor ferrite nanoparticles with tunable magnetic properties like Curie temperature and saturation magnetization.

1.7 Overview of Thesis

This thesis presents the studies on the effect of different doping elements (Co, Zn, Na and Mn) on the phase transition and magnetic properties of ferrite nanoparticles prepared using coprecipitation and microwave method. It consists of eight chapters. The summary of each chapter is given below

Chapter 1 gives a brief introduction to magnetic nanomaterials and their technological applications. The structure and magnetism of ferrite nanoparticles are discussed in detail. An extensive literature review on synthesis and phase transition studies in iron oxide nanoparticles has been presented. Various methods adopted for preparing magnetite nanoparticles with high temperature phase stability by doping, coating, core-shell etc. are also discussed. **Chapter 2** discusses the synthesis methods and characterization techniques used for the studies. **Chapter 3** deals with the effect of Co^{2+} ion doping in magnetite (Fe_3O_4) on its crystal structure, magnetic properties and phase stability during air and vacuum annealing. **Chapter 4** discusses the effect of Zn^{2+} doping on the crystal structure, magnetic properties and the high temperature phase stability of magnetite nanoparticles under air and vacuum annealing. The synthesis of magnetite nanoparticles doped with Na^+ ions by co-precipitation method is discussed in **Chapter 5**. The effect of Na doping on magnetic and thermal properties are presented in this chapter. **Chapter 6** deals with the effect of synthesis reaction temperature on the phase stability of magnetite nanoparticles prepared using microwave method. Magnetite nanoparticles of size ranging from 7-10 nm are prepared from aqueous solutions of Fe^{2+} and Fe^{3+} salts by microwave irradiation at different reaction temperatures ranging from 50 to 200 ºC. The thermal stability and magnetic properties of these nanoparticles are studied under air atmosphere. The tuning of Curie temperature of Mn doped $ZnFe_2O_4$ nanoparticles are discussed in **Chapter 7**. Microwave assisted synthesis method has been used to prepare $Mn_xZn_{1-x}Fe_2O_4$ nanoparticles, with x varying from 0 to 1 and their magnetic properties are discussed. **Chapter 8** summarizes the results obtained, conclusions drawn and the scope for future work.

Chapter II

Synthesis and Characterization Techniques

2.1 Introduction

During the last few years, there have been many reports on efficient synthesis routes to produce shape-controlled, highly stable, and monodisperse magnetic nanoparticles. The synthesis of superparamagnetic nanoparticles is a complex process because of their smaller size limit. In general for synthesis of nanoparticles, the first important challenge is to identify experimental conditions, to produce monodisperse magnetic nanocrystals of suitable size. The second challenge is to select a reproducible process that can be scaled up without any complex purification procedure, such as ultracentrifugation, size-exclusion chromatography, magnetic filtration and fractionation.

Among various techniques for synthesis of magnetite, co-precipitation method is a convenient approach to produce nanoparticles from aqueous salt solution. In co-precipitation method, the respective (Fe^{2+} and Fe^{3+} in case of magnetite) salt solutions with correct stochiometric ratio are mixed in a synthesis reactor. The synthesis reactor is equipped with an external temperature probe, mechanical stirrer (or magnetic stirrer) and pH meter. The pH of the initial solution is maintained at a low value in order to prevent oxidation of the metal ions. After the desired temperature is reached, alkali is added to the mixture to precipitate metal oxide nanoparticles. A typical schematic of co-precipitation method experimental set up is shown in Fig 2.1.

The nanoparticles used in the present studies are prepared by co-precipitation and microwave assisted synthesis methods. The particles are characterized using X-ray diffraction (XRD), transmission electron microscopy (TEM), small angle X-ray scattering (SAXS), atomic emission spectroscopy (AES), Fourier transform infrared spectroscopy (FTIR), thermogravimetric (TGA) and differential scanning calorimetry (DSC), Vibrating sample magnetometer (VSM) and zeta potential measurements. The details of the synthesis procedures and experimental techniques are discussed in the next section.

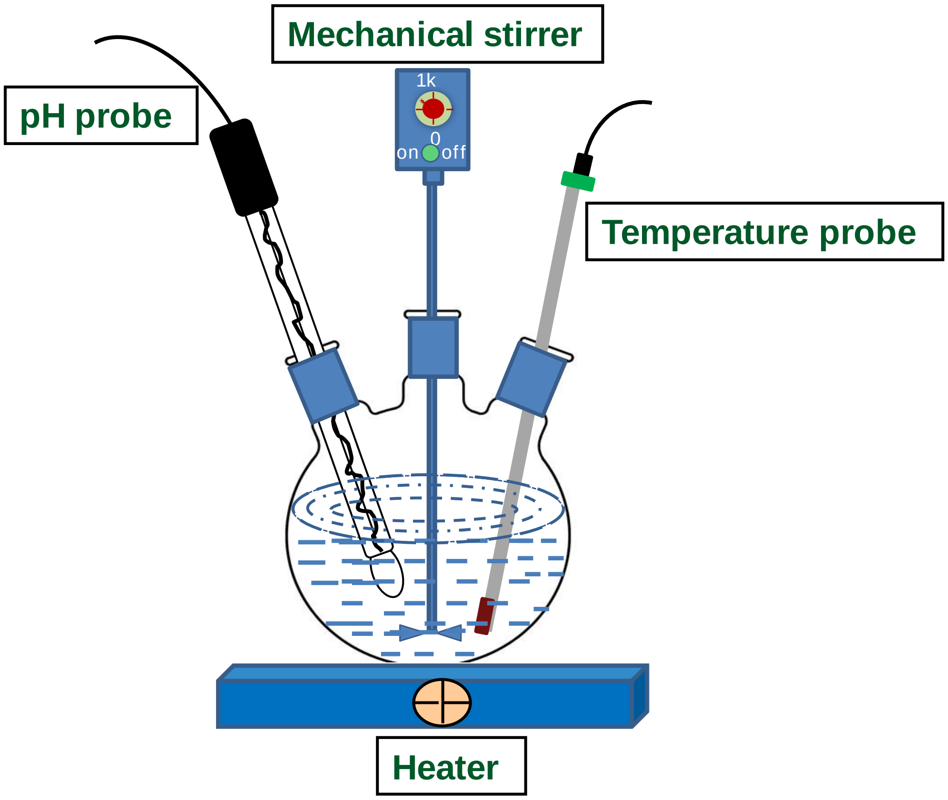

Fig 2.1: Schematic representation of experimental set up used for the co-precipitation method.

2.2 Synthesis Methods

2.2.1 Co-precipitation method

2.2.1.1 Synthesis of $M_xFe_{3-x}O_4$ nanoparticles (M = Fe, Zn & Co)

$M_xFe_{3-x}O_4$ nanoparticles are prepared by co-precipitation method using ammonium hydroxide as an alkali[35]. The chemicals $FeCl_3.6H_2O$, $FeSO_4.7H_2O$, $CoCl_2.6H_2O$, 30% NH_4OH, and acetone used to synthesize $M_xFe_{3-x}O_4$ nanoparticles are procured from E-Merck. All the chemicals are of GR grade with 99% purity. Chemicals are used without any further purification. Elga water with a resistivity of 15 MΩ-cm is used in all our experiments. 1M $FeCl_3.6H_2O$, 0.5M $FeSO_4.7H_2O$, 0.5M $Zn(NO_3)_2.6H_2O$ and 0.5M $CoCl_2.6H_2O$ are freshly prepared. The ratio of M^{2+} and Fe^{3+} solution concentration is varied to synthesize nanoparticles with different doping concentrations ($x = 0$-0.6). The solutions are mixed at respective fractions at a stirring rate of 800 rpm. 200 ml of 30% ammonium hydroxide is added at 85 ºC, at an addition rate of 10 ml/sec. The pH is found to be 10 after the addition of ammonium hydroxide. The sample is digested for 30 min at a constant stirring speed of 800 rpm. After attaining a pH of 8.5, the sample is washed two times with water to remove inorganic impurities and the particles are dried at 150 ºC for 30 min in a vacuum furnace.

2.2.1.2 Synthesis of Na doped Fe_3O_4 nanoparticles

The Fe_3O_4 nanoparticles prepared by the above procedure are soaked in NaOH solutions at four different concentrations (0, 0.3, 0.5 and 2 M) for 24 hrs and then dried in a vacuum oven. The dried particles are washed several times with hot water (~90 ºC) till the pH becomes 7. This is done to remove the excess Na^+ present in the solution and on the surface of the nanoparticles. Finally the particles are dried and the Na^+ concentrations are measured using Atomic Emission Spectroscopy (AES).

2.2.2 Microwave assisted method

2.2.2.1 Synthesis of Fe_3O_4 nanoparticles

Aqueous solutions of $FeCl_3.6H_2O$ (0.4M), $FeSO_4.7H_2O$ (0.2M) and NaOH (2M) are freshly prepared. $FeCl_3.6H_2O$ (0.4M), $FeSO_4.7H_2O$ (0.2M) and NaOH (2M) are mixed properly and then microwave irradiated (Anton Paar Monowave 300) for 5 min at a stirring speed of 600 rpm. The temperature of the reactant solution is maintained at 50, 100, 130, 160, 200 ºC. The black precipitate formed after the reaction is separated and washed several times with water to remove inorganic impurities. The sample was vacuum dried at 100 ºC for 20 min and then used for further studies.

2.2.2.2 Synthesis of $Mn_xZn_{1-x}Fe_2O_4$ nanoparticles

Aqueous solutions of $FeCl_3 \cdot 6H_2O$ (0.4M), $Zn(NO_3)_2 \cdot 6H_2O$ (0.2M), $MnCl_2 \cdot 4H_2O$ (0.2M), and NaOH (2M) are freshly prepared. Fe^{3+} solution is mixed with Mn^{2+} and Zn^{2+} in a 30 ml microwave synthesis vial followed by addition of 2M NaOH solution. A reddish brown precipitate is observed instantly after the addition of NaOH due to formation of iron hydroxide. The solution is mixed uniformly and kept inside the microwave synthesis reactor (monowave 300) at 180 ºC for 5 minutes at 600 rpm. A deep black precipitate is obtained after the reaction. The final product is washed using water and acetone several times to remove all inorganic and organic impurities. The particles are dried in vacuum oven for 30 minutes and used for further studies. The ratio of the Zn^{2+} and Mn^{2+} is varied to prepare $Mn_xZn_{1-x}Fe_2O_4$ nanoparticles of different concentrations (x = 0-1).

2.3 Characterization Techniques

2.3.1 X-Ray Diffraction

Since the wavelengths of hard X-rays are similar to the size of atoms, they are also useful for determining crystal structures by X-ray Crystallography[120]. The principle of crystallography is based on Bragg’s law. Consider crystal planes as shown in Fig 2.2. AO and CP are the two incident X-rays on two consecutive crystal planes. OB and PD are the corresponding diffracted rays of AO and CP respectively. OK and OL are the perpendiculars drawn from O on CP and PD respectively. d_{hkl} is the distance between two consecutive crystal planes.

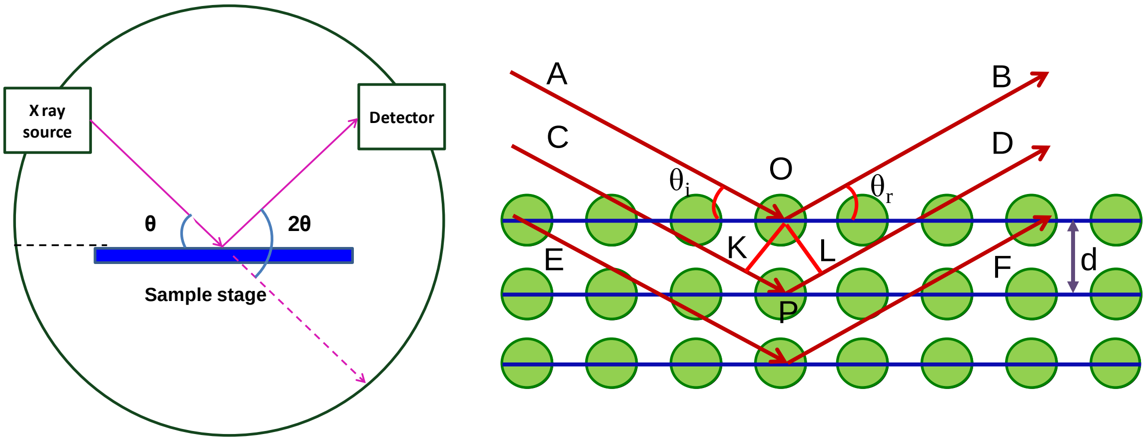

Fig 2.2: Schematic of X-ray diffractometer and Bragg's law of diffraction pattern.

The path difference between two rays can be given as

$$KP+PL = 2d_{hkl}\sin\theta \tag{2.1}$$

For constructive interference the Bragg's law should be satisfied which is given as

$$2d_{hkl}\sin\theta = n\lambda \tag{2.2}$$

Where, n is the order of diffraction and λ is the wavelength of X-ray used. X-ray diffraction is very useful in determining the phase, structure and lattice constant using the Miller indices (h, k, and l) values.

The crystallite size of the particles is usually measured using the Scherer's equation[121]. Consider θ_1 and θ_2 are the diffraction angles from crystal planes n+1 and n-1. Hence, the full width at half maxima (β) of the peak can be expressed as,

$$\beta = \frac{1}{2}\left(2\theta_1 - 2\theta_2\right) = \theta_1 - \theta_2 \tag{2.3}$$

Applying Bragg's condition to both the diffraction angles,

$$(n+1)\lambda = 2dSin\theta_1 \qquad 2.4$$

$$(n-1)\lambda = 2dSin\theta_2 \qquad 2.5$$

Now subtracting equation 2.5 from 2.4,

$$\lambda = d(Sin\theta_1 - Sin\theta_2)$$

i.e. $\lambda = 2dCos\left(\frac{\theta_1+\theta_2}{2}\right)Sin\left(\frac{\theta_1-\theta_2}{2}\right)$

Since, $\left(\frac{\theta_1+\theta_2}{2}\right) = \theta_{\max}$ and $Sin\left(\frac{\theta_1-\theta_2}{2}\right) = \frac{\theta_1-\theta_2}{2}$,

$$\lambda = d(\theta_1 - \theta_2)Cos\theta_{\max} \qquad 2.6$$

Using equation 2.3 in equation 2.6,

$$\lambda = d\beta Cos\theta_{\max} \qquad 2.7$$

The above equation is known as Scherrer’s formula for determination of crystallite size. For spherical particles the equation for crystallite size can be written as,

$$d = \frac{0.89\lambda}{\beta Cos\theta_{\max}} \qquad 2.8$$

Where, d is the crystallite size of the particles, 0.89 is a proportionality constant for spherical particles; β is the full width at half maxima, θ is the angle of diffraction and λ is the wavelength of the X-ray source (for CuKα, λ=1.5416Å).

A Rigaku Ultima IV instrument is used for all room temperature XRD measurements. The diffraction pattern for 2θ values from 25 to 70 degree is obtained using CuK_{α} radiation in the Bragg-Brentano geometry. A scan rate of 2 deg/min with a step size of 0.02 degree is maintained for each measurement. Acquisition and preliminary data analysis is performed using PDXL software and the data is compared with the JCPDS data.

2.3.2 High Temperature XRD

A Philips- X'pert MPD system equipped with the Buhler high vacuum heating stage is used for in situ high temperature studies. The resistance heating stage consists of a thin tantalum foil (~80 µm), on top of which a small quantity of sample is placed. The temperature is measured by a W-Re thermocouple, which is spot welded at the bottom of the tantalum resistive heater. The temperature is controlled with an accuracy of ±1 ºC. 2θ values are taken from 25 to 68º in the Bragg-Brentano geometry. A copper target serves as X-ray source for producing CuK_{α} radiation. A heating rate of 2 ºC /min. and a holding time of 30 min. before scanning at each temperature are maintained. The specimen stage is flushed with high purity Ar and a vacuum level of about 10^{-5} mbar is achieved before starting the experiment and it is maintained by low heating rate. Control, acquisition and preliminary analysis of the data are performed by the Philips- X'pert pro software and the XRD patterns are verified by comparing with the Joint Committee on Powder Diffraction Standards (JCPDS) patterns. JCPDS Pcpdfwin, Version 2.4 is exclusively used for comparision[122]. The peak position and full width half maximum are determined by fitting the peak with voigt function using the PEAKFIT program from Jandel Scientific[123]. Rietveld analysis is performed using Materials Analysis Using Diffraction (MAUD) version 2.33[124].

2.3.3 Small Angle X-ray Scattering

Small angle X-ray scattering is a very well-established measurement tool for obtaining information about structures ranging from tens to thousands of angstroms. The primary experimental requirement for SAXS is a well-collimated X-ray beam with a small cross-section. The intensity of the scattering beams at small angle is recorded. An extended sample-detector distance is required to spread out scattered photons from the main beam and also to reduce the detected X-ray background. In SAXS, the scattering intensity from a collection of like objects is given by, $I(q) = NF(q)S(q)$ where, N is the number of objects, F(q) is the form factor, S(q) is the structure factor and q is the wave vector given by $4\pi/\lambda \sin\theta$[125]. F(q) gives information about the internal density distributions of the particles whereas S(q) carries the information about their spatial arrangement. As the length scales become smaller than the size of the primary particles, the structure factor becomes constant and the scattered intensity is proportional to the form factor F(q).

In general, the influence of shape and particle size distribution cannot be separated in SAXS[126]. They are taken together as polydispersity and accounted for smearing the form factor with a suitable particle size distribution $D(d, d_0, \sigma)$;

$$\overline{F(q)} = \int_0^\infty F(q,d)D(d,d_0,\sigma)d(d) \qquad 2.9$$

where 'd' is the length scale of interest, d_0 and σ are measures of the distribution, typically mean particle size and standard deviation, respectively. The Gaussian and Schultz distributions are frequently used and are equivalent for the narrow particle size distributions that give rise to Porod oscillations. The F(q) for spherical particle of diameter 'd' given as[125]

$$F(q,d) = V^2 \left[\frac{Sin\left(\frac{qd}{2}\right) - \left(\frac{qd}{2}\right) Cos\left(\frac{qd}{2}\right)}{\left(\frac{qd}{2}\right)^3} \right]^2 \qquad 2.10$$

where V is the volume of the sphere. This function is oscillatory with overall q^{-4} (Porod) dependence. The first zero occurs at q ~ 9.0/d[127]. These zeroes are smeared out by polydispersity, resulting in Porod oscillation that becomes increasingly damped with increasing polydispersity.

The shape and particle size distributions are obtained by fitting the intensity of the scattered X-rays with suitable models. The model equation for spherical particles is given as[127]

$$I(q) = |\Delta\rho|^2 \left| \frac{4\pi}{q^3} \left[\sin\left(\frac{qd}{2}\right) - \frac{qd}{2} \cos\left(\frac{qd}{2}\right) \right] \right|^2 \qquad 2.11$$

where, Δρ is the difference in electron density of particle and the medium[128]. Dilute or non interacting polydisperse systems demonstrate a Guinier region tapering to Porod region ($I \sim q^{-4}$) with increasing q. In these dilute systems, the volume weighted particle size distribution is obtained by fitting the Guinier and Porod’s regimes. But these methods fail when the system is dense due to interparticle correlations.

A Rigaku Ultima IV instrument which uses CuKα (λ=1.5418 Å) as X-ray source and a scintillation detector is used for SAXS measurements. The measurements are performed in the transmission mode in the 2θ range of 0.01° to 2.2°.

2.3.4 Transmission Electron Microscopy

TEM exploits three different interactions of electron beam-specimen i.e. un-scattered electrons (transmitted beam), elastically scattered electrons (diffracted beam) and inelastically scattered electrons. The intensity of transmitted electrons is inversely proportional to the specimen thickness. Areas of the specimen that are thicker will have fewer transmitted electrons and so will appear darker; conversely the thinner areas will appear lighter due to more transmission. The scattered part of the incident beam is transmitted through the remaining portions of the specimen. All incident electrons have the same energy and enter the specimen normal to its surface. All incidents that are scattered by the same atomic spacing will be scattered by the same angle. These scattered electrons can be collimated using magnetic lenses to form a pattern of spots, each spot corresponding to a specific atomic spacing (a plane). This pattern can then yield information about the orientation, atomic arrangements and phases present. Also, incident electrons can interact with the specimen inelastically and loose its energy during the interaction. These electrons are then transmitted through the rest of the specimen [129].

Typically, a TEM consists of three stages of lensing. The stages are the condensor lenses, the objective lenses, and the projector lenses. The condensor lenses are responsible for primary beam formation, whilst the objective lenses focus the beam that comes through the sample itself (in STEM scanning mode, there are also objective lenses above the sample to make the incident electron beam convergent). The projector lenses are used to expand the beam onto the phosphor screen or other imaging device, such as film. The magnification of the TEM is due to the ratio of the distances between the specimen and the objective lens' image plane. Additional quad or hexapole lenses allow for the correction of asymmetrical beam distortions, known as astigmatism. It is noted that TEM optical configurations differ significantly with implementation, with manufacturers using custom lens configurations, such as in spherical aberration corrected instruments or TEMs utilizing energy filtering to correct electron chromatic aberration.

TEM investigations are carried out using JEOL 2011 TEM with an acceleration voltage of 200 kV. A drop of the magnetite dispersion was placed on a carbon coated copper grid (0.3 cm diameter, mesh size of 200 holes/cm) and left it to dry overnight at room temperature.

2.3.5 Fourier Transform Infrared Spectroscopy

For a molecule to absorb infrared waves, the vibrations or rotations within a molecule must cause a net change in the dipole moment of the molecule[130]. The alternating electrical field of the radiation interacts with fluctuations in the dipole moment of the molecule. If the frequency of the radiation matches the vibrational frequency of the molecule then radiation will be absorbed, causing a change in the amplitude of molecular vibration. Molecular vibrations are divided into stretching and bending. FTIR has three major advantages over other infrared spectrometers which are high signal-to-noise ratio, multiplex advantage and wavenumber precision. It is vital that the wavenumbers, and hence peak positions, in an infrared spectrum be measured reproducibly. FTIR contains a laser that acts as an internal wavenumber standard, which gives rise to a precision of ±0.01 cm^{-1}.

The heart of the FTIR is an optical device known as interferometer. The most popular interferometer used in FTIR instruments is Michelson interferometer. The top arm contains the infrared source and a collimating mirror to collect the light from the source and make its rays parallel. The bottom arm contains a fixed mirror. The right arm of the interferometer contains a moving mirror which is capable of moving left and right. The left arm of the interferometer contains the sample and detector. At the centre of the interferometer, there is a beam splitter that transmits a portion of the light and reflects the rest of the light incident upon it. The light transmitted by the beamsplitter travels toward the fixed mirror, and the light reflected by the beamsplitter travels toward the moving mirror. The light beams reflected from these mirrors travel back to the beamsplitter, where they are recombined into a single light beam that leaves the interferometer, interacts with the sample, and strikes the detector.

The resulting signal is called an interferogram which has the unique property that every data point (a function of the moving mirror position) which makes up the signal has information about every infrared frequency which comes from the source. Because the analyst requires a frequency spectrum (a plot of the intensity at each individual frequency) in order to make identification, the measured interferogram signal cannot be interpreted directly. The “decoding” the individual frequencies are accomplished by Fourier transformation.

An ABB BOMEM MB 3000 FT-IR spectrometer is used for IR absorption studies in the spectral range 3700–400 cm^{-1}. The spectral resolution of the instrument is 4 cm^{-1}. The sample pellets are prepared by uniform mixing of nanoparticles with KBr in the ratio 1:3.

2.3.6 Thermogravimetric Analysis-Differential Scanning Calorimetry

Differential scanning calorimetry is a thermoanalytical technique in which the difference in the amount of heat required to increase the temperature of a sample and reference are measured as a function of temperature. Both the sample and reference are maintained at very nearly the same temperature throughout the experiment. Generally, the temperature program for a DSC analysis is designed such that the sample holder temperature increases linearly as a function of time. The reference sample should have a well-defined heat capacity over the range of temperatures to be scanned. The basic principle underlying this technique is that, when the sample undergoes a physical transformation such as phase transitions, more (or less) heat will need to flow to it than the reference to maintain both at the same temperature. Whether more or less heat must flow to the sample depends on whether the process is exothermic or endothermic. By observing the difference in heat flow between the sample and reference, differential scanning calorimeters are able to measure the amount of heat absorbed or released during such transitions. DSC may also be used to observe more subtle phase changes, such as glass transitions. DSC is widely used in industrial settings as a quality control instrument due to its applicability in evaluating sample purity and for studying polymer curing. The result of a DSC experiment is a heating or cooling curve. This curve can be used to calculate enthalpies of transitions. This is done by integrating the peak corresponding to a given transition. DSC is a useful tool to measure a number of characteristic properties such as fusion, crystallization and glass transition temperatures. DSC is also an important tool to study oxidation, as well as other chemical reactions.

TGA provides complimentary and supplementary characterization information to DSC. It measures the amount and rate of change in the mass of a sample as a function of temperature or time in a controlled atmosphere. The measurements are used primarily to determine the thermal and oxidative stabilities of materials as well as their compositional properties. The technique can analyze materials that exhibit either mass loss or gain due to decomposition, oxidation or structural transitions.

For the present work, Mettler Toledo system was used to carry out the TGA-DSC measurements simultaneously in the temperature range 30-1000 ºC at a heating rate of 10 ºC/min under air atmosphere. A special arrangement was done for performing magnetic properties measurements.

150 μl alumina crucible with 25 mg of sample was used for each measurement. The analysis of enthalpy and phase transitions was performed using the $STAR^e$.

2.3.7 Vibrating Sample Magnetometer

A vibrating sample magnetometer (VSM) operates on Faraday's law of induction i.e. a changing magnetic field produces an electric field[16]. This electric field can give information about the changing magnetic field. A VSM is used to measure the magnetic behavior of magnetic materials. A schematic of vibrating scanning magnetometer is shown in Fig. 2.3.

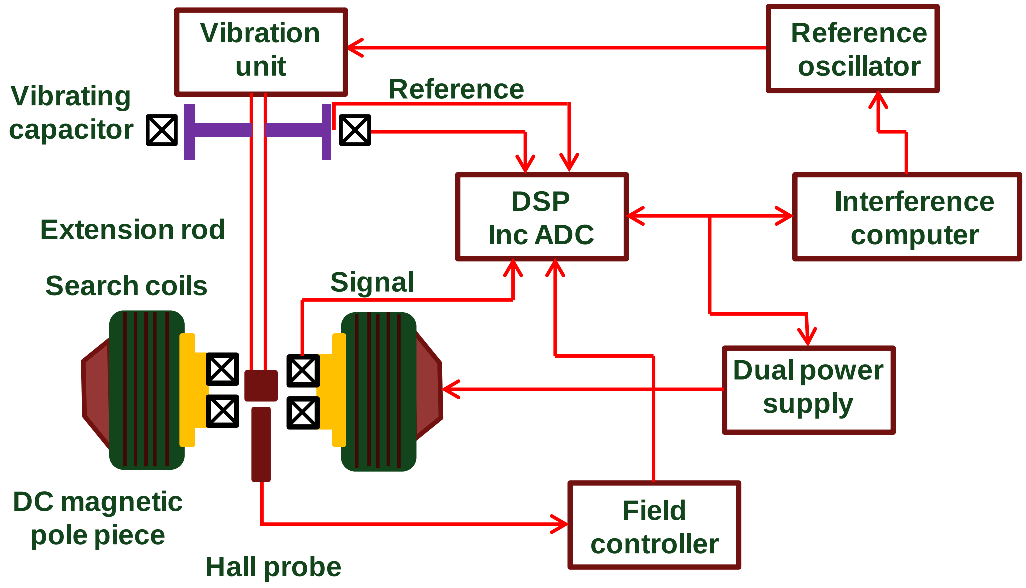

Fig 2.3: Schematic diagram of vibrating sample magnetometer.

A VSM operates by first placing the sample to be studied in a constant magnetic field. If the sample is magnetic, this constant magnetic field will magnetize the sample by aligning the magnetic domains, or the individual magnetic spins, with the field. The stronger the constant field, the larger the magnetization will be. The magnetic dipole moment of the sample will create a magnetic field around the sample, called the magnetic stray field. As the sample is moved up and down, this magnetic stray field is changing as a function of time that is sensed by a set of pick-up coils. The oscillating magnetic field will cause an electric field in the pick-up coils according to Faraday's law of induction. This current will be proportional to the magnetization of the sample. The induction current is amplified by a trans-impedance amplifier and lock-in amplifier. The various components are controlled by a computer interface. The magnetic moment of the sample is measured in terms of electromagnetic unit (emu). Later, the magnetic moment is converted to emu/g scale and plotted against the applied magnetic field. For the present work, a cryogen-free vibrating sample magnetometer (M/s Cryogenics, UK) is used for magnetization measurements in the applied magnetic field range of -1.5 to 1.5 T. The temperature dependant magnetization measurements (Zero field cooled (ZFC)-Field cooled (FC)) were performed in the range of 4 to 600K at magnetic field strength of 100 Oe. For ZFC measurements, the sample was cooled down to 4K with zero magnetic fields and then the magnetization data was obtained by heating the sample till 300K with an applied field of 100 Oe. Then the sample is cooled to 4K, with the above applied field, and the FC curve is obtained.

2.3.8 Atomic Emission Spectroscopy

Atomic emission spectroscopy uses quantitative measurement of the optical emission from excited atoms to determine analyte concentration. Analyte atoms in solution are aspirated into the excitation region where they are desolvated, vaporized, and atomized by a flame, discharge, or plasma. These high-temperature atomization sources provide sufficient energy to promote the atoms into high energy levels. The atoms decay back to lower levels by emitting light. Since the transitions are between distinct atomic energy levels, the emission lines in the spectra are narrow. The obtained congested spectra of samples containing many elements are analyzed (spectral separation of nearby atomic transitions) by using a high-resolution spectrometer. Since all atoms in a sample are excited simultaneously, they can be detected simultaneously using a polychromator with multiple detectors. This ability to simultaneously measure multiple elements is a major advantage of AES compared to atomic-absorption spectroscopy (AAS). The AES studies have been performed using a HORIBA JOBINYVON make instrument.

2.3.9 Zeta Potential

The development of a net charge at the particle surface affects the distribution of ions in the surrounding interfacial region, resulting in an increased concentration of counter ions close to the surface and creates an electrical double layer exists around each particle[131]. The liquid layer surrounding the particle exists as two parts; (a) the stern layer (inner region), with strongly bound ions and (b) diffused layer (outer region) with less firmly bound ions. The diffuse layer contains a notional boundary inside which the ions and particles form a stable entity. When a particle moves, ions within the boundary move with it, but any ions beyond the boundary do not travel with the particle. This boundary is called the surface of hydrodynamic shear or slipping plane and the potential at this boundary is known as zeta potential. The magnitude of the zeta potential gives an indication of the potential stability of the colloidal system. In general, if all the particles in suspension have a large negative or positive zeta potential then they will tend to repel each other thus preventing agglomeration or flocculation. However, if the particles have low zeta potential values then there is no force to prevent the particles coming together and aggregating/flocculating. The dividing line between stable and unstable suspensions is generally taken at either +30 mV or -30 mV. Particles with zeta potentials more positive than +30 mV or more negative than -30 mV are normally considered stable. However if the particles have a density different from the dispersant, they will eventually sediment because of the gravitational force. The important factors affecting the zeta potential are pH, conductivity and concentration of the formulation.

The principle used for zeta potential measurement is electrophoresis. When an electric field is applied across an electrolyte, charged particles suspended in the electrolyte are attracted towards the electrode of opposite charge. Viscous forces acting on the particles tend to oppose this movement. When equilibrium is reached between these two opposing forces, the particles move with constant velocity, which is dependent on the strength of the electric field or voltage gradient, the dielectric constant of the medium, the viscosity of the medium and the zeta potential. Fig 2.4 shows the schematic of hydration sphere and zeta potential.

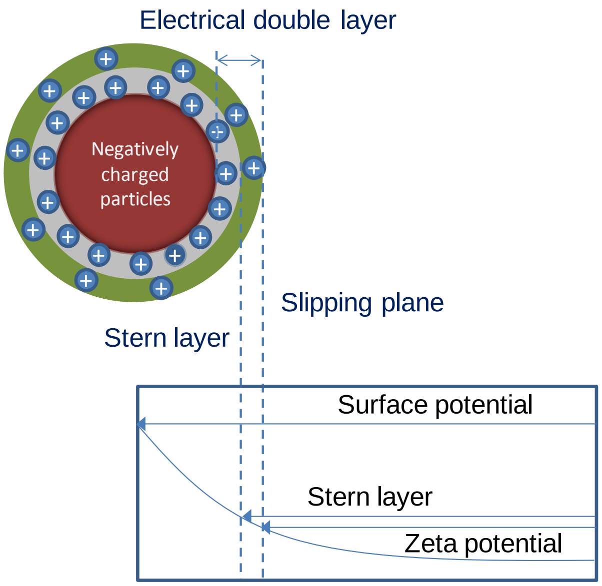

Fig 2.4: Schematic of the Zeta potential measurement.

The velocity of a particle in an electric field is referred to as its electrophoretic mobility. Zeta potential is related to the electrophoretic mobility by the Henry equation[131]

$$U_E = \frac{2\varepsilon\zeta f(ka)}{3\eta} \qquad 2.12$$

where U_E is the electrophoretic mobility, ζ is the zeta potential, ε is the dielectric constant, η is the viscosity and $f(\kappa a)$ is the Henry's function. The units of κ, termed the Debye length, are reciprocal length and κ^{-1} is often taken as a measure of the "thickness" of the electrical double layer.

The instrument used in the present study is the Malvern's Zetasizer-Nano which uses a combination of laser Doppler velocimetry and phase analysis light scattering (PALS) to measure particle electrophoretic mobility. Implementation of PALS enables even samples of very low mobility to be analyzed and their mobility distributions calculated. For zeta potential measurements, the laser light source is split to provide an incident and reference beam. The incident laser beam passes through the centre of the sample cell, and the scattered light is detected at an angle of 173°. When an electric field is applied to the cell, any particles moving through the measurement volume will cause the intensity of light detected to fluctuate with a frequency proportional to the particle speed and this information is passed to a digital signal processor and then to a computer. The Zetasizer-Nano software calculates a frequency spectrum from which the electrophoretic mobility and hence zeta potential is calculated. The intensity of the detected and the scattered light must be within a specific range for the detector to successfully measure it. This is achieved by using an attenuator, which adjusts the intensity of the light reaching the sample and hence the intensity of the scattering. To correct for any differences in the cell wall thickness and dispersant refraction, compensation optics are installed to maintain optimum alignment.

Chapter III

High temperature phase transformation studies in $Co_xFe_{3-x}O_4$ nanoparticles

3.1 Introduction

$CoFe_2O_4$ is thermally more stable than Fe_3O_4 nanoparticles in air as well as under vacuum annealing conditions[117]. But, the magnetic property of $CoFe_2O_4$ (80 emu/g) is comparatively lower than Fe_3O_4 (92emu/g)[132]. Therefore, it is necessary to find the minimum doping concentration of Co which can effectively increase the thermal stability of Fe_3O_4 nanoparticles without affecting its magnetic property. Although, earlier studies show that the γ-Fe_2O_3 to α-Fe_2O_3 phase transition temperature can be enhanced by 100 ºC by doping of Co using combustion method[105], a systematic study on the effect Co doping on thermal and magnetic properties of Fe_3O_4 in a wide range is still missing in literature.

The objective of the present work is to probe the effect of Co(II) ion doping on phase stability of maghemite nanoparticles during air and vacuum annealing without compromising magnetization property. Further, it is also aimed at exploring new approaches to enhance the phase stability of magnetite. Earlier studies show that the phase transition temperatures increase with various dopants of larger volume fractions[103, 104, 111], but the present study reveals that 0.1 fraction of Co^{2+} metal ion doping in magnetite can lead to a considerable enhancement in the non-magnetic phase transition temperature.

3.2 Synthesis of $Co_xFe_{3-x}O_4$ nanoparticles

$Co_xFe_{3-x}O_4$ nanoparticles (x=0 to 0.6) are prepared using co-precipitation method. The detail of the synthesis procedure is discussed in chapter II, Section 2.2.1.1.

3.3 Results and Discussion

3.3.1 Room temperature XRD studies

The room temperature XRD of $Co_xFe_{3-x}O_4$ (for x = 0, 0.1, 0.2, 0.4 and 0.6) are shown in Fig 3.1. The observed peaks that originate from the (220), (311), (400), (511) and (440) planes confirm the spinel ferrites structure for all the studied samples (JCPDS card no-880315). The particle size varies from 11±1 to 9 ± 1 nm with increase in cobalt fraction from 0 to 0.6. The error estimation is made from the experimental noise present in the XRD diffraction pattern using the approach of Roman Pielaszek[133].

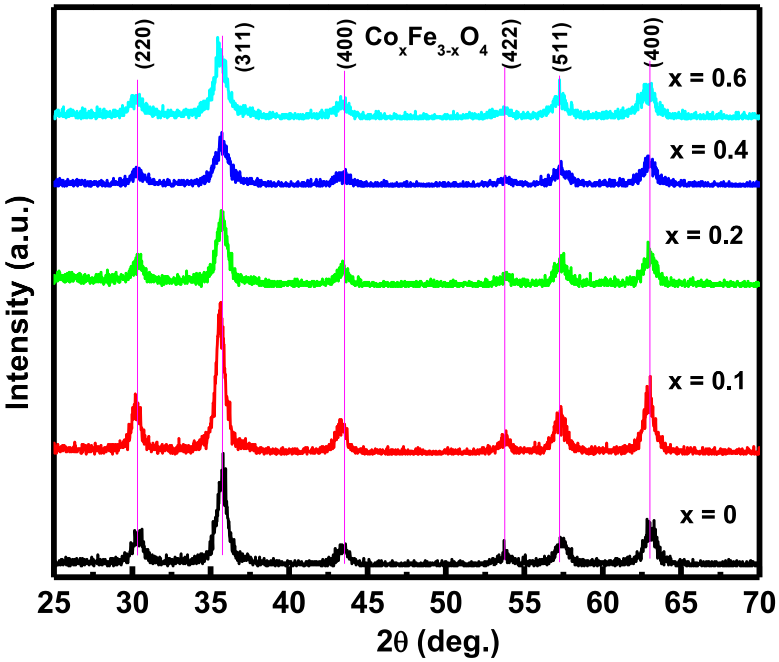

Fig 3.1: The room temperature XRD patterns of $Co_xFe_{3-x}O_4$ nanoparticles for x= 0, 0.1, 0.2, 0.4 and 0.6.

With increase in cobalt fraction from 0 to 0.6, the lattice parameter is found to vary from 8.33 to 8.36 Å. However, no clear trend is observed in the variations of lattice parameter with the cobalt content. The observed variation in the lattice parameter could be due to the slight differences in precipitation conditions during each synthesis. Fig 3.2(a) shows the scattering intensity as a function of scattering vector and (b) the particle size distribution obtained from the best fit on SAXS data for cobalt fractions of 0, 0.1, 0.2, 0.4 and 0.6.

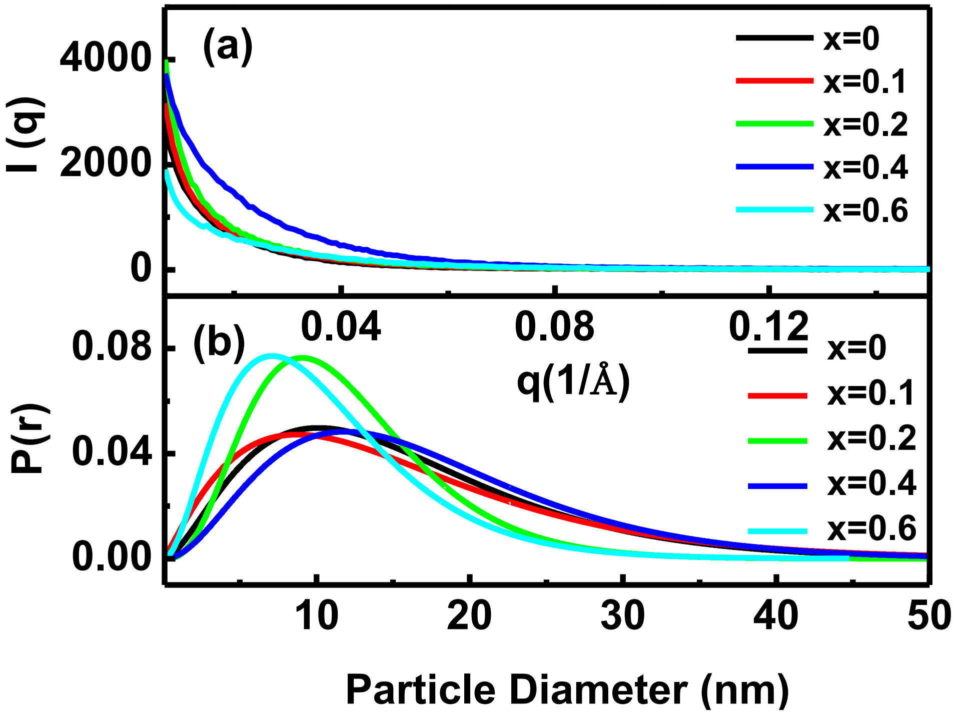

Fig 3.2: (a) Scattering Intensity as a function of scattering vector and (b) the size distributions obtained from the best fit on SAXS data for cobalt fractions of 0, 0.1, 0.2, 0.4 and 0.6.

The polydispersity of nanoparticles is calculated using the equation, $\sigma_{eff} = \frac{\sigma_0}{d_{avg}}$ where, σ_0 is the standard deviation and d_{avg} is the average particle diameter obtained from SAXS[125]. The most probable particle size varies from 11.8 to 7.1 nm. The fit on the scattering data shows that the particles are spherical in shape, as confirmed from TEM. The most probable particle size and polydispersity (SAXS), phase decomposition temperatures under vacuum (HTXRD), phase transition temperature in air (XRD and DSC) and enthalpy changes (obtained from DSC) for various fractions of cobalt doping (x = 0-0.6) are listed in Table 3.1. Fig 3.3 shows the TEM image of un-doped (x = 0) and doped (x = 0.1) sample.

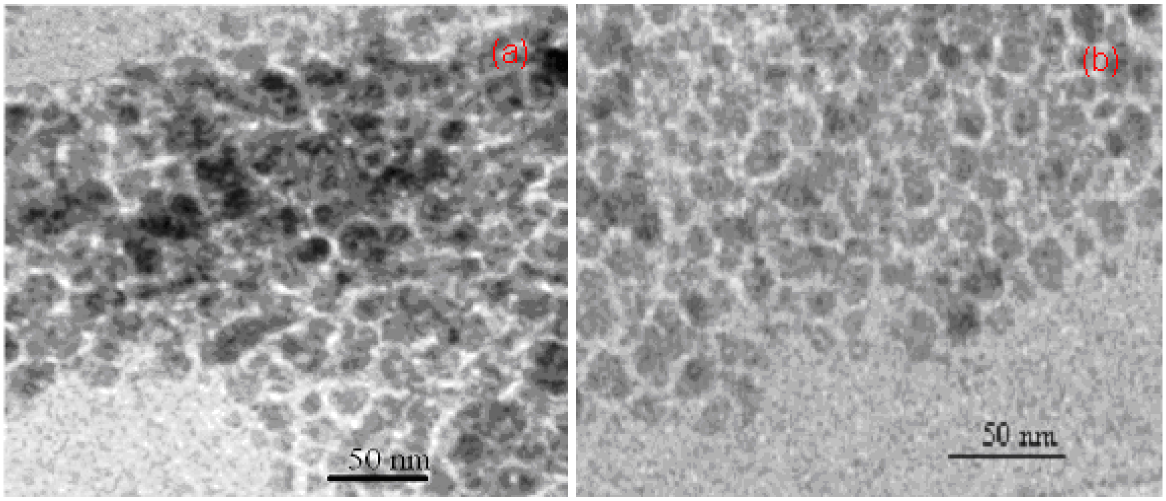

Fig 3.3: The TEM images of $Co_xFe_{3-x}O_4$ nanoparticles for (a) x = 0 and (b) 0.1.

Table 3.1: The most probable particle size and polydispersity (SAXS), phase decomposition temperatures under vacuum (HTXRD), phase transition temperature under air (XRD and DSC) and enthalpy changes (DSC) for various fractions of cobalt doping (x = 0-0.6).

Sl. No.	Fraction of Co^{2+} in $Co_xFe_{3-x}O_4$ (x)	Size from SAXS (nm)	Polydisp-ersity σ_{eff} (%)	Under Vacuum annealed up to 1000 °C (Fe_3O_4 to γ-Fe_2O_3 + FeO phase transition temperature in °C)	Under air annealing (γ-Fe_2O_3 to α-Fe_2O_3 phase transition temperature in °C) (start-End)	γ-Fe_2O_3 to α-Fe_2O_3 Transition temperature from DSC in oxygen (°C)	Enthalpy change obtained from DSC ($J.g^{-1}$)
1	0	11.8	55.6	700	450 - 600	577-615	89
2	0.1	10.1	60.2	Not converted	550 - 600	618-647	71
3	0.2	8.8	67.0	Not converted	550 - 600	626-659	55
4	0.4	9.1	48.9	Not converted	600	637-680	39
5	0.6	7.1	57.2	Not converted	600	663-716	18

Fig 3.4 and 3.5 show the room temperature XRD patterns of samples annealed in air with x = 0 and 0.1 respectively. It has been reported that pure magnetite with particle size below 300 nm is oxidized above 220 ºC, and forms γ-Fe_2O_3 phase[98]. Therefore, for x = 0, magnetite should have oxidized to γ-Fe_2O_3 phase at 350 ºC, though it was not evident from the XRD. However, the conversion of γ-Fe_2O_3 to α-Fe_2O_3 starts at 450 ºC, which is clearly evident from the evolution of (104) peak. Pure α-Fe_2O_3 phase is observed at 500 ºC. Annealing at 600 and 1000 ºC results in no further changes in the α-Fe_2O_3 phase, which is in good agreement with an earlier report[100]. For x = 0.1, XRD results reveal that the γ-Fe_2O_3 is stable up to 500 ºC. The conversion from γ-Fe_2O_3 to α-Fe_2O_3 starts at 550 ºC and is completed at 600 ºC and the α-Fe_2O_3 phase is retained even at 1000 ºC annealing.

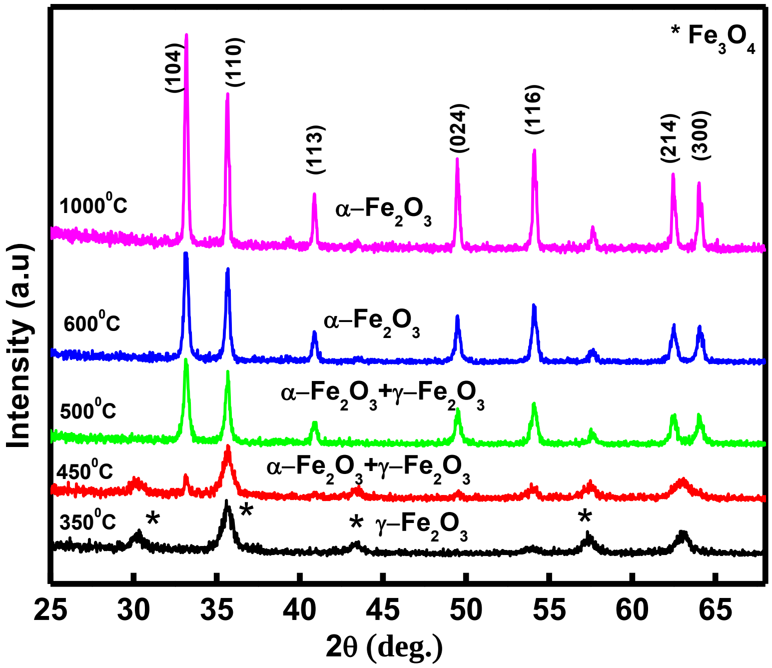

Fig 3.4: The room temperature XRD patterns of Fe_3O_4 nanoparticles annealed at 350, 450, 500, 600 and 1000 ºC in air.

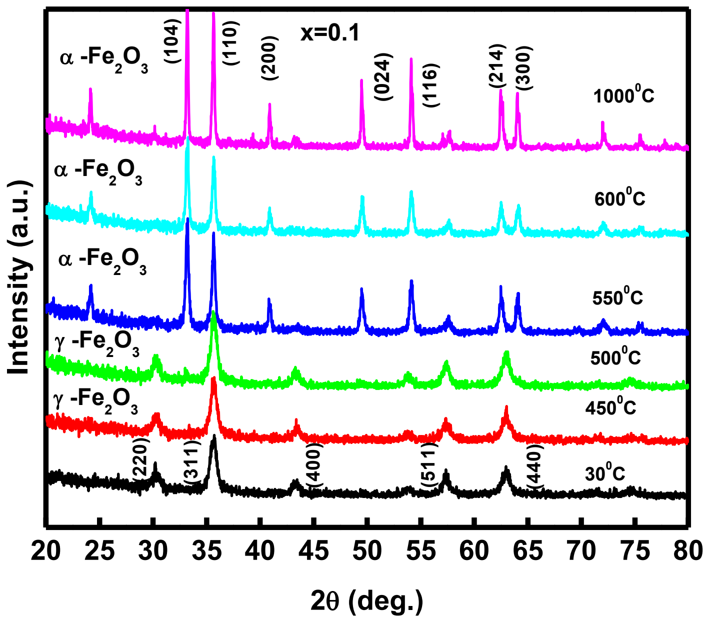

Fig 3.5: The room temperature XRD patterns of $Co_{0.1}Fe_{2.9}O_4$ nanoparticles at 30 ºC and air annealed at 450, 500, 550, 600 and 1000 ºC.

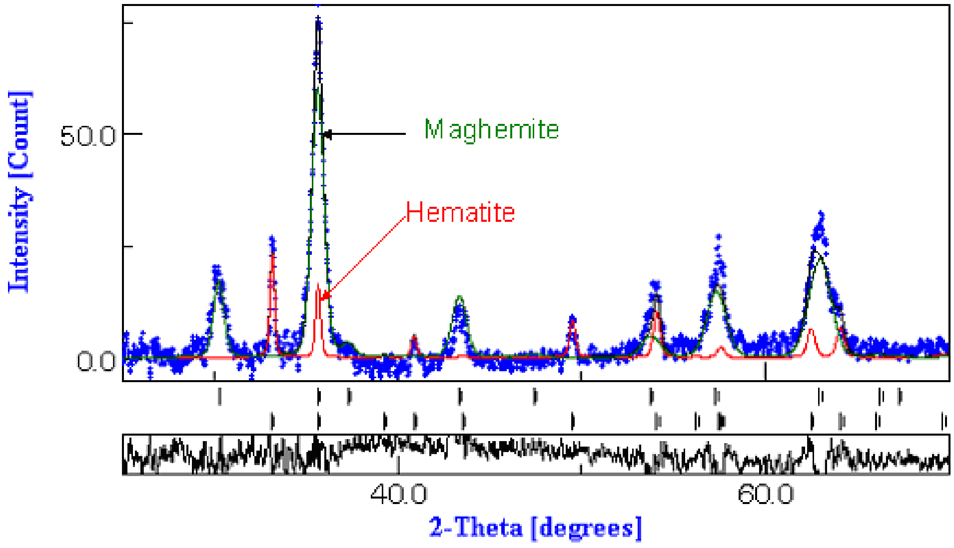

Fig 3.6: Rietveld fitting of XRD pattern of magnetite nanoparticles air annealed at 450 ºC. Analysis shows that the end product is a mixture of maghemite and hematite of 81 and 19%, respectively.

The Rietveld fitting of XRD pattern of magnetite nanoparticles air annealed at 450 ºC is shown in Fig 3.6. The green line shows maghemite phase and the red one shows the hematite phase. It is observed that 19% of nanoparticles were converted to hematite after annealing at 450 ºC whereas 81% remains as maghemite phase. Rietveld analysis is also performed for other annealed nanoparticles and the results are summarized in Table 3.2.

Table 3.2: Rietveld analysis results of air annealed nanoparticles. Annealing temperature and the corresponding phases (percentage) for x = 0, 0.1, 0.2, 0.4 and 0.6.

Annealing Temp. (ºC)	x = 0		x = 0.1		x = 0.2		x = 0.4		x = 0.6	
	γ-Fe_2O_3 (%)	α-Fe_2O_3 (%)	γ-Fe_2O_3 (%)	α-Fe_2O_3 (%)	γ-Fe_2O_3 (%)	α-Fe_2O_3 (%)	γ-Fe_2O_3 (%)	α-Fe_2O_3 (%)	γ-Fe_2O_3 (%)	α-Fe_2O_3 (%)
350	100	0	100	0	100	0	100	0	100	0
450	81	19	100	0	100	0	100	0	100	0
500	1	99	100	0	100	0	100	0	100	0
550	0	100	5	95	-	-	-	-	-	-
600	0	100	0	100	0	100	37	63	63	37

Fig 3.7 shows the room temperature XRD patterns of $Co_xFe_{3-x}O_4$ samples after air annealing at 1000 ºC. Intensity ratio of (110) and (104) is an indicator of the γ-Fe_2O_3 to α-Fe_2O_3 conversion ratio. It is reported that peak intensity ratio greater than 70:100 represents a mixture of γ-Fe_2O_3 and α-Fe_2O_3 phases whereas the ratio below 70:100 represents the α-rich phase[100]. For x = 0, 0.1 and 0.2, the intensity ratio of (110) and (104) observed is less than 70:100 that indicates the dominance of alpha phase. But for x = 0.4 and 0.6, the intensity ratio is more than 70:100 that shows presence of a mixture of alpha and gamma phases. For x = 1, which corresponds to $CoFe_2O_4$, the $CoFe_2O_4$ phase is stable up to 1000 ºC[117].

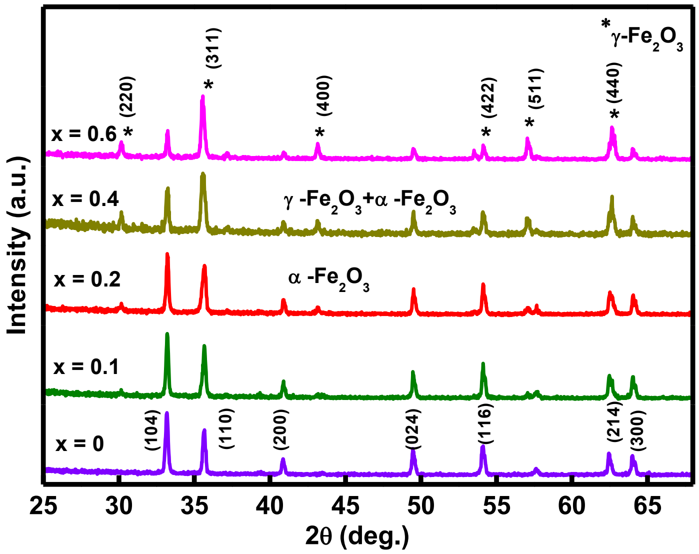

Fig 3.7: The room temperature XRD patterns of $Co_xFe_{3-x}O_{4,}$ after air annealing at 1000 °C for x = 0, 0.1, 0.2, 0.4 and 0.6.

The reported maximum phase transition temperature for γ-Fe_2O_3 to α-Fe_2O_3 conversion is 700 °C for nanoparticles of 15 nm size with a silica protective shell[107]. This enhancement in phase transition is attributed to the strong oxide-oxide interaction between maghemite and silica. For uncoated magnetite nanoparticles, the maximum γ-Fe_2O_3 to α-Fe_2O_3 phase transition temperature reported is 600 °C[100]. XRD results shows that under air annealing the γ-Fe_2O_3 to α-Fe_2O_3 phase transition commences only around 550-600 °C in 0.1 fraction cobalt doped samples whereas it occur at 450 °C in un-doped samples.

3.3.2 In situ high temperature XRD studies

Fig 3.8 shows in situ high-temperature XRD pattern of uncoated Fe_3O_4 nanoparticles at different temperatures of 30, 300, 400, 500, 600, 700, 800, 900, and 1000 °C and cooled back to room temperature which is consistent with earlier reports[112].

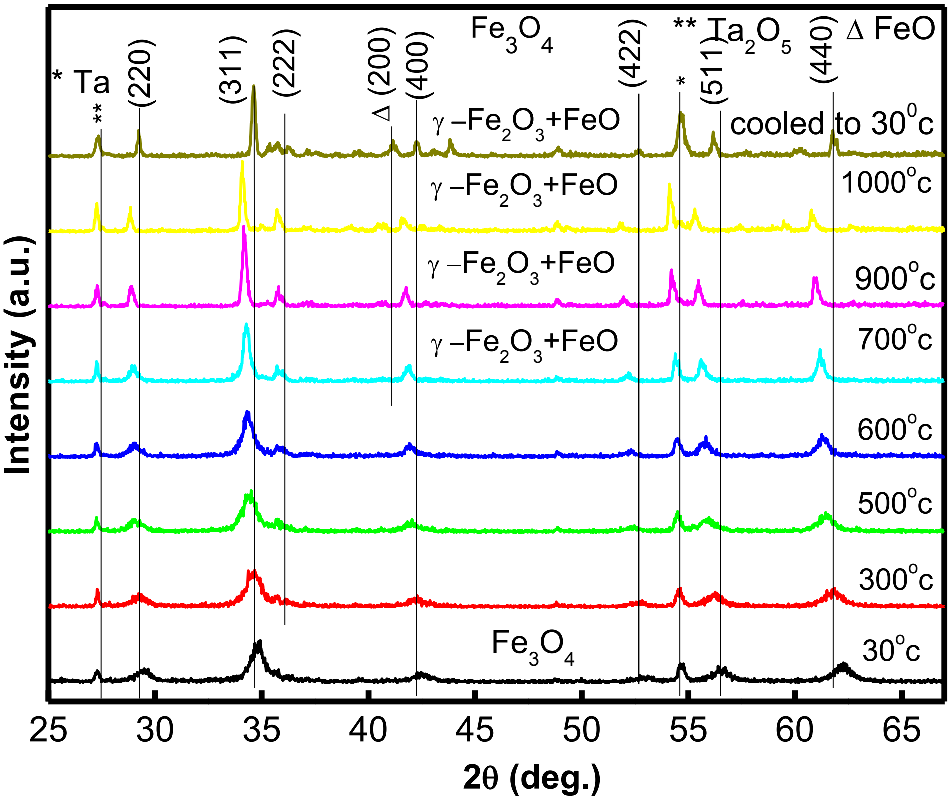

Fig 3.8: The in-situ high temperature XRD patterns of Fe_3O_4 nanoparticles under vacuum annealing.

The diffraction peaks observed at 30 ºC can be indexed to cubic spinel structure of Fe_3O_4 phase. The Fe_3O_4 phase is observed in the temperature range of 300 to 600 ºC. On further heating, two distinct changes are observed. The observed peaks became narrower and more intense at higher temperatures and the peaks are shifted toward lower angle. The first change is attributed to an increase in particle size due to coalescence of the particles by solid-state diffusion and the latter is attributed to lattice expansion with increasing temperature. Above 700 ºC, Fe_3O_4 is decomposed into γ-Fe_2O_3 and FeO phases. From 800 to 1000 ºC, the XRD pattern matched with the γ-Fe_2O_3 and FeO standards with additional high-intensity (110), (200) and (220) diffraction peaks. The particle size of uncoated Fe_3O_4 changed from 9±1 to 18±2 nm as the temperature increased from room temperature to 700 ºC. The calculated lattice constant at room temperature is 8.348 Å. The lattice constant increases from 8.348 to 8.446 Å as the temperature is increased from 300 to 600 ºC, as a result of the increase of the particle volume with temperature.

In situ high temperature XRD patterns of $Co_{0.1}Fe_{2.9}O_4$ (x = 0.1) nanoparticles under similar annealing protocols is shown in Fig. 3.9.

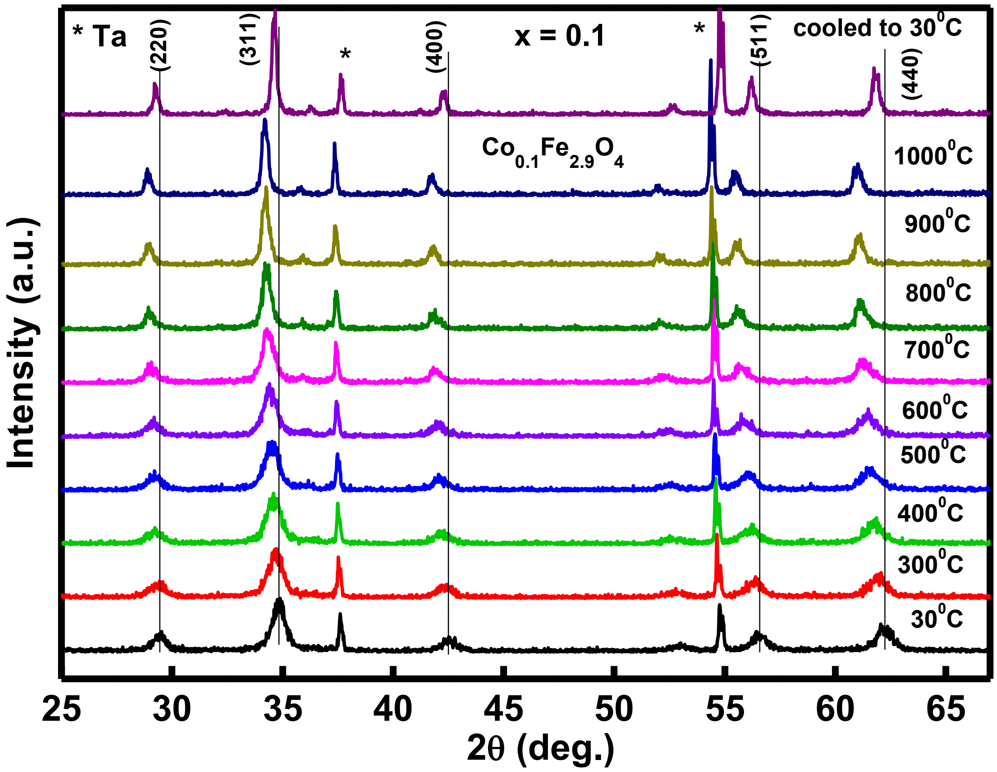

Fig 3.9: The in-situ high temperature XRD patterns of $Co_{0.1}Fe_{2.9}O_4$ nanoparticles under vacuum annealing.

In the temperature range of 30-1000 ºC, the observed diffraction peaks confirm the cubic spinel structure. In contrast to the decomposition of Fe_3O_4 nanoparticles at 700 ºC, the $Co_{0.1}Fe_{2.9}O_4$ is found to be stable up to 1000 ºC and the phase remains intact even after cooling back to room temperature. The 'd' and 'a' values increases from 15±2 to 35±4 nm and 8.37 to 8.68 Ǻ respectively as the temperature increases from 30 to 1000 ºC. It is interesting to note that the growth of Co^{2+} doped particles is slow compared to pure Fe_3O_4 nanoparticles. Lai et al. found that doping of Fe_3O_4 with Mn(III) enhances the phase transition temperature up to 600 ºC due to the more free volume present in cubic Mn^{3+} than Fe^{3+}, which ultimately increases the activation energy required for the transition[103, 134]. The activation energy was calculated for γ-Fe_2O_3 to α-Fe_2O_3 phase transition from the Schott equation[118] given by, $d = A\exp\left(\frac{-Ea}{RT}\right)$, Where d is the particle size, E_a is the activation energy, T is the absolute temperature, A and R represents Arrhenius constant and universal gas constant respectively. A plot of lnd vs 1/T gives a linear plot where the intercept and slope corresponds to lnA and E_a/R, respectively. The activation energy is obtained from the slope of the linear fit and is found to be 16.04, 18.79, 20.61, 19.54 and 27.02 KJ/mol for x=0, 0.1, 0.2, 04 and 0.6, respectively. The obtained value of "A" from the intercept of the best fit is found to be 48 KJ/mol, which was much smaller than the value of 140 KJ/mol reported in zinc ferrite system[118].

Fig 3.10 shows the variation of activation energy with cobalt content and the experimental data is best fitted with an equation, $Ea = 15.125x + 16.467$. The observed increase in the activation energy for the phase transition with increasing cobalt fraction is attributed to the stabilization of cubic structure by Co^{2+}. As the size of nanoparticles with x=0.1 is comparable to that of un-doped sample the possibility of size effect on the enhancement can be ruled out. A study on size dependence of phase transition temperatures in pure magnetite shows that the phase transition temperature increases with decrease in particle size due to the increase in surface spin disorder[119]. Therefore, the observed enhancement in phase transition temperature originates from the dopant. The results show that the γ-Fe_2O_3 phase is extremely stable (up to 1000 ºC) with cobalt fraction of 0.1 or above. Particle size is found to increase with increase in temperature. The lattice parameter also increases from 8.5 to 8.7 Å due to lattice expansion at higher temperature.

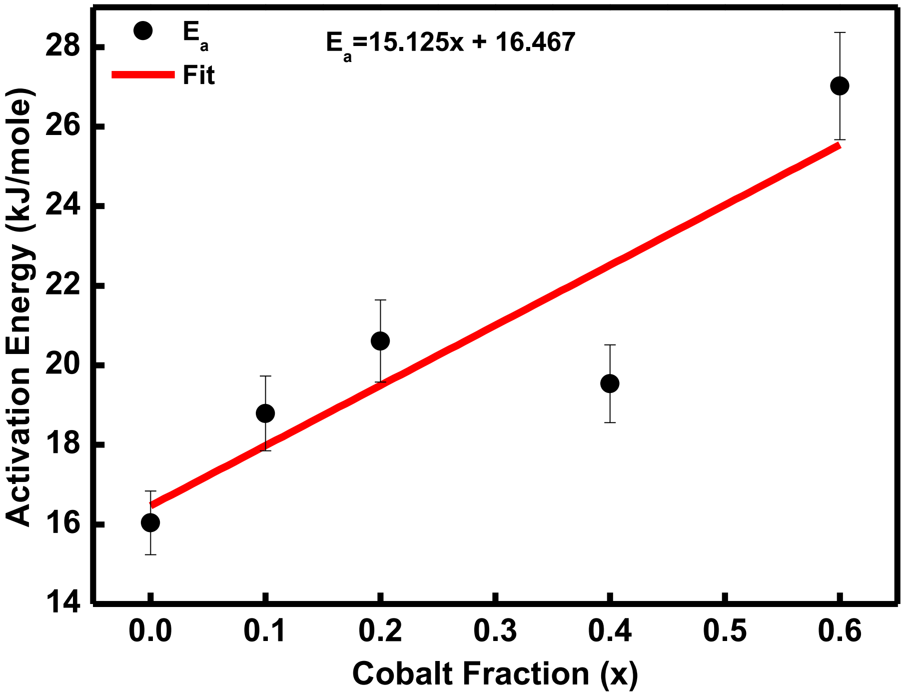

Fig 3.10: The variation of activation energy with increasing cobalt content in Fe_3O_4.

3.3.3 TGA-DSC studies

To compare the XRD results of transition temperatures obtained from air annealed samples (section 3.3.1), simultaneous TGA-DSC studies have been carried out under air. Fig 3.11(a) represents the heat flow and weight loss as a function of temperature for Fe_3O_4 nanoparticles (x = 0) and $Co_{0.1}Fe_{2.9}O_4$ nanoparticles (x = 0.1). The 5% weight loss in the range of 50 – 300 ºC is due to removal of moisture content in the samples. A sharp exothermic peak observed at 597 ºC in the heat flow curve corresponds to a phase transition from γ-Fe_2O_3 to α-Fe_2O_3[135]. The peak starts at 573 ºC and ends at 615 ºC, indicates the starting and completion of phase transition respectively. A change in enthalpy of 89 Jg^{-1} is observed during the phase transition, which corresponds to the energy released during the exothermic process.

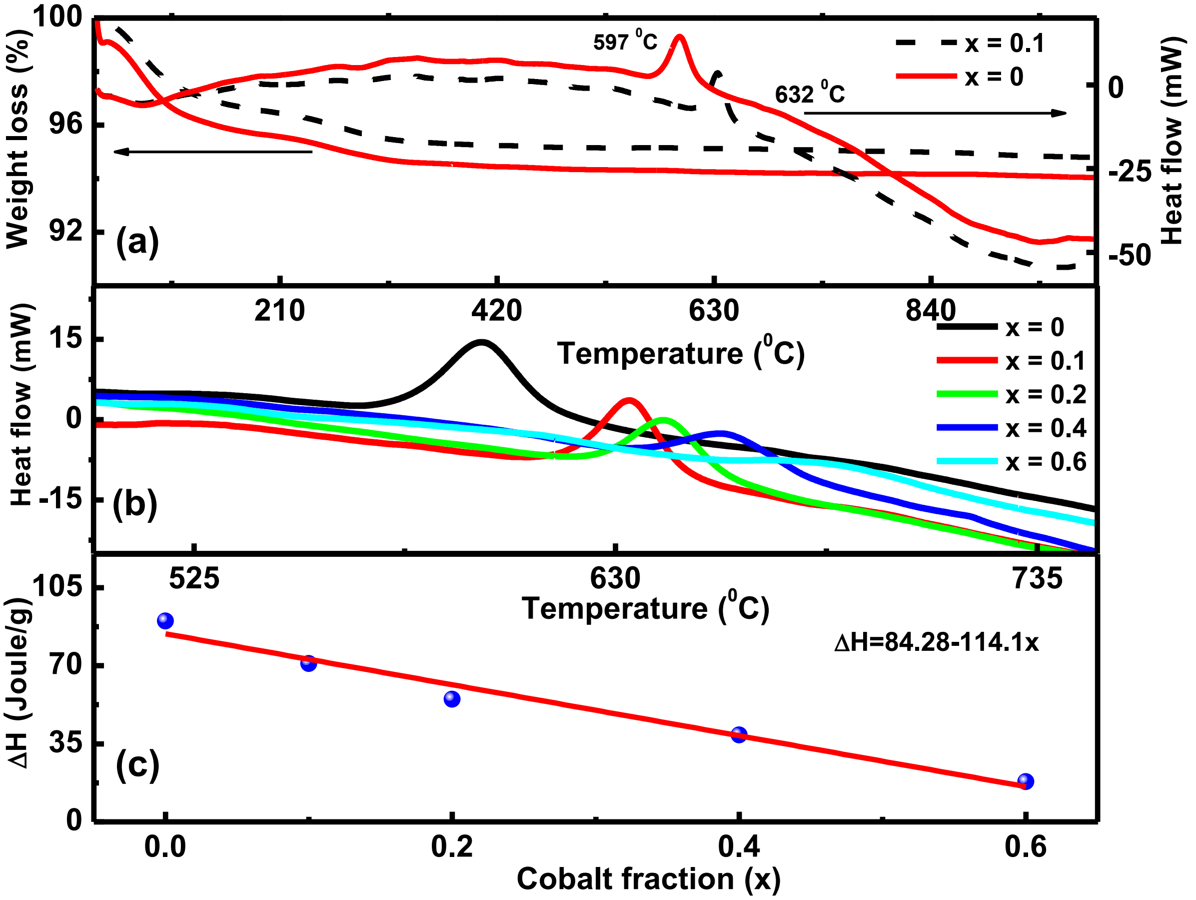

Fig 3.11: (a) The weight loss and heat flow for Fe_3O_4 (x = 0; solid lines) and $Co_{0.1}Fe_{2.9}O_4$ (x = 0.1; dashed lines) nanoparticles annealed in air. (b) The heat flow curve of $Co_xFe_{3-x}O_4$ nanopaticles in oxygen atmosphere for x = 0, 0.1, 0.2, 0.4 and 0.6. (c) The variation of enthalpy change during phase transition vs. cobalt fractions (x = 0-0.6).

For x = 0.1, an exothermic peak is clearly observed at 632 ºC that corresponds to a transition from γ to a more stable α phase. The peak starts at 618 ºC and ends at 647 ºC, where the enthalpy change drops to 71 from 89 Jg^{-1}. The enhancement in the γ-Fe_2O_3 to α-Fe_2O_3 phase transition temperature in 0.1 fraction of Co doping is found to be 35 ºC in DSC whereas it was 100 ºC in XRD. The difference in the transition temperature observed in these two experiments is due to the fact that the DSC is done at a heating rate of 10 ºC/min and is a dynamic experiment, whereas in XRD, experiments are done after annealing of the samples for two hours. However, both these results unambiguously confirm the fact that Co doping enhances the transition temperature of Fe_3O_4.

Fig 3.11(b) shows the variation of heat flow with temperature for the samples with different cobalt doping. The exothermic peaks between 600 and 650 ºC corresponds to maghemite to hematite transition. The peak temperatures are 597, 632, 643, 658 and 687 ºC for x = 0, 0.1, 0.2, 0.4 and 0.6 respectively. It can be seen clearly that the exothermic peaks shift towards higher temperature as the cobalt content increases. Fig 3.11(c) shows that the peak area decreases with increase in cobalt content. Here, the enthalpy change decreases from 89.86 to 17.62 Jg^{-1} as the cobalt content increased from 0 to 0.6. The decrease in the area under the peak is due to the fact that the degree of conversion from maghemite to hematite decreases with cobalt content. This leads to lower energy release from the system and hence a lower enthalpy change. From the thermodynamic point of view, the change in free energy governs a chemical or physical change. The equation relating free energy change and enthalpy is given by, $\Delta G = \Delta H - T\Delta S$; where, ΔG is the change in free energy, ΔH is the change in enthalpy, ΔS is the change in entropy and T represents absolute temperature. The details of DSC results are summarized in Table 3.1. As the system always prefers to stay in a state of lower free energy, the more negative the free energy change, more stable the system is. The enthalpy change depends on the amount of energy absorbed or released during the physical change. In present case, the conversion of maghemite to hematite occurs, as the latter is more stable state than the former, which explains the evolution of an exothermic peak. Again, the amount of energy release depends on the amount of conversion (i.e. maghemite to hematite).

3.3.4 Magnetic properties studies

Fig 3.12(a) shows the room temperature magnetization data of $Co_xFe_{3-x}O_4$ nanoparticles. It is observed that for $0.1 \leq x \leq 0.6$, the M-H loop does not show any magnetic hysteresis with saturation magnetization value ranging from 64 to 72 emu/g. The saturation magnetization value of bulk cobalt ferrite and magnetite are 80 and 92 emu/g respectively[132]. The slightly lower value of saturation magnetization observed in the samples is attributed to the dead layers present on the surface in lower particle size[136]. Further, these results show that the strongly magnetic nature of all the samples remains the same irrespective of the doping concentration[137].

Fig 3.12(b) shows the magnetization curves of Fe_3O_4 (x=0) nanoparticles air annealed at different temperatures. The M_s value for x = 0 sample is 60 emu/g. After annealing at 450 and 500 ºC, the saturation magnetization values are reduced to 54 and 14 emu/g respectively. The sharp reduction in the M_s values is due to the conversion of cubic γ-Fe_2O_3 phase to hexagonal α-Fe_2O_3 phase. Fig 3.12(c) represents the magnetization curves of air annealed samples for x = 0.1. The M_s value for the as prepared sample is 70.5 emu/g. After annealing at 450 and 500 ºC, the saturation magnetization values are reduced to 63.5 and 55 emu/g respectively but interestingly the samples still retain their superparamagnetic nature.

But on further increase in annealing temperature to 550 ºC, the M_s value decreases to 7 emu/g due to substantial conversion of cubic (γ-Fe_2O_3) to hexagonal (α-Fe_2O_3) phase. The decrease in saturation magnetization after annealing at high temperatures is due to the weakening of A-B exchange interaction because of thermal fluctuations. In general, cobalt ferrite exhibits inverse spinel structure.

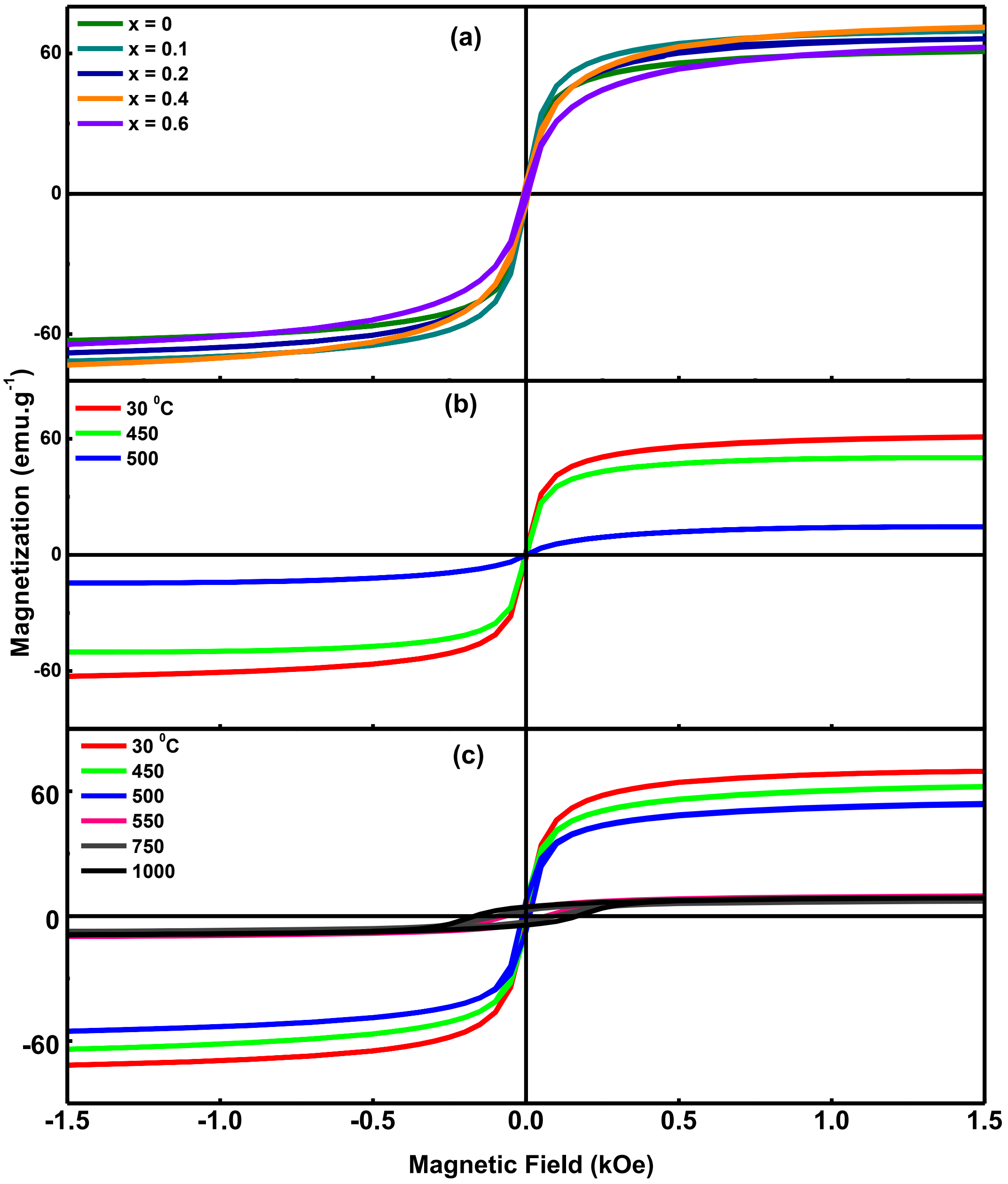

Fig 3.12: (a) Room temperature Magnetization curves of $Co_xFe_{3-x}O_4$ nanoparticles for x = 0, 0.1, 0.2, 0.4 and 0.6. (b) Fe_3O_4 nanoparticles air annealed at 30, 450 and 500 ºC (c) $Co_{0.1}Fe_{2.9}O_4$ nanopaticles air annealed at 450, 500, 550, 750 and 1000 ºC.

It consists of oxide ions in the cubic close-packed arrangement in which 1/3 of tetrahedral interstices and 2/3 of octahedral interstices coordinate with oxygen. All Co(II) ions occupy the octahedral interstices, and half of the Fe(III) occupies the tetrahedral interstices (A) and remaining half of the Fe(III) in octahedral interstices (B). Electron spins of Fe(III) ions in octahedral interstices are aligned anti-parallel to those in tetrahedral interstices. The Co(II) ions align their spins parallel to Fe(III) ions in adjacent octahedral sites leading to a net magnetization of 3.7μB per formula unit[16]. Mossbauer spectroscopy study shows that there exists a tendency for the Co^{2+} ions to be in the octahedral as well as tetrahedral with a preference towards octahedral[138]**.** Another study shows that the magnetostriction increases with substitution of manganese and decreases with substitution of iron in $Co_{1.2}Fe_{1.8-x}Mn_xO_4$[139]. The observed increase in magnetization from 68 to 79 emu/g for x = 0 to 0.1, is explained in terms of the occupancy of manganese ions in the octahedral sites, which contain more free electrons than Co. On increasing the doping, Mn ions occupy the tetrahedral site, leading to an invariant magnetization[139].

3.4 Conclusions

present studies show that a small fraction of cobalt doping (x = 0.1) in magnetite can significantly enhance their magnetic phase stability under air annealing, due to the increased activation energy for γ-Fe_2O_3 to α-Fe_2O_3 phase transition in presence of Co^{2+}. The room temperature M_s value of the sample for x=0.1, is found to be 70.5 emu/g, which is reduced to 55 emu/g after air annealing at 500 ºC, due to the weakening of A-B exchange interaction because of thermal fluctuations. The DSC results corroborate the XRD findings of increase in the γ-Fe_2O_3 to α-Fe_2O_3 phase transition temperature with cobalt fraction (x). The enthalpy decrease from 89.86 to 17.62 Jg^{-1} as the cobalt content increases from 0 to 0.6 which clearly indicates that the degree of conversion from maghemite to hematite decreases with cobalt content, which was in good agreement with the γ-Fe_2O_3 and α-Fe_2O_3 fractions observed in the Rietveld analysis data. These results are promising as they reveal a new approach to tune the transition temperature of ferrites by varying the doping concentrations.

Chapter IV

High temperature phase transition studies in $Zn_xFe_{3-x}O_4$ nanoparticles

4.1 Introduction

Studies show that $ZnFe_2O_4$ nanoparticles are thermally stable upto 1000 ºC under air as well as vacuum annealing conditions but exhibit paramagnetic behavior at room temperature[118, 140]. A study on the effect of thermal annealing of pure zinc ferrite under vacuum shows a sudden drop of lattice parameter at 800 ºC because of a conversion of the cubic structured $ZnFe_2O_4$ from normal to inverse spinel structure due to canting of ions between the tetrahedral and octahedral interstitial sites[118, 140, 141]. It is reported that the occupancy of Fe^{3+} ion in the tetrahedral A-site increases with decreasing particle size[142]. It was observed that formation of α-Fe_2O_3 decreases with increase in Zn doping in γ-Fe_2O_3[104]. Earlier, calorimetric studies have shown that α-Fe_2O_3 to γ-Fe_2O_3 phase transition temperature can be enhanced by 160 ºC when doped with 1% of Zn[108]. Even though there are few reports on room temperature studies on Zn^{2+} doped magnetite nanoparticles, high temperature studies in Zn^{2+} doped magnetite system is lacking. Understanding of physical properties, and phase transition temperatures are essential for better utilization of these materials for practical applications.

With the above objectives in mind, systematic studies on zinc doped magnetite nanoparticles, synthesized by chemical co-precipitation approach, are undertaken. The studies are focused on the effect of dopant concentrations on the crystal structure, high temperature phase transition temperatures and magnetic properties, blocking and curie temperatures of Zn doped magnetite under vacuum and air annealing upto 1000 ºC.

4.2 Synthesis of $Zn_xFe_{3-x}O_4$ nanoparticles

$Zn_xFe_{3-x}O_4$ nanoparticles (x=0 to 0.6) are prepared using co-precipitation method. The details of the synthesis procedure are discussed in chapter II, Section 2.2.1.1.

4.3 Results and Discussion

4.3.1 Room Temperature XRD Studies

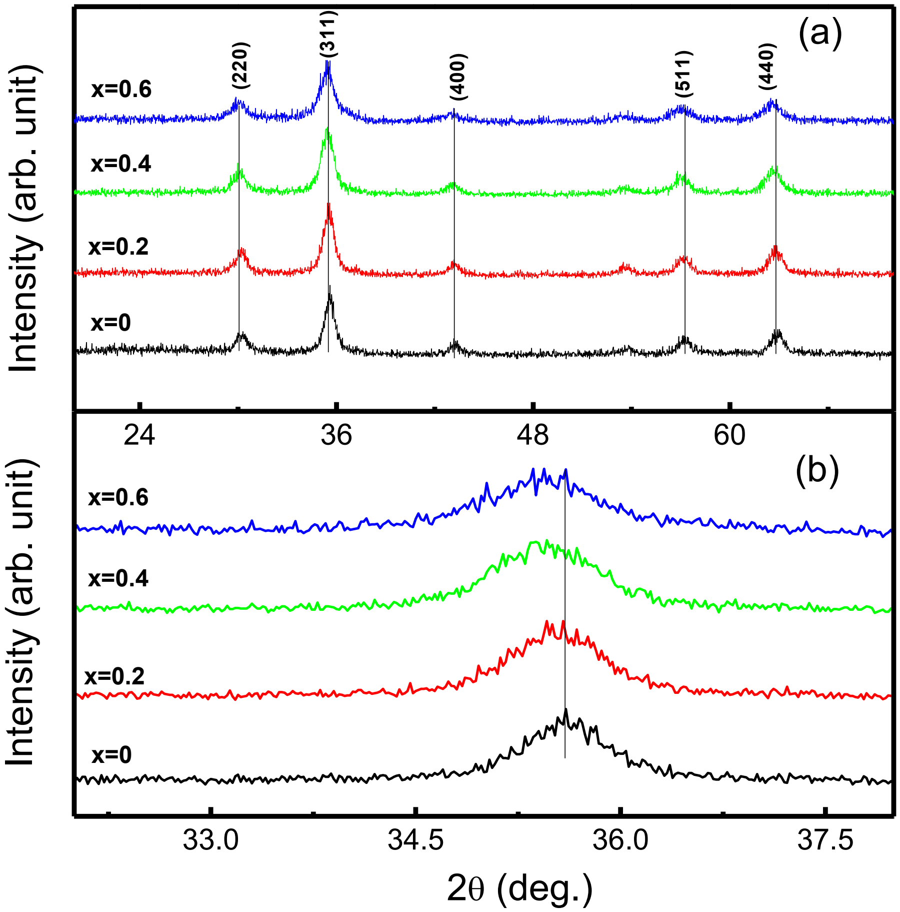

Fig 4.1: XRD pattern of $Zn_xFe_{3-x}O_4$ nanoparticles for x = 0, 0.2, 0.4 and 0.6.

Fig 4.1(a) shows the room temperature XRD patterns of $Zn_xFe_{3-x}O_4$ nanoparticles of different dopant concentrations x = 0, 0.2, 0.4 and 0.6. The peaks correspond to the crystal planes

(220), (311), (400), (511) and (440) and matches with the JCPDS card no-880315 of spinel ferrite. Fig 4.1(b) shows the magnified view of the (311) peak, which shifts towards lower 2 theta value with increase in zinc fraction. This observation is consistent with previous reports[143]. The XRD diffraction peaks of all the samples resemble that of pure magnetite, which indicate a crystal unit of face-centered cubic inverse-spinel structures for all the samples. The most intense diffraction peak from the (311) plane is fitted to the voigt function for the calculation of crystallite size. The crystallite size of the particles is found to reduce from 11(±1) to 8(±1) nm as the zinc content increases from 0 to 0.6. Fig 4.2 shows the scattering intensity as a function of wave vector and the probability distribution vs particle size for particle prepared with doping concentrations of x = 0, 0.2, 0.4 and 0.6.

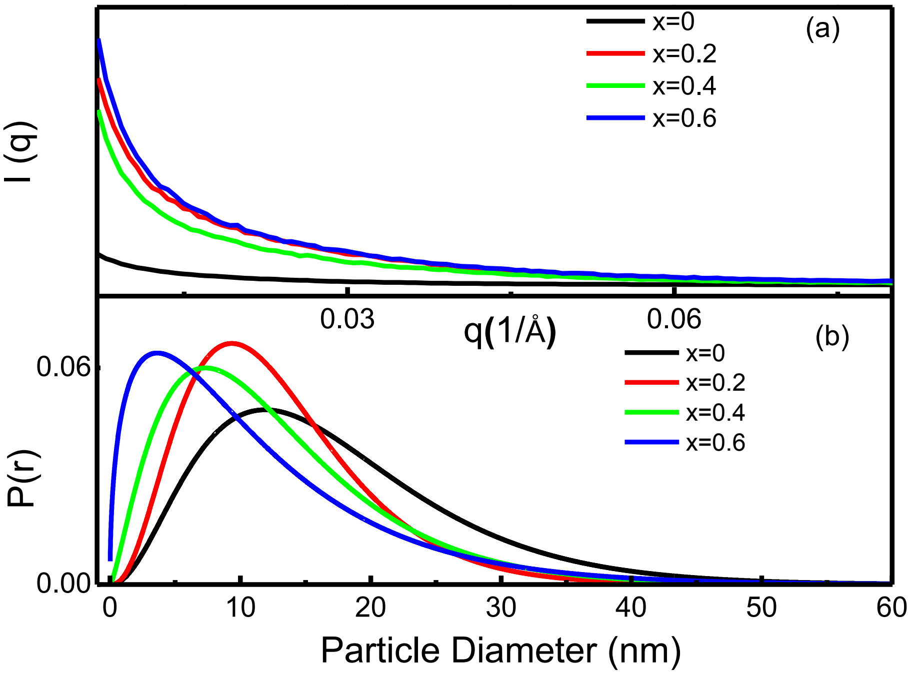

Fig 4.2: (a) Intensity as a function of scattering vector and (b) probability distribution as a function of particle size for x = 0, 0.2, 0.4 and 0.6.

The particles size and their distribution observed from SAXS confirm that the particle size and polydispersity indeed decrease with the doping concentration. Further, the SAXS analysis shows that all the particles are nearly spherical in shape (i.e. $I(q) \propto q^{-4}$). The average particle size is found to vary from 15(±2) to 11(±1) nm for the x values 0 to 0.6.

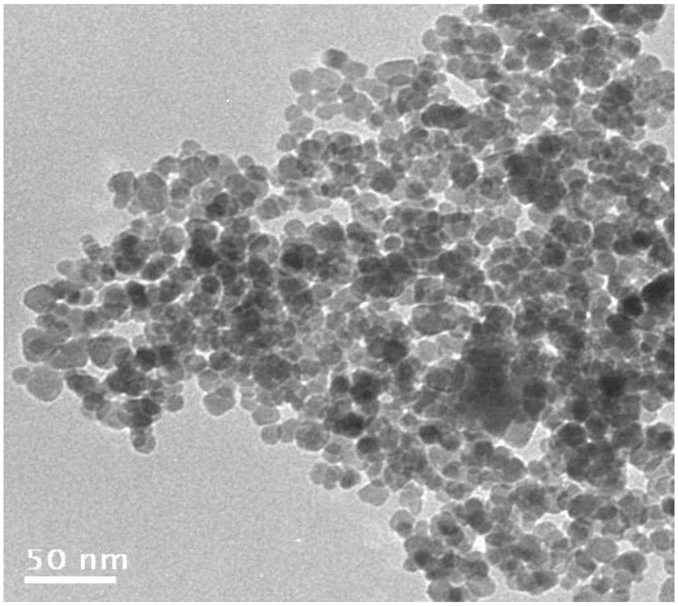

Fig 4.3: TEM image of Fe_3O_4 nanoparticles (x = 0).

Fig 4.3 shows the TEM image for x = 0 (Fe_3O_4), where the average particle size is found to be 13(±1.5) nm. The measured values of lattice parameter and crystallite size of nanoparticles plotted as a function of zinc fraction is shown in Fig 4.4. The lattice parameter (a) increases from 8.35 to 8.39 Å as the Zn^{2+} ion concentration increases from 0 to 0.2. The reported values of lattice parameter for Fe_3O_4 and $ZnFe_2O_4$ are 8.33 and 8.35 Å, respectively which is fairly in agreement with the observed values[143]. Due to the affinity of Zn^{2+} ions for strong, nearly covalent, sp^3 bonding with oxygen ions, the Zn^{2+} ions prefer to occupy the tetrahedral sites by pushing the oxygen atoms along the body diagonals of the octants of the spinel structure. The resultant shrinkage of octahedral sites enables the occupancy of the Fe^{3+} ions under strain.

Therefore, the lattice parameter of Zn ferrite is slightly higher compared to cubic structured inverse spinel magnetite[118].

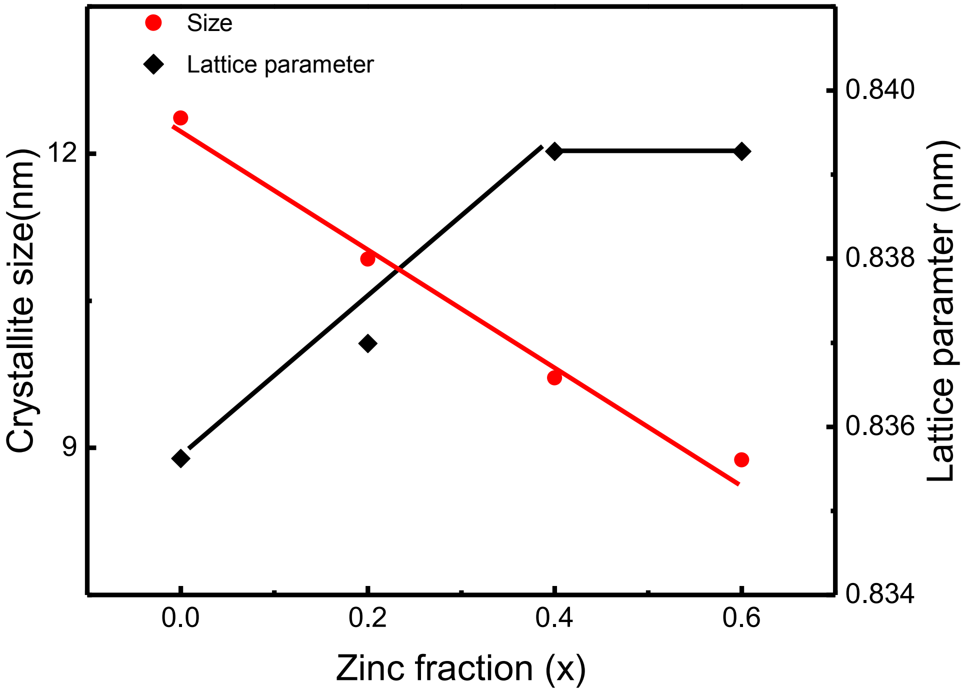

Fig 4.4: Variation of crystallite size and lattice parameter as a function of Zn^{2+} fraction (0 - 0.6).

Usually in a close packed structure, the radius of the tetrahedral site is about 0.866 times smaller than the octahedral site[144]. The ionic radius of the Zn^{2+} ion (~74 pm) is larger than that of Fe^{3+} ion located in the A site. A reduction in unit cell with decreasing size in ionic systems and an expansion in covalent systems is predicted by Lennard-Jones[145]. It has been shown that an expansion of the unit cell can occur with reduction in partially covalent oxides of ferroelectrics, ferromagnets, superconductors, and structural ceramics[146].

4.3.2 High Temperature XRD studies

The *in situ* high temperature XRD patterns of Fe_3O_4 nanoparticles (x=0) annealed under vacuum from 30 to 1000 ºC in steps of 100 ºC and after cooling back to room temperature (RT) shows cubic spinel structure of iron oxide (Chapter III, Fig. 3.8). Above 700 ºC, iron oxide phase is decomposed into a mixture of FeO and γ-Fe_2O_3 phases, which is evident from the appearance of (200) and (111) peaks of FeO along with (311) crystal plane of γ-Fe_2O_3. Rietveld analysis is performed to confirm the γ-Fe_2O_3 and FeO phases (Fig. 4.5).

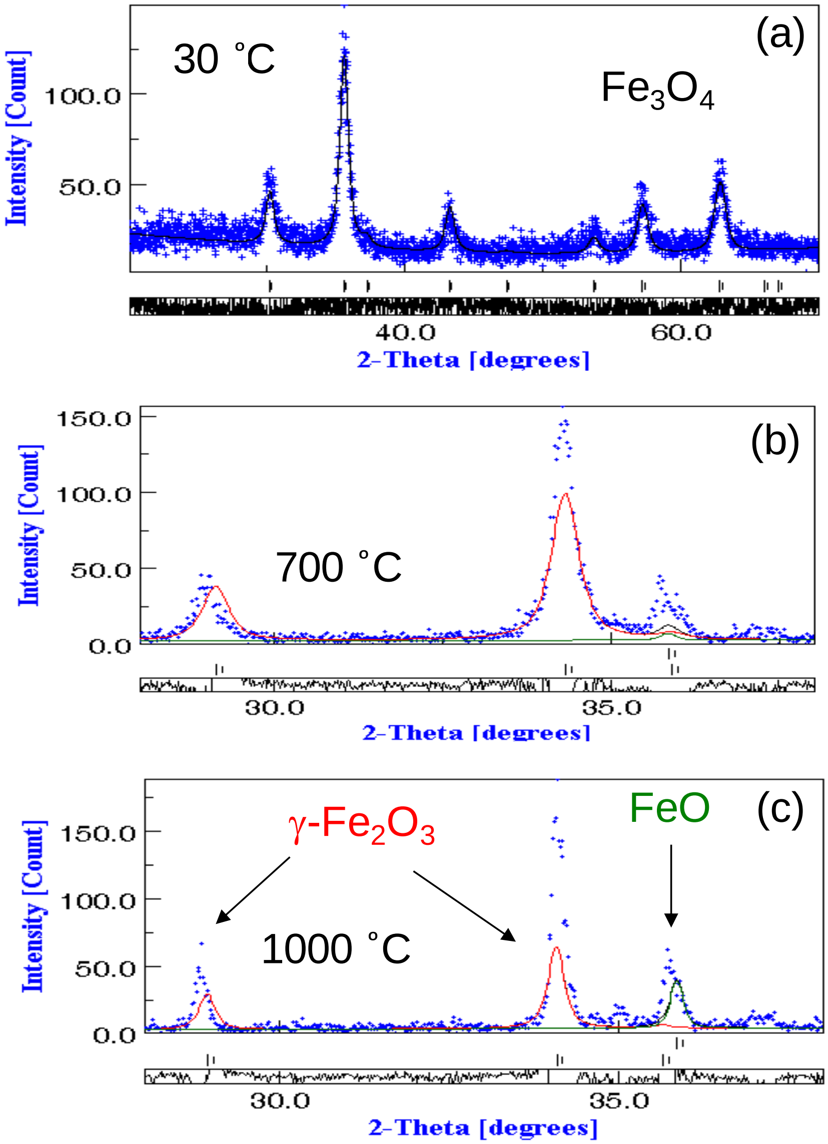

Fig 4.5: Rietveld analysis for XRD pattern of Fe_3O_4 nanoparticles after vacuum annealing at 30, 700 and 1000 ºC.

The analysis clearly shows that before vacuum annealing, only the spinel Fe_3O_4 phase is present whereas after vacuum annealing at 700 ºC, the contribution from FeO phase starts to increase. A distinct peak of FeO (i.e (200) crystal plane) is observed along with γ-Fe_2O_3 after 1000 ºC. The goodness of fit (GoF) and expected R-factor are found to be 1.40 and 22%, respectively. The variation in particle size and lattice parameter values as a function of temperature is plotted in Fig. 4.6.

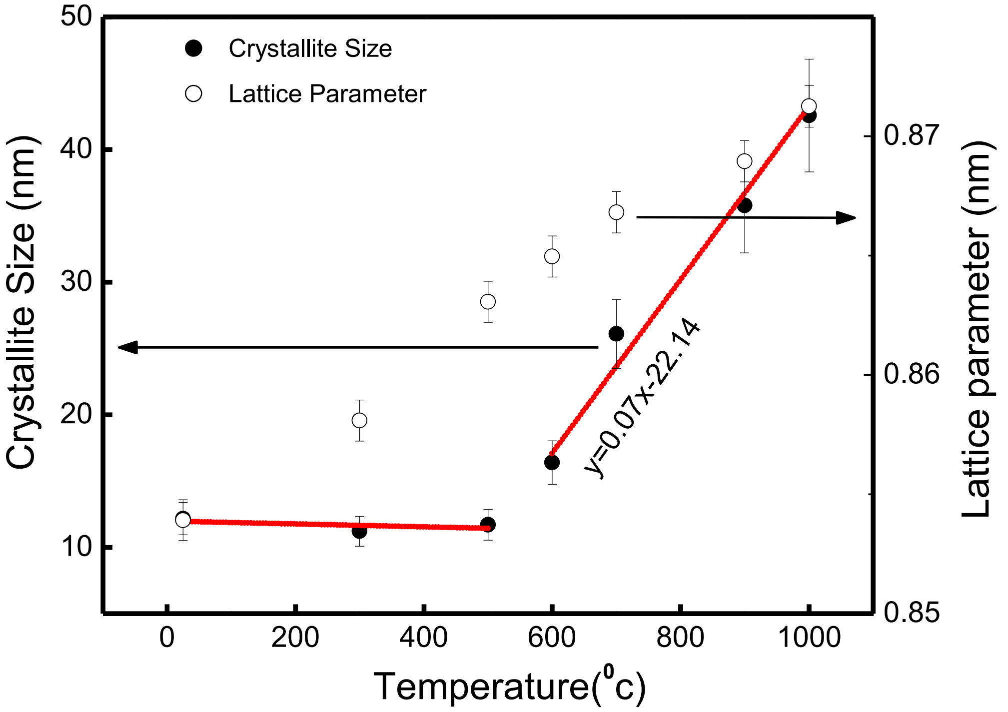

Fig 4.6: Variation of crystallite size and lattice parameter as a function of temperature for x = 0 under vacuum.

The 'd' and 'a' values of as-synthesized Fe_3O_4 particles increases from 12 to 16 nm and 8.53 – 8.64 Å, respectively as the temperature is increased from 30 to 700 ºC. From 700 to 1000 ºC, 'd' ('a') of γ-Fe_2O_3 phase increases almost linearly from 16 to 42 nm (8.64-8.71 Å) due to coalescence. The slope of the linear fit on the crystallite size was 0.07, which shows the slow growth of particle size. Table 4.1 shows the summary of the findings of high temperature XRD studies at different temperatures under vacuum environment. The phases observed at different annealing temperature, 2θ values and the crystallite size are given.

Table 4.1: HTXRD Phase analysis results of magnetite nanoparticles after annealing under vacuum at different temperatures.

Temperature (ºC)	Phase	2θ (degree)	Crystallite Size (nm)
30	Fe_3O_4	34.81	12.2
300	Fe_3O_4	34.64	11.2
500	Fe_3O_4	34.43	11.7
600	Fe_3O_4	34.35	16.4
700	γ-Fe_2O_3+FeO	34.27+40.68	26.1+40.1
900	γ-Fe_2O_3+FeO	34.19+40.64	35.7+20.9
1000	γ-Fe_2O_3+FeO	34.09+40.68	42.5+34.1

For x = 0.2 ($Zn_{0.2}Fe_{2.8}O_4$), the *in situ* XRD pattern of nanoparticles under vacuum annealing at different temperature is shown in Fig 4.7. In the temperature range 30 to 900 ºC, the observed diffraction peaks confirm the cubic spinel structure of ferrite phase. In contrast to the phase decomposition at 700 ºC for x = 0.2, the $Zn_{0.2}Fe_{2.8}O_4$ is found to be stable upto 900 ºC and the particles decompose at 1000 ºC to FeO phase along with the γ-Fe_2O_3 phase. These phases remain intact even after cooling the sample back to room temperature. This observation suggests that the replacement of Fe^{3+} with larger diameter Zn^{2+} in the A site leads to an enhanced thermal stability. Fig 4.8 shows the variation of ‘d’ and ‘a’ values of as-synthesized $Zn_{0.2}Fe_{2.8}O_4$ nanoparticles as a function of temperature. In the temperature range of 30 to 500 ºC, the particle size remains almost unchanged, above which it increase from 10 to 36 nm as the temperature increases from 30 to 1000 ºC. A steady increase in the lattice parameter from 8.54 to 8.69 Å is observed in the above temperature range. Similar results are observed for x=0.4 and 0.6.

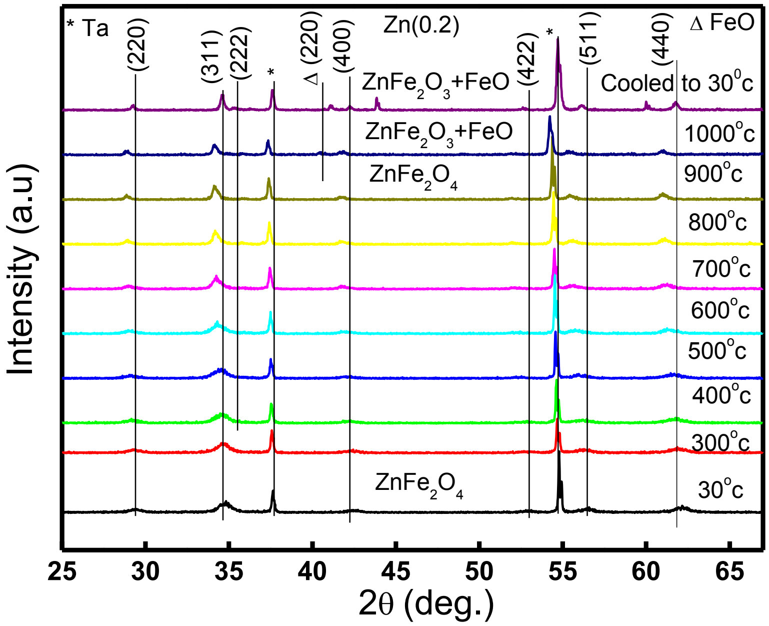

Fig 4.7: XRD pattern of $Zn_xFe_{3-x}O_4$ nanoparticles for x = 0.2 vacuum annealed at different temperatures from 30 to 1000 ºC and cooled back to room temperature.

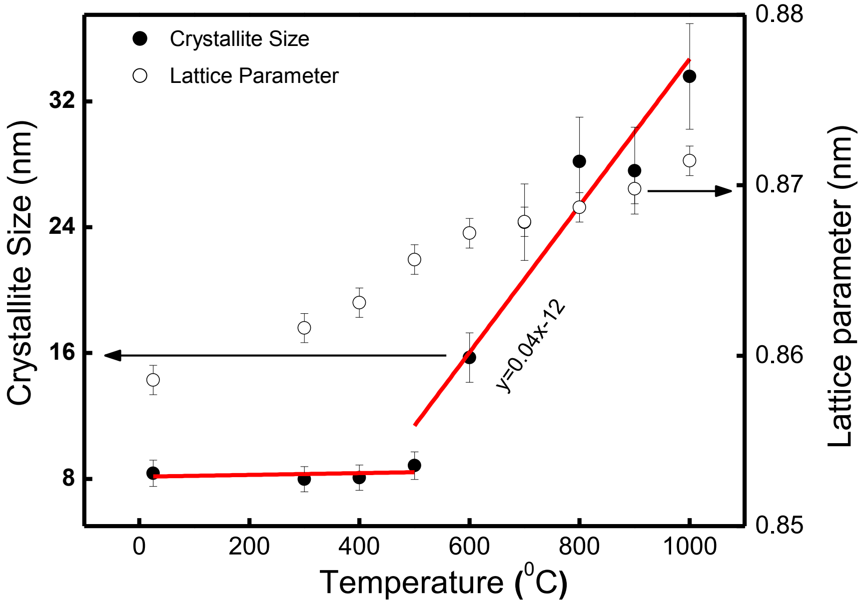

Fig 4.8: Variation of crystallite size and lattice parameter as a function of temperature for x = 0.2 under vacuum.

To obtain the reason for the observed enhanced stability, the activation energy of doped samples are obtained using the Schott equation[118]. Fig 4.9 shows the variation of activation energy with increasing zinc content. The results show that the activation energy increases from 11 to 20 kJ.mol^{-1} as the doping concentration increases from 0 to 0.6. In the doping concentration range 0 to 0.4, the activation energy increases from 11 to 13 kJ.mol^{-1}.

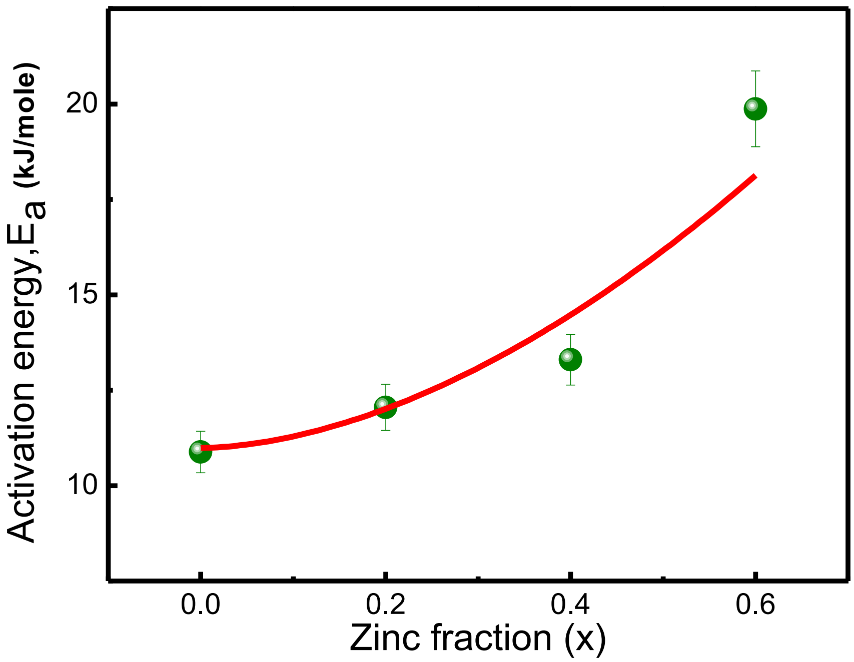

Fig 4.9: Calculated activation energy (in kJ.mol^{-1}) as a function of x from 0 to 0.6. The best fit to the experimental points is $E_a = 11 + 17.6x^{1.77}$.

In the doping concentration range of 0.2 to 0.6, as the particle size reduced from 11 to 8 nm, one would expect that the size effect may play a role on the enhanced phase transition temperatures. Earlier studies clearly show that the phase transition temperature is indeed decreases with decrease in particle size for uncoated nanoparticles[100, 119]. Therefore, the enhanced phase transition temperature with Zn^{2+} doping appears to be due to the strong exchange interaction.

The observed enhanced stability of the ferrite phase by with Zn^{2+} doping ($x \leq 0.2$ fractions) is significant from application point of view. The consolidated results of phase transition studies are listed in Table 4.2.

Table 4.2: The phase transition temperatures of nanoparticles under vacuum and air atmosphere for zinc concentration of 0, 0.2, 0.4 and 0.6.

x	$Fe_3O_4 \rightarrow \gamma\text{-}Fe_2O_3 + FeO$ (Under Vacuum) in ºC	$\gamma\text{-}Fe_2O_3 \rightarrow \alpha\text{-}Fe_2O_3$ (DSC Peak in air) in ºC
0	700	575
0.2	1000	634
0.4	1000	646
0.6	1000	656

4.3.3 TGA-DSC studies

Fig 4.10 (a-d) shows the heat flow curve as a function of temperature for $Zn_xFe_{3-x}O_4$ nanoparticles for x = 0, 0.2, 0.4 and 0.6. For x = 0, an endothermic peak is observed in the temperature range of 30-300 ºC due to removal of moisture present in the sample. At ~575 ºC, a sharp exothermic peak is observed due to the phase transition from $\gamma\text{-}Fe_2O_3$ to $\alpha\text{-}Fe_2O_3$[102]. The peak starts at 555 ºC and ends at 595 ºC with an enthalpy change of 90 Jg^{-1} for x = 0. For x = 0.2, an exothermic peak is observed at 634 ºC that corresponds to a transition from $\gamma\text{-}Fe_2O_3$ to $\alpha\text{-}Fe_2O_3$ phase. The peak starts at 616 ºC and ends at 653 ºC with an enthalpy change of 98 Jg^{-1}. For x = 0.4, an exothermic peak is observed at 646 ºC with an enthalpy change of 52 Jg^{-1}. For x = 0.6, the $\gamma\text{-}Fe_2O_3$ to $\alpha\text{-}Fe_2O_3$ phase transition temperature further increases where the exothermic peak is observed at 656 ºC with an enthalpy change of 19.2 Jg^{-1}.

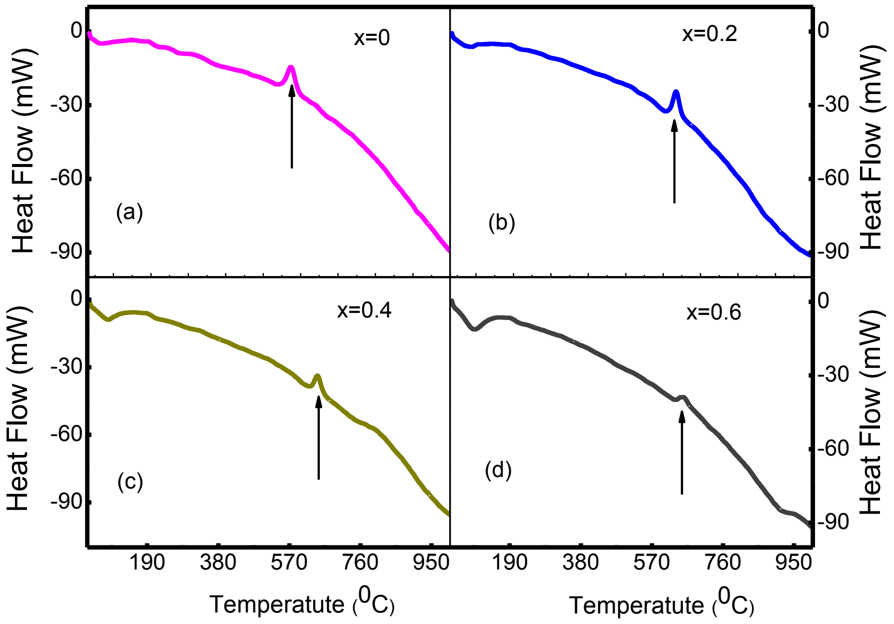

Fig 4.10: The heat flow curves of $Zn_xFe_{3-x}O_4$ nanoparticles for (a) x = 0, (b) x = 0.2, (c) x = 0.4 and (d) x = 0.6 from 30 to 1000 ºC under air annealing conditions.

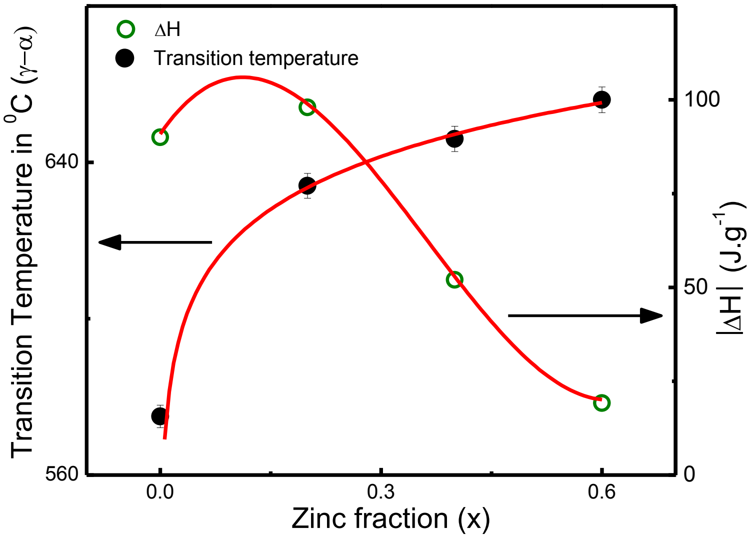

Fig 4.11: Variation of γ-Fe_2O_3 to α-Fe_2O_3 phase transition temperature (T) and enthalpy change (ΔH) from DSC as a function of x under air annealing conditions. The best fit of the T vs. x is $T_{\gamma-\alpha} = 666.x^{0.03}$.

Fig 4.11 shows the variation of γ-Fe_2O_3 to α-Fe_2O_3 phase transition temperature and enthalpy change as a function of zinc concentration. The increase in the γ-Fe_2O_3 to α-Fe_2O_3 phase transition temperature with increasing Zn concentrations is indeed due to the increase in the activation energy (Fig. 4.10) of the system due to the presence of Zn^{2+} in the A site (Fe^{3+} ions replaced by Zn^{2+}).

Fig 4.12 (a-d) shows the weight loss curves as a function of temperature for Zn^{2+} doped magnetite nanoparticles under an external magnet. When the sample is magnetic, it experiences a weight loss due to the magnetic force and gains weight when it becomes non-magnetic. For x = 0, on increasing the temperature from 30 to 100 ºC, about 2% of weight loss is observed which is due to the evaporation of moisture. On further increase in temperature, the sample gains weight due to loss of its magnetic property with an increase in thermal fluctuations under external field. The amount of increase in the weight depends on the magnetic nature of the sample i.e. for sample with high magnetic property (M_S), the weight gain will be more. The weight gain occurs till all the particles are converted to non-magnetic, above which a plateau is observed. Above this saturation point (known as the Curie temperature), the particles exhibit paramagnetic behavior. It is known that the A-A interactions are about 10 times weaker than the A-B and B-B interactions and the T_c depends on the respective exchange integrals J, the number of nearest exchange-coupled neighbors and the absolute spin[147]. For x =0, the T_C is found to be 578 ºC where γ-Fe_2O_3 to α-Fe_2O_3 phase transition occur. Interestingly, for x=0, two distinct slopes are observed in the temperature range of 150- 578 ºC (temperature range of 150 ºC to ~330 ºC and from 330 ºC to 578 ºC). The slope change observed at 330 ºC should be due to the conversion of magnetite to maghemite. The T_C for 0.2, 0.4 and 0.6 are 500, 419 and 367 ºC, respectively.

Interestingly, the T_C is found to decrease with increase in Zn^{2+} doping concentration whereas γ to α phase transition temperature is found to increase with Zn^{2+} concentration.

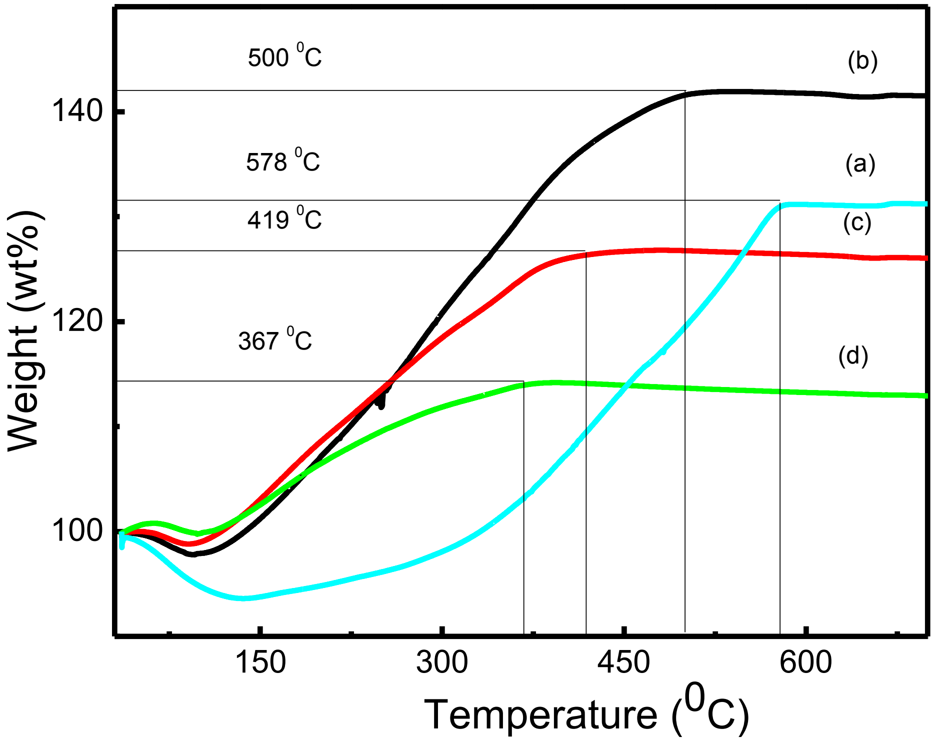

Fig 4.12: The weight as a function of temperature for (a) x = 0, (b) x = 0.2, (c) x = 0.4 and (d) x = 0.6 fractions zinc doped magnetite nanoparticles in air atmosphere under an external magnet.

This indicates that, Zn^{2+} doping increases the phase stability of the magnetite nanoparticles by increasing the activation energy but at the same time the Curie point decreases due to the non magnetic nature of Zn. Table 4.3 summarizes the weight gain, T_C and γ to α phase transition temperature for x = 0, 0.2, 0.4 and 0.6.

4.3.4 Magnetic properties

The magnetization results show that for x= 0, 0.2, 0.4 and 0.6 fraction, the nanoparticles show superparamagnetic behavior with nearly zero coercivity and remanence for all the samples

(Fig 4.13). For pure Fe_3O_4 nanoparticles, the observed M_s is ~61 emu/g. The reported value of M_S for the bulk Fe_3O_4 particles is 92 emu/g[132].

Table 4.3: The values of M_S, weight gain (%), magnetic to non-magnetic transition temperature, γ-α phase transition temperature and T_B obtained from magnetization and TGA-DSC measurements.

x	M_s (emu/g)	Wt gain (%)	T_C (ºC)	$T_{(\gamma-\alpha)}$ (ºC)	T_B(K)
0	61	31	578	575	262
0.2	69	42	500	634	196
0.4	59	27	419	646	144
0.6	52	14	367	656	153

The magnetic properties of spinels are sensitive to the type of cations and their distribution among the two interstitial sites of spinel lattices and the relative strength of inter (J_{AB}) and intra sublattice (J_{AA} and J_{BB}) interactions[148, 149]. On doping with 0.2 fraction of Zn^{2+}, the M_s increases to 69 emu/g , which was about 13% more than the pure iron oxide M_s value. On further increase of zinc fraction to 0.4, 0.6 the M_s decreases gradually to 59, 52 emu/g respectively. Upon doping of zinc into the Fe_3O_4, Zn^{2+} replaces Fe^{3+} from the tetrahedral (A) site. The Fe^{3+} (electronic configuration of is $[Ar]^{18}$ $3d^5$) has five unpaired electrons which contributes to the magnetic moment[150]. However, Zn^{2+} (electronic configuration is $[Ar]^{18}$ $3d^{10}$) has all the electrons are paired and is diamagnetic in nature. When one Fe^{3+} is replaced with one Zn^{2+} ions, Fe^{2+} ion in the B-site changes to Fe^{3+} ion with same spin direction by electron emission to preserve electric neutrality of the crystal unit[143]. For x = 0.2, electron transfer occurs for two Fe^{3+} ions. Above x = 0.3, the antiparallel spin alignment of some of the Fe^{3+} ions can lead to a decrease in the magnetization, through a superexchange interaction (predominant over the double exchange interaction) between the Fe^{2+} and Fe^{3+} ions through an oxygen ion in the B-site.

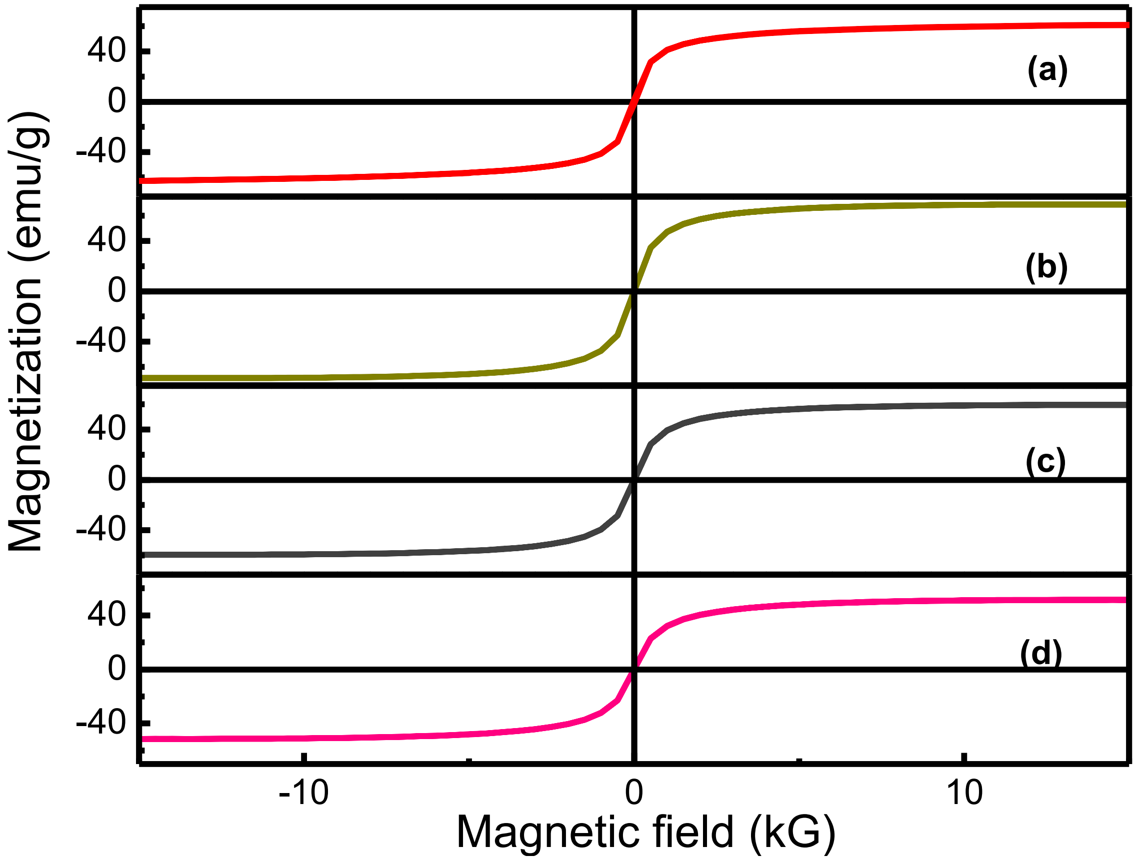

Fig 4.13: Room temperature M-H curves of (a) x = 0, (b) x = 0.2, (c) x = 0.4 and (d) x = 0.6 nanoparticles.

For x = 0.4, the total magnetization of Fe^{3+} ions in the B-site should be similar to that of x=0, as the magnetization associated with four resultant Fe^{3+} ions in the B-site becomes zero. Interestingly, this is found to be true in the present study where the M_s value for x=0 and x= 0.4 are found to be 60 and 59 emu/g, respectively. For x>0.4, a slight reduction in the M_S is observed, which was consistent with earlier studies[151]. Studies in zinc-doped ferrites nanoparticle samples (with x = 0, 0.17, 0.33, 0.50, and 0.67) prepared with the hydro thermal method, show that increasing zinc content from 0 to 0.33 increases the saturation magnetization, while it decreases on further increase in Zn content[151]. Further, their systematic studies using X-ray absorption one structure confirmed that most of dopant Zn atoms occupy A site, and only a few Fe atoms at B site are substituted by Zn atoms. The numerical calculation by Liu et al. [143] predicts an expansion of the a-axis with doping and an instability of the crystal at x = 0.5 or above. Their studies suggest that the doping of zinc beyond x=0.4 is impossible. Though our results are consistent with the experimental and theoretical calculations of Liu et al. upto x=0.4, we observe that Zn doping upto x=0.6 is possible and the crystal structure is stable. Interestingly, a slight reduction in both M_s and lattice parameter is observed, which suggest that the Zn^{2+} to Fe^{3+}ions exchange in B-site is not happening above x=0.4. The EDS analysis of the doped samples of iron oxide shows that Zn becomes more intense in proportion to x and the intensity ratio (Zn/Fe) obtained from the spectra was found to be slightly higher than x/(3 - x). At x = 0.3, it is expected that the spin directions of two Fe_x^{3+} ions among three Fe_x^{3+} ions are antiparallel leading to a decrease in the magnetization and a superexchange interaction between the resultant Fe_x^{3+} and original Fe_x^{2+} ions through an oxygen ion in the B-site[143].

Fig 4.14(a-d) shows the zero field cooled and field cooled magnetization curves of $Zn_xFe_{3-x}O_4$ nanoparticles for x = 0, 0.2, 0.4 and 0.6. The ZFC magnetization curve increases monotonically with temperature and reaches a maximum value at the blocking temperature. Beyond T_B, ZFC shows a decrease in magnetization with temperature as the thermal energy dominates over the magneto-crystalline anisotropy. When the sample is cooled under the same magnetic field of 100 Oe, the FC magnetization curve overlaps with ZFC up to T_B and remains almost constant below T_B. With increasing Zn concentration, the slope of the ZFC curves is found to increase. For x =

0, the blocking temperature (T_B) was obtained at 262K. The T_B values were found to be 196, 144 and 153K for 0.2, 0.4 and 0.6 fraction of zinc respectively.

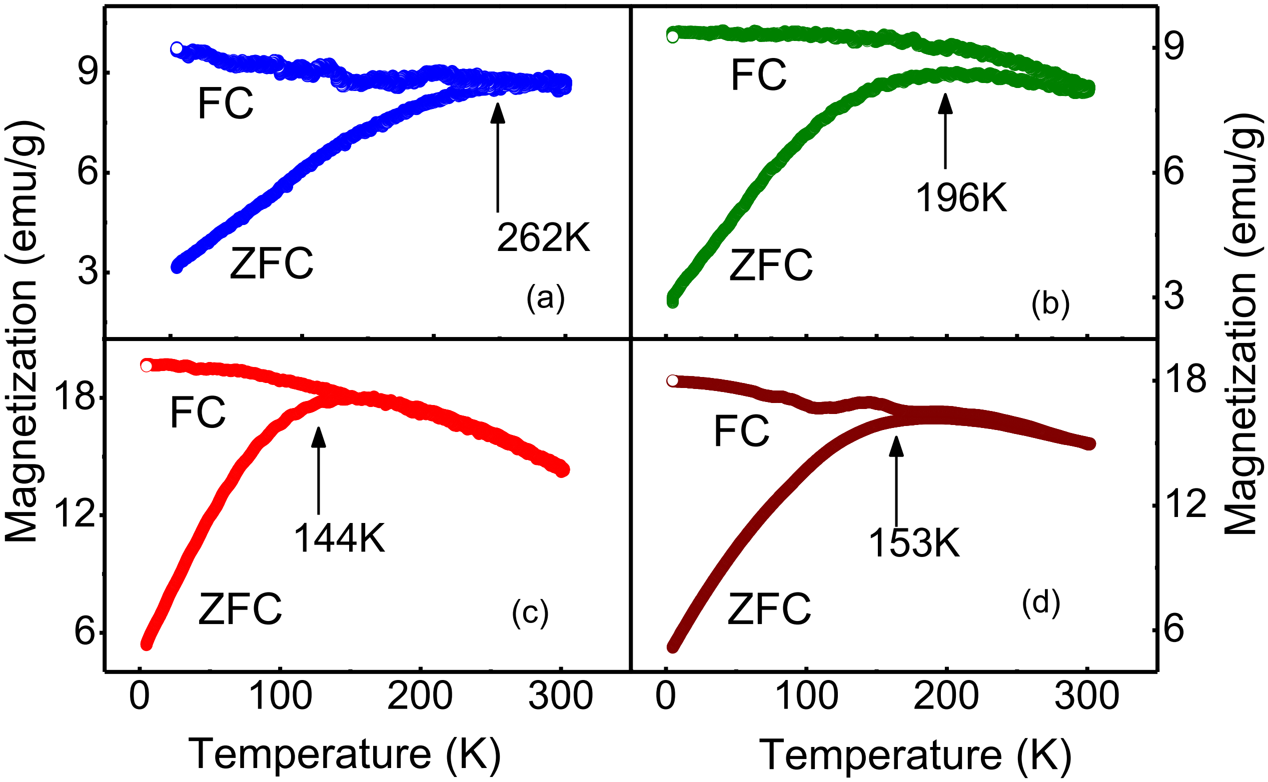

Fig 4.14: Zero field cooled (ZFC) and Field cooled (FC) curves of (a) x = 0, (b) x = 0.2, (c) x = 0.4 and (d) x = 0.6 nanoparticles. The blocking temperatures are shown by the arrows.

Fig 4.15 shows the variation of the blocking temperature as a function of Zn doping fractions. In general, a reduction in T_B is attributed to weak dipole–dipole interactions and local exchange coupling between nanoparticles. It should be noted that in the above doping concentrations, the particle size decreases from 11 (±1) to 8(±1) nm. A reduction in T_B is expected due to the increase in spin disorder with decrease in particle size[41, 152]. In the case of fine magnetic iron oxide particles, the T_B is found to decrease from 210K to 45K(at 5Oe field) as the size decreases from 8 to 2 nm. As the size of the magnetic particle is decreased below a critical size, a large fraction of atoms reside at the surface of the particles with broken translation symmetry. Here, the magnetic behavior of these nanoparticles becomes highly dependent on the magnetic anisotropy energy of the individual particle and the magnetic dipole-dipole interaction between particles. Superparmagnetism originates because of the dominant magnetic anisotropy over the dipole-dipole interaction. Above T_B, the thermal energy exceeds the anisotropy energy and the magnetization of each particle begins to fluctuate between the two easy axes.

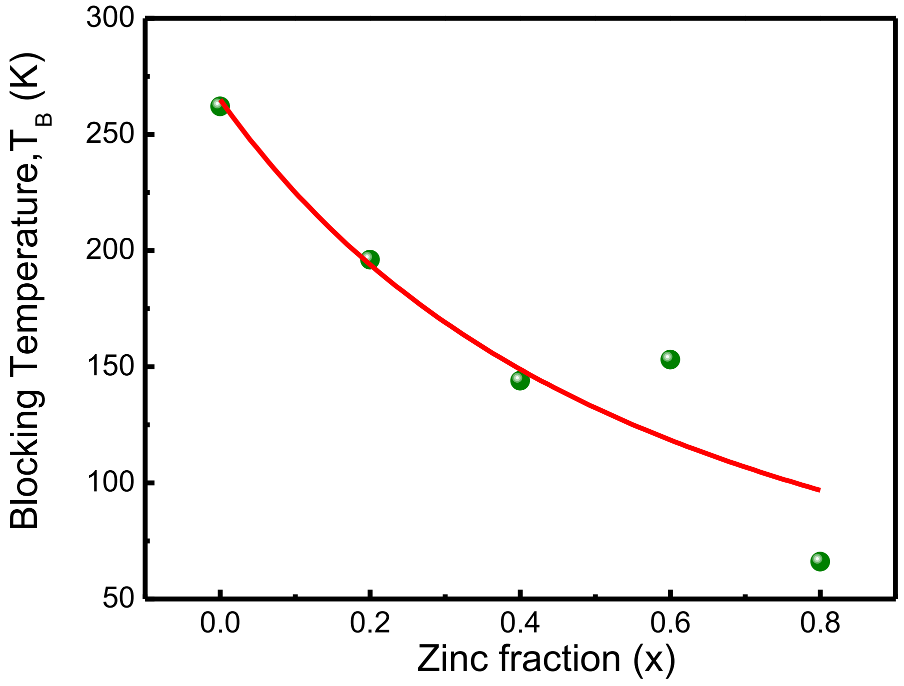

Fig 4.15: Variation of blocking temperature T_B (K) with Zn^{2+} doping fraction in magnetite.

The T_B is directly proportional to the volume (V) of the nanoparticles as $T_B = \frac{KV}{25k_B}$, where, K is the anisotropy constant and k_B is the Boltzmann constant. For temperatures below $T_{B,}$ the magnetic moments becomes frozen and the system exhibits memory effect and magnetic hysteresis. The anisotropy constant of nanoparticles obtained using the above equation are found to be 11.95×10^5, 12.92×10^5, 13×10^5 and 18.29×10^5 erg/cm^3 for x = 0, 0.2, 0.4 and 0.6, respectively. The reported value of anisotropy constants for the bulk Fe_3O_4 was 1.35x10^5 erg/cm^3 and for 5 nm size Fe_3O_4 particles, it was 12 x10^5 erg/cm^3. Interestingly, the anisotropy constant values remain almost the same as that for pure Fe_3O_4 particles upto x=0.4, above which it increases dramatically. The increase in the K value with decrease in size is in good agreement with the reported trend in the size dependent anisotropy constant[119]. The K depends on magnetocrystalline, shape, surface, and stress magnetic anisotropies and the dipolar and/or exchange interactions among the particles[153]. The increase in K for x>0.4 could be due to the combined effect of magnetocrystalline and stress magnetic anisotropies due to Zn^{2+} in the A site.

4.4 Conclusions

High temperature phase transition studies have been performed in zinc doped magnetite nanoparticles under vacuum and air annealing conditions. Vacuum annealing studies show that the magnetite forms a mixed phase of FeO and γ-Fe_2O_3 above 700 ºC whereas, doping with 0.2 to 0.6 fractions of zinc the mixed phase transition occurs only at 1000 ºC. In the case of air annealing, the γ-Fe_2O_3 to α-Fe_2O_3 phase transition occurs at 575 ºC with enthalpy change of 90 J.g^{-1}as observed in the heat flow curve. The γ-Fe_2O_3 to α-Fe_2O_3 phase transition temperature is increased to 634 ºC after doping with 0.2 fraction of zinc. The increase in transition temperature is attributed to the increase in activation energy of the maghemite to hematite phase transition after the replacement of Fe^{3+} with larger diameter Zn^{2+} in the A site. The saturation magnetization increases from 61 to 69 emu/g with a Zn^{2+} doping fraction of 0.2. The M_S decreases on further increase in Zn^{2+} concentration. The blocking temperature is found to decreases with increase in zinc fraction due to increase in spin disorder.

Chapter V

Effect of Na^+ doping on the thermal stability of magnetite nanoparticles and magnetic fluids

5.1 Introduction

Doping of transition metal ions is one of the common methods for augmentation of maghemite to hematite phase transition temperature. However, Na^+ doping is found to have intriguing effect on thermal and magnetic properties of magnetite nanoparticles[100]. It was observed that the thermal stability of γ-Fe_2O_3 increases from 450 to 600 ºC when NH_4OH was replaced by NaOH as precipitating agent in co-precipitation process. The results show that the activation energy of the magnetite nanoparticles increased due to diffusion of Na^+ ions into the magnetite. A study on $Ni_{0.4-x}Zn_{0.6}Cu_xFe_2O_4$ (x = 0–0.20) confirms that Na^+ ions can affect the crystalline structures and magnetic properties of ferrites[136].

Stability of nanofluids depends on various parameters such as pH, particle size, stabilizing agent, interactions etc. In ionic magnetic nanofluids, the particles are suspended at low pH (2 to 3) or high pH (12 to 13) where electrostatic repulsion is effective[35] but in case of hydrocarbon based magnetic nanofluids, steric repulsion is the dominant mechanism of stabilization[154]. In ionic fluids, the surface polyoxy –hydroxy native molecular layer plays a key role in positively charging the suspended nanoparticles at low pH values[155]. At high pH values, the particles are negatively charged. In the past, several efforts have been made to produce stable magnetic nanofluids[156-158]. Muthukumaran et al. prepared stable magnetic nanofluid with different particle sizes using co-precipitation method by dynamic coating during precipitation[159]. It was shown that the size and magnetization of nanoparticles increase with the incubation temperature due to supersaturation at elevated temperatures. Jain et al. prepared stable water based ferrofluid of very high concentration (>65 wt%) at high ionic strength[160]. Highly crystalline and monodisperse maghemite nanoparticles were synthesized by thermal decomposition of metal-oleate complex in presence of oleic acid[156,161] and transferred to an aqueous medium using phase transfer reagents[162]. Wooding et al. produced stable nanofluids by using saturated and unsaturated fatty acids as primary and secondary surfactants[157]. Aqueous magnetic nanofluids synthesized using high molecular weight polymers as stabilizing agent are studied for their long term stability, pH or electrolyte tolerance[158, 163, 164]. Suspensions of sterically stabilized magnetite nanoparticles using lower molecular weight steric stabilizers were found to be more stable when the coating thickness is less[160].

In an effort to produce magnetic nanoparticles with high temperature stability and stable nanofluids without surfactants, magnetite nanoparticles with different amount of sodium doping (0-500 ppm) have been prepared. The samples are annealed in air and vacuum and their phase stability is studied.

5.2 Synthesis of Na^+ doped Fe_3O_4 nanoparticles

Na doped Fe_3O_4 nanoparticles are prepared using a two step method. Fe_3O_4 nanoparticles are first prepared using co-precipitation method and then soaked in NaOH solution to prepare the desired Na doped magnetite nanoparticles. The details of the procedure are discussed in chapter II, Section 2.2.1.2.

5.3 Result and Discussion

5.3.1 Room temperature XRD studies

Fig 5.1 shows the room temperature XRD patterns of Fe_3O_4 nanoparticles doped with different concentrations of Na^+ ions. The diffraction peaks from the (220), (311), (400), (511), (440) crystal planes. Comparison of peaks with the standard Fe_3O_4 peaks (JCPDS card no-880315) confirm the spinel ferrite structure of Fe_3O_4. The size and lattice parameters obtained from the analysis are summarized in Table 5.1.

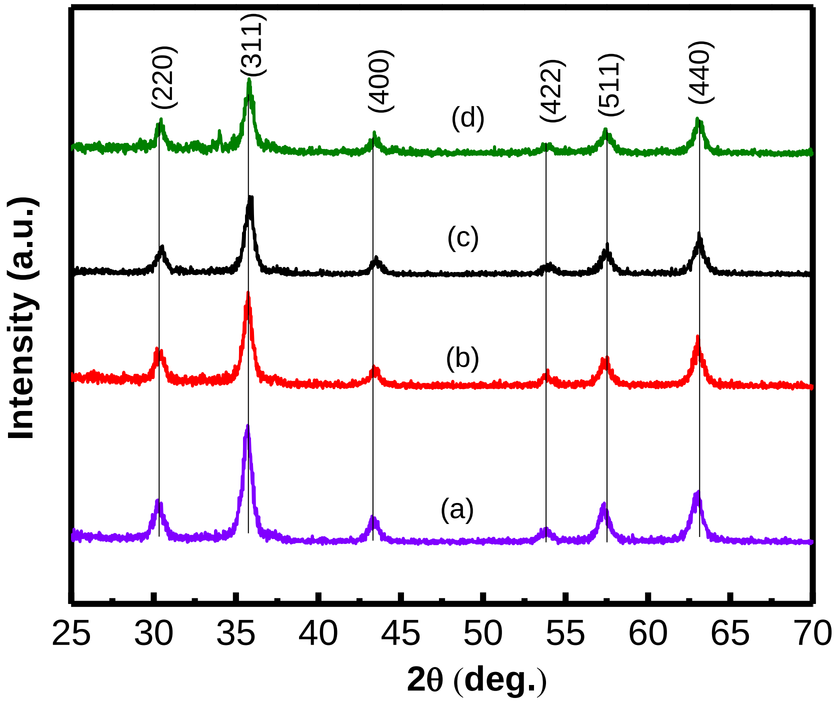

Fig 5.1: The room temperature XRD pattern of Fe_3O_4 nanoparticles with Na^+ concentrations (a) 0 (b) 350 (c) 391 and (d) 500 ppm.

No significant variation in the crystallite size and lattice parameters was observed after the doping of nanoparticles with Na^+ ions. The size varied within the range 12±1 to 13±1 nm whereas the lattice parameter varied between 8.30-8.33 Å.

Fig. 5.2(a) and (b) shows the TEM images of sample A and sample D, respectively. The average size obtained from TEM image analysis are 13(±1) and 12 (±1) nm for sample A and D, respectively. The slight reduction in the average particle size in Na doped samples is due to the fact that the polydispersity of pure Fe_3O_4 particle is slightly reduced down due to the repeated washing and centrifugation after the Na doping. Fig. 5.2(c) and (d) show the particle size distribution of sample A and D nanoparticles obtained from SAXS measurements. The inset of Fig. 5.2(c) and (d) shows the scattered intensity (I(q)) as a function of wave vector (q). Results show that the particles are spherical in shape and fairly monodisperse. The most probable particle sizes are found to be 11.88(±0.6) and 9.52(±0.5) nm for sample A and sample D, respectively from the SAXS measurements. The observed sizes are fairly consistent with sizes obtained from XRD and TEM.

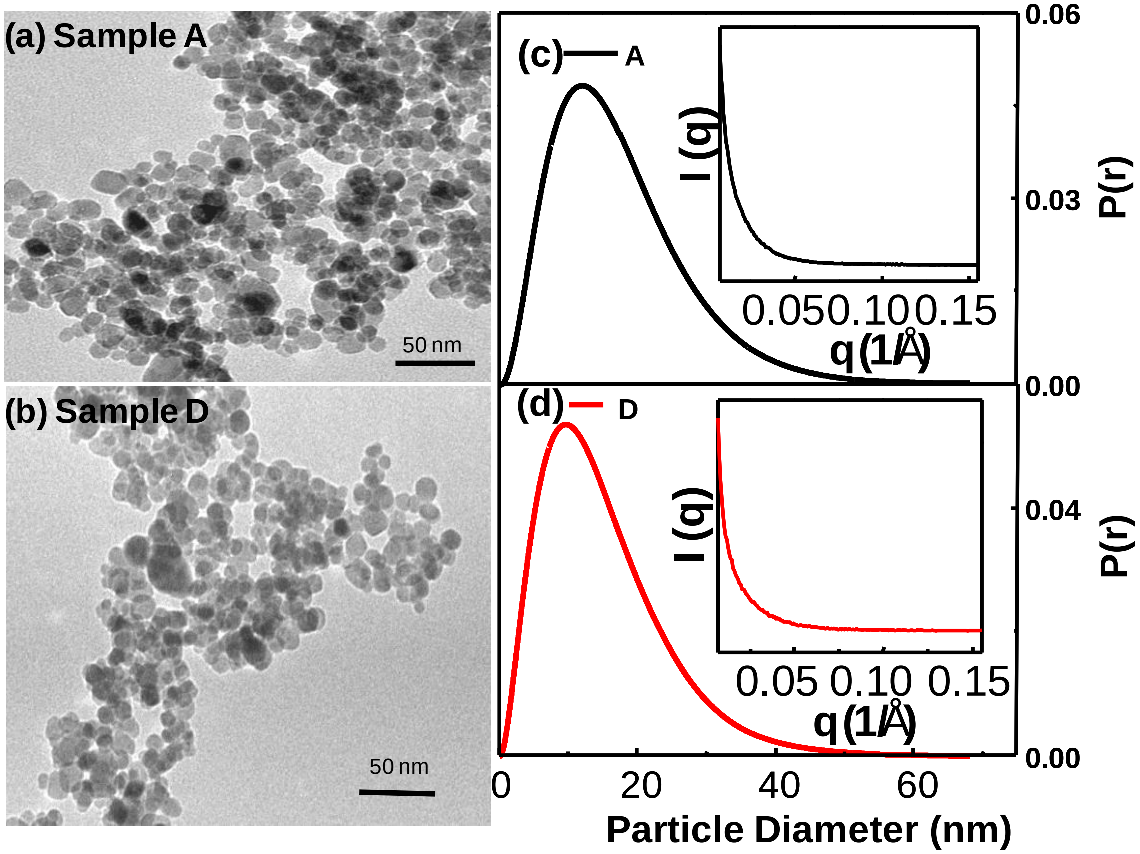

Fig 5.2: TEM image of (a) sample A and (b) sample D nanoparticles. Size distribution obtained from SAXS for (c) sample A and (d) sample D respectively. The inset of (c) and (d) shows the I(q) vs.q for the sample A and (b) sample D, respectively.

Table 5.1: The crystallite size, lattice parameter and saturation magnetization (M_s) of Na^+ doped magnetite nanoparticles before annealing.

Sample	Na^+ Conc. (ppm)	Crystallite size from XRD (nm)	Lattice Parameter (Å)	M_s (emu/g)
A	0	12.9±1	8.33	65
B	350	13.0±1	8.33	59
C	391	12.5±1	8.30	57
D	500	12.0±1	8.31	48

Fig 5.3 shows the FTIR spectra of sample A, B and D. For all the three samples, the signature peaks of Fe-O stretching in the range 450 to 650 cm^{-1} are observed. The peaks in the range of 470 to 490 cm^{-1} is due to the Fe-O stretching in the octahedral site of Fe_3O_4 nanoparticles while the peaks in the range of 550-650 cm^{-1} correspond to Fe-O stretching generated from the tetrahedral site of Fe_3O_4 nanoparticles[165].

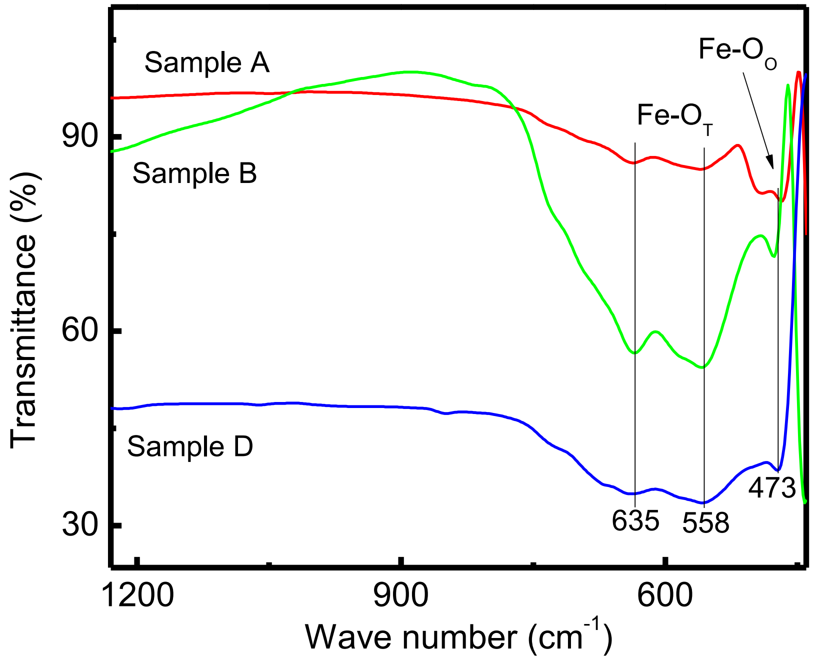

Fig 5.3: The FTIR spectra of Fe_3O_4 nanoparticles with Na^+ concentration of sample A, sample B and sample D.

Fig 5.4 shows XRD pattern of nanoparticles (sample A-D) after air annealing at 600 ºC. For sample A, pure α-Fe_2O_3 phase is evident from the peaks from (104), (110), (113), (024), (116), (214), (300) crystal planes. The peak intensity ratio of (104) to (110) is found to be 100:70, which indicates a complete phase conversion of γ-Fe_2O_3 to α-Fe_2O_3 phase. This observation is consistent with the literature reports on air annealing of ammonia based magnetite nanoparticles[100]. The peak intensity ratio of (104) to (110) is found to be 100:85 for sample B, which indicates that a small amount of γ-Fe_2O_3 phase exists along with α-Fe_2O_3.

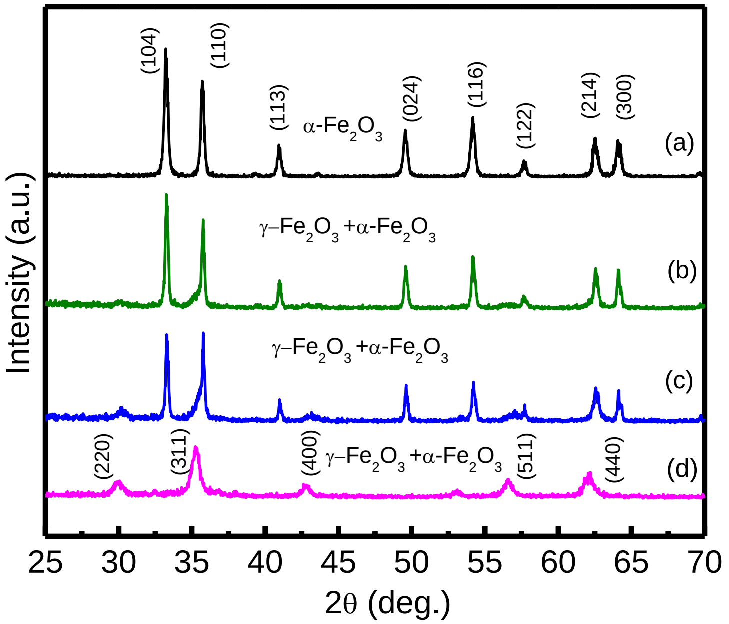

Fig 5.4: Room temperature XRD of air annealed Fe_3O_4 nanoparticles at 600 ºC with Na^+ concentrations of (a) 0 (b) 350 (c) 391 and (d) 500 ppm.

This is evident from the broadening of the (110) peak, due to the contribution from (311) peak of maghemite. For sample C, the intensity of (104) crystal plane is found to be less than that of (110) along with presence of (220), (400), (511) peaks of γ-Fe_2O_3. This indicates that the percentage of maghemite (γ-Fe_2O_3) present in sample C is more than that of sample B.

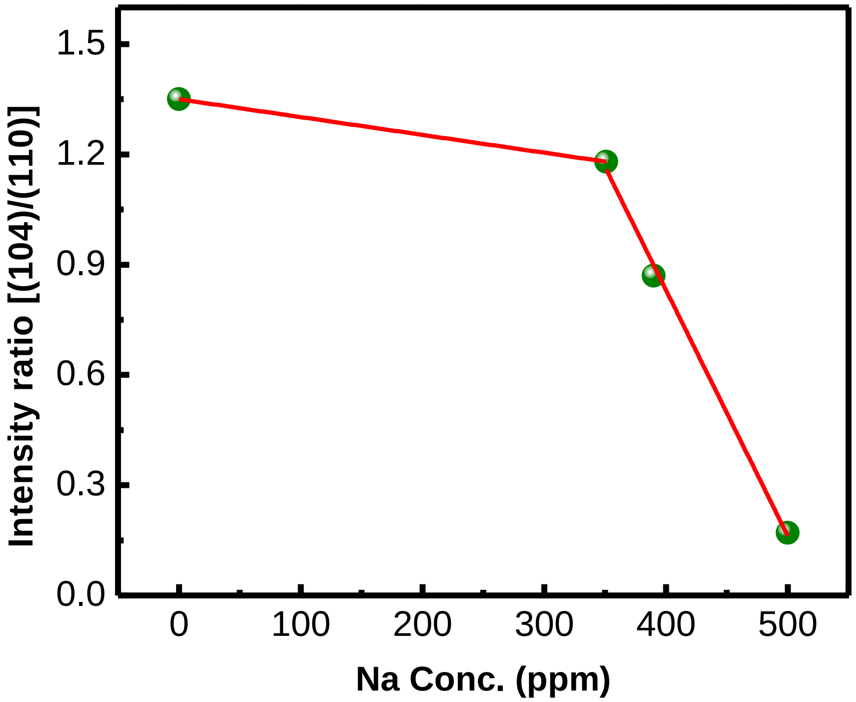

Fig 5.5: The variation in (104) to (110) peak intensity ratio of hematite phase as a function of Na concentration after air annealing at 600 ºC.

The intensity ratio is found to be 87:100 for sample C. For sample D, γ-Fe_2O_3 is found to be a major phase with the peaks originating from the crystal planes of (220), (311), (400), (511) and (440). A very low intensity (104) peak is observed because of the evolution of α-Fe_2O_3 phase. The intensity ratio is found to be 17:100 which shows the dominance of γ-Fe_2O_3 phase over the α-Fe_2O_3 phase. Fig 5.5 shows the variation of intensity ratio [(104) to (110)] as a function of sodium concentration.

Fig. 5.6 (a, b and c) shows the Rietveld fitting on XRD data for sample A, C and D after air annealing at 600 ºC. Fig 5.6a shows that after annealing at 600 ºC, ~ 99% of the nanoparticles are present in α-Fe_2O_3 form, which is consistent with the results obtained from the intensity ratio calculations. Fig 5.6b shows the Rietveld analysis of sample C after air annealing at 600 ºC. The data fits well for 36% of maghemite and 64% of hematite phases (red line represents γ-Fe_2O_3 and green line represents α-Fe_2O_3).

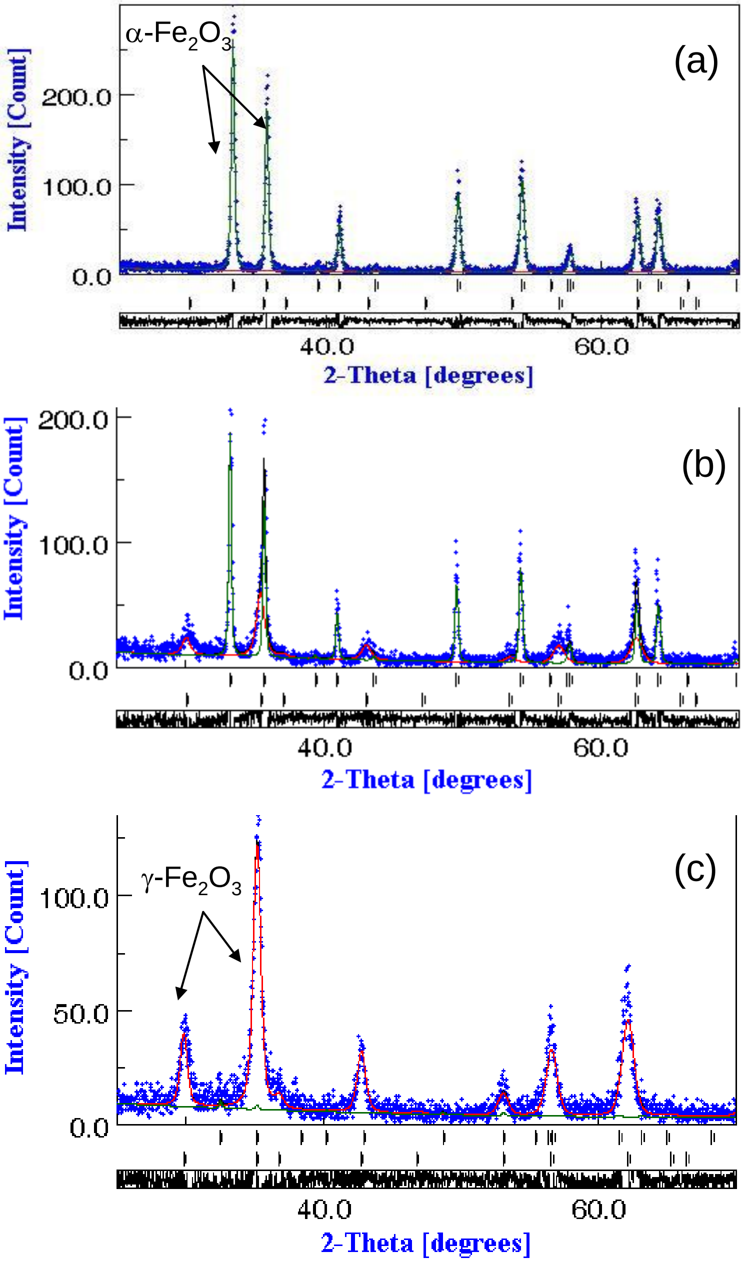

Fig 5.6: Rietveld analysis of air annealed Na^+ doped Fe_3O_4 nanoparticles at 600 ºC with Na^+ concentration of (a) 0 (b) 391 and (c) 500 ppm.

Table 5.2: Quantitative phase analysis results of annealed pure Fe_3O_4 nanoparticles using Rietveld method. The percentage of different phases present at different annealing temperatures and the lattice parameter values are tabulated.

Annealing Temp. (ºC)	Calculated Wt% of phases after annealing in air		Lattice parameters (Å)
	γ-Fe_2O_3	α-Fe_2O_3	
30	100	0	8.338±0.009
350	100	0	8.343±0.0013
450	81±1	19±1	8.343±0.0010 5.029±0.0013 13.74±0.0053
500	1±0.5	99±1	5.033±0.002 13.737±0.009
1000	0	100	5.038±0.002 13.739±0.009

The samples A and D are air annealed at different temperatures (30 to 1000 ºC) to study the effect of sodium doping on high temperature phase stability. The sample A is air annealed at 350, 450, 500, 600 and 1000 ºC and the corresponding XRD patterns are shown in Fig 3.4 (*Chapter III*). Table 5.2 shows the percentage of different phases present at different annealing temperatures and the lattice parameter values obtained in sample A using Rietveld refinement [166].

The maghemite phase is found to be stable till 350 ºC. The formation of hematite phase starts at 450 ºC which is consistent with literature data[100]. Complete conversion from maghemite to hematite takes place above 500 ºC, which remains intact upto 1000 ºC. Fig. 5.7 shows XRD pattern of sample D at various air annealing temperatures. Table 5.3 shows the percentage of different phases present at different annealing temperatures and the lattice parameter values obtained in sample D using Rietveld refinement. After annealing at 550 ºC the peaks become sharper and intense as particles undergo coalescence to lower the surface free energy[167].

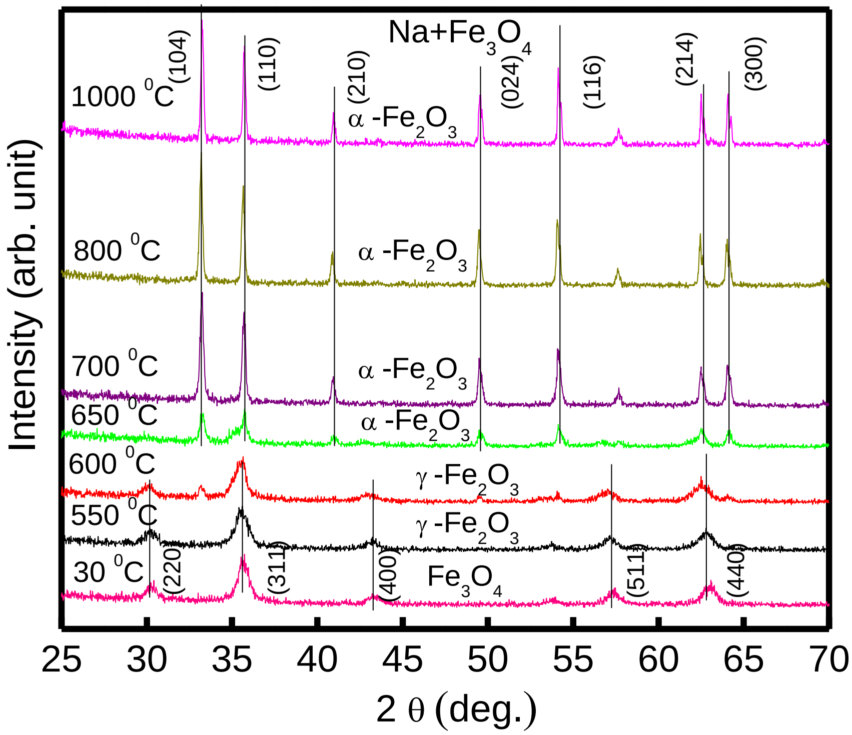

Fig 5.7: Room temperature XRD of 500 ppm sodium doped nanoparticles annealed at 550, 600, 650, 700, 800 and 1000 ºC in air.

At 600 ºC, emergence of (104) peak along with the prominent peaks of maghemite confirms the partial formation of hematite. The variation of crystallite size of A and D nanoparticles annealed at different temperatures, obtained from the diffraction peaks using Debye Scherrer equation, are plotted as a function of temperature in Fig 5.8.

For sample A, the crystallite size increases from 12.3 to 17 nm as the annealing temperature is increased from 30 to 450 ºC. But on further increase in annealing temperature, the particle size increases dramatically. The average particle sizes are 38, 43 and 67 nm for annealing temperatures of 500, 600 and 1000 °C, respectively. These results show that the growth of α-Fe_2O_3 is much faster than γ-Fe_2O_3[102]. The γ-Fe_2O_3 is a metastable phase with oxygen atoms arranged in a face centered cubic structure while the former (α-Fe_2O_3) is a stable phase with a hexagonal close-packed structure (Fig 1.9, Chapter I). For sample D, the crystallite size increases from 11.6 to 19 nm when the temperature is increased from 30 to 650 °C.

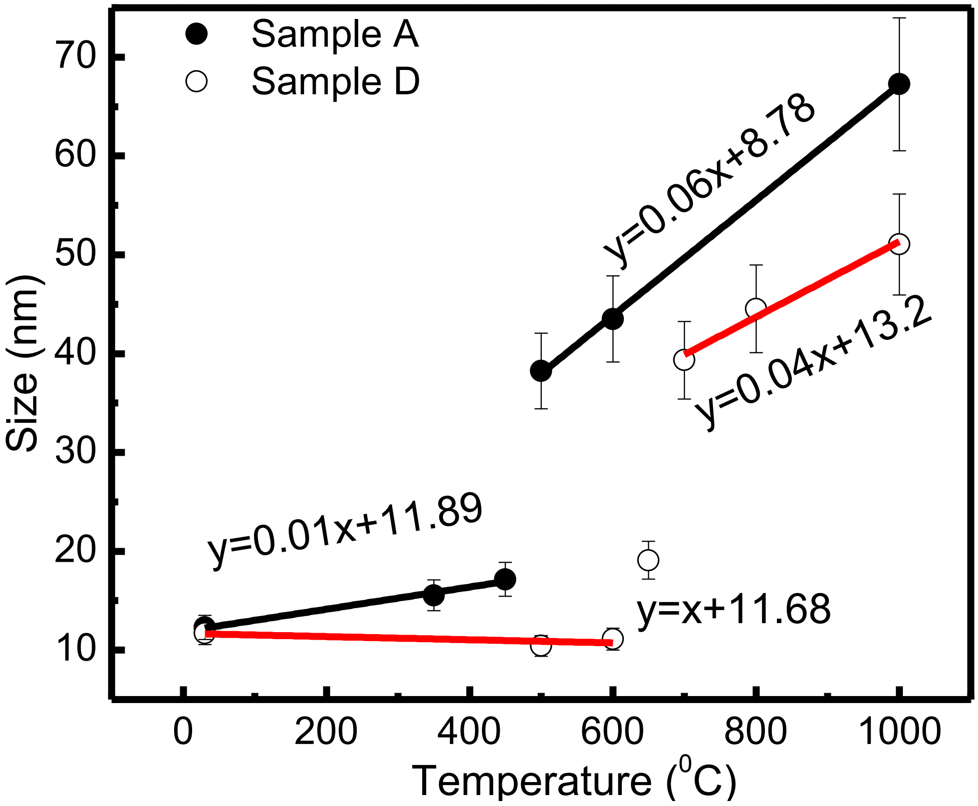

Fig 5.8: Size variation of sample A and D nanoparticles annealed in air with temperature.

But on increasing the annealing temperature from 650 to 700 °C particle size increases sharply from 19 to 40 nm that justifies the fact that the freshly formed α-Fe_2O_3 phase grows rapidly in this temperature range. Further, increase in the annealing temperature upto 1000 °C leads to an increase in size from 40 to 51 nm.

Table 5.3: Quantitative phase analysis results of annealed Na doped (500 ppm) Fe_3O_4 nanoparticles using Rietveld method. The percentage of different phases present at different annealing temperatures and the lattice parameter values are tabulated.

Annealing Temp. (ºC)	Calculated wt.% of phases after annealing in air.		Lattice parameters (Å)
	γ-Fe_2O_3	α-Fe_2O_3	
30	100	0	8.34±0.001
550	100	0	8.36±0.001
600	84±1	16±1	8.39±0.001 5.03±0.001 13.74±0.006
650	30±1	70±1	8.44±0.003 5.025±0.006 13.713±0.003
700	0	100	5.029±0.002 13.721±0.001
800	0	100	5.0336±0.002 13.726±0.009
1000	0	100	5.028±0.002 13.731±0.001

5.3.2 Differential Scanning Calorimetric studies

Fig 5.9 (a, b, c and d) represents the heat flow curves of samples A, B, C and D in the temperature range of 30-1000 ºC. Though the phase transition temperatures of DSC experiments cannot be compared directly with the phase transition temperatures obtained from XRD, it gives an idea of the phase transition temperature trend and the enthalpy change during the phase transition. The main reason for the difference between phase transition temperatures obtained from DSC and XRD is that in the former, the temperature scan is done at a faster rate (10º C/min.). On the contrary, air annealing is done for a period of 2 hrs. Fig 5.9a shows the heat flow curve for sample A. An endothermic peak observed in the temperature range of 30 to 200 ºC, can be attributed to the removal of moisture content from the sample. The distinct exothermic peak observed at 574 ºC indicates the phase transition of maghemite (γ-Fe_2O_3) to hematite (α-Fe_2O_3).

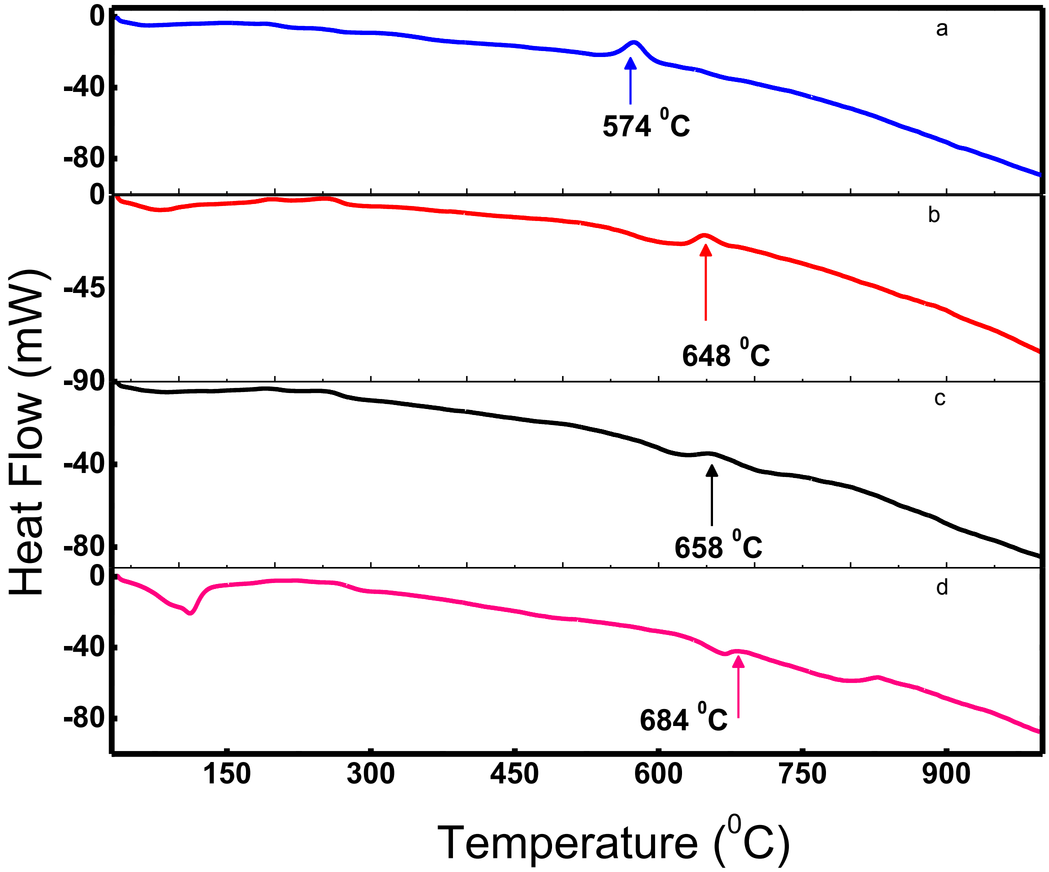

Fig 5.9: Heat flow curves as a function of temperature (30 -1000 ºC) for Na^+ concentrations of (a) 0 (b) 350 (c) 391 and (d) 500 ppm.

Fig 5.9b shows the heat flow curve of sample B where the phase transition temperature increases from 574 to 648 ºC. However, the peak becomes broader and less intense than that for sample A. Fig 5.9c shows the heat flow curve of sample C. It was observed that the phase transition temperature further increase to 658 ºC and the peak becomes broader. The heat flow curve for sample D (Fig 5.9d) shows that the phase transition temperature increases to 684 ºC and the peak become less prominent. These results clearly demonstrate that the maghemite (γ-Fe_2O_3) to hematite (α-Fe_2O_3) phase transition temperature increases with increase in Na^+ concentration.

Fig 5.10 shows the variation of maghemite (γ-Fe_2O_3) to hematite (α-Fe_2O_3) phase transition temperature with Na^+ concentration (x). It is observed that the phase transition temperature linearly increases with Na^+ concentration according to the equation $T = 573.5 + 0.22x$ with a slope of 0.22. The area under the DSC peak gives the change in enthalpy (ΔH) during that particular physical process (phase transition).

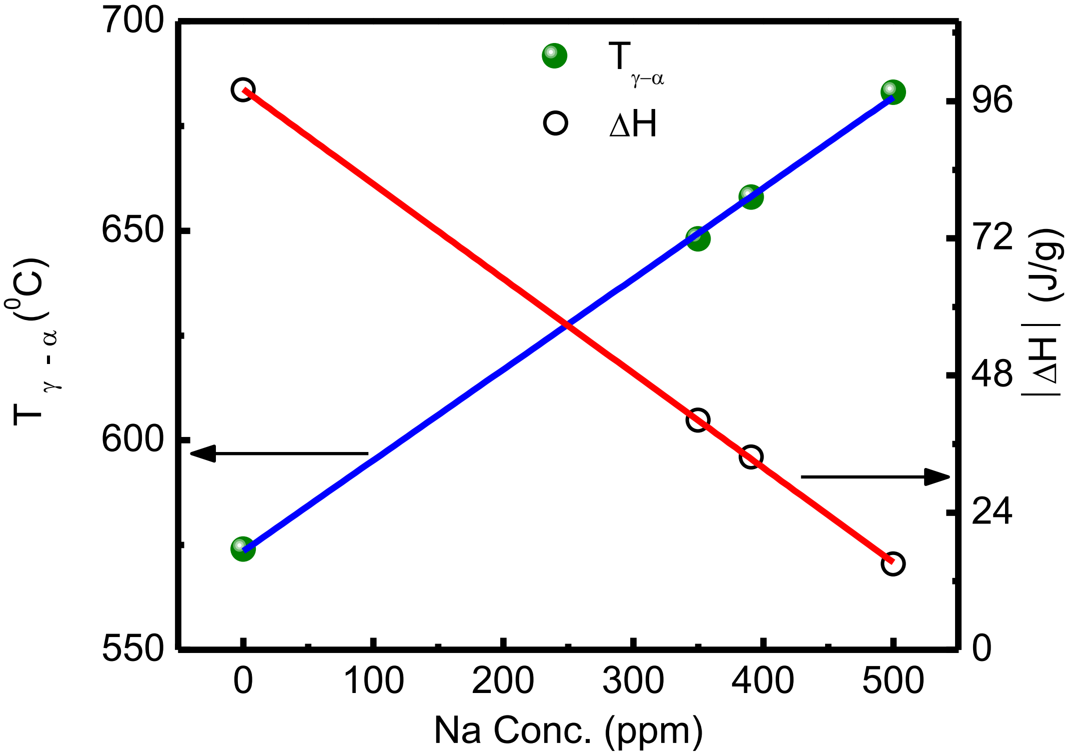

Fig 5.10: The γ-Fe_2O_3 to α phase transition temperature ($T_{\gamma-\alpha}$) and enthalpy change (ΔH) during phase transition as a function of temperature from DSC.

The ΔH values for samples A, B, C and D are found to be 98, 64, 34 and 15 J/g, respectively. The value obtained for Fe_3O_4 (sample A) is consistent with earlier reports. Fig 5.10 (secondary

Y-axis) shows the ΔH variation as a function of Na^+ concentration. The experimental data points are fitted with linear equation; $\Delta H = 98.1 - 0.17x$. The enthalpy change is related to activation energy of the phase transition process. A higher negative enthalpy value indicates a less activation energy for the phase transition. Hence, these results suggest that the activation energy for the phase transition from maghemite (γ-Fe_2O_3) to hematite (α-Fe_2O_3) increases with increase in Na^+ ion concentration. It is speculated that the Na^+ ions get trapped in the magnetite crystal. This is consistent with the earlier reports on magnetite nanoparticles synthesized using NaOH as alkali showed enhanced temperature stability because of the trapped Na^+ ions[100].

5.3.3 High temperature XRD studies under vacuum

The HTXRD pattern of sample A annealed under vacuum is shown in Fig. 3.8 (*Chapter III*). Above 700 ºC, the formation of FeO phase along with γ-Fe_2O_3 phase is evident from the characteristics peak from the crystal plane (200) [112]. The particle size for the as synthesized Fe_3O_4 nanoparticles increases from 12.1 to 16.5 nm as the annealing temperature increases from RT to 600 ºC, above which the size increases drastically from 16.5 to 42.5 nm as the temperature is increased to 1000 ºC. The variation in the lattice parameter in the above temperature range was 8.64-8.7 Å. The increase in lattice parameter at elevated temperatures is due to volume expansion of the particles at high temperatures [112, 168]. Size of FeO also increases significantly from 20 to 34 nm with a constant lattice parameter of 4.31 Å.

Fig. 5.11 shows the HTXRD pattern of sample D nanoparticles at different annealing temperature under vacuum. In contrast to pure Fe_3O_4 nanoparticles, no decomposition of the sample is observed till 1000 ºC. The star symbol shows the characteristic peaks of tantalum sample holder. The solid lines represent the characteristic peaks of magnetite.

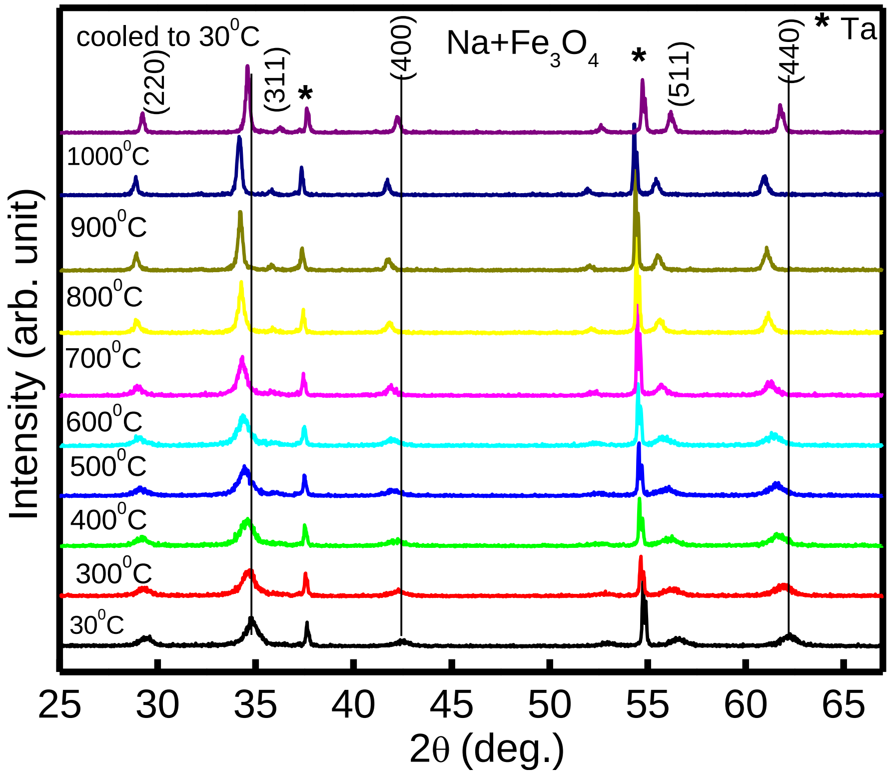

Fig 5.11: In situ high temperature XRD pattern of 500 ppm Na doped Fe_3O_4 nanoparticles annealed at different temperatures under vacuum.

Size and lattice parameter of particles are plotted as a function of temperature in Fig. 5.12. The average particle size is found to increase from 11.3 to 31.4 nm as the temperature in increased from 30 to 1000 ºC. In the above temperature range, the lattice parameter increases from 8.54 to 8.7 Å. The best fit on the experimental data points are shown by the solid lines.

The atomic emission spectroscopy studies show that 500 ppm of sodium is present in the samples after washing. The enhancement in phase transition temperature in sample D is attributed to the diffusion of sodium ions in the cubic lattice that should increase the total activation energy of the system for the transition from γ-Fe_2O_3 to α-Fe_2O_3 [100]. Such diffusion of ions into the crystal lattice at moderate temperature was reported earlier [169]. The diffused ions are accommodated in the vacancy sites present in the magnetite nanocrystal[170]. The ionic radii of Na^+, Fe^{3+}, Fe^{2+} and O^{2-} ions are 1.02, 0.645, 0.78 and 1.40 Å, respectively [171]. So the Na^+ ions can diffuse through the O^{2-} vacancy sites and can be trapped inside the crystal. The above results demonstrate that the thermal stability of iron oxide nanoparticles can be increased with doping of sodium ions. The activation energy is calculated for γ-Fe_2O_3 to α-Fe_2O_3 phase transition from the Schott equation[118].

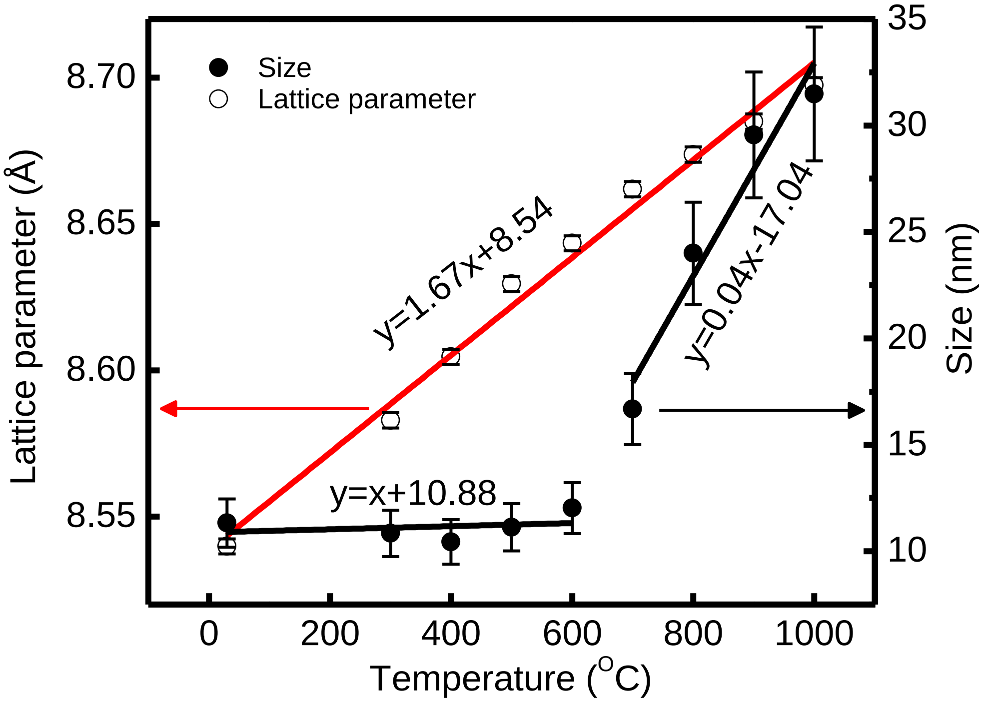

Fig 5.12: Size and lattice parameter variation of sample D nanoparticles annealed under vacuum with temperature. The best fits on the data are shown by the solid lines.

Fig. 5.13 shows ln(d) vs. 1/T for sample A and D. Both the data show a linear fit where the intercept and slope corresponds to lnA and E_a/R, respectively. The activation energy is obtained from the slope and is found to be 9.39 and 13.11 kJ/mole for sample A and D, respectively. The reported activation energy for pure zinc ferrite nanoparticles is 140 kJ/mole and for nickel ferrite nanoparticles is 16.6 kJ/mole [118, 172]. These results corroborate the fact that the presence of Na^+ enhances the activation energy for phase transition. Earlier studies show the existence of a strong oxide-oxide interactions between iron oxide and silica which was evident from the suppression of the transformation of γ-Fe_2O_3 to α-Fe_2O_3 under oxygen annealing, where Si^{4+} diffuses into the cubic lattice and has a preferential co-ordination with tetrahedral sites[107].

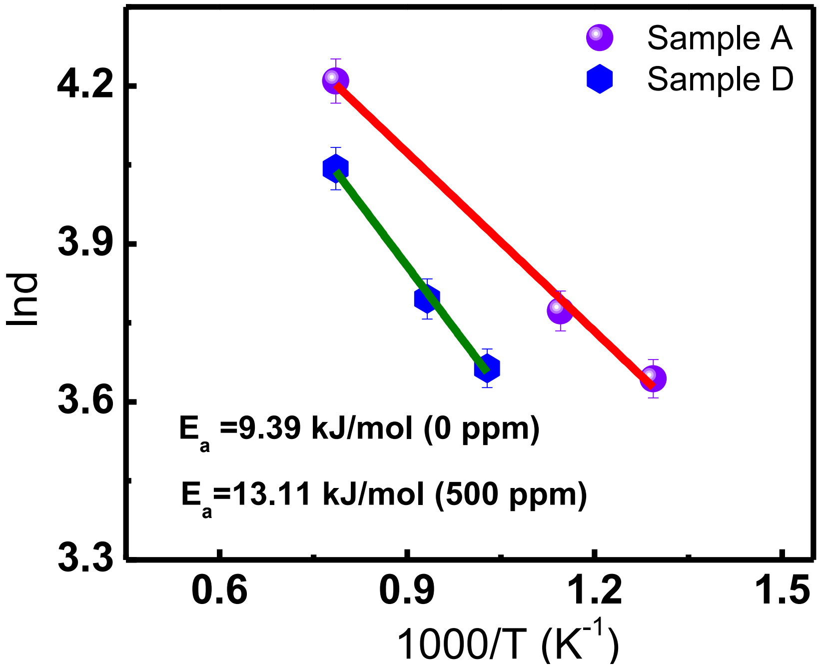

Fig 5.13: Plot of ln(d) vs 1/T and its linear fit using the Schott equation. The activation energy is calculated from the slope.

In magnetite nanocrystals electron hopping takes place where all of the octahedral Fe^{2+} and Fe^{3+} cations undergo rapid exchange of an electron. The substitution of cations in the tetrahedral sites near the surface should eventually displace the Fe^{3+} cations into neighbouring octahedral sites. The displaced Fe^{3+} is expected to be transferred to adjacent octahedral sites and continue to engage in electron hopping process.

The intriguing aspect here is that the diffusion of Na^+ into the lattice of nanocrystals occurs when the sample is simply soaked with NaOH. However, earlier studies show that a room temperature reaction of Na with spinel, λ-MnO_2 induces an irreversible phase transformation to Na_xMnO_2 [173]. Another study suggests that ultrasonication of amorphous magnetite nanoparticles with $Mn_2(CO)_{10}$ can lead to amorphous mixed oxide of Fe(III) and Mn(III) [134]. Further, using computer simulation, it has been shown that heterogeneous nucleation on an impurity is not only microscopic but also is more than four orders of magnitude faster than homogeneous nucleation [174]. Therefore, the observed diffusion of Na^+ to cubic lattice is not really surprising.

5.3.4 Magnetic properties

Fig 5.14 shows the room temperature M-H loops of samples A, B, C and D. The saturation magnetization (M_s) for sample A was found to be 65 emu/g, which is much less than the M_s value (92 emu/g) of bulk magnetite[135]. In general, magnetic properties of nanostructured materials are less in comparison to bulk materials due to the lack of structural periodicity that leads to the formation of non-collinear spin configuration or spin canting at the surface of the particles. This reduction in the magnetization with particle size is associated with the existence of surface disorder shell thickness (g). The disorder shell thickness (g) is related to M_s by the relation[175] $M_s = M_{bulk}\left(1 - \frac{6g}{d}\right)$ where, M_{bulk} is the bulk magnetization value of Fe_3O_4, ‘*g*’ is the disorder shell thickness and ‘*d*’ is the average particle size. Therefore, the magnetic properties of the particles are attributed to the collective magnetostatic interaction between them. The reduced M_s value in both the cases can be attributed to the dead layer present on the surface[176]. The M_s values for samples B, C and D are found to be 59, 57, and 48 emu/g respectively. The decrease in M_s value can be attributed to the increase in nonmagnetic Na^+ concentration in magnetite.

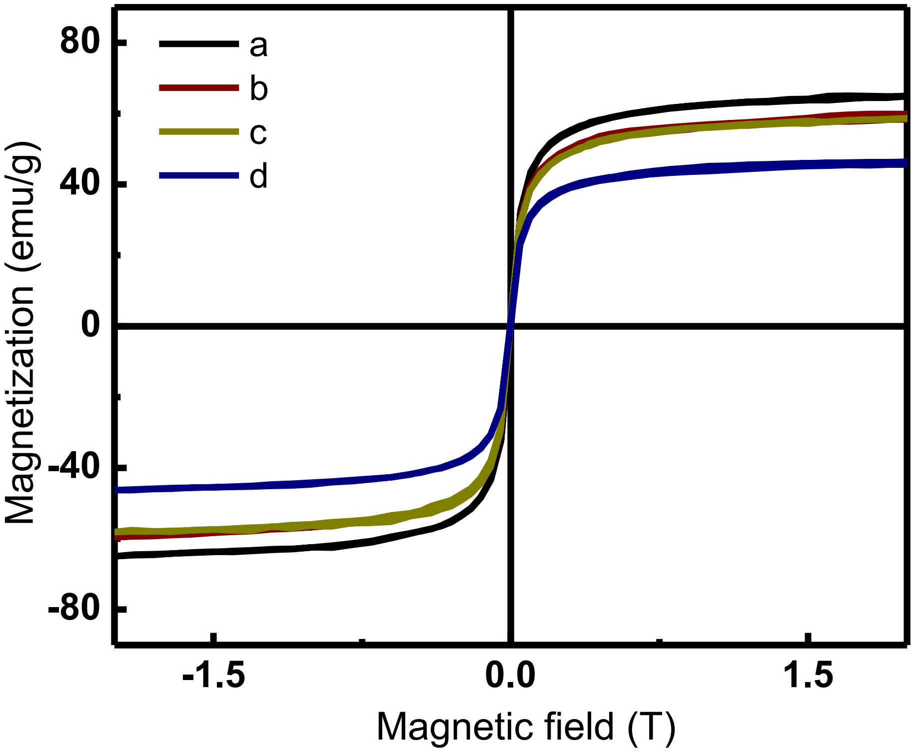

Fig 5.14: Room temperature M-H curves of Fe_3O_4 nanoparticles with Na^+ concentrations of (a) 0 (b) 350 (c) 391 and (d) 500 ppm.

Fig 5.15 shows the room temperature M-H curves for samples A, B, C and D after air annealing at 600 °C. The saturation magnetization for sample A is found to be 1 emu/g after annealing. This indicates the complete phase transition of maghemite to hematite after annealing at 600 °C as observed from Rietveld analysis. Sample B shows an M_s value of 11 emu/g after annealing. The higher M_s value of sample B is due to the presence 4% of maghemite in the sample. The M_s value for sample C is found to be 23 emu/g while that of sample D is 46 emu/g. This shows that the magnetic properties of iron oxide nanoparticles can be retained even after annealing at 600 °C in air by a small percentage of Na^+ doping. Therefore, the phase transition temperature as well as the magnetic properties can be improved with Na^+ doping, without compromising the M_S values.

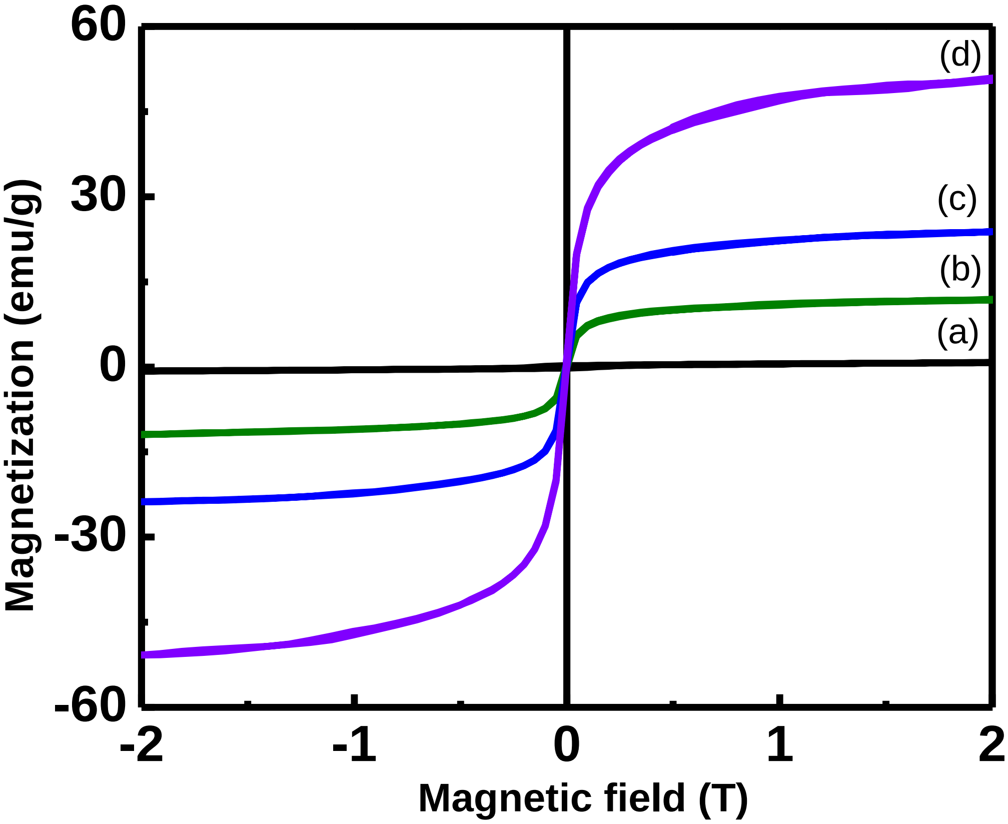

Fig 5.15: Room temperature M-H curves of air annealed Fe_3O_4 nanoparticles at 600 ºC with Na^+ concentrations of (a) 0 (b) 350 (c) 391 and (d) 500 ppm.

Fig 5.16 shows the variation of M_s as a function of Na^+ concentration before and after annealing at 600 ºC in air. It is observed that prior to annealing, the M_s value decreases from 65 to 48 emu/g as the doping concentration is increased from 0 to 500 ppm. After annealing, the M_s value of sample D is almost retained (46 emu/g) where as it is reduced to 1 emu/g for sample A.

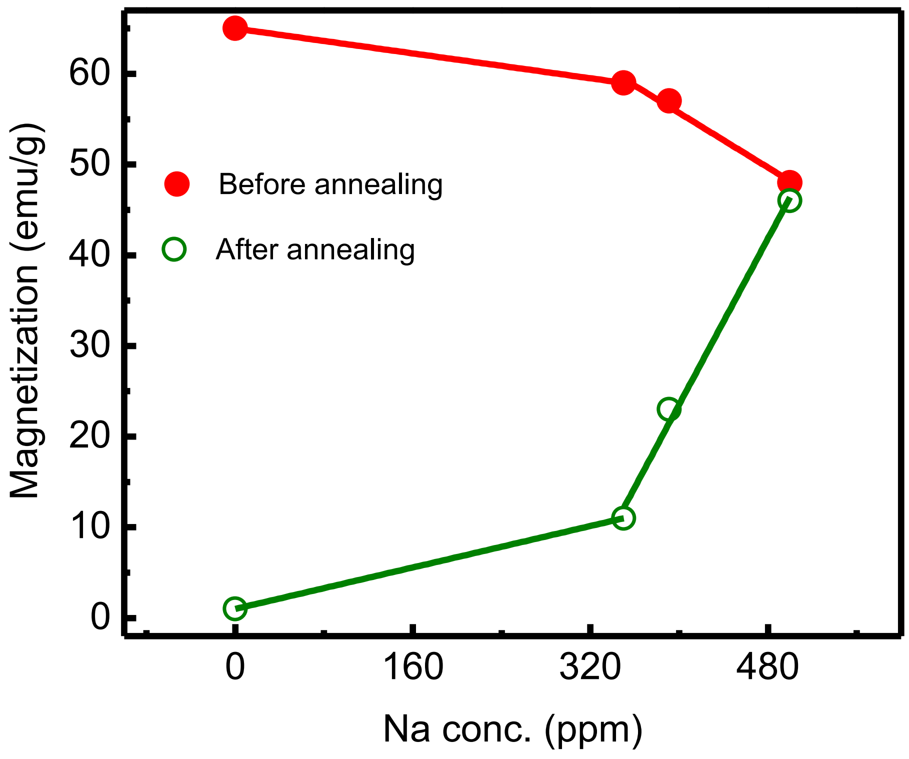

Fig 5.16: The variation of M_s as a function of Na concentration before and after air annealing at 600 ºC.

Fig. 5.17 shows the room temperature M-H curves of sample A and D after air annealing at different temperature. The M_s of as synthesized sample A particles is reduced to 50 emu.g^{-1} after air annealing at 450 ºC because of partial conversion of maghemite to alpha phase, with the former as the majority phase. At 500 ºC annealing, the M_s decreases drastically to 14.5 emu.g^{-1} due to the conversion of large amount of magnetic phase to hematite. For sample D, the as synthesized particles show M_s of 46 emu.g^{-1} after annealing at 600 ºC due to the formation of mixed ferrite of γ-Fe_2O_3 and α-Fe_2O_3. On further annealing at 650 ºC the M_s is reduced to 14 emu.g^{-1}.

Fig. 5.18 shows the zero field cooled and field cooled curves of sample A and D nanoparticles in the temperature range of 5 to 300K. The magnetization value of sample D is found to be little less than sample A due to a decrease in the particle size distribution after washing. The blocking temperatures of samples A and D are found to be 263 and 258K, respectively.

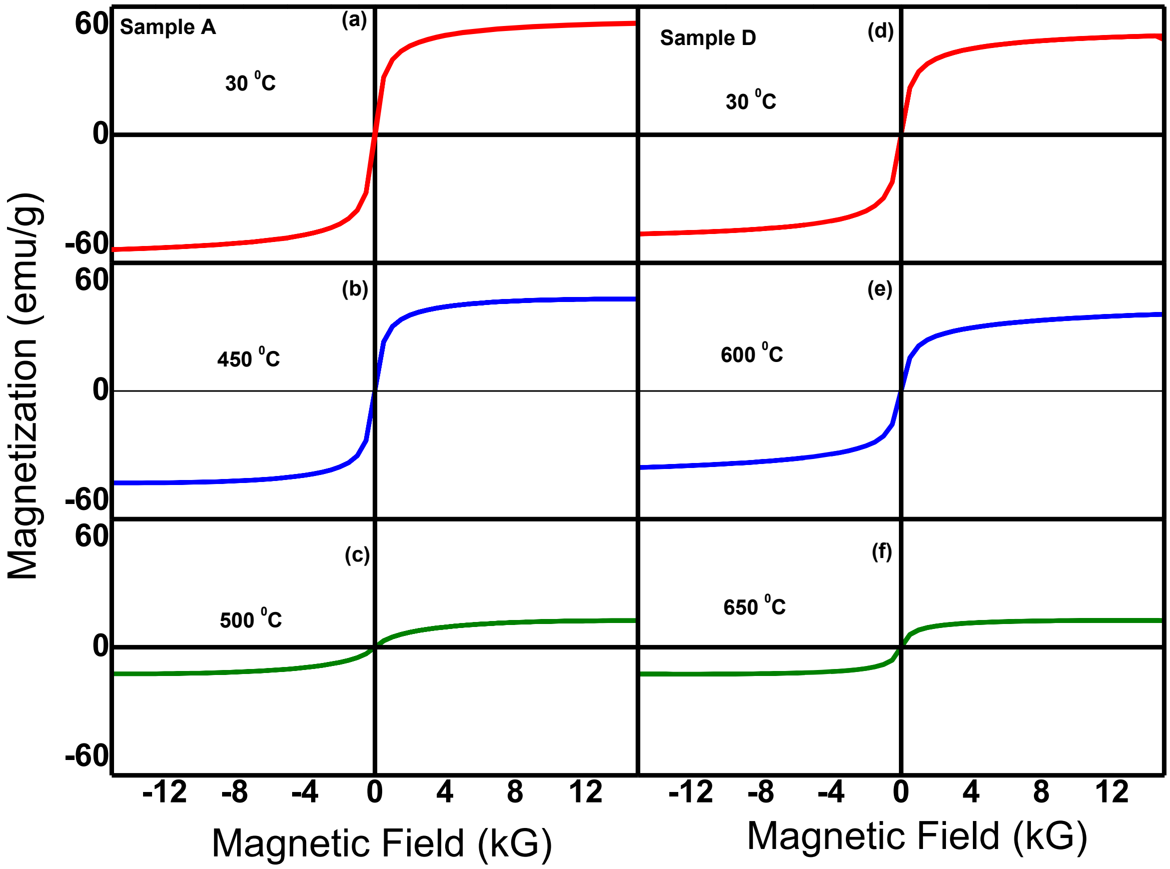

Fig 5.17: Room temperature M-H curves of Fe_3O_4 nanoparticles air annealed at (a) 30 ºC (b) 450 ºC (c) 500 ºC and 500 ppm Na doped Fe_3O_4 nanoparticles air annealed at (d) 30 ºC (e) 600 ºC (f) 650 ºC.

On cooling below $T_{B,}$ the magnetic moments are frozen and the system exhibits memory effect and magnetic hysteresis. The anisotropy energy constant K (calculated using the equation T_B=KV/25K_B where V is the volume of nanoparticles, k_B is the Boltzmann constant and T_B is the blocking temperature) is found to be $9.1x10^5$ and $11x10^5$ erg/cm^3 for sample A and D nanoparticles, respectively. These values are comparable to the reported anisotropy energy of Fe_3O_4 nanoparticles of size 13 nm (6 x10^5 erg/cm^3) and 8 nm (13 x10^5 erg/cm^3)[152]. These results confirm that a small amount of sodium impurity does not alter the memory effect.

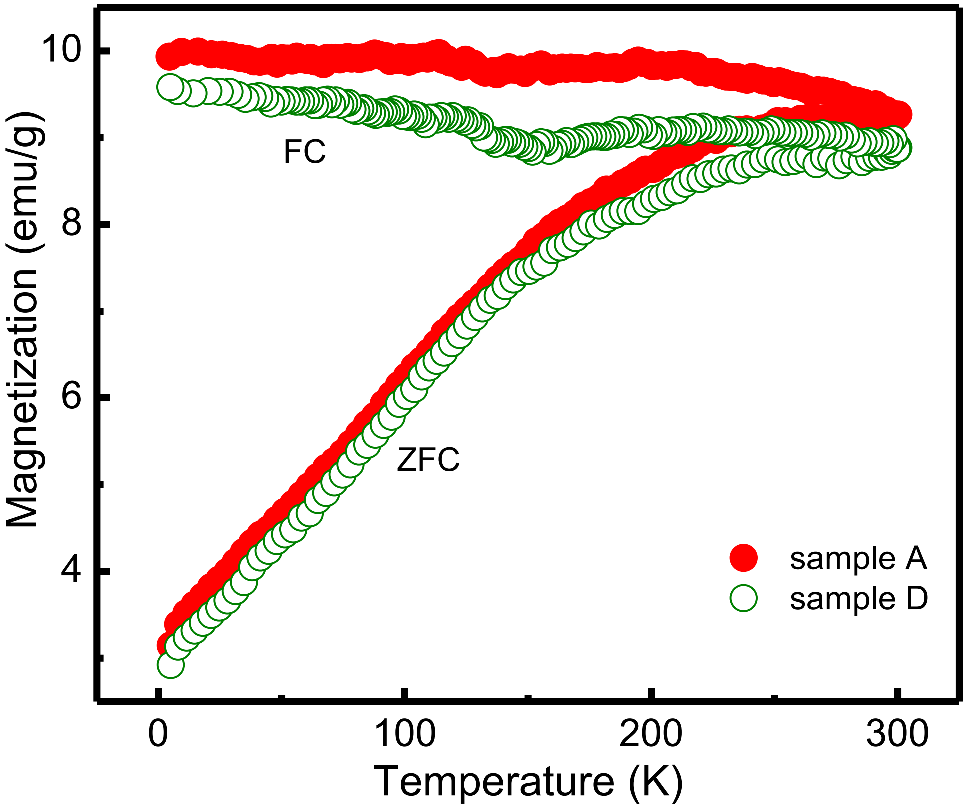

Fig 5.18: Zero field cooled (ZFC) and Field cooled (FC) curves of sample A and D nanoparticles in the temperature range of 5 to 300K.

5.3.5 Zeta potential of nanofluids

Fig 5.19 shows the zeta potential of sample A (0 ppm) and sample D (500 ppm) in water medium. Pure uncoated Fe_3O_4 nanoparticles are neutral and this results in very weak interaction between the OH^- ions present in water and the nanoparticles. Hence, the pure nanoparticles show a lower zeta potential of -28 mV. In nanofluids, the development of a net charge at the particle surface affects the distribution of ions in the surrounding interfacial region, resulting in an increased concentration of counter ions close to the surface. Thus an electrical double layer exists around each particle[131].

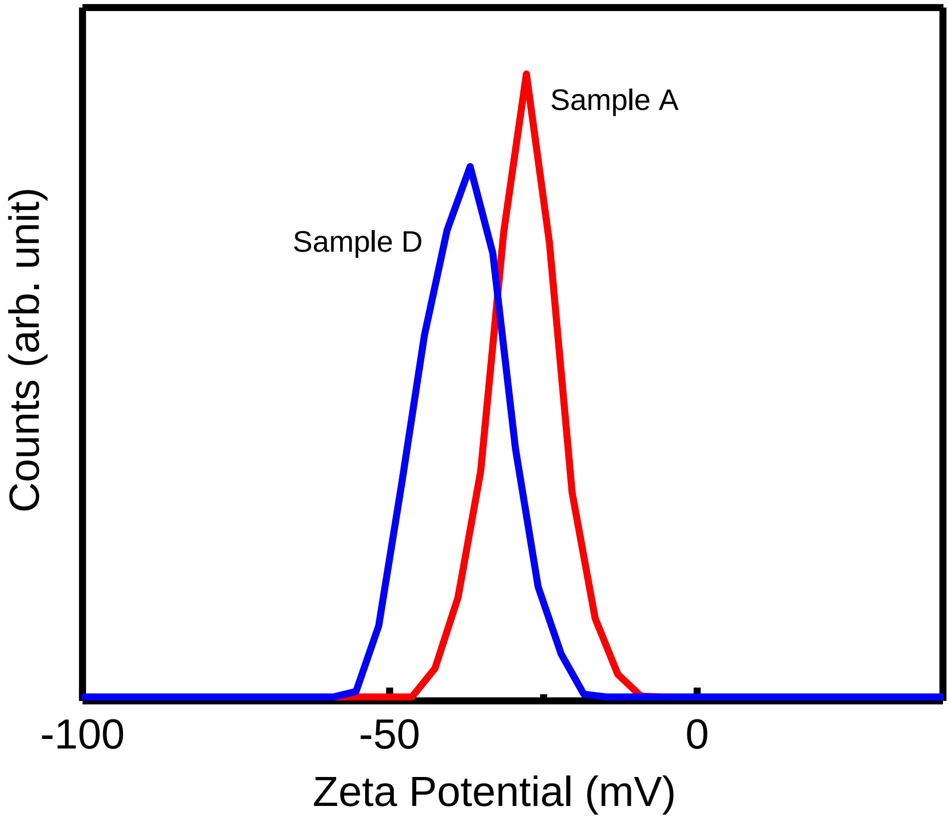

Fig 5.19: The zeta potential distribution curves of 0 (sample A) and 500 ppm sodium doped magnetite nanoparticles in water (sample D).

The liquid layer surrounding the particle exists as two parts; an inner region, called the Stern layer, where the ions are strongly bound and an outer diffuse region where they are less firmly attached. Within the diffuse layer there is a notional boundary. Within the boundary, the ions and particles form a stable entity. When a particle moves, ions within the boundary also move with it, but any ions beyond the boundary do not travel with the particle. This boundary is called the surface of hydrodynamic shear or slipping plane. The potential that exists at this boundary is known as the Zeta potential. The magnitude of the zeta potential gives an indication of the potential stability of the colloidal system.

For nanoparticles doped with 500 ppm of Na^+ ions, the zeta potential was found to be -37 mV. The questions are (a) Why does the zeta potential increases upon introduction of Na^+ ions? (b) Where are the doped Na^+ ions located? (c) Do they remain at the surface of the nanoparticles or do they diffuse into the lattice? Since the doped samples were washed with water several times, the possibility of ions at the interface is ruled out. If free Na^+ ions were present, the nanofluid would have shown a reduced the zeta potential due to the neutralization of the negative charge (OH^- ions). Therefore, the observed increase in zeta potential value with Na^+ doping indicates that the Na^+ ions indeed diffuse into the lattice of the magnetite nanoparticles. The diffused Na^+ ions augment the formation of strong counter OH^- ions that leads to a better electrostatic repulsion between the particles and the formation of a stable dispersion.

5.3.6 Mechanism of stabilization

5.20 (a) – (e) show the photographs of samples A and D after 0, 1, 4, 24 and 48 hrs of preparation (without magnetic field). Fig 14 (f) shows the photograph of samples A and D in the presence of an external magnetic field. Sample A was stable initially but started settling after 1 hr whereas sample D remained stable even after 48 hrs and also under the influence of a strong magnetic field. Magnetite (Fe_3O_4) nanoparticles have spinel structure with cation and anion vacancies. It has been shown that diffusion of metal ions in nanocrystalline state needs lower energy of activation[169]. Therefore, during soaking of Fe_3O_4 nanoparticles in NaOH solution, Na^+ ions starts diffusing through the vacancies and get trapped in the crystal lattice of Fe_3O_4.

Previously, it was reported that Na^+ ions can get trapped into the magnetite nanoparticles when synthesized with NaOH as alkali medium[100].

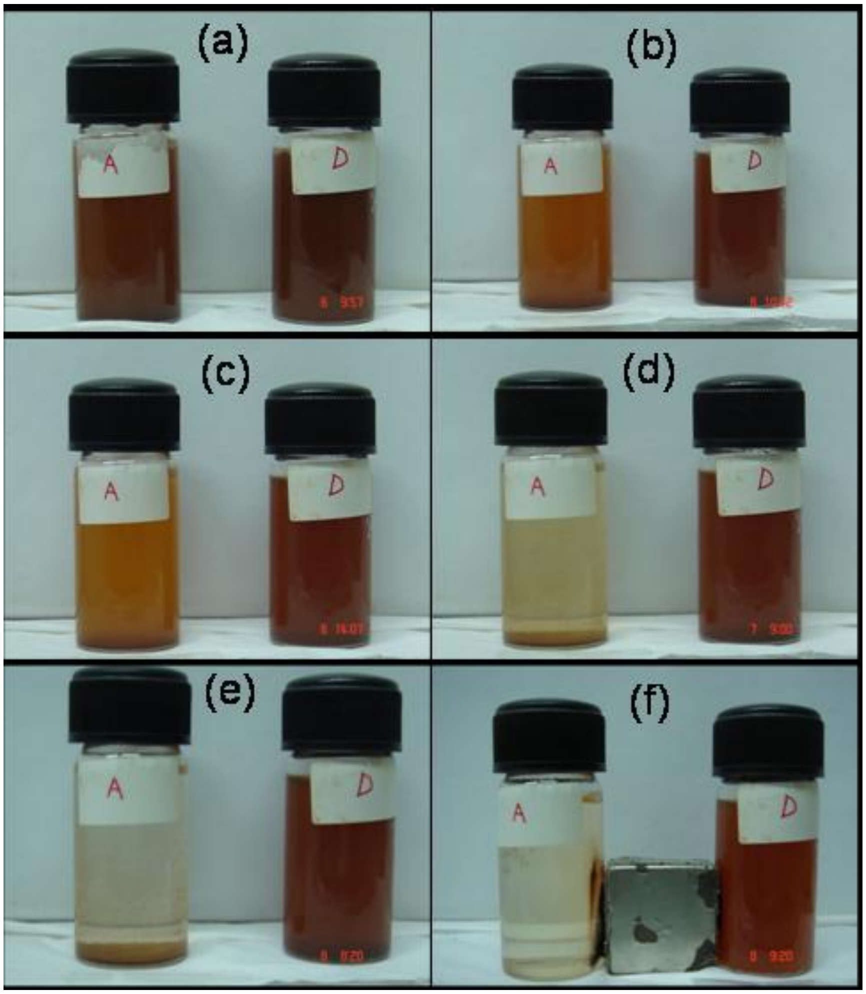

Fig 5.20: Photographs of water based nanofluids prepared with sample A (0 ppm) and D (500 ppm) after different time intervals of preparation (a) 0 hr. (b) 1hr (c) 4 hrs (d) 24 hrs (e) 48 hrs and (f) samples A and D under the influence of a magnetic field.

These trapped Na^+ ions allow the magnetite nanoparticles to be stable in water medium by attracting stronger counter ion (OH^-) sphere, which might not affect the pH of the bulk solution, as the ion concentration is very low. Fig 5.21 shows the schematic of the counter ion sphere formed in aqueous medium at different concentrations of Na^+ ions.

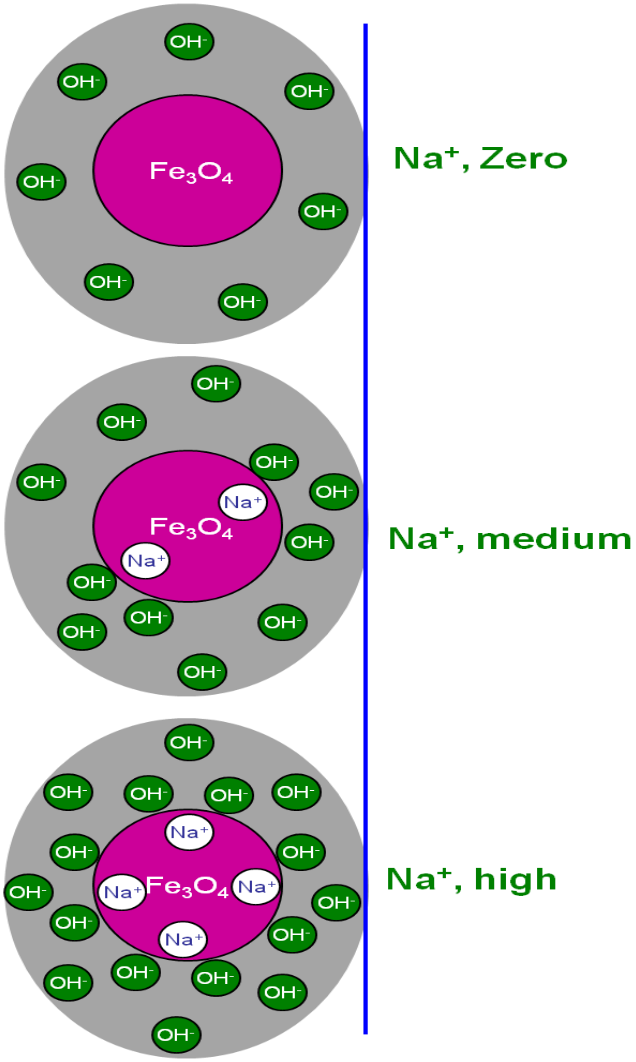

Fig 5.21: Schematic of electrostatic stabilization of magnetite nanoparticles in water medium at different concentrations of Na^+ ions.

In case of undoped Fe_3O_4 nanoparticles (sample A), only a few counter ions are present around the particles that leads to a weak electrostatic stabilization. In the presence of moderate amount of Na^+ ions (sample B), more OH^- ions are present that enhances the stability of the suspension. With more diffused Na^+ ions (sample D); the electrostatic repulsion is further enhanced.

5.4 Conclusions

Magnetite nanoparticles doped with different concentrations of Na^+ ions are prepared by co-precipitation method and are characterized by XRD, TEM, VSM, DSC and FTIR. The HTXRD and DSC results unambiguously confirm that the γ-Fe_2O_3 to α-Fe_2O_3 phase transition temperature is found to increase with Na^+ doping and the doped cations are trapped in the lattice. The phase analysis done using Rietveld method shows that the percentage of hematite (α-Fe_2O_3) formed after air annealing at 600 ºC decreases with increase in Na^+ ion concentration. The differential scanning calorimetric studies also confirm an enhanced stability of Na^+ ion doped samples. The zeta potential results unambiguously confirm that Na^+ ions diffused into the magnetite crystals, which enhances the electrostatic stabilization of the suspended particles.

Chapter VI

Microwave assisted synthesis of magnetite nanoparticles and their phase stability

6.1 Introduction

Studies show that the thermal stability of magnetite nanoparticles can be enhanced through doping[103], protecting shell[107, 113] and particle size[102, 119]. However, there are few studies which show that the change of reaction conditions during co-precipitation process can also affect the phase transition temperature temperatures of iron oxide nanoparticles. Gnanaprakash et al.[100] showed that the alkali used in the synthesis has a crucial role in the phase transition of iron oxide nanoparticles. They observed that magnetite nanoparticles precipitated using ammonia convert to hematite at 500 ºC whereas particles prepared by NaOH as precipitating agent retain the magnetic (maghemite) phase upto 600 ºC. The enhancement was found to be due to the trapping of Na^+ ions in the magnetite crystal structure. In another study, Ayyappan et al. studied the influence of particle size on oleic acid surfactant coated Fe_3O_4 nanoparticles by varying the reaction conditions[119]. Therefore, understanding the effects of reaction parameters such as temperature, reaction time, synthesis technique on phase stability is necessary from fundamental as well as application point of view.

The present study focuses on the effect of microwave-assisted synthesis parameters on the physical properties of synthesized Fe_3O_4 nanoparticles and its phase stability under air annealing.

6.2 Synthesis of Fe_3O_4 nanoparticles

Fe_3O_4 nanoparticles are prepared using microwave assisted synthesis method. The details of the synthesis are described in Chapter II, section 2.2.2.1.

6.3. Results and Discussion

6.3.1 Room temperature XRD, SAXS and FTIR studies

Fig 6.1 shows the room temperature XRD pattern of magnetite nanoparticles prepared at 50, 100, 130, 160 and 200 ºC.

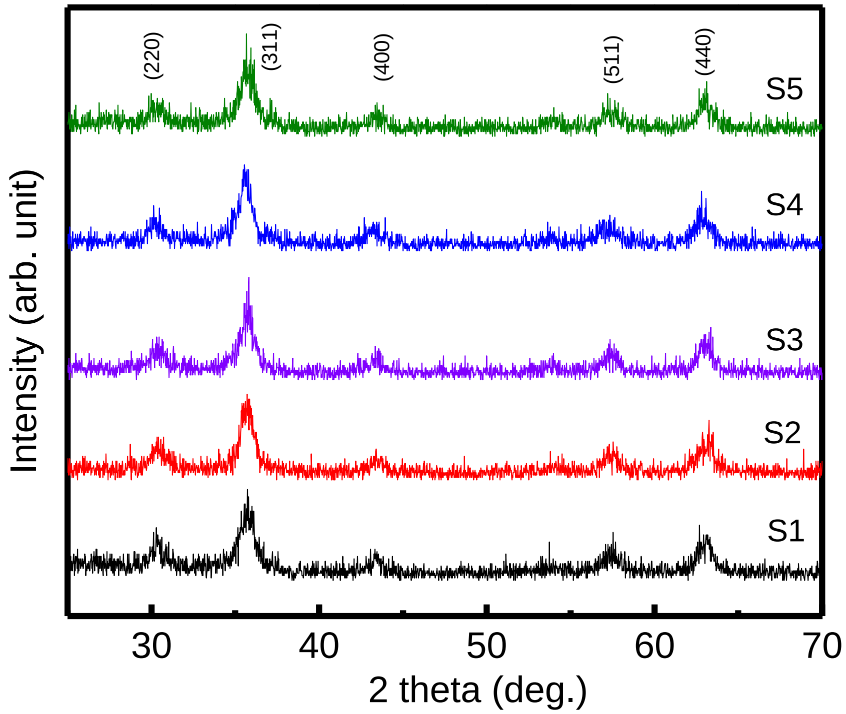

Fig 6.1: Room temperature XRD pattern of Fe_3O_4 nanoparticles (a) S1 (b) S2 (c) S3 (d) S4 and (e) S5 prepared at 50, 100, 130, 160 and 200 ºC, respectively using microwave assisted synthesis.

These samples are referred as S1, S2, S3, S4 and S5, respectively. The diffraction peaks were indexed to (220), (311), (400), (511) and (440) planes with the major peak as (311).The observed XRD pattern matches with the standard JCPDS card number 880315 of pure magnetite with inverse spinel structure. The crystallite size calculated is found to be in the range of 7.5±1 to

9.5±1 nm. The corresponding lattice parameter is in the range of 8.32 to 8.35 Å. The reported values of lattice constant of magnetite and maghemite are 8.39 and 8.35 Å, respectively[177]. The lattice parameter contrast in magnetite nanoparticles is attributed to the very high surface energy of the particles and the existence of the maghemite impurity, especially at the surface of the particles[50]. The surface ions Fe(II) of magnetite oxidizes to a more stable Fe(III) ions resulting in the formation of maghemite.

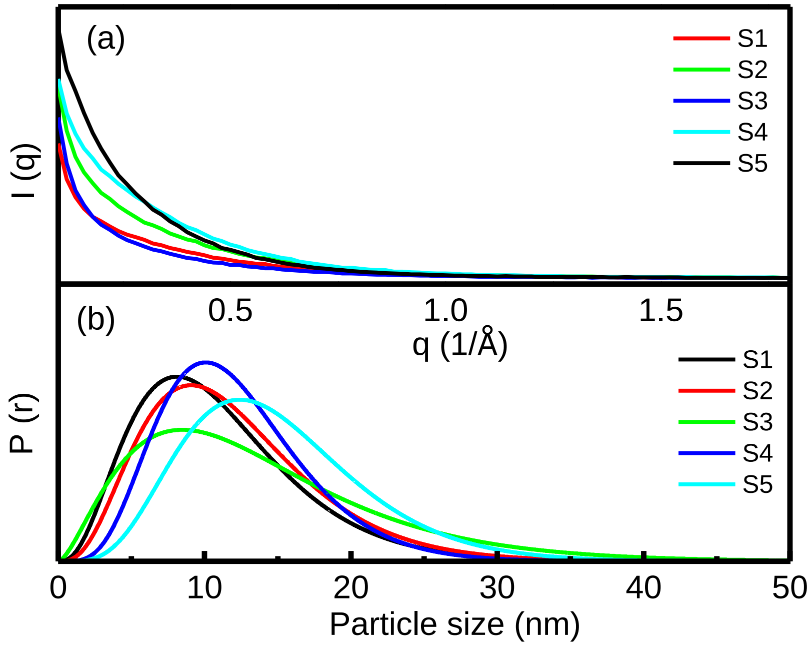

Fig 6.2: (a) scattering intensity as a function of wave vector and (b) particle size distribution obtained from Small angle X-ray scattering measurements of Fe_3O_4 nanoparticles (i) S1 (ii) S2 (iii) S3 (iv) S4 and (v) S5 prepared at 50, 100, 130, 160 and 200 ºC, respectively.

Fig 6.2 shows the SAXS intensity distribution for S1 to S4 nanoparticles (top) and their corresponding particle size distribution obtained from the SAXS analysis using a spherical model. The average particle size is found to vary from 11 to 15 nm when the reaction temperature is increased from 50 to 200 ºC. The sizes obtained from SAXS are found to be larger than that from XRD. Fig 6.3 shows the TEM image of the sample S2, where the average particle size is found to be ~ 12 nm, which is consistent with the average size obtained from SAXS.

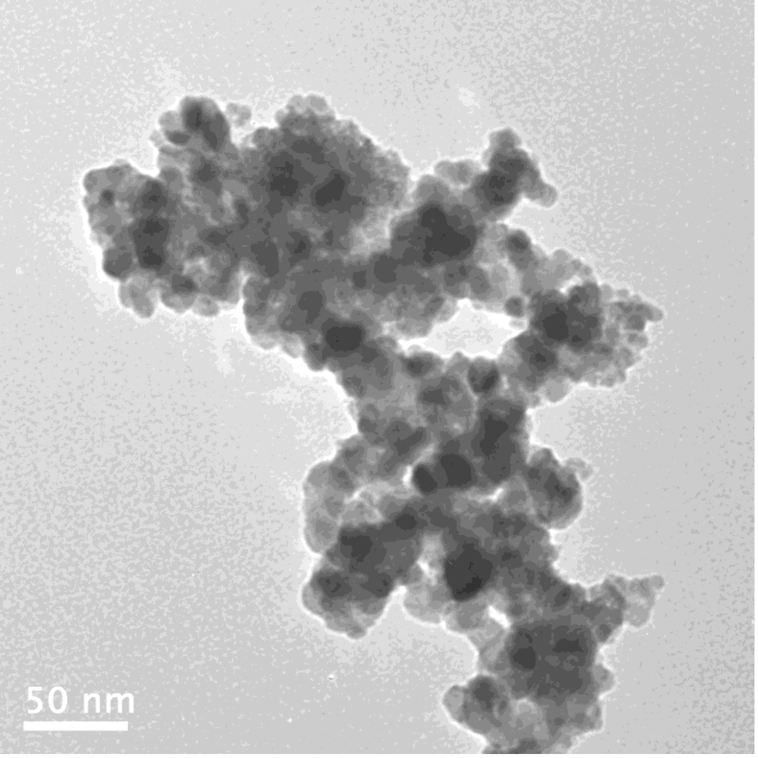

Fig 6.3: TEM image of Fe_3O_4 nanoparticles prepared at reaction temperature of 100 ºC (S2).

Fig 6.4 shows the FTIR spectra for S1, S3, S4 and S5 nanoparticles. For pure magnetite, peaks at ~400 and ~590cm^{-1} correspond to stretching of bonds between octahedral and tetrahedral metal ions to oxide ions[165, 178]. In the present case the octahedral and tetrahedral stretching peaks appear at 455 cm^{-1} and 556 (& 660) cm^{-1}, respectively, probably due to the interaction of Na^+ ions with O^{2-} ions. The transmission spectra of all the samples are found to be similar, which shows that the reaction temperature has not altered the lattice vibration of oxide ions and the cations in the octahedral and tetrahedral sites.

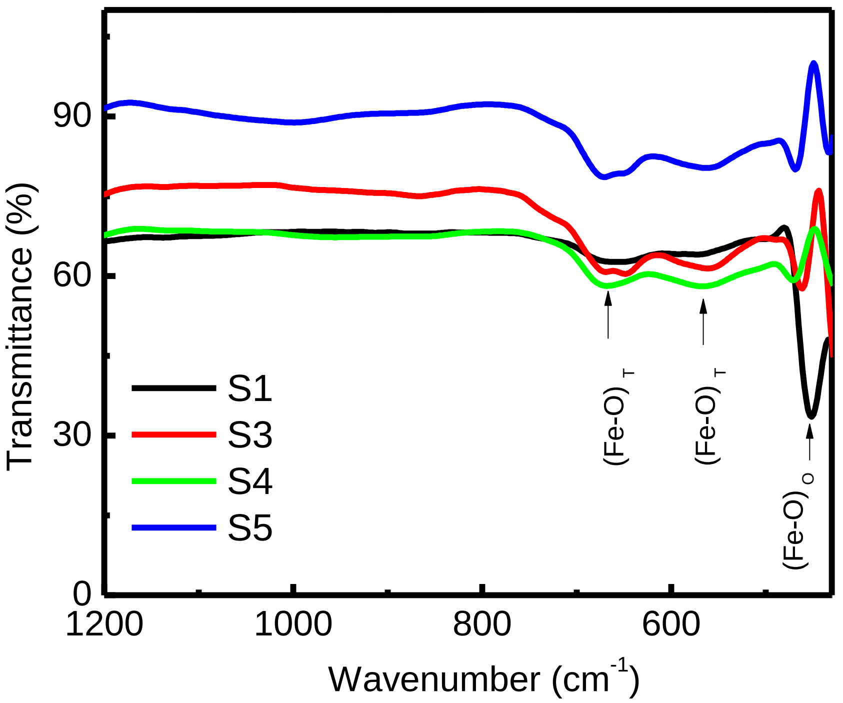

Fig 6.4: Transmission spectra obtained from FTIR for Fe_3O_4 nanoparticles (a) S1 (b) S3 (c) S4 and (d) S5 prepared at 50, 130, 160 and 200 ºC, respectively using microwave assisted synthesis.

6.3.2 High temperature phase transition studies

Fig 6.5 shows the weight loss under an external magnetic field and the heat flow curves of S1, S2, S3, S4, and S5 nanoparticles as a function of temperature from 30 to 1000 ºC. The weight of the sample is found to decrease (up to ~ 10%) initially due to evaporation of water molecules adsorbed in the magnetic nanoparticles. Above 120 ºC, the weight of the sample starts increasing because of the reduction in the magnetic moment due to an increase in thermal fluctuation. The increase in the weight continues till the Curie temperature (T_C ~595 ºC) where the magnetic particles become paramagnetic with zero net magnetic moment. The weight gain curves show two different slopes, one in the temperature range of 120 to 310 ºC and the other in the range of 310 to 595 ºC. The first slope change occurring at ~310 ºC attributed to the magnetite to maghemite phase transition, which generally occurs around 300 ºC[98]. The second slope change occurs at the Curie temperature where the spins became random and the system behaves like a paramagnetic phase.

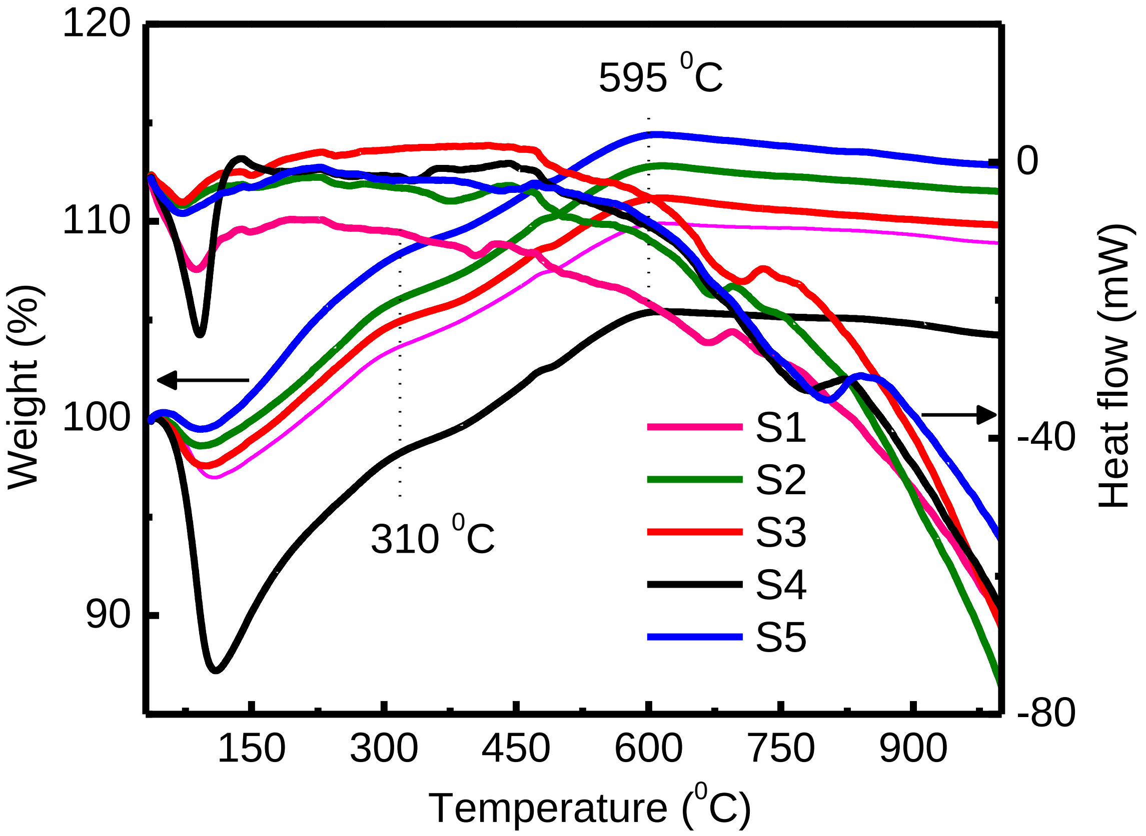

Fig 6.5: Weight and heat flow curves of Fe_3O_4 nanoparticles (a) S1 (b) S2 (c) S3 (d) S4 and (e) S5 prepared at 50, 100, 130, 160 and 200 ºC, respectively.

Fig 6.6 shows the schematic of the magnetic weight loss for Fe_3O_4 nanoparticles (S4) as a function of temperature. Interestingly, the Curie temperature is found to be invariant (595 ºC) for nanoparticles prepared at different reaction temperatures. According to finite size scaling theory[22], the shift in the curie temperature with respect to the bulk should vary as $\frac{T_C(d) - T_c(bulk)}{T_c(bulk)} = \pm(d/d_0)^{-\lambda c}$, where T_C (d) and T_C (bulk) are the curie temperatures of the particle of size d and the bulk material, respectively. The exponent is found to be ~1.42 for ferromagnetic $MnFe_2O_4$ of particles in the size range of 7.4 to 24.5 nm and the system dependent sign can be either positive or negative. The value of d_0 depends on the microscopic dimensions of the system[179]. As the particle size remains almost the same, irrespective of the reaction temperature, the T_C is expected to be the same.

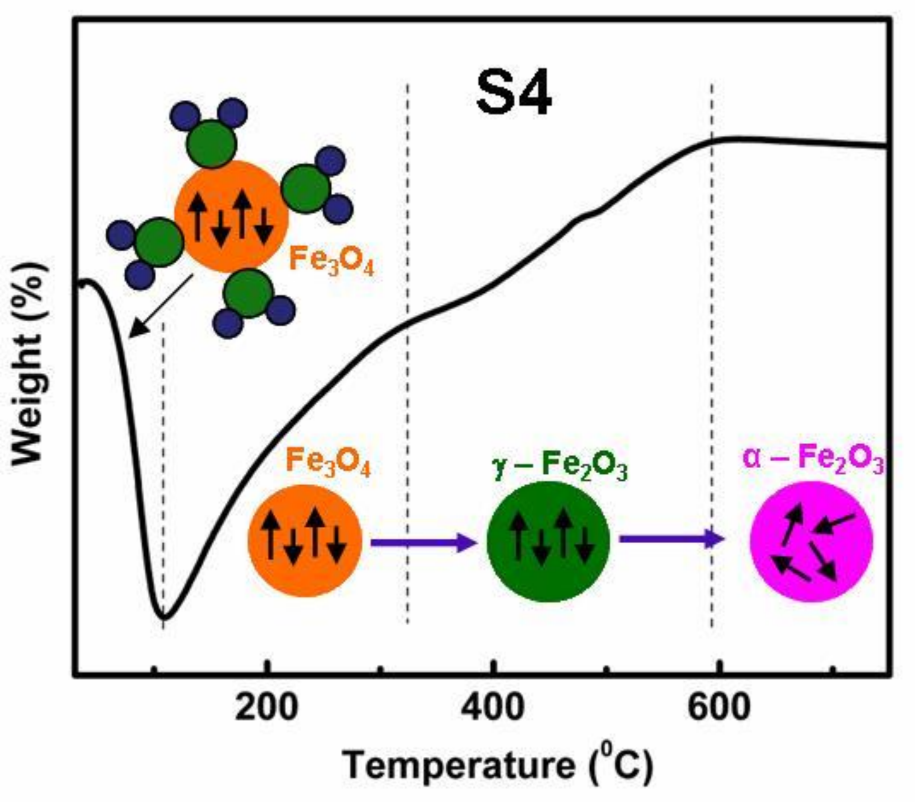

Fig 6.6: Schematic of the magnetic weight loss for Fe_3O_4 nanoparticles (S4) as a function of temperature. The temperature at which evaporation of water molecules adsorbed on the magnetic nanoparticles, Fe_3O_4 to γ-Fe_2O_3 and γ-Fe_2O_3 to α-Fe_2O_3 phase transitions occur are shown by the dotted lines.

The heat flow curves show an endothermic peak at ~120 ºC, which is due to evaporation of adsorbed water molecules. The exothermic peaks observed at 695, 696, 728, 820, and 850 ºC for

S1, S2, S3, S4, and S5, respectively; confirm the maghemite (cubic) to a thermodynamically stable antiferromagnetic hematite (hexagonal) phase transition. The values of the phase transition temperature, Curie temperature and enthalpy change from TGA-DSC measurements are presented in Table 6.1.

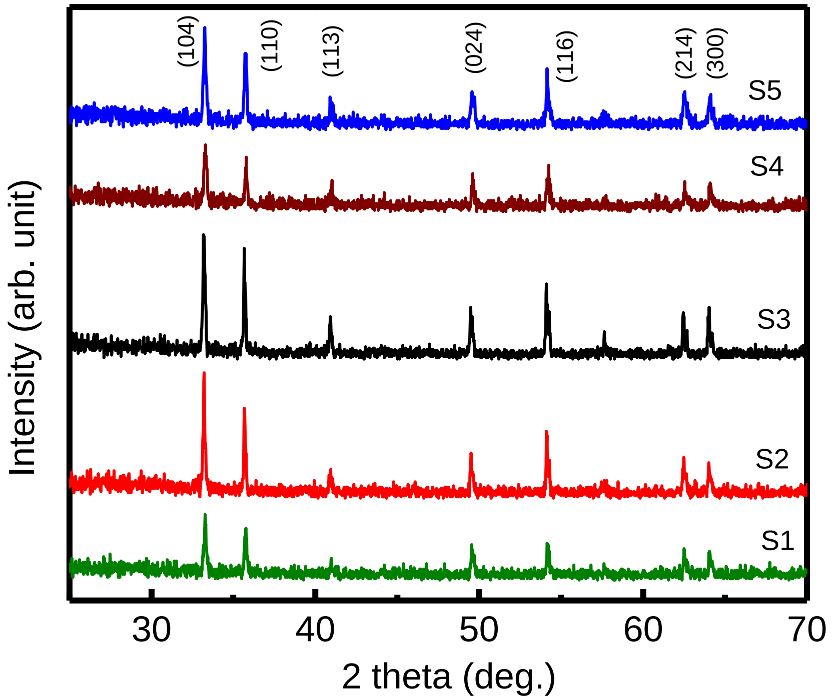

Fig 6.7: Room temperature XRD pattern of nanoparticles S1 to S5 air annealed at 1000 ºC.

Fig 6.7 shows the XRD pattern of S1, S2, S3, S4, and S5 after 1000 ºC annealing under air (i.e. after the DSC measurements). The XRD pattern confirms that the particles have a common chemically ordered hexagonal structure, with the major characteristic diffraction peaks of (104), (110), (113), (024), (116), (214), and (300). This shows that the γ-Fe_2O_3 to α-Fe_2O_3 phase transformation is complete at 1000 ºC. It has been known that the amorphous Fe_2O_3 is converted to ferromagnetic γ-Fe_2O_3 upon air annealing at 300 ºC for ~ 3 h and antiferromagnetic α-Fe_2O_3 when the sample is air annealed at 500 ºC[103].

Fig 6.8 shows the variation of enthalpy and the γ-Fe_2O_3 to α-Fe_2O_3 phase transition temperature as a function of reaction temperature. For Fe_3O_4 nanoparticles prepared at 50 ºC, the change in enthalpy, ΔH, is found to be -13 J/g. For the samples prepared at reaction temperatures 100, 130, 160, and 200 ºC, the ΔH values are found to be -23, -31, -69, and -113 J/g, respectively. The γ-Fe_2O_3 to α-Fe_2O_3 phase transition temperature is found to be almost constant (~ 696 ºC) for samples prepared upto 100 ºC but it increases sharply to 850 ºC as the reaction temperature is increased to 200 ºC. This means that those samples prepared at higher reaction temperatures show enhanced activation energy for the cubic to a more compact hexagonal transition, which requires a lattice contraction.

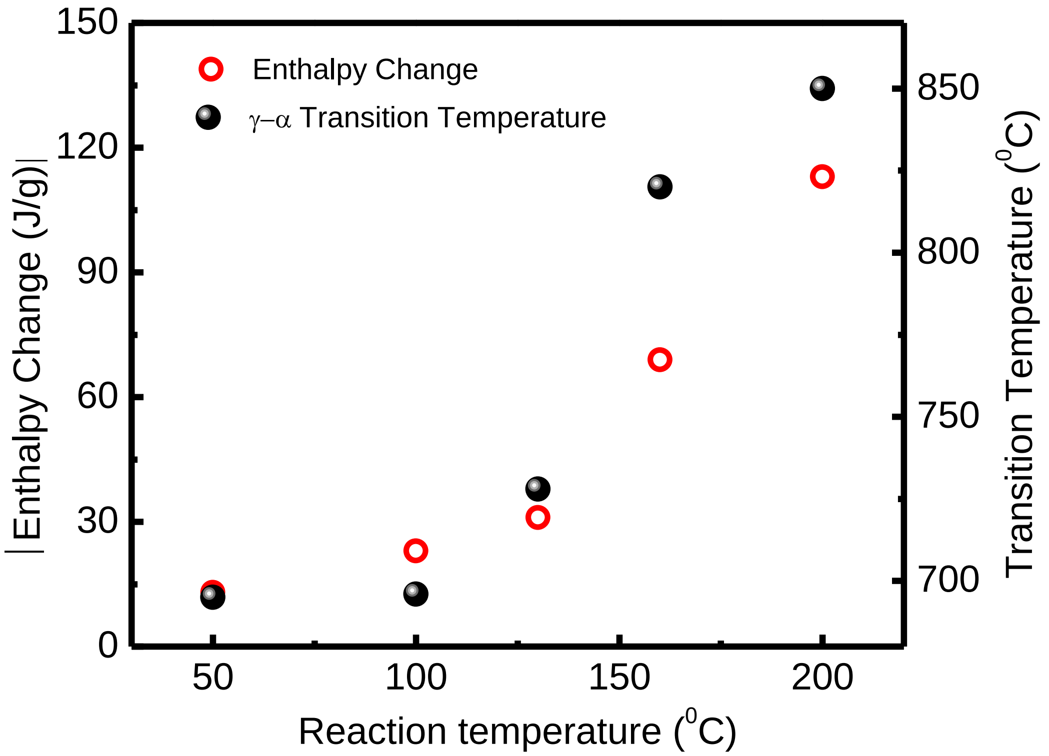

Fig 6.8: Variation of enthalpy and the γ-Fe_2O_3 to α-Fe_2O_3 phase transition temperature as a function of reaction temperature.

Studies show that the Li ions diffuse into the spinel and occupy the tetrahedral sites[170]. The individual Li when hopping between neighboring tetrahedral sites pass through intermediate octahedral sites where the migration barriers are sensitive to the overall Li concentration[170]. In present case, the phase stability is explained in terms of the Na^+ diffusion into the cubic lattice. The interstitial and vacancy diffusion can occur in solids[180]. Interstitial diffusion is fast and strongly depends on temperature. On the contrary, to progress vacancy diffusion, which is usually a slow process, breaking of bonds with neighboring atoms is required. The diffusion phenomena can be explained by the Fick's law $J_D = -D\frac{dC}{dl}$ where, J_D is the diffusion flux, C is the concentration, *l* is the diffusion length and D is the diffusion coefficient[180]. Further, the diffusion coefficient 'D' is related to the temperature by the equation $D = D_0 \exp\left(-\frac{E_a}{RT}\right)$ where, D_0 , E_a , R and T are the maximum diffusion constant, activation energy and the universal gas constant, respectively. This means that the diffusion coefficient increases with increasing temperature. Therefore, the amount of Na^+ diffused into the magnetite crystals at higher reaction temperature would have been higher. To confirm this, flame photometry experiments is performed to determine the concentration of Na^+ in the magnetite nanoparticles prepared at 200 and 50 ºC (S5 and S1, respectively). The concentrations of sodium were found to be 210 and 190 ppm for S1 and S5, respectively. This shows that the Na^+ concentration in Fe_3O_4 nanoparticles at higher reaction temperature was slightly lower. However, the Na^+ concentration (~350 ppm) was much lower than that required to affect the phase transition temperature of magnetite nanoparticles (Chapter V). This shows that the increase in the phase stability or activation energy for magnetic to non-magnetic phase transition is originating from the location and distribution sites of Na^+ within the cubic lattice.

6.3.3 Magnetic properties

Fig 6.9 shows the room temperature magnetization curves of S1, S2, S3, S4, and S5 nanoparticles. The particles are found to be superparamagnetic nature in all the cases. The saturation magnetization (M_s) values are found to be 52, 61, 53, 53, and 47 emu/g for S1, S2, S3, S4 and S5 nanoparticles, respectively, which were lower than the saturation magnetization of bulk magnetite (92 emu/g) due to reduced coordination symmetry of oxygen atoms at the surface[132]. These results show that the reaction temperature does not affect the magnetic property significantly although it increases the phase transition temperature dramatically.

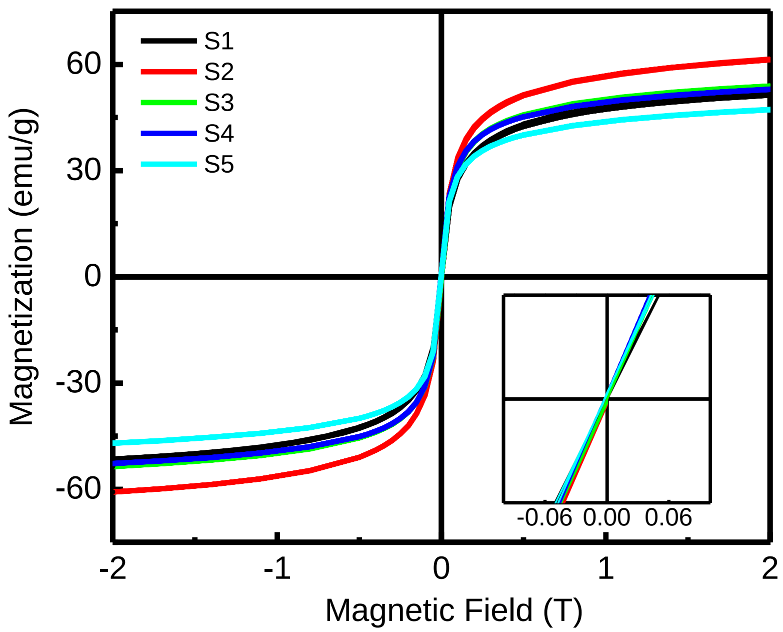

Fig 6.9: Room temperature M-H curves of Fe_3O_4 nanoparticles (a) S1 (b) S2 (c) S3 (d) S4 and (e) S5 prepared at 50, 100, 130, 160 and 200 ºC, respectively. Inset shows the zoomed view of hysteresis loop at lower fields.

Fig 6.10 shows the ZFC and FC curves of magnetite nanoparticles synthesized at 100 and 130 ºC. In the ZFC curve, the magnetization value increases with increase in temperature till the T_B.

Above T_B, the thermal energy dominates over the anisotropy energy and the magnetization of each particle begins to fluctuate between the two easy axes. Above the blocking temperature the magnetization value decreases due to a decrease in the magnetic ordering. The blocking temperature for S2 and S3 are found to be 215 and 220K, respectively. The anisotropy constant is found to be 19.4×10^5 and 19.8×10^5 erg/cm^3 for S2 and S3, respectively. Earlier studies show that with increasing particle size, the blocking temperature increases due to lower surface anisotropy or anisotropy constant[41, 152].

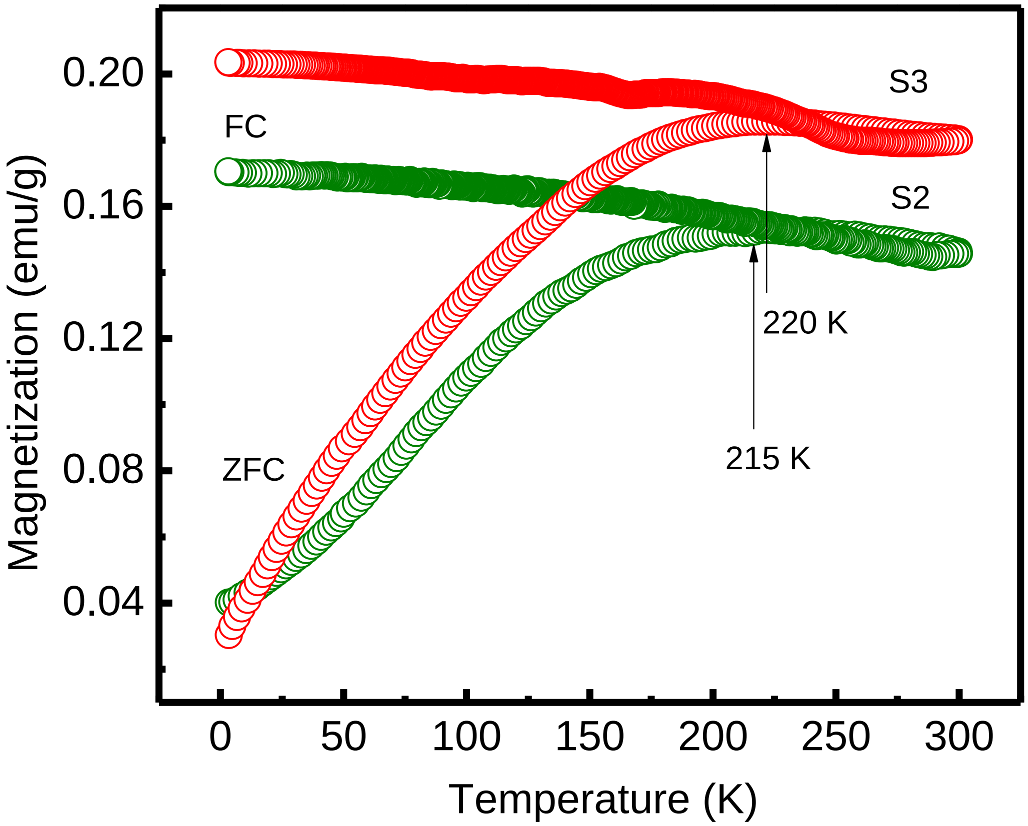

Fig 6.10: ZFC-FC curves of magnetite nanoparticles (S2 and S3) prepared at reaction temperature of 100 and 130 ºC, respectively.

The T_B is found to decrease from 210 to 45K when the magnetite nanoparticles particle size was decreased from 8 to 2 nm at 5Oe magnetic field due to the broken symmetry below a critical size[41]. The K value also depends on magnetocrystalline shape, surface, dipolar or exchange interactions and stress magnetic anisotropy among the particles[153]. The nearly invariant anisotropy constant and T_B for S2 and S3 is due to the same particle size distribution in these two cases. It also shows that the diffusion of sodium into the cubic lattice does not alter the anisotropy constant. The values of the phase transition temperature, Curie temperature and enthalpy change from TGA-DSC measurements are presented in Table 6.1.

Table 6.1: Crystallite size, γ to α phase transition temperature, change in enthalpy, Curie temperature, and saturation magnetization.

Samples	Reaction Temp. (°C)	Size (nm)	$T_{\gamma-\alpha}$ (°C)	ΔH (J/g)	T_c (°C)	M_s (emu/g)
S1	50	7.3	695	13	595	52
S2	100	8.7	696	23	595	61
S3	130	9.0	728	31	595	53
S4	160	9.4	820	69	595	53
S5	200	7.6	850	113	595	47

6.4 Conclusions

Pure Fe_3O_4 nanoparticles of size raging from 7-10 nm are successfully synthesized by varying the reaction temperature from 50 to 200 °C using microwave assisted method. Aqueous solutions of Fe^{2+} and Fe^{3+} and NaOH are used for the synthesis. The average particle size obtained from SAXS is found to vary from 11 to 15±1 nm when the reaction temperature is increased from 50 to 200 °C. The XRD results show that pure magnetite nanoparticles are formed irrespective of the reaction temperature. The magnetite to maghemite phase transition and the Curie temperatures are obtained from the TGA/DSC curves. The Curie temperature is found to be ~595 °C for the prepared nanoparticles. The ferromagnetic γ-Fe_2O_3 to antiferromagnetic α-Fe_2O_3 phase transition temperature is found to increase by 154 °C for the sample prepared at 200 °C due to the enhanced activation energy for the cubic to a more compact hexagonal transition. The increase in the phase stability of nanoparticles prepared at elevated temperature is attributed to the distribution and location of Na^+ within the cubic lattice.

Chapter VII

Microwave assisted synthesis of $Mn_xZn_{1-X}Fe_2O_4$ nanoparticles with tunable Curie temperature

7.1 **Introduction**

Magnetic nanoparticles with Curie temperature in the range of 42-50 ºC and high saturation magnetization are ideal for hyperthermia applications[181]. Among mixed ferrite systems, $Mn_xZn_{1-x}Fe_2O_4$ is widely studied because of its tunable Curie temperature by varying the fraction of Mn[182-196]. Further, due to their potential applications in magnetic hyperthermia and heat-inducible transgenic expression, there has been a renewed interest in such $Mn_xZn_{1-x}Fe_2O_4$ [197-200]. The preferential occupation of diamagnetic Zn^{2+} in tetrahedral site in $ZnFe_2O_4$, the magnitude of octahedral-tetrahedral interaction becomes very weak leading to a paramagnetic behavior. $MnFe_2O_4$ has a partial inverse spinel structure with Mn^{2+} randomly distributed in octahedral and tetrahedral site resulting in a strong magnetic moment with a Curie temperature of 573K for bulk samples[201]. Thus, Mn-Zn ferrites are temperature sensitive and hence find interesting applications in ferrofluids. $Mn_{0.2}Fe_{0.8}Fe_2O_4$ nano particles of particle size ~40 nm, prepared using co-precipitation method, is found to have a Curie temperature of 329.5K and saturation magnetization of ~23 emu/g[190]. Lan et al. [202] showed that the Curie temperature of mixed ferrite, prepared by co-precipitation method, decreases from 605 to 310 K as the Zn fraction is increased from 0 to 0.7. Rath et al.[189] reported that the crystallite size decreases from ~11 to 5 nm with an increasing zinc fraction from 0 to 1 in $Mn_{1-x}Zn_xFe_2O_4$ nanoparticles. -Though mixed ferrites of $Mn_xZn_{1-x}Fe_2O_4$ nanoparticle of different fractions of Mn have been prepared by various routes, the tuning of Curie temperature for the entire Mn concentration range(x=0-1.0) has not been attempted. Therefore, synthesis of such particles using simple, one-pot approach is important for practical industrial applications.

This Chapter discusses the preparation of $Mn_xZn_{1-x}Fe_2O_4$ nanoparticles (x = 0-1) using microwave assisted method and the results on tuning of Curie temperature and saturation magnetization.

7.2 Synthesis of $Mn_xZn_{1-x}Fe_2O_4$ nanoparticles

$Mn_xZn_{1-x}Fe_2O_4$ nanoparticles were prepared by microwave assisted synthesis method. The details of the synthesis procedure are discussed in Chapter II, section 2.2.2.2.

7.3 Results and Discussion

7.3.1 Room temperature structural studies

Fig 7.1a shows the room temperature XRD patterns of $Mn_xZn_{1-x}Fe_2O_4$ nanoparticles for x = 0 to 1. The observed diffraction peaks are well defined, and the peaks (220), (311), (400), (511), and (440) are indexed to a single phase spinel structure (JCPDS card no-891012). Unlike in hydrothermal technique,[189] no additional phases like hematite (α-Fe_2O_3) in $MnFe_2O_4$ is observed in the microwave assisted approach. Fig 7.1b shows the lattice constant as a function of Mn content. The lattice constant decreases from 8.435 to 8.41 Å as the Mn^{2+} is increased from 0 to 0.3 fractions. Further, increase in the Mn^{2+} fraction leads to a monotonic increase in the lattice parameter. Earlier studies on $Mn_xZn_{1-x}Fe_2O_4$ synthesized by other methods also showed a similar linear increase in the lattice constant from 8.44 to 8.55Å, as the x is increased from 0 to 1.0[189, 193]. It should be noted that in the above studies, limited number of fractions were attempted (no fraction between 0-0.35). The reason for the observed decrease in the lattice constant for x= 0 to 0.3 fractions is not clear. Detailed Mossbauer or extended x-ray-absorption fine-structure spectroscopy or neutron diffraction studies are necessary to shed more light on the symmetry, valence of the iron cations, site occupancy in ferrites and magnetic structure[203].

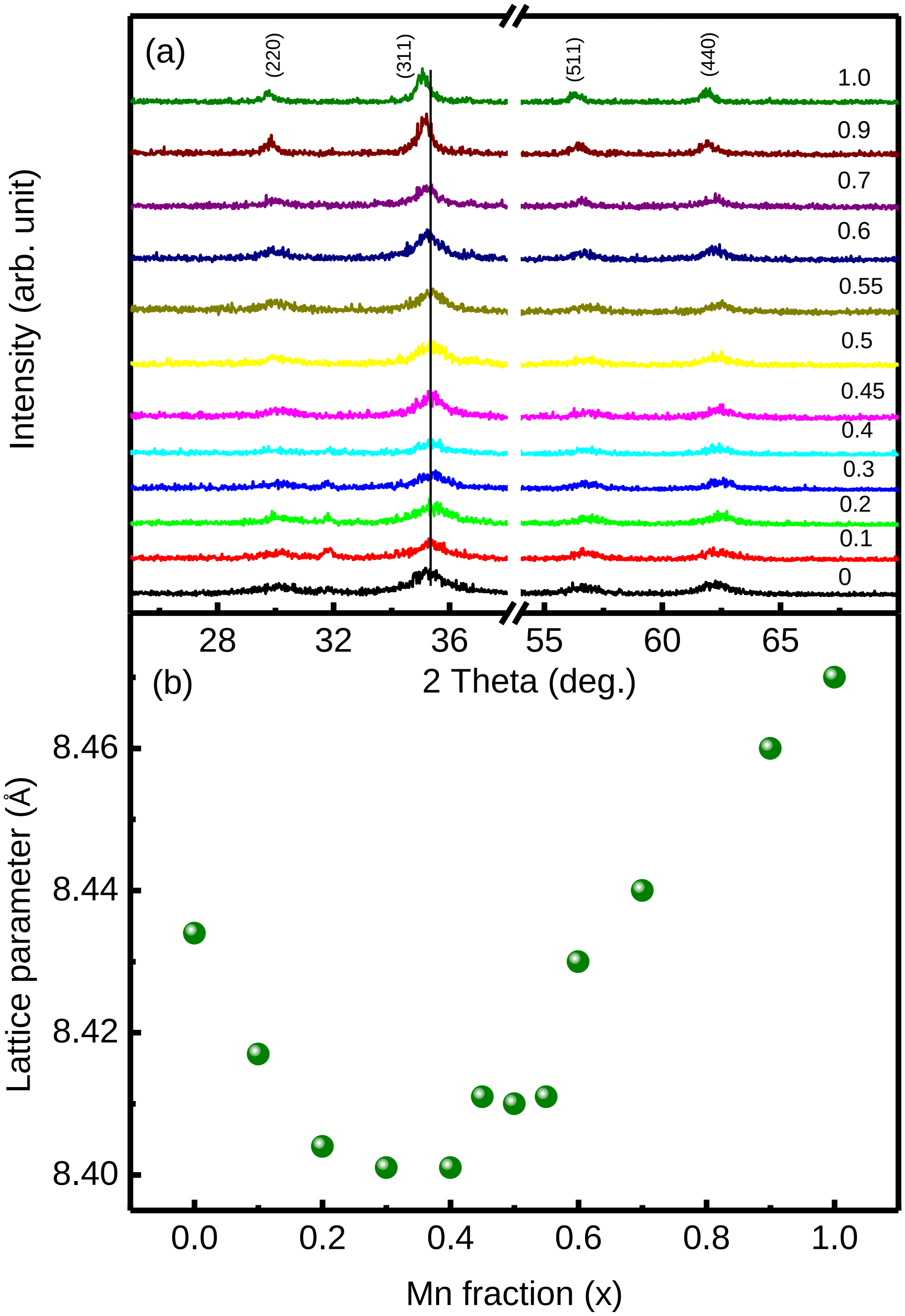

Fig 7.1: (a) Room temperature XRD patterns of $Mn_xZn_{1-x}Fe_2O_4$ nanoparticles with x varying from 0 to 0.1 (b) lattice constant as a function of Mn^{2+} content.

The high field Mossbauer study in manganese zinc ferrites by Morrish and Clark [193] showed that a small number of Fe^{3+} ions occupy the tetrahedral sites (~ 8% for x = 0) at low concentrations of diamagnetic Zn^{2+}, whereas ~ 99% of the Fe^{3+} ions ($3d^5$) are located at octahedral sites for x=0.5 and above. Ionic radii of metal ions vary as a function of valence, coordination number and spin state.

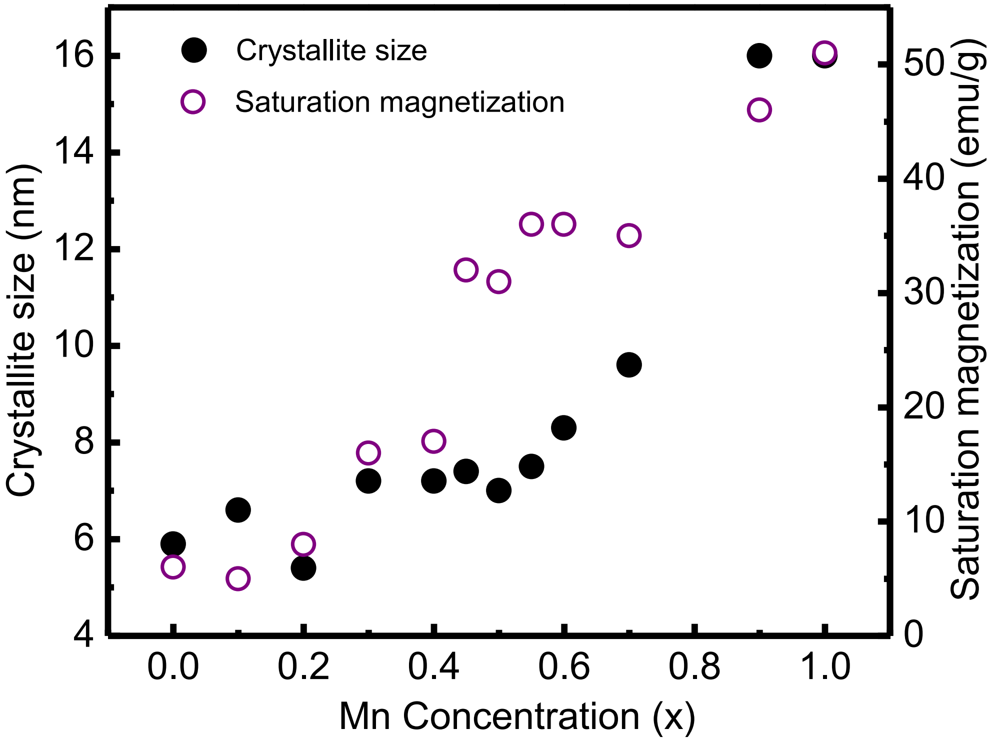

Fig 7.2: The variation of crystallite size, calculated from the most intense (311) peak and the saturation magnetization as a function of Mn^{2+} fraction.

In general, the ionic radii of metal cations decrease with increase in valence[204]. In tetrahedral site (coordination number 4), all the Fe^{3+} and Mn^{2+} ions reside in the high spin state. The reported values of ionic radii for Fe^{3+} and Mn^{2+} ions are 0.77, 0.80 Å, respectively. Zn^{2+} ($3d^{10}$) has an ionic radii is 0.74 Å. In the octahedral site (coordination number 6), Mn^{2+} and Fe^{3+} flip between the high and low spin states. The ionic radii of Fe^{3+} in the low spin and high spin state are 0.69 and 0.785Å, respectively in the octahedral site whereas the ionic radii of Mn^{2+} in low spin and high spin state of the octahedral site are 0.85 and 0.97Å, respectively. The ionic radius of Zn^{2+} in octahedral site is 0.88 Å. Fig 7.2 shows the variation of crystallite size and the saturation magnetization as a function of Mn^{2+} fraction. The crystallite size is found to increase from 5.9±1 to 16±1 nm as x is increased from 0 to 1. For the Mn-Zn mixed ferrites prepared by hydrothermal approach, the particle size was found to increase from 4 to 13 nm as the Mn concentration was increased from 0 to 1[189]. Another study in manganese zinc ferrite showed that the crystallite size increases with increase in Zn^{2+} concentration[205]. The dependence of Mn^{2+} fraction on the particle size should depend on the chemical affinity of cations to the A or B sites during the nucleation and growth process. The extended x-ray absorption fine structure (EXAFS) studies[188] showed that Zn^{2+} ($3d^{10}$)cations predominately occupy A sites. Their study further concludes that an increase in the percentage of Fe^{3+} ions($3d^5$) and a decrease in the percentage of Mn^{2+} ($3d^5$) cations in the A site can result in an increase in the saturation magnetization.

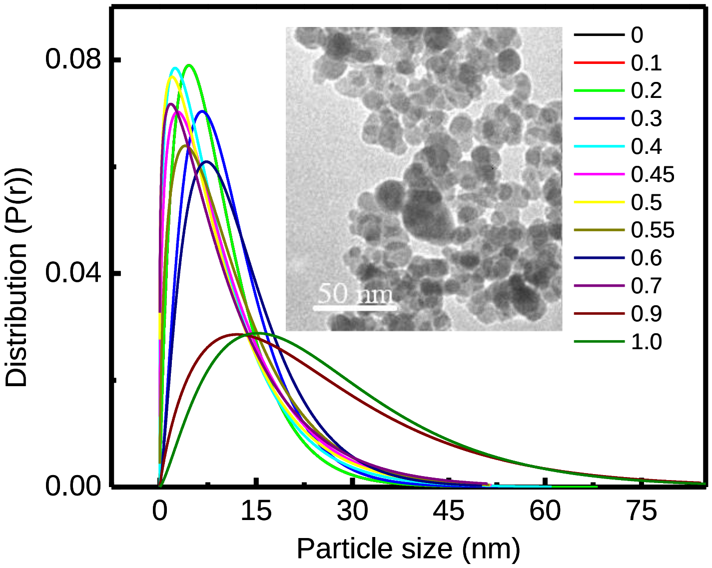

Fig 7.3: The particle size distribution obtained from small angle X-ray scattering measurements in $Mn_xZn_{1-x}Fe_2O_4$ nanoparticles with x varying from 0 to 0.1. The inset shows the TEM image of a sample with x=0.7.

Fig 7.3 shows the particle size distribution obtained from small angle X-ray scattering measurements. The average particle size increases from 9±1 to 26±1 nm as the manganese fraction is increased from 0 to 1. The size obtained from SAXS is higher than the crystallite size obtained from XRD because the former measures the grain size whereas the latter measures the effective size. The grain size is related to the effective size by the relation, $d_{eff} = \frac{3}{4} d$ where, d is the grain size. Inset of Fig 7.3 shows the TEM image of the sample with x=0.7.

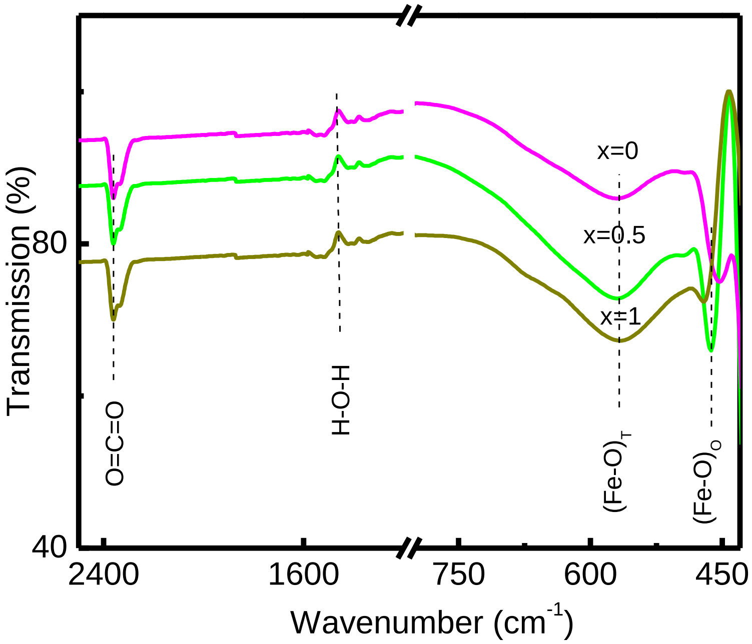

Fig 7.4: FTIR transmission spectra of nanoparticles with Mn^{2+} fractions x = 0, 0.5 and 1.0.

Fig 7.4 shows the FTIR transmission spectra of nanoparticles with Mn fractions x = 0, 0.5 and 1.0. The well resolved wavebands at 460 cm^{-1} and 565 cm^{-1} correspond to metal-oxygen bonds, confirming the ferrite phase. In additions, the bands of CO_2 and H_2O are also seen. The peak around 460 cm^{-1} is due to the Fe-O stretching in octahedral sites of ferrite nanoparticles where as the peak at 565 cm^{-1} is attributed to the Fe-O stretching in tetrahedral sites[165]. The observed shift of the Fe-O stretching (452 to 470 cm^{-1}) with increasing Mn^{2+} fraction is attributed to the change in the Mn^{2+} occupancy in octahedral site. The extended x-ray-absorption fine structure cum IR study shows a shift in the first absorption region in the far IR from 566.98 to 549.62 cm^{-1}, which is attributed to a change in the percentage of octahedral sites occupied by manganese from roughly 25% to 12%[206].

7.3.2 Thermogravimetric studies

Fig 7.5 shows the thermogravimetric curve of $Mn_xZn_{1-x}Fe_2O_4$ nanoparticles in the temperature range of 300 to 1273K. The weight loss measurements are performed in the presence of an external magnetic field to detect the Curie temperature. Below the Curie temperature, the magnetic sample is under the influence of magnetic force but the sample loses its influence above the Curie temperature, resulting in a weight gain.

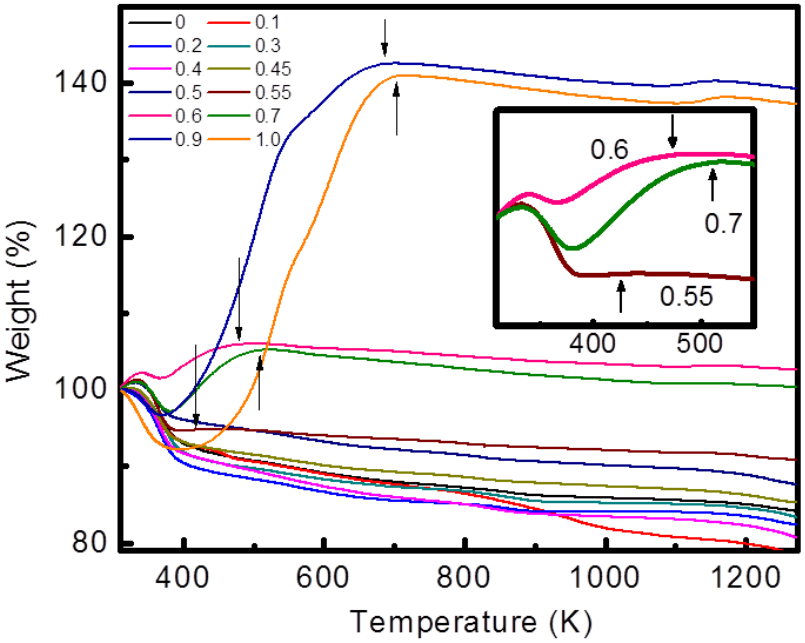

Fig 7.5: Thermogravimetric curves of $Mn_xZn_{1-x}Fe_2O_4$ nanoparticles in the range of 300 to 1273K. The arrow shows the Curie temperatures for various fractions of Mn^{2+}. Inset shows the zoomed view for x=0.55, 0.6 and 0.7.

The initial weight loss of ~ 10% observed with increase in temperature up to ~395 K is attributed to the evaporation of adsorbed water molecules from the sample. For x = 0 to 0.45, very little weight change is observed up to 395 K because of the lower magnetic moment of nanoparticles due to higher Zn^{2+} content. As the Curie temperatures of those particles were below ~395K, it was not possible to detect because the weight loss due to dehydration was more than that of the magnetic weight gain in the above temperature range. The Curie temperatures obtained from the magnetic weight gain curves are tabulated in Table 7.1.

7.3.3 Magnetic properties studies

Fig 7.6 shows the room temperature magnetization curves of $Mn_xZn_{1-x}Fe_2O_4$ nanoparticles from -1.5 to 1.5T. For x = 0 to 0.2, the samples show paramagnetic behavior. The magnetization values are 6 and 8 emu/g at 1.5T for x =0 and 0.2, respectively.

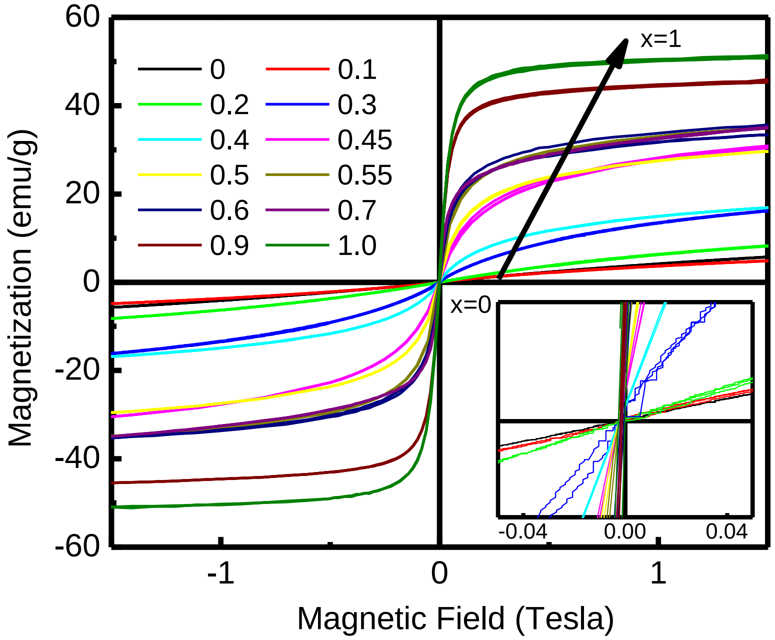

Fig 7.6: Room temperature M-H curves of $Mn_xZn_{1-x}Fe_2O_4$ nanoparticles from -1.5 to 1.5T. Inset shows the zoomed view of the hysteresis loops at low field values.

On further increase in the Mn^{2+} fraction to 0.3, the sample shows superparamagnetic nature with a saturation magnetization of 16 emu/g. The saturation magnetization values for different fractions of Mn^{2+} are tabulated in Table 7.1. The observed saturation magnetization value of 52 emu/g for $MnFe_2O_4$ nanoparticles is found to be much lower than that of the bulk $MnFe_2O_4$ (80 emu/g)[132]. The study by Morrish and Clark[193] found that a relatively stable ferrimagnetic structure is formed when x< 0.20 and the Fe^{3+} ions are canted with respect to the applied field direction when x=0.5.

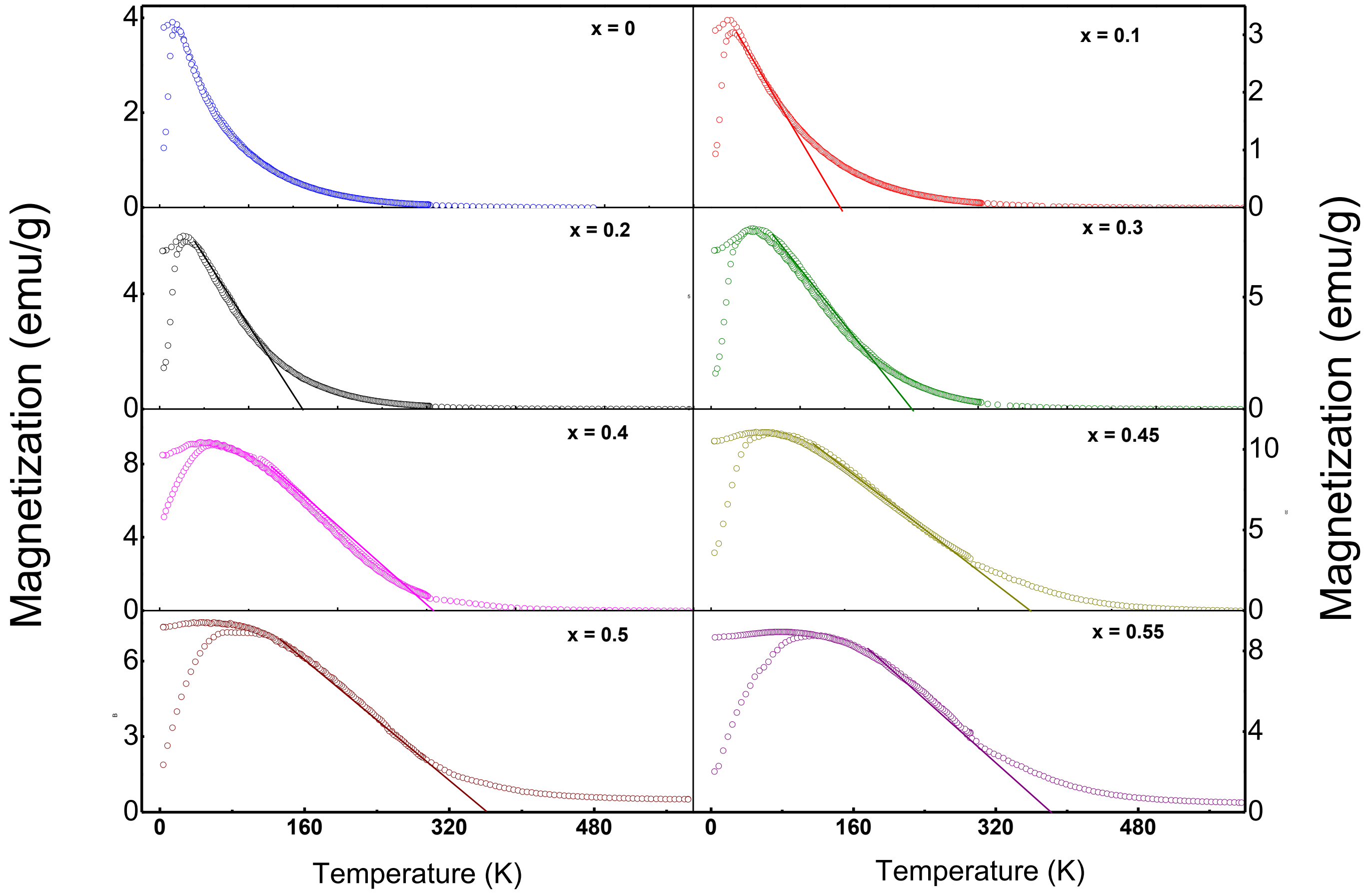

Fig 7.7: Temperature dependence of magnetization (M-T) curves of $Mn_xZn_{1-x}Fe_2O_4$ nanoparticles in the temperature range of 4K to 600K at 100 Oe.

Fig 7.7 shows temperature dependent magnetization curves of $Mn_xZn_{1-x}Fe_2O_4$ nanoparticles in the temperature range of 4K to 600K at 100 Oe. As the temperature increases from 4K, the magnetization value increases drastically followed by a steep decrease, a characteristic of superparamagnetic materials. Above T_B, thermal energy dominates over the magnetic anisotropy energy of ferri-ferromagnetic nanoparticles and the magnetization of each particle begins to fluctuate between the two easy axes, which are separated by energy barriers. Below T_B, anisotropy energy dominates over the thermal energy leading to spin freezing.

The T_B values for different fractions of Mn^{2+} are tabulated in Table 7.1. Fig 7.8 shows the variation of T_B as a function of Mn^{2+} fraction and the crystallite size. The T_B is found to increase almost linearly with Mn^{2+} fraction. For pure $MnFe_2O_4$ nanoparticle, the T_B value obtained from the literature (16 nm crystallite size) is used[207]. With increase in the Mn fraction, a flatness in the peak region of the M-T curve is observed. Such flatness observed in the FC susceptibility at low temperature is attributed to spin-glass like phase[208]. At nanosize, surface disorder becomes more prominent due to bond frustration of exchange interaction between ferrimagnetically coupled spins of different sub lattices near the surface[209]. According to Stoner-Wohlfarth theory, T_B is related to the particle size/volume as $T_B = \frac{KV}{25k_B}$, where K is the anisotropy constant and k_B is the Boltzmann constant. On cooling below T_B, the magnetic moments are frozen where the system exhibits memory effect and magnetic hysteresis. The ZFC magnetization increases monotonically with temperature till T_B. Above T_B, magnetization decreases with temperature due to the thermal energy domination over the magneto-crystalline anisotropy. The anisotropy constants values for different fractions of Mn^{2+} are tabulated in Table 7.1.

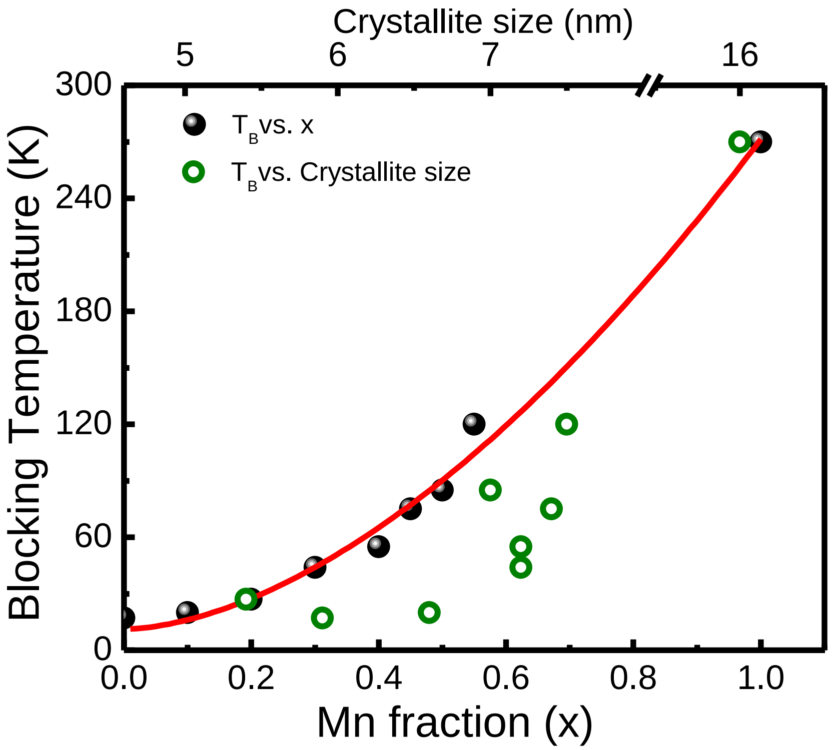

Fig 7.8: Variation of T_B as a function of Mn fraction in the range 0 to 1. The crystallite sizes corresponding to various Mn^{2+} fractions (x) is also shown in the Figure.

Except for x=0.2, the anisotropy constant is found to increase with the Mn^{2+} content. The observed values of K were comparable to the reported value of anisotropy constant 12 $x10^5$ erg/cm^3 for 5 nm size Fe_3O_4 particles[152]. The observed variation in K with Mn^{2+} content is attributed to the combined effect of the inter particle interaction, size effect and the surface anisotropy. In general, as the particle size decreases, the anisotropy value increases due to incomplete coordination and broken bonds at the surface.

Fig 7.9 shows the variation of T_c as a function of Mn^{2+} fractions. The T_c is obtained by extrapolating the linear part of the M-T curve to zero[185]. The Curie temperature values obtained from the M-T curves for different fractions of Mn are tabulated in Table 7.1. The T_c is found to increase linearly with the Mn fraction. The data points are fitted with a straight line fit (

$T_c = 55.7 + 662\,x$, where R^2 is 98%). The Curie temperature values reported by various researchers using different synthesis approaches are also shown in the Figure 7.9[185, 189]. It can be seen that our results are fairly in agreement with the result of those samples produced by hydrothermal and coprecipitation approach. These results suggest that mixed ferrites of $Mn_xZn_{1-x}Fe_2O_4$ with tunable Curie temperature can be obtained using microwave assisted approach.

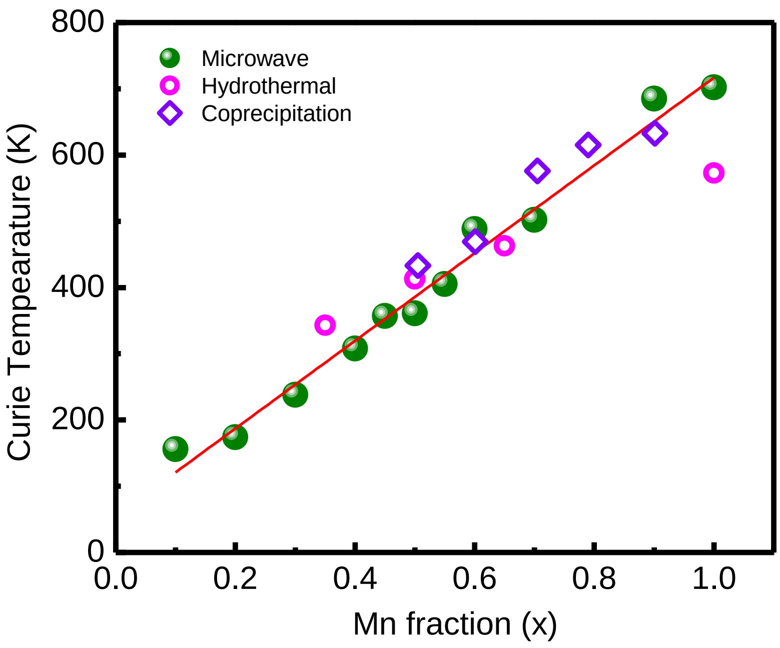

Fig 7.9: The variation of T_c values as a function of Mn^{2+} fractions. The experimental data points is fitted with a linear equation $T_c = 55.1 + 662\,x$. The open circles and the open squares show the data point of Rath et al.[189] and Arulmurugan et al.[185], respectively.

Table 7.1: Mn^{2+} fraction(x), crystallite size obtained from XRD, blocking temperature, Curie temperature (from TGA and M-T curves), magnetic anisotropy constant and saturation magnetization.

Sl. No.	x	Crystallite Size from XRD (nm)	T_B (K)	T_C (K)		K ($x10^5$ erg/cm^3)	M_S (emu/g)
				TGA	M-T		

1	0	5.9	17	-	-	9.22	6
2	0.1	6.6	20	-	148	8.15	5
3	0.2	5.4	27	-	162	20.10	8
4	0.3	7.2	44	-	226	13.81	16
5	0.4	7.2	55	-	304	17.26	17
6	0.45	7.4	68	-	357	19.65	32
7	0.5	7.0	80	-	361	27.33	31
8	0.55	7.5	115	405	390	35.94	36
9	0.6	8.3	-	488	-	-	36
10	0.7	9.6	-	502	-	-	35
11	0.9	16	-	685	-	-	46
12	1.0	16	-	702	-	-	52

7.4 Conclusions

Phase pure $Mn_xZn_{1-x}Fe_2O_4$ nanoparticles with different Curie temperature is prepared using Microwave assisted synthesis method. The XRD results confirm the cubic spinel structure for all the samples. The crystallite size is found to vary from 5.9 to 16 nm as the Mn^{2+} fraction is increased from 0 to 1. The Curie temperature increases linearly from 148 to 390 K as the Mn fraction is increased from 0.1 to 0.55. Except for x=0.2, the anisotropy constant is found to increase with the Mn^{2+} content. Results show that the relative fraction of Mn^{2+} and Zn^{2+} in ferrite structure influences the particle size, lattice parameter, curie temperature and the magnetic properties. Further, our results suggest that the microwave assisted synthesis is a simple approach to produce Mn-Zn ferrite nanoparticles.

Chapter VIII

Summary and Future Scopes

This chapter presents the results obtained, conclusions drawn and the scope for future work. The important findings of this thesis are briefly described below:

8.1 Effect of doping (Co, Zn and Na) on γ-Fe_2O_3 to α-Fe_2O_3 phase transition temperature

- It has been demonstrated that the thermal stability of Fe_3O_4 nanoparticles can be dramatically enhanced by doping it with a low concentration of Co, Zn and Na. Under air atmosphere, the maghemite to hematite phase transition is enhanced by 100 ºC with 0.1 fraction of Co.
- The enthalpy change during the γ-Fe_2O_3 to α-Fe_2O_3 phase transition decreases from 90 to 17 J/g as the Co fraction is increased from 0 to 0.6, which indicates that the degree of conversion from maghemite to hematite decreases with the Co content.
- Under air atmosphere, the magnetic phase (γ-Fe_2O_3) is retained till 656 ºC with 0.6 fraction of Zn doping. The saturation magnetization increases from 61 to 69 emu/g when doped with 0.2 fraction of Zn.
- The Na doping in Fe_3O_4 nanoparticles confirms that γ-Fe_2O_3 to α-Fe_2O_3 phase transition temperature increases with Na^+. The zeta potential results indicate that the Na^+ ions are diffused into the crystal lattice.
- *In situ* XRD study, under vacuum annealing, on Zn doped Fe_3O_4 system shows that 0.2 fraction of Zn doping can enhance the phase transformation temperature of Fe_3O_4 by ~300 ºC. The spinel ferrite phase is found to be stable upto 1000 ºC, with 0.1 fraction of Co. Under vacuum annealing, no phase transition is observed up to 1000 ºC in Fe_3O_4 nanoparticles doped with 500 ppm of Na.

8.2 Synthesis of Fe_3O_4 nanoparticles using microwave assisted method and their phase stability

- Phase pure magnetite nanoparticles of size raging from 7-10 nm are prepared by varying the reaction temperature from 50 to 200 ºC using microwave assisted method.
- The average particle size obtained from SAXS is found to vary from 11 to 15±1 nm as the reaction temperature is increased from 50 to 200 ºC.
- The ferromagnetic γ-Fe_2O_3 to antiferromagnetic α-Fe_2O_3 phase transition temperature is found to increase by 154 ºC in the sample prepared at 200 ºC, which is attributed to the diffusion of Na^+ within the cubic lattice during synthesis.

8.3 Synthesis of $Mn_xZn_{1-x}Fe_2O_4$ nanoparticles and Curie temperature tuning

- Microwave assisted synthesis method has been successfully used to prepare $Mn_xZn_{1-x}Fe_2O_4$ nanoparticles for the first time.
- The Curie point was found to increase linearly from 148 to 390 K as the Mn fraction is increased from 0.1 to 0.55.
- The results show that by varying the relative fraction of Mn and Zn in ferrite structure, the particle size, lattice parameter, Curie temperature and the magnetic properties of Mn-Zn ferrites can be tuned.

8.4 Future scopes

- Experiments to confirm the location of diffused cations in the crystal lattice.
- Effect of cation size on phase stability of ferrites.
- Synthesis of magnetic nanomaterials of different morphologies using microwave synthesis approach and the studies on their structure dependant magnetic and thermal properties.

- Effects of alkaline earth metal (K, Li, Mg, Ca) doping on magnetic and thermal properties of magnetic nanoparticles like Fe_3O_4, $MnFe_2O_4$ and $CoFe_2O_4$.
- Development of water based stable magnetic nanofluid with tunable Curie temperature for biomedical applications.

List of References

1. Feynman, R. P., There's Plenty of Room at the Bottom. *Eng. Sci.* **1960,** 23, 22–36.
2. Klabunde, K. J., *Nanoscale Materaterials in Chemistry*. John Wiley & Sons: USA, 2001.
3. Laurent, S.; Forge, D.; Port, M.; Roch, A.; Robic, C.; Elst, L. V.; Muller, R. N., Magnetic Iron Oxide Nanoparticles: Synthesis, Stabilization, Vectorization, Physicochemical Characterizations, and Biological Applications. *Chem. Rev.* **2008,** 108, 2064.
4. Abajo, F. J. G. d., Microscopy: plasmons go quantum. *Nature* **2012,** 483, 417-418.
5. Rosi, N. L.; Mirkin, C. A., Nanostructures in Biodiagnostics. *Chem. Rev.* **2005,** 105, 1547.
6. Reddy, L. H.; Arias, J. L.; Nicolas, J.; Couvreur, P., Magnetic Nanoparticles: Design and Characterization, Toxicity and Biocompatibility, Pharmaceutical and Biomedical Applications. *Chem. Rev.* **2012,** 112, 5818-5878.
7. Daniel, M. C.; Astruc, D., Gold Nanoparticles: Assembly, Supramolecular Chemistry, Quantum-Size-Related Properties, and Applications toward Biology, Catalysis, and Nanotechnology. *Chem. Rev.* **2004,** 104, 293−346.
8. Mahmoudi, M.; Hosseinkhani, X. H.; Hosseinkhani, M.; Boutry, S.; Simchi, A.; Journeay, W. S.; Subramani, K.; Laurent, S., Magnetic Resonance Imaging Tracking of Stem Cells in Vivo Using Iron Oxide Nanoparticles as a Tool for the Advancement of Clinical Regenerative Medicine. *Chem. Rev.* **2011,** 111, 253-280.
9. Jun, Y. W.; Huh, Y. M.; Choi, J. S.; Lee, J. H.; Song, H. T.; Kim, S.; Yoon, S.; Kim, K. S.; Shin, J. S.; Suh, J. S.; Cheon, J., Nanoscale Size Effect of Magnetic Nanocrystals and Their Utilization for Cancer Diagnosis via Magnetic Resonance Imaging *J. Am. Chem. Soc.* **2005,** 127, 5732.
10. Son, S.; Reichel, J.; He, B.; Schuchman, M.; Lee, S., Magnetic nanotubes for magnetic-field-assisted bioseparation, biointeraction, and drug delivery. *J. Am. Chem. Soc.* **2005,** 127, 7316.
11. Dzamukova, M. R.; Naumenko, E. A.; Lannik, N. I.; Fakhrullin, R. F., Surface-modified magnetic human cells for scaffold-free tissue engineering. *Biomaterials Science* **2013,** 1, (8), 810-813.
12. Mitra, A.; Deutsch, B.; Ignatovich, F.; Dykes, C.; Novotny, L., Nano-optofluidic Detection of Single Viruses and Nanoparticles. *ACS Nano* **2010,** 4, 1305.
13. Raj, K.; Moskowitz, R., Commercial Applications of Ferrofluids. *J. Magn. Magn. Mater.* **1990,** 85, 233.
14. Callister, W., *Materials science and engineering an introduction*. Sixth ed.; John Wiley & Sons: New York, 2003.
15. Spaldin, N., *Magnetic materials: Fundamentals and device aplications*. Cambridge University press: Cambridge, 2003.
16. Cullity, B. D., *Introduction to magnetic materials*. Addision - Wesley: New York, 1972.
17. Kodama, R. H.; Berkowitz, A. E.; McNiff, E. J.; Jr.; Foner, S., Surface spin disorder in ferrite nanoparticles (invited) *J. Appl. Phys.* **1997,** 81, 5552.
18. Stewart, S. J.; Mercader, R. C.; Vandenberghe, R. E.; Cernicchiaro, G.; Scorzelli, R. B., Magnetic anomalies and canting effects in nanocrystalline spinel copper ferrites $Cu_xFe_{3-x}O_4$. *J. Appl. Phys.* **2005,** 97, 054304.
19. Kittel, C., Physical Theory of Ferromagnetic Domains. *Rev. Mod. Phys.* **1949,** 21, 541.
20. Frenkel, J.; Dorfman, J., Spontaneous and Induced Magnetisation in Ferromagnetic Bodies. *Nature* **1930,** 136, 274-275.
21. Morrish, A. H., *The physical principles of magnetism*. John Willey & Son: New York, 1965.
22. Barber, M. N., *Phase transitions and critical phenomena*. Academic: New York, 1983; Vol. 8.
23. Zheng, M.; Wu, X. C.; Zou, B. S.; Wang, Y. J., Magnetic properties of nanosized $MnFe_2O_4$ particles. *J. Magn. Magn. Mater.* **1998,** 183, 152-156.

24. Vedantam, T. S.; Liu, J. P.; Zeng, H.; Sun, S., Thermal stability of self-assembled FePt nanoparticles. *J. Appl. Phys.* **2003,** 93, 7184.

25. Grimes, C. A.; Horn, J. L.; Bush, G. G.; Allen, J. L.; Eklund, P. C., Curie temperature enhancement in Fe_3C nanoparticles made by laser pyrolysis. *IEEE Trans. Magn.* **1997,** 33, 3736-3738.

26. Shima, P. D.; Philip, J.; Raj, B., Magnetically controllable nanofluid with tunable thermal conductivity and viscosity. *Appl. Phys. Lett.* **2009,** 95, 133112.

27. Liong, M.; Shao, H.; Haun, J. B.; Lee, H.; Weissleder, R., Carboxymethylated Polyvinyl Alcohol Stabilizes Doped Ferrofl uids for Biological Applications. *Adv. Mater.* **2010,** 22, 5168.

28. Mahendran, V.; Philip, J., Nanofluid based optical sensor for rapid visual inspection of defects in ferromagnetic materials. *Appl. Phys. Lett.* **2012,** 100, 073104.

29. Mahendran, V.; Philip, J., Sensing of biologically important cations such as Na+ , K+ , Ca2+ , Cu2+ , and Fe3+ using magnetic nanoemulsions. *Langmuir* **2013,** 29, 4252-4258.

30. Philip, J.; V.Mahendran; Felicia, L. J., A Simple, in-expensive and ultrasensitive magnetic nanofluid based sensor for detection of toxic cations, ethanol and ammonia-A Review. *J. Nanofluids* **2013,** 2, 112-119.

31. Philip, J.; Laskar, J. M., Optical Properties and Applications of Ferrofluids—A Review. *J. Nanofluids* **2012,** 1, 3-20.

32. Wickham, D. G.; Goodenough, J. B., Suggestion concerning magnetic interaction in spinels. *Phys. Rev.* **1959,** 115, 1156.

33. Anderson, P. W., Antiferromagnetism: Theory of superexchange interaction. *Phys. Rev* **1950,** 79, 350.

34. Hogan, C. L., Ferrites. *Scientific American* **1960,** 202, 92.

35. Massart, R., Preparation of Aqueous Magnetic Liquids in Alkaline and Acidic Media *IEEE Trans. Magn.* **1981,** 17, 1247.

36. Yu, W. W.; Falkner, J. C.; Yavuz, C. T.; Colvin, V. L., Synthesis of monodisperse iron oxide nanocrystals by thermal decomposition of iron carboxylate salts. *Chem. Commun.* **2004**, 2306.

37. Cannas, C.; Musinu, A.; Peddis, D.; Piccaluga, G., Synthesis and Characterization of $CoFe_2O_4$ Nanoparticles Dispersed in a Silica Matrix by a Sol-Gel Autocombustion Method. *Chem. Mater.* **2006,** 18, 3835.

38. Cote, L. J.; Teja, A. S.; Wilkinson, A. P.; Zhang, Z. J., Continuous hydrothermal synthesis of CoFe2O4 nanoparticles. *Fluid Phase Equilibria* **2003,** 210, 307.

39. Sun, S.; Zeng, H., Size-Controlled Synthesis of Magnetite Nanoparticles. *J. Am. Chem. Soc.* **2002,** 124, 8204-8205.

40. Martínez, B.; Roig, A.; Molins, E.; González-Carreño, T.; Serna, C. J., Magnetic characterization of γ-Fe_2O_3 nanoparticles fabricated by aerosol pyrolysis. *J. Appl. Phys* **1998,** 83, 3256.

41. Perez, J. A. L.; Quintela, M. A. L.; Mira, J.; Rivas, J.; Charles, S. W., Advances in the Preparation of Magnetic Nanoparticles by the Microemulsion Method. *J. Phys. Chem. B* **1997,** 101, 8045.

42. Rana, S.; Philip, J.; Raj, B., Micelle based synthesis of cobalt ferrite nanoparticles and its characterization using Fourier Transform Infrared Transmission Spectrometry and Thermogravimetry. *Mater. Chem. Phys.* **2010,** 124, 264-269.

43. Moon, J. W.; Rawn, C. J.; Rondinone, A. J.; Love, L. J.; Roh, Y.; Everett, S. M.; Lauf, R. J.; Phelps, T. J., Large-scale production of magnetic nanoparticles using bacterial fermentation. *J. Ind. Microbiol. Biotechnol.* **2010,** 37, 1023-1031.

44. Bharde, A.; Wani, A.; Shouche, Y.; Joy, P. A.; Prasad, B. L. V.; Sastry, M., Bacterial Aerobic Synthesis of Nanocrystalline Magnetite. *J. Am. Chem. Soc.* **2005,** 127, 9326.

45. Baghbanzadeh, M.; Carbone, L.; Cozzoli, P. D.; Kappe, C. O., Microwave-Assisted Synthesis of Colloidal Inorganic Nanocrystals. *Angew. Chem. Int. Ed.* **2011,** 50, 11312.

46. Ahn, T.; Kim, J. H.; Yang, H. M.; Lee, J. W.; Kim, J. D., Formation Pathways of Magnetite Nanoparticles by Coprecipitation Method. *J. Phys. Chem. C* **2012,** 116, 6069.

47. Babes, L.; Denizot, B.; Tanguy, G.; Jeune, J. J. L.; Jallet, P., Synthesis of Iron Oxide Nanoparticles Used as MRI Contrast Agents: A Parametric Study. *J. Colloid Interface Sci.* **1999,** 212, 474.

48. Lu, A.-H.; Salabas, E. L.; Schuth, F., Magnetic Nanoparticles: Synthesis, Protection, Functionalization, and Application. *Angew. Chem. Int. Ed.* **2007,** 46, 1222-1244.

49. Willard, M. A.; Kurihara, L. K.; Carpenter, E. E.; Calvin, S.; Harris, V. G., *Encyclopedia of Nanoscience and Nanotechnology*. American Scientific Publishers: Valencia, CA, 2004; Vol. 1.

50. Sun, S.; Zeng, H.; Robinson, D. B.; Raoux, S.; Rice, P. M.; Wang, S. X.; Li, G., Monodisperse MFe2O4 (M) Fe, Co, Mn) Nanoparticles. *J. Am. Chem. Soc.* **2004,** 126, 273.

51. Chen, D.; Xu, R., Hydrothermal synthesis and characterization of nanocrystalline Fe_3O_4 powders. *Mat. Res. Bull.* **1998,** 33, 1015-1021.

52. Li, Z.; Sun, Q.; Gao, M., Preparation of water-soluble magnetite nanocrystals from hydrated ferrite salts in 2-pyrrolidone: mechanism leading to Fe_3O_4. *Angew. Chem. Int. Ed.* **2005,** 44, 123.

53. Hu, F. Q.; Wei, L.; Zhou, Z.; Ran, Y. L.; Gao, Z. L. M. Y., Preparation of biocompatible magnetite nanocrystals for in vivo magnetic resonance detection of cancer. *Adv. Mater.* **2006,** 18, 2553.

54. Brinker, C. J.; Sherrer, G. W., *Sol-Gel Science*. Academic Press: New York, 1990.

55. Cannas, C.; Gatteschi, D.; Musinu, A.; Piccaluga, G.; Sangregorio, C., Structural and Magnetic Properties of Fe_2O_3 Nanoparticles Dispersed over a Silica Matrix. *J. Phys. Chem. B* **1998,** 102, 7721-7726.

56. Ennas, G.; Musinu, A.; Piccaluga, G.; Zedda, D.; Gatteschi, D.; Sangregorio, C.; Stanger, J. L.; Concas, G.; Spano, G., Characterization of Iron Oxide Nanoparticles in an Fe_2O_3 SiO_2 Composite Prepared by a Sol Gel Method. *Chem. Mater.* **1998,** 10, 495-502.

57. Raileanu, M.; Crisan, M.; Petrache, C.; Crisan, D.; Jitianu, A.; Zaharescu, M.; Predoi, D.; Kuncser, V.; Filoti, G., Sol-Gel Fe_xO_y-SiO_2 nanocmposites. *Rom. J. Phys.* **2005,** 50, 595-606.

58. Jézéquel, D.; Guenot, J.; Jouini, N.; Fiévet, F., Submicrometer zinc oxide particles: Elaboration in polyol medium and morphological characteristics. *J. Mater. Res.* **1995,** 10, 77-83.

59. Merikhi, J.; Jungk, H. O.; Feldmann, C., Sub-micrometer $CoAl_2O_4$ pigment particles - synthesis and preparation of coatings. *J. Mater. Chem.* **2000,** 10, 1311-1314.

60. Suslick, K. S., Nanostructured Materials Generated by High-Intensity Ultrasound: Sonochemical Synthesis and Catalytic Studies. *Chem. Mater.* **1996,** 8, 2172-2179.

61. Kim, E. H.; Lee, H. S.; Kwak, B. K.; Kim, B. K., Synthesis of ferrofluid with magnetic nanoparticles by sonochemical method for MRI contrast agent. *J. Magn. Magn. Mater.* **2005,** 289, 328-330.

62. Hasany, S. F.; Ahmed, I.; J, R.; Rehman, A., Systematic review of the preparation techniques of iron oxide magnetic nanoparticles *Nanosci. Nanotech.* **2012,** 2, 148-158.

63. Alvarez, G. S.; Muhammed, M.; Zagorodni, A. A., Novel flow injection synthesis of iron oxide nanoparticles with narrow size distribution. *Chem. Eng. Sci.* **2006,** 61, 4625-4633.

64. Carreno, T. G.; Morales, M. P.; Gracia, M.; Serna, C., Preparation of uniform γ-Fe_2O_3 particles with nanometer size by spray pyrolysis. *Mater. Lett.* **1993,** 18, 151.

65. Pecharroman, C.; Gonzalez Carreno, T.; Iglesias, J. E., The infrared dielectric properties of maghemite, γ-Fe_2O_3, from reflectance measurement on pressed powders. *Phys. Chem. Miner.* **1995,** 22, 21-29.

66. Tavakoli, A.; Sohrabi, M.; Kargari, A., A review of methods for synthesis of nanostructured metals with emphasis on iron compounds. *Chem. Papers* **2007,** 61, 151-170.

67. Alexandrescu, R.; Morjann, I.; Crunteanu, A.; Cojocaru, S.; Petcu, S.; Teodorescu, V.; Huisken, F.; Koh, B.; Ehbrecht, M., Iron-oxide-based nanoparticles produced by pulsed infrared laser pyrolysis of $Fe(CO)_5$. *Mat. Chem. Phys.* **1998,** 55, 115-121.

68. Tartaj, P.; Morales, M. P.; Carreno, T. G.; Verdaguer, S. V.; Serna, C. J., Advances in magnetic nanoparticles for biotechnology applications. *J. Magn. Magn. Mater.* **2005,** 290, 28-34.

69. Komeili, A.; Hojatollah, V.; Beveridge, T. J.; Newman, D. K., Magnetosome vesicles are present before magnetite formation, and MamA is required for their activation. *Proc. Natl. Acad, Sci.* **2004,** 101, 3839.

70. Calugay, R. P.; Miyashita, H.; Okamura, Y.; Matsunaga, T., Siderophore production by the magnetic bacterium Magnetospirillum magneticum AMB-1. *FEMS Microbiol. Lett.* **2003,** 218, 371.

71. Naguchi, Y.; Fujiwara, T.; Yoshimatsu, K.; Fukumori, Y., Iron Reductase for Magnetite Synthesis in the Magnetotactic Bacterium Magnetospirillum magnetotacticum. *J. Bacteriol.* **1999,** 181, 2142.

72. Glasauer, S.; Langley, S.; Beveridge, T. J., Intracellular Iron Minerals in a Dissimilatory Iron-Reducing Bacterium. *Science* **2002,** 295, 117.

73. Lovley, D. R.; Stolz, J. F.; Nord Jr, G. L.; Phyllips, E. J. P., Anaerobic production of magnetite by a dissimilatory iron-reducing microorganism. *Nature* **1987,** 330, 252.

74. Müller, A.; Heim, O.; Panneerselvam, M.; Porada, M. W., Polyol method for the preparation of nanosized Gd_2O_3, boehmite and other oxides. *Mat. Res. Bull.* **2005,** 40, 2153–2169.

75. Dozier, D.; Palchoudhury, S.; Bao, Y., Synthesis of iron oxide nanoparticles with biological coating. *J. Sci. Health Univ. Albama* **2010,** 7, 14-18.

76. Kamruzzaman, M.; Luna, T. R.; Podder, J.; Anowar, M. G. M., Synthesis and characterization of the as-deposited $Cd_{1-x}Pb_xS$ thin films prepared by spray pyrolysis technique. *Semicond. Sci. Technol.* **2012,** 27, 035017.

77. Laudise, R. A., Hydrothermal synthesis of crystals. *Chem. Engg. News* **1987,** 65, 30.

78. Singamaneni, S.; Bliznyuk, V. N.; Binek, C.; Tsymbal, E. Y., Magnetic nanoparticles: recent advances in synthesis, self-assembly and applications. *J. Mater. Chem.* **2011,** 21, 16819-16845.

79. Park, Y. I.; Piao, Y.; Lee, N.; Yoo, B.; Kim, B. H.; Choi, S. H.; Hyeon, T., Transformation of hydrophobic iron oxide nanoparticles to hydrophilic and biocompatible maghemite nanocrystals for use as highly efficient MRI contrast agent. *J. Mater. Chem.* **2011,** 21, 11472.

80. Wang, D., Superparamagnetic Fe_2O_3 Beads-CdSe/ZnS Quantum Dots Core-Shell Nanocomposite Particles for Cell Separation. *Nano Lett.* **2004,** 4, 409-413.

81. Hwang, D. W.; Ko, H. Y.; Kim, S.-K.; Kim, D.; Lee, D. S.; Kim, S., Development of a quadruple imaging modality by using nanoparticles. *Chem. Eur. J* **2009,** 15, 9387-9393.

82. Martinez-Boubeta, C.; Simeonidis, K.; Makridis, A.; Angelakeris, M.; Iglesias, O.; Guardia, P.; Cabot, A.; Yedra, L.; Estradé, S.; Peiró, F.; Saghi, Z.; Midgley, P. A.; Conde-Leborán, I.; Serantes, D.; Baldomir, D., Learning from Nature to Improve the Heat Generation of Iron-Oxide Nanoparticles for Magnetic Hyperthermia Applications. *Sci. Rep.* **2013,** 3, 1652.

83. Colombo, M.; Romero, S. C.; Casula, M. F.; Gutierrez, L.; Morales, M. P.; Bohm, I. B.; Heverhagen, J. T.; Prosperi, D.; Parak, W. J., Biological applications of magnetic nanoparticles. *Chem. Soc. Rev.* **2012,** 41, 4306.

84. Vadahanambi, S.; Lee, S.-H.; Kim, W.-J.; Oh, I.-K., Arsenic Removal from Contaminated Water Using Three-Dimensional Graphene-Carbon Nanotube-Iron Oxide Nanostructures. *Env. Sci. Tech.* **2013,** 47, 10510-10517.

85. Koehler, F. M.; Rossier, M.; Waelle, M.; Athanassiou, E. K.; Limbach, L. K.; Grass, R. N.; Günther, D.; Stark, W. J., Magnetic EDTA: coupling heavy metal chelators to metal nanomagnets for rapid removal of cadmium, lead and copper from contaminated water. *Chem. Commun.* **2009**, (32), 4862-4864.

86. Schätz, A.; Reiser, O.; Stark, W. J., Nanoparticles as Semi-Heterogeneous Catalyst Supports. *Chem. Eur. J.* **2010,** 16, 8950–8967.

87. Philip, J.; Jaykumar, T.; Kalyanasundaram, P.; Raj, B.; Mondain-Monval, O., Effect of polymer-surfactant association on colloidal force. *Phys. Rev. E* **2002,** 66, 011406

88. Calderon, F. L.; Stora, T.; Monval, O. M., Direct measurements of colloidal forces. *Phys. Rev. Lett.* **1994,** 72, 2959-2962.

89. Mondain-Monval, O.; Espert, A.; Omarjee, P.; Bibette, J.; Leal-Calderon, F.; Philip, J.; Joanny, J. F., Polymer-Induced Repulsive Forces: Exponential Scaling. *Phys. Rev. Lett.* **1998,** 80, 1778-1781.

90. Liu, R.; Guo, Y.; Odusote, G.; Qu, F.; Priestley, R. D., Core−Shell Fe3O4 Polydopamine Nanoparticles Serve Multipurpose as Drug Carrier, Catalyst Support and Carbon Adsorbent. *Appl. Mat. Inter.* **2013 (In Press)**.

91. Atkins, P.; Paula, J. D., *Atkins' Physical Chemistry*. 8 ed.; Oxford University Press: 2006.

92. Machala, L.; Tucek, J.; Zboril, R., Polymorphous transformations of nanometric iron(III) oxide: A review. *Chem. Mater.* **2011,** 23, 3255.

93. Emmett, P. H.; Love, K. S., A comparision of the catalytic and chemical characteristics of cubic and rhombohedral Fe_2O_3. *J. Phys. Chem.* **1930,** 34, 41-62.

94. DeBoer, F. E.; Selwood, P. W., The Activation Energy for the Solid State Reaction γ-Fe_2O_3 → α-Fe_2O_3. *J. Am. Chem. Soc.* **1954,** 76, 3365-3367.

95. Egger, K.; Feitknecht, W., Uber die Oxydation von Fe_3O_4 zu γ- und α-Fe_2O_3. Die differenzthermoanalytische (DTA) und thermogravimetrische (TG) Verfolgung des Reaktionsablaufes an kunstlichen Formen von Fe_3O_4. *Helv. Chim. Acta.* **1962,** 45, 2042.

96. Colombo, U.; Gazzarrini, F.; Lanzavecchia, G.; Sironi, G., Magnetite Oxidation: A Proposed Mechanism. *Science* **1965,** 147, 1033.

97. Feitknecht, W.; Mannweiler, U., Der Mechanismus der Umwandlung von γ- zu α-Eisensesquioxid. *Helv. Chim. Acta.* **1967,** 50, 570.

98. Gallagher, K. J.; Feitknecht, W.; Mannweiler, U., Mechanism of oxidation of magnetite to γ-Fe_2O_3. *Nature* **1968,** 217, 1118.

99. Chakrabarti, S.; Chaudhuri, S.; Nambissan, P. M. G., Positron annihilation lifetime changes across the structural phase transition in nanocrystalline Fe_2O_3. *Phys. Rev. B* **2005,** 71, 064105.

100. Gnanaprakash, G.; Ayyappan, S.; Jayakumar, T.; Philip, J.; Raj, B., Magnetic nanoparticles with enhanced γ -Fe_2O_3 to α-Fe_2O_3 phase transition temperature *Nanotechnology* **2006,** 17, 5851-5857.

101. Ennas, G.; Marongiu, G.; Musinu, A.; Falqui, A.; Ballirano, P.; Caminiti, R., Characterization of nanocrystalline γ–Fe_2O_3 prepared by wet chemical method. *J. Mater. Res* **1999,** 14, 1570.

102. Ye, X.; Lin, D.; Jiao, Z.; Zhang, L., The thermal stability of nanocrystalline maghemite Fe_2O_3. *J. Phys. D: Appl. Phys.* **1998,** 31, 2739-2744.

103. Lai, J.; Shafi, K. V. P. M.; Loos, K.; Ulman, A.; Lee, Y.; Vogt, T.; Estournes, C., Doping γ-Fe_2O_3 Nanoparticles with Mn(III) Suppresses the Transition to the α-Fe_2O_3 Structure. *J. Am. Chem. Soc.* **2003,** 125, 11470-11471.

104. Deka, S.; Joy, P. A., Enhancement of the phase transition temperature of γ–Fe_2O_3 by Zn^{2+} doping. *J. Mater. Chem.* **2007,** 17, 453-456.

105. Sidhu, P. S., Transformation of trace element-substituted maghemite to hematite. *Clays Clay Miner.* **1988,** 36, 31-38.

106. Haneda, K.; Morrish, A. H., Magnetite to hematite transformation in ultrafine particles. *J. Phys. Colleque* **1977,** 38, C1-321-C1-323.

107. Lund, C. R. F.; Dumesic, J. A., Strong oxide-oxide interactions in silica-supported magnetite catalysts. 1. X-ray diffraction and Moessbauer spectroscopy evidence for interaction. *J. Phys. Chem.* **1981,** 85, 3175-3180.

108. Sidhu, P. S.; Gilkes, R. J.; Posner, A. M., The Behavior of Co, Ni, Zn, Cu, Mn, and Cr in Magnetite during Alteration to Maghemite and Hematite. *Soil Sci. Soc. Amer. J.* **1980,** 44, 135-138.

109. Sarda, C.; Rousset, A., Thermal stability of barium-doped iron oxides with spine structure. *Therm. Acta* **1993,** 222, 21.

110. Yen, F. S.; Chen, W. C.; Yang, J. M.; Hong, C. T., Crystallite Size Variations of Nanosized Fe_2O_3 Powders during γ-to α-Phase Transformation. *Nano Lett.* **2002,** 2, 245.

111. Liang, X.; Zhong, Y.; Tan, W.; Zhu, J.; Yuan, P.; He, H.; Jiang, Z., The influence of substituting metals (Ti, V, Cr, Mn, Co and Ni) on the thermal stability of magnetite. *J. Therm. Anal. Calorim.* **2013,** 111, 1317.

112. Ayyappan, S.; Gnanaprakash, G.; Panneerselvam, G.; Antony, M. P.; Philip, J., Effect of Surfactant Monolayer on Reduction of Fe_3O_4 Nanoparticles under Vacuum. *J. Phys. Chem. C* **2008,** 112, 18376-18383.

113. Xu, X.; Ge, M.; Wang, C.; Jiang, J. Z., High temperature stable monodisperse superparamagnetic core-shell iron-oxide@SnO_2 nanoparticles. *Appl. Phys. Lett.* **2009,** 95, 183112.

114. Ninjbadgar, T.; Yamamoto, S.; Takano, M., Thermal properties of the γ-Fe_2O_3/poly(methyl methacrylate) core/shell nanoparticles. *Solid state sci.* **2005,** 7, 33-36.

115. Azadmanjiri, J.; Simon, G. P.; Suzuki, K.; Selomulya, C.; Cashion, J. D., Phase reduction of coated maghemite (γ-Fe_2O_3) nanoparticles under mocrowave-induced plasma heating for rapid heat treatment. *J. Mater. Chem.* **2012,** 22, 617-625.

116. Vichery, C.; Maurin, I.; Bonville, P.; Boilot, J. P.; Gacoin, T., Influence of Protected Annealing on the Magnetic Properties of γ-Fe_2O_3 Nanoparticles. *J. Phys. Chem. C* **2012,** 116, 16311.

117. Ayyappan, S.; Panneerselvam, G.; Antony, M. P.; Philip, J., High temperature stability of surfactant capped $CoFe_2O_4$ nanoparticles. *Mater. Chem. Phys.* **2011,** 130, 1300.

118. Philip, J.; Gnanaprakash, G.; Panneerselvam, G.; Antony, M. P.; Jayakumar, T.; Raj, B., Effect of thermal annealing under vacuum on the crystal structure, size, and magnetic properties of $ZnFe_2O_4$ nanoparticles *J. Appl. Phys.* **2007,** 102, 054305.

119. Ayyappan, S.; Panneerselvam, G.; Antony, M. P.; Rao, N. V. R.; Thirumurugan, N.; Bharathi, A.; Philip, J., Effect of initial particle size on phase transformation temperature of surfactant capped Fe_3O_4 nanoparticles. *J. Appl. Phys* **2011,** 109, 084303.

120. Cullity, B. D.; Stock, S. R., *Elements of X-Ray Diffraction*. Prentice Hall: London, 2001.

121. Holzwarth, U.; Gibson, N., The Scherrer equation versus the 'Debye–Scherrer equation'. *Nat. Nanotechnol.* **2011,** 6, 534.

122. Joint Committee on Powder Diffraction Standards (JCPDS), International Centre for Diffraction Data (ICDD) Version 2.4. **2003**.

123. *Jandel Scientific AISN Software, Version2.01*, 1990.

124. Lutterotti, L., Materials Analysis Using Diffraction (MAUD) Version 2.33. **2011**.

125. Rieker, T.; Hanprasopwattana, A.; Datye, A.; Hubbard, P., Particle size distribution inferred from small-angle X-ray scattering and transmission electron microscopy. *Langmuir* **1999,** 15, 638.

126. Alexander, L. E., *X-ray Diffraction Methods in Polymer Science*. Robert E. Krieger Publishing Co.: Huntington, New York, 1979.

127. Guinier, A.; Fournet, G., *Small-Angle Scattering of X-rays*. John Willey and Sons: New York, 1955.

128. Glatter, O.; Kratky, O., *Small Angle X-ray Scattering*. Academic Press: London, 1982.

129. Owens, F. J.; Jr., C. P. P., *The physics and chemistry of nanosolids*. Jon Wiley & Sons: New Jersy, 2008.

130. Smith, B. C., *Fundamentals of Fourier Transform Infrared Spectroscopy*. CRC Press: Boca Raton, 2011.

131. Hunter, R. J., *Zeta potential in colloid science: principles and applications*. Academic Press: London, 1981.

132. Brabers, V. A. M., *Handbook of Magnetic Materials*. Elsevier: New York, NY, USA, 1995; Vol. 8.

133. Pielaszek, R.; Lojkowski, W.; Gierlotka, S.; Doyle, S., Error estimation in XRD crystallite size measurements. *Solid State Phenom.* **2006,** 114, 313-320.

134. Lai, J.; Shafi, K. V. P. M.; Ulman, A.; Loos, K.; Yang, N.-L.; Cui, M.-H.; Vogt, T.; Estournes, C.; Locke, D. C., Mixed Iron Manganese Oxide Nanoparticles. *J. Phys. Chem. B* **2004,** 108, 14876-14883.

135. Grigorova, M.; Blythe, H. J.; Blaskov, V.; Rusanov, V.; Petkov, V.; Masheva, V.; Nihtianova, D.; Martinez, L. M.; Munoz, J. S.; Mikhov, M., Magnetic properties and Mossbauer spectra of nanosized $CoFe_2O_4$ powders. *J. Magn. Magn. Mater.* **1998,** 183 163-172.

136. Xia, A.; Jin, C.; Du, D.; Sun, Y.; Tong, L., Effects of impurity Na^+ ions on the structural and magnetic properties of Ni–Zn–Cu ferrite powders: An improvement for chemical coprecipitation method. *J. Magn. Magn. Mater.* **2011,** 323, 2080-2082.

137. Ahmed, M. A.; Okasha, N.; El-Dek, S. I., Influence of Co content on the characterization and magnetic properties of magnetite. *Ceram. Int.* **2010,** 36, 1529.

138. Nakagomi, F.; Silva, S. W. d.; Garg, V. K.; Oliveira, A. C.; Morais, P. C.; Junior, A. F.; Lima, E. C. D., The influence of cobalt population on the structural properties of $Co_xFe_{3-x}O_4$. *J. Appl. Phys.* **2007,** 101, 09M514.

139. Bhame, S. D.; Joy, P. A., Enhanced Magnetostrictive properties of Mn substituted cobalt ferrite $Co_{1.2}Fe_{1.8}O_4$. *J. Appl. Phys* **2006,** 99, 073901.

140. Ayyappan, S.; Paneerselvam, G.; Antony, M. P.; Philip, J., Structural stability of $ZnFe_2O_4$ nanoparticles under different annealing conditions. *Mater. Chem. Phys.* **2011,** 128, (3), 400-404.

141. Ayyappan, S.; Raja, S. P.; Venkateswaran, C.; Philip, J.; Raj, B., Room Temperature Ferromagnetism in vacuum annealed $ZnFe_2O_4$ Nanoparticles *Appl. Phys. Lett.* **2010,** 96, 143106.

142. Kamiyama, T.; Haneda, K.; Sato, T.; Ikeda, S.; Asano, H., Cation distribution in $ZnFe_2O_4$ fine particles studied by Neutron powder diffraction. *Solid State Comm.* **1992,** 81, 563.

143. Liu, J.; Bin, Y.; Matsuo, M., Magnetic behavior of Zn-doped Fe_3O_4 nanoparticles estimated in terms of crystal domain size. *J. Phys. Chem. C* **2012,** 116, 134-143.

144. West, A. R., *Solid State Chemistry and Its Applications*. Wiley: New York, 1984.

145. Jones, J. E. L., *Z. Crystallogr.* **1930,** 75, 215.

146. Ayyub, P.; Palkar, V. R.; Chattopadhyay, S.; Multani, M., Effect of crystal size reduction on lattice symmetry and cooperative properties. *Phys. Rev. B* **1995,** 51, 6135.

147. Zaag, P. J. v. d.; Noordermeer, A.; Johnson, M. T.; Bongers, P. F., Comment on size dependent Curie temperature in nanoscale $MnFe_2O_4$ *Phys. Rev. Lett.* **1992,** 68, 3112.

148. L. R. Bickford, J., The Low Temperature Transformation in Ferrites. *Rev. Mod. Phys.* **1953,** 25, 75–79.

149. Leung, L. K.; Evans, B. J.; Morrish, A. H., Low-Temperature Mössbauer Study of a Nickel-Zinc Ferrite: $Zn_xNi_{1-x}Fe_2O_4$. *Phys. Rev. B* **1973,** 8, 29-43.

150. Lee, J. D., *Concise Inorganic Chemistry*. Fifth ed.; Blackwell Science Ltd.: London, 2005.

151. Li, Y.; Li, Q.; Wen, M.; Zhang, Y.; Zhai, Y.; Xie, Z.; Xu, F.; Wei, S., Magnetic properties and local structure studies of Zn doped ferrites. *J. Electron Spectrosc.* **2007,** 160, 1-6.

152. Martínez-Boubeta, C.; Simeonidis, K.; Angelakeris, M.; Pazos-Pérez, N.; Giersig, M.; Delimitis, A.; Nalbandian, L.; Alexandrakis, V.; Niarchos, D., Critical radius for exchange bias in naturally oxidized Fe nanoparticles. *Phys. Rev. B* **2006,** 74, 054430.

153. Carta, D.; Casula, M. F.; Falqui, A.; Loche, D.; Mountjoy, G.; Sangregorio, C.; Corrias, A., A Structural and Magnetic Investigation of the Inversion Degree in Ferrite Nanocrystals MFe_2O_4 (M) Mn, Co, Ni). *J. Phys. Chem. C* **2009,** 113, 8606.

154. Buske, N., Application of magnetite sols in environmental technology. *Progr. Colloid Polym. Sci.* **1994,** 95, 175-180.

155. Morais, P. C.; Silva, S. W. d.; Soler, M. A. G.; Buske, N., Raman spectroscopy in magnetic fluids. *Biomol. Eng.* **2001,** 17, 41-49.

156. Hyeon, T.; Lee, S. S.; Park, J.; Chung, Y.; Na, H. B., Synthesis of Highly Crystalline and Monodisperse Maghemite Nanocrystallites without a Size-Selection Process. *J. Am. Chem. Soc.* **2001,** 123, 12798.

157. Wooding, A.; Kilner, M.; Lambrick, D. B., Studies of the double surfactant layer stabilization of water-based magnetic fluids. *J. Colloid Interface Sci.* **1991,** 144, 236-242.

158. Underhill, R. S.; Liu, G., Triblock Nanospheres and Their Use as Templates for Inorganic Nanoparticle Preparation. *Chem. Mater.* **2000,** 12, 2082-2091.

159. Muthukumaran, T.; Gnanaprakash, G.; Philip, J., Synthesis of Stable Magnetic Nanofluids of Different Particle Sizes. *J. Nanofluids* **2012,** 1, 85-92.

160. Jain, N.; Wang, Y.; Jones, S. K.; Hawkett, B. S.; Warr, G. G., Optimized Steric Stabilization of Aqueous Ferrofluids and Magnetic Nanoparticles. *Langmuir* **2009,** 26, 4465-4472.

161. Park, J.; An, K.; Hwang, Y.; Park, J.; Noh, H.; Kim, J.; Park, J.; Hwang, N.; Hyeon, T., Ultra-large-scale syntheses of monodisperse nanocrystals. *Nat. Mater.* **2004,** 3, 891.

162. Euliss, L. E.; Grancharov, S. G.; O'Brien, S.; Deming, T. J.; Stucky, G. D.; Murray, C. B.; Held, G. A., Cooperative Assembly of Magnetic Nanoparticles and Block Copolypeptides in Aqueous Media. *Nano Lett.* **2003,** 3, 1489.

163. Pardoe, H.; Chua-anusorn, W.; Pierre, T. G. S.; Dobson, J., Structural and magnetic properties of nanoscale iron oxide particles synthesized in the presence of dextran or polyvinyl alcohol. *J. Magn. Magn. Mater.* **2001,** 225, 41.

164. Harris, L. A.; Goff, J. D.; Carmichael, A. Y.; Riffle, J. S.; Harburn, J. J.; Saunder, S., M., Magnetite Nanoparticle Dispersions Stabilized with Triblock Copolymers. *Chem. Mater.* **2003,** 15, 1367-1377.

165. Waldron, R. D., Infrared spectra of Ferrites. *Phys. Rev.* **1955,** 99, 1727.

166. Rietveld, H. M., A profile refinement method for nuclear and magnetic structures. *J. Appl. Cryst.* **1969,** 2, 65-71.

167. Nanda, K. K.; Maisels, A.; Kruis, F. E.; Fissan, H.; Stappert, S., Higher Surface Energy of Free Nanoparticles. *Phys. Rev. Lett.* **2003,** 90, 106102.

168. Stoneham, A. M., Measurement of surface tension by lattice parameter changes : theory for facetted microcrystals. *J. Phys. C: Solid State Phys.* **1977,** 10, 1175-1179.

169. Schumacher, S.; Birringer, R.; Straw, R.; Gleiter, H., Diffusion of silver in nanocrystalline copper between 300 and 373K. *Acta. Metall.* **1989,** 37, 2485-2488.

170. Bhattacharya, J.; Ven, A. V. d., Phase stability and nondilute lithium diffusion in spinel $Li_{1+x}Ti_2O_4$. *Phys. Rev. B* **2010,** 81, 104304.

171. Lee, J. D., *Concise Inorganic Chemistry*. Fifth ed.; Blackwell Science Ltd.: London, 2005.

172. Yang, H.; Zhang, X.; Ao, W.; Qiu, G., Formation of $NiFe_2O_4$ nanoparticles by mechanochemical reaction. *Mater. Res. Bull.* **2004,** 39, 833-837.

173. Tarascon, J. M.; Guyomard, D. G.; Wilkens, B., Chemical and electrochemical insertion of Na into the spinel λ-MnO_2 phase. *Solid State Ionics* **1992,** 57, 113-120.

174. Sear, R. P., Heterogeneous and Homogeneous Nucleation Compared: Rapid Nucleation on Microscopic Impurities. *J. Phys. Chem. B* **2006,** 110, 4985-4989.

175. Chen, J. P.; Sorensen, C. M.; Klabunde, K. J.; Hadjipanayis, G. C.; Devlin, E.; Kostikas, A., Size-dependent magnetic properties of MnFe2O4 fine particles synthesized by coprecipitation. *Phys. Rev. B* **1996,** 54, 9288-9296.

176. Junior, A. F.; Zapf, V.; Egan, P., Magnetic properties of nanoparticles of $Co_xFe_{3-x}O_4$ prepared by combustion reaction
J. Appl. Phys. **2007,** 101, 09M506.

177. He, Y. P.; Miao, Y. M.; Li, C. R.; Wang, S. Q.; Cao, L.; Xie, S. S.; Yang, G. Z.; Zou, B. S.; Burda, C., Size and structure effect on optical transitions of iron oxide nanocrystals. *Phys. Rev. B* **2005,** 71, 125411.

178. Gnanaprakash, G.; Philip, J.; Jayakumar, T.; Raj, B., Effect of Digestion Time and Alkali Addition Rate on Physical Properties of Magnetite Nanoparticles. *J. Phys. Chem. B* **2007,** 111, 7978.

179. Tang, Z. X.; Sorensen, C. M.; Klabunde, K. J.; G.C.Hadjipanayis, Size depencent Curie Temp. in MnFe2O4. *Phys. Rev. Lett.* **1991,** 67, 3602.

180. Treybal, R. E., *Mass-transfer operations*. McGraw-Hill: New York, 1980; Vol. 3.

181. Giri, J.; Ray, A.; Dasgupta, S.; Datta, D.; Bahadur, D., Investigation on T_c tuned nano particles of magnetic oxides for hyperthermia applications. *Biomed. Mater. Eng.* **2003,** 13, 387-399.

182. Alaan, U. S.; Wong, F. J.; Grutter, A. J.; Iwata-Harms, J. M.; Mehta, V. V.; Arenholz, E.; Suzuki, Y., Structure and magnetism of nanocrystalline and epitaxial $(Mn,Zn,Fe)_3O_4$ thin films. *J. Appl. Phys.* **2012,** 111, 07A337.

183. Guo, L.; Wang, X.; Zhong, C.; Li, L., Template-based synthesis and magnetic properties of Mn-Zn ferrite nanotube and nanowire arrays. *J. Appl. Phys.* **2012,** 111, 026104.

184. Jeyadevan, B.; Chinnasamy, C. N.; Shinoda, K.; Tohji, K.; Oka, H., Mn–Zn ferrite with higher magnetization for temperature sensitive magnetic fluid. *J. Appl. Phys.* **2003,** 93, 8450.

185. Arulmurugan, R.; Vaidyanathan, G.; Sendhilnathan, S.; Jeyadevan, B., Mn–Zn ferrite nanoparticles for ferrofluid preparation: Study on thermal–magnetic properties. *J. Magn. Magn. Mater.* **2006,** 298, 83-94.

186. Poddar, P.; Srikanth, H.; Morrison, S. A.; Carpenter, E. E., Inter-particle interactions and magnetism in manganese–zinc ferrite nanoparticles. *J. Magn. Magn. Mat.* **2005,** 288, 443-451.

187. Beji, Z.; Hanini, A.; Smiri, L. S.; Gavard, J.; Kacem, K.; Villain, F.; Grenèche, J. M.; Chau, F.; Ammar, S., Magnetic properties of Zn-substituted $MnFe_2O_4$ nanoparticles synthesized in polyol as potential heating agents for hyperthermia. Evaluation of their toxicity on Endothelial cells. *Chem. Mater.* **2010,** 22, 5420.

188. Morrison, S. A.; Cahill, C. L.; Carpenter, E. E.; Calvin, S.; Harris, V. G., Preparation and characterization of MnZn–ferrite nanoparticles using reverse micelles. *J. Appl. Phys.* **2003,** 93, 7489.

189. Rath, C.; Anand, S.; Das, R. P.; Sahu, K. K.; Kulkarni, S. D.; Date, S. K.; Mishra, N. C., Dependence on cation distribution of particle size, lattice parameter, and magnetic properties in nanosize Mn–Zn ferrite. *J. Appl. Phys.* **2002,** 91, 2211.

190. Hejase, H.; Hayek, S. S.; Qadri, S.; Haik, Y., MnZnFe nanoparticles for self-controlled magnetic hyperthermia. *J. Magn. Magn. Mat.* **2012,** 324, 3620-3628.

191. Rath, C.; Sahu, K. K.; Anand, S.; Date, S. K.; Mishra, N. C.; Das, R. P., Preparation and characterization of nanosize Mn–Zn ferrite. *J. Magn. Magn. Mater.* **1999,** 202, 77-84.

192. Naseri, M. G.; Saion, E. B.; Ahangar, H. A.; Hashim, M.; Shaari, A. H., Synthesis and characterization of manganese ferrite nanoparticles by thermal treatment method. *J. Magn. Magn. Mat.* **2011,** 323, 1745-1749.

193. Morrish, A. H.; Clark, P. E., High field Mossbauer study of manganese zinc ferrites. *Phys. Rev. B* **1975,** 11, 278.

194. Shultz, M. D.; Carpenter, E. E.; Morrison, S. A.; Calvin, S., Cation occupancy determination in manganese zinc ferritesusing Fourier transform infrared spectroscopy. *J. Appl. Phys.* **2006,** 99 08M901.

195. Yamashita, O.; Ikeda, T., Effect of polishing stress on Raman spectra of the Mn–Zn ferrite. *J. Appl. Phys.* **2004,** 95, 1743.

196. Mandal, K.; Chakraverty, S.; Mandal, S. P.; Agudo, P.; Pal, M.; Chakravorty, D., Size-dependent magnetic properties of $Mn_{0.5}Zn_{0.5}Fe_2O_4$ nanoparticles in SiO_2 matrix. *J. Appl. Phys.* **2002,** 92, 501.

197. Jordan, A.; Scholz, R.; Wust, P.; Schirra, H.; Schiestel, T.; Schmidt, H.; Felix, R., Endocytosis of dextran and silan-coated magnetite nanoparticles and the effect of intracellular hyperthermia on human mammary carcinoma cells in vitro. *J. Magn. Magn. Mater.* **1999,** 194, 185-196.

198. Kikuchi, T.; Kasuya, R.; Endo, S.; Nakamura, A.; Takai, T.; Metzler-Nolte, N.; Tohji, K.; Balachandran, J., Preparation of magnetite aqueous dispersion for magnetic fluid hyperthermia. *J. Magn. Magn. Mater.* **2011,** 323, 1216.

199. Kim, D.-H.; Nikles, D. E.; Johnson, D. T.; Brazel, C. S., Heat generation of aqueously dispersed CoFe2O4 nanoparticles as heating agents for magnetically activated drug delivery and hyperthermia *J. Magn. Magn. Mater.* **2008,** 320, 2390.

200. Sharifi, I.; Shokrollahi, H.; Amiri, S., Ferrite-based magnetic nanofluids used in hyperthermia applications. *J. Magn. Magn. Mater.* **2012,** 324, 903-915.

201. Kulkarni, G. U.; Kannan, K. R.; Arunarkavalli, T.; Rao, C. N. R., Particle size effect on the value of TC of MnFe2O4 Evidence for finite size scalling. *Phys. Rev. B* **1994,** 49, 724.

202. Lan, N. T.; Hien, T. D.; Duong, N. P.; Truong, D. V., Magnetic properties of $Mn_{1-x}Zn_xFe_2O_4$ ferrite nanoparticles prepared by using co-precipitation. *J. Korean Phys. Soc.* **2008,** 52, 1522-1525.

203. Calvin, S.; Carpenter, E. E.; Ravel, B.; Harris, V. G.; Morrison, S. A., Multiedge refinement of extended x-ray-absorption fine structure of manganese zinc ferrite nanoparticles. *Phys. Rev. B* **2002,** 66, 224405.

204. Shannon, R. D., Revised effective ionic radii and systematicstudies of interatomie distances in halides and chaleogenides *Acta Cryst.* **1976,** A32, 751-767.

205. Varshney, D.; Verma, K.; Kumar, A., Structural and vibrational properties of $Zn_xMn_{1-x}Fe_2O_4$ (x = 0.0, 0.25, 0.50, 0.75, 1.0) mixed ferrites. *Mater. Chem. Phys.* **2011,** 131, 413.

206. Shultz, M. D.; Allsbrook, M. J.; Carpenter, E. E., Control of the cation occupancies of MnZn ferrite synthesized via reverse micelles
J. Appl. Phys. **2007,** 101, 09M518.

207. Mohapatra, J.; Mitra, A.; Bahadur, D.; Aslam, M., Surface controlled synthesis of MFe_2O_4 (M=Mn, Fe, Co, Ni and Zn) nanoparticles and their magnetic characteristics. *Cryst. Eng. Comm.* **2013,** 15, 524-532.

208. Suzuki, M.; Fullem, S. I.; Suzuki, I. S., Observation of superspin-glass behavior in Fe3O4 nanoparticles. *Phys. Rev. B* **2009,** 79, 024418.

209. Ibrahim, E. M. M., Effect of Dy^{+3} on the structure and static magnetic properties of spin-glass MnZn ferrite nanoparticles. *J. Appl. Phys.* **2013,** 113, 154301.